

# Exploring Airfoil Table Generation Using XFOIL and OVERFLOW

a project presented to  
The Faculty of the Department of Aerospace Engineering  
San José State University

in partial fulfillment of the requirements for the degree  
*Master of Science in Aerospace Engineering*

by

**Kristen Kallstrom**

December 2021

approved by

Dr. Gloria K. Yamauchi  
Mentor

Dr. Periklis Papadopoulos  
Faculty Advisor



**San José State**  
UNIVERSITY

© 2021  
Kristen Kallstrom  
ALL RIGHTS RESERVED

## ABSTRACT

### **Airfoil Table Generation Using XFOIL and OVERFLOW**

Kristen Kallstrom

The rotorcraft design process is a continuously evolving field of research that incorporates a number of software programs. An accurate airfoil table is critical in the design and testing process for rotorcraft. With multiple flow solvers available and flow conditions of multirotor UAM vehicles potentially covering a wide range of Reynolds and Mach numbers, a documented approach for developing airfoil tables is needed. Using benchmark data from legacy airfoil tables and wind tunnel tests for comparison, simulations for a comprehensive test matrix could guide rotorcraft design engineers in generating their own airfoil tables using the XFOIL and OVERFLOW solvers. The motivation for this study is to investigate flow solver features to develop a best practices document for airfoil table generation. The study uses the OVERFLOW and XFOIL flow solvers, coupled with the airfoil table generator AFTGen, to analyze three airfoils for a specific Reynolds numbers flow regime and provide details on how well each flow solver performs within a specific angle of attack range, Mach number range, Reynolds number range, and in different flow conditions, such as turbulent and transitional flow. OVERFLOW analyses in AFTGen for fully turbulent and transition flow are compared with XFOIL results and experimental test data for the section lift, section drag, and pressure coefficients. XFOIL ultimately yields results that are accurate within the linear angle of attack range and below a Mach number of 0.4 but tends to overpredict lift and underpredict drag unless the flow is in the compressible regime. XFOIL cannot accurately model stall and post-stall conditions due to the nature of the solver. This is evident in nearly every case run with XFOIL, where the linear range is usually predicted acceptably, and the lift coefficient is overpredicted as the stall angle of attack is approached (with the exception being the generally poor correlation with most of the SSC-A09 cases). OVERFLOW is limited at low Mach numbers, and appears to perform best at Mach numbers of 0.4 and above. The exploration of airfoil table generation using XFOIL and OVERFLOW yielded moderately successful results for the NACA 0012 airfoil, reasonably good results for the RC(4)-10 airfoil, and less accurate results for the SSC-A09 airfoil.

## ACKNOWLEDGEMENTS

I would love to express my sincere and heartfelt appreciation to several people that provided me with support, advice, and feedback throughout this graduate study. Firstly, I would like to thank my mentor Dr. Gloria K. Yamauchi for her enduring patience and support throughout this study. Meeting once, sometimes twice a week kept me motivated and my head above water, and all of her help working through some of the many challenges is sincerely appreciated. Since this is the start of what is sure to be a long-term development of airfoil table best practices, I am looking forward to continuing to explore this research area under your continued guidance and with your expertise. A sincere thank you for your limitless kindness, understanding, and encouragement. I would also like to thank Dr. Ethan Romander for training me to be the next super nerd in the branch throughout this master's project. He helped me navigate the unfamiliar waters of accessing Pleiades and using PBS scripts to set up AFTGen jobs to run OVERFLOW cases. Ethan saved me from a fate of using standard desktop computers to run literally thousands of cases. His advice and training classes on how to use some of the software were invaluable. I would like to thank Dr. Pieter Buning and Brian Allan for your willingness to meet with me to discuss OVERFLOW results, ask questions, and benefit from your expertise with OVERFLOW and CFD. Our progress meetings and the recommendations for next steps to improve results were incredibly helpful. I would like to thank Dr. Periklis Papadopoulos and Dr. Nikos Mourtos for their guidance and support over the years. Their patience and expertise were sincerely appreciated. I would finally like to thank my family, friends, and colleagues for putting up with my stress level and intermittent ghosting this year - I couldn't have managed this without their unwavering understanding and support.

# TABLE OF CONTENTS

ABSTRACT .....	3
ACKNOWLEDGEMENTS .....	iv
TABLE OF CONTENTS .....	v
LIST OF TABLES .....	1
LIST OF FIGURES .....	2
NOMENCLATURE .....	6
Chapter 1. Introduction.....	1
1.1. Airfoil Tables Overview.....	1
1.2. Rotorcraft Design Process .....	2
1.3. Legacy Airfoil Tables.....	4
1.4. Airfoil Selection .....	4
1.4.1. NACA 0012.....	4
1.4.2. RC(4)-10.....	5
1.4.3. SSC-A09.....	7
1.5. Applicability .....	9
1.5.1. Low Reynolds Number Applications.....	10
1.6. Project Objective .....	11
1.6.1. Methodology .....	11
Chapter 2. Mathematical Model.....	13
2.1. Boundary Layers.....	13
2.2. XFOIL Panel Methods.....	15
2.3. OVERFLOW .....	17
Chapter 3. Computational Approach.....	19
3.1. AFTGen .....	19
3.2. Primary Case Setup .....	19
3.3. AFTGen with XFOIL Setup.....	19
3.4. AFTGen with OVERFLOW Setup.....	20
3.4.1. 2D Grid.....	20
3.4.2. Time Grid .....	21
3.4.3. Run Control Options .....	21
3.4.4. Numerical Scheme .....	22
Chapter 4. Results and Discussion .....	24
4.1. OVERFLOW Leading Edge Geometry Improvements.....	24
4.2. OVERFLOW Trailing Edge and Clustering Iterations Study .....	25
4.3. XFOIL and OVERFLOW Results.....	33
4.3.1. NACA 0012.....	33

4.3.2. RC(4)-10.....	40
4.3.3. SSC-A09.....	45
Chapter 5. Conclusion .....	54
Chapter 6. Future Work.....	55
References .....	56
Appendix A - NACA 0012 Airfoil Table.....	58
Appendix B - NACA 0012 XFOIL and OVERFLOW Results .....	62
Appendix C - RC(4)-10 XFOIL and OVERFLOW Results .....	76
Appendix D - SSC-A09 XFOIL and OVERFLOW Results .....	93

## LIST OF TABLES

Table 1.1. Line 1 description for typical .c81 table. ....	2
Table 1.2. Summarized $c_{l_{max}}$ and drag divergence values for the RC(4)-10 versus the VR-7 (where applicable) [12]. ....	5
Table 1.3. Airfoil characteristics, plus $c_{l_{max}}$ and drag divergence at zero lift, adapted from data in Flemming [14]. ....	8
Table 3.1 Angle of attack, Mach number, and Reynolds number input range for each airfoil. ...	19
Table 3.2. XFOIL run control and boundary layer inputs. ....	20
Table 3.3. Amplification factor for airfoil surface roughness in various conditions. ....	20
Table 3.4. Preliminary 2D grid inputs for AFTGen using the OVERFLOW solver. ....	21
Table 3.5. Time Grid settings for all airfoil cases. ....	21
Table 3.6. Default run control options in AFTGen with OVERFLOW. ....	22
Table 4.1. AFTGen inputs for the trailing edge and clustering iterations studies. ....	25
Table 4.2. NACA 0012 AFTGen inputs for airfoil table generation in XFOIL and OVERFLOW. ....	33
Table 4.3. Calculated stagnation pressure coefficients at all Mach numbers for the NACA 0012 airfoil. ....	39
Table 4.4. RC(4)-10 primary inputs for XFOIL and OVERFLOW. ....	40
Table 4.5. Calculated stagnation pressure coefficients at all Mach numbers for the RC(4)-10 airfoil. ....	43
Table 4.6. SSC-A09 primary inputs for XFOIL and OVERFLOW. Total pressure is included for completeness. ....	45
Table 4.7. Summary of maximum lift and minimum drag coefficients for the SSC-A09 airfoil results. ....	47
Table 4.8. SSC-A09 hand calculated pressure coefficients at the stagnation point. ....	48

## LIST OF FIGURES

Figure 1.1. Aerodynamic forces acting on an airfoil. [1].....	1
Figure 1.2. Partial example of the standard 0012 airfoil table commonly used by NASA and industry. [2].....	2
Figure 1.3. Rotor blade radial stations from the blade tip inward [2].....	3
Figure 1.4. Rotorcraft design process in the NASA Aeromechanics Office [2].....	3
Figure 1.5. NACA 0012 symmetrical airfoil profile [8].....	5
Figure 1.6. RC(4)-10 lift coefficient versus zero lift angle of attack, as compiled by Noonan [12]. .....	6
Figure 1.7. RC(4)-10 drag coefficient versus lift coefficient, as compiled by Noonan [12].	6
Figure 1.8. Re versus Mach for both 1 atm and 1.4 atm test conditions [14].....	7
Figure 1.10. SC1095, A-2, and SSC-A09 airfoil contours [15].....	8
Figure 1.11. The RAM process, as provided by Murphy, Buning, and Simmons [16].....	9
Figure 1.12. Sectional lift, drag, and moment coefficients for the SSC-A09 airfoil [17].....	9
Figure 1.13. NASA research areas for the development of next generation, fully electric aircraft [18]. .....	10
Figure 2.1. Boundary layer properties on a flat plate [1].....	13
Figure 2.2. Panel coordinate system used in XFOIL [20].	16
Figure 2.3. Simplification of structured O-grid and C-grid options in OVERFLOW [23].	17
Figure 2.4. OVERFLOW transport equation with generalized $\xi$ , $\eta$ , and $\zeta$ coordinates [24].	18
Figure 4.1. Close up of the leading edge of the RC(4)-10 airfoil; default coordinates (left) and the denser leading edge coordinates (right).	24
Figure 4.2. Close up of the leading edge of the SSC-A09 airfoil; default coordinates (left) and denser leading-edge coordinates (right).	24
Figure 4.3. TE point change for the NACA 0012 at $M = 0.3$ and $Re/M = 5.2 \times 10^6$ .	26
Figure 4.4. TE point change for the NACA 0012 at $M = 0.4$ and $Re/M = 5.2 \times 10^6$ .	26
Figure 4.5. Lift coefficient versus $\alpha$ for the RC(4)-10 airfoil at $M = 0.34$ and $Re = 3.9 \times 10^6$ .	27
Figure 4.6. Lift coefficient versus $\alpha$ for the RC(4)-10 airfoil at $M = 0.49$ and $Re = 3.8 \times 10^6$ .	28
Figure 4.7. Lift coefficient versus $\alpha$ for the RC(4)-10 airfoil at $M = 0.63$ and $Re = 7.9 \times 10^6$ .	28
Figure 4.8. Effect on the overall RC(4)-10 grid for 11 TE points (top) and 33 TE points (bottom). .....	29
Figure 4.9. Change in CI for the NACA 0012 at $M = 0.3$ and $Re/M = 5.2 \times 10^6$ .	29
Figure 4.10. Change in CI for the NACA 0012 at $M = 0.4$ and $Re/M = 5.2 \times 10^6$ .	30
Figure 4.11. RC(4)-10 clustering iterations study at $M = 0.44$ and $Re = 6 \times 10^6$ , $c_l$ vs $\alpha$ .	30
Figure 4.12. RC(4)-10 clustering iterations study at $M = 0.44$ and $Re = 6 \times 10^6$ , $c_d$ vs $\alpha$ .	31
Figure 4.13. CI at the leading edge; 17a: 20K CI; 17b: 60K CI.	31
Figure 4.14. SSC-A09 CI study, Run 65 at $M = 0.599$ and $Re = 5.16 \times 10^6$ , $c_l$ vs $\alpha$ .	32
Figure 4.15. SSC-A09 CI study, Run 65 at $M = 0.599$ and $Re = 5.16 \times 10^6$ , $c_d$ vs $\alpha$ .	32
Figure 4.16. $C_p$ vs $x/c$ for the NACA 0012 airfoil at Mach 0.3. Digitized from Figure 40a [8].	35
Figure 4.17. $C_p$ vs $x/c$ for the NACA 0012 airfoil at Mach 0.6. Experimental data digitized from Figure 40e [8].	36
Figure 4.18. Pressure coefficient contour and vector plots at Mach 0.3 for the NACA 0012.	37
Figure 4.19. Mach contour and vector plots at Mach 0.3 for the NACA 0012.	37
Figure 4.20. Pressure coefficient contour and vector plots at Mach 0.6 for the NACA 0012.	38
Figure 4.21. $C_p$ vs $x/c$ for the RC(4)-10 airfoil at Mach 0.34, Reynolds $4.8 \times 10^6$ . Experimental data digitized from Figure 24a [13].	42

Figure 4.22. $C_p$ vs $x/c$ for the RC(4)-10 airfoil at Mach 0.44, Reynolds $6.0 \times 10^6$ . Experimental data digitized from Figure 24b [13].	42
Figure 4.23. $C_p$ vs $x/c$ for the RC(4)-10 airfoil at Mach 0.59, Reynolds $7.5 \times 10^6$ . Experimental data digitized from Figure 24e [13].	43
Figure 4.24. Pressure coefficient and Mach number contours for the RC(4)-10 airfoil at Mach 0.34 and a Reynolds number of $4.8 \times 10^6$ .	44
Figure 4.25. Pressure coefficient and Mach number contours for the RC(4)-10 airfoil at Mach 0.44 and a Reynolds number of $6.0 \times 10^6$ .	44
Figure 4.26. Pressure coefficient and Mach number contours for the RC(4)-10 airfoil at Mach 0.59 and a Reynolds number of $7.5 \times 10^6$ .	44
Figure 4.27. SSC-A09 pressure coefficient plot for Run 60.	49
Figure 4.28. Pressure and Mach contour for the SSC-A09 airfoil, Run 60.	49
Figure 4.30. SSC-A09 pressure coefficient plot for Run 65.	50
Figure 4.31. Pressure coefficient contour for the SSC-A09 airfoil, Run 60.	50
Figure 4.32. Mach number contour for the SSC-A09 airfoil, Run 60.	51
Figure 4.33 SSC-A09 grid resolution study, with a 20% increase in grid size.	52
Figure C.1 NACA 0012 lift curve at Mach 0.2.	62
Figure C.2 NACA 0012 lift curve at Mach 0.3.	62
Figure C.3 NACA 0012 lift curve at Mach 0.4.	63
Figure C.4. NACA 0012 lift curve at Mach 0.5.	63
Figure C.5 NACA 0012 lift curve at Mach 0.6.	64
Figure C.6 NACA 0012 lift curve at Mach 0.7.	64
Figure C.7 NACA 0012 lift curve at Mach 0.75.	65
Figure C.8 NACA 0012 lift curve at Mach 0.8.	65
Figure C.9. NACA 0012 lift curve at Mach 0.9.	66
Figure C.10 NACA 0012 lift curve at Mach 1.0.	66
Figure C.11 NACA 0012 drag bucket at Mach 0.18.	67
Figure C.12 NACA 0012 drag bucket at Mach 0.28.	67
Figure C.13 NACA 0012 drag bucket at Mach 0.38.	68
Figure C.14 NACA 0012 drag bucket at Mach 0.48.	68
Figure C.15 NACA 0012 drag bucket at Mach 0.62.	69
Figure C.16 NACA 0012 drag bucket at Mach 0.72.	69
Figure C.17 NACA 0012 drag bucket at Mach 0.77.	70
Figure C.18 NACA 0012 drag bucket at Mach 0.82.	70
Figure C.19 NACA 0012 moment coefficient versus $\alpha$ at Mach 0.2.	71
Figure C.20 NACA 0012 moment coefficient versus $\alpha$ at Mach 0.3.	71
Figure C.21 NACA 0012 moment coefficient versus $\alpha$ at Mach 0.4.	72
Figure C.22 NACA 0012 moment coefficient versus $\alpha$ at Mach 0.5.	72
Figure C.23 NACA 0012 moment coefficient versus $\alpha$ at Mach 0.6.	73
Figure C.24 NACA 0012 moment coefficient versus $\alpha$ at Mach 0.7.	73
Figure C.25 NACA 0012 moment coefficient versus $\alpha$ at Mach 0.75.	74
Figure C.26 NACA 0012 moment coefficient versus $\alpha$ at Mach 0.8.	74
Figure C.27 NACA 0012 moment coefficient versus $\alpha$ at Mach 0.9.	75
Figure D.1 RC(4)-10 lift curve at Mach 0.34 and a Reynolds number of $3.9 \times 10^6$ .	76
Figure D.2 RC(4)-10 lift curve at Mach 0.34 and a Reynolds number of $4.8 \times 10^6$ .	76
Figure D.3 RC(4)-10 lift curve at Mach 0.37 and a Reynolds number of $3.8 \times 10^6$ .	77

Figure D.4 RC(4)-10 lift curve at Mach 0.39 and a Reynolds number of $3.8 \times 10^6$ .....	77
Figure D.5 RC(4)-10 lift curve at Mach 0.39 and a Reynolds number of $5.4 \times 10^6$ .....	78
Figure D.6 RC(4)-10 lift curve at Mach 0.42 and a Reynolds number of $3.8 \times 10^6$ .....	78
Figure D.7 RC(4)-10 lift curve at Mach 0.42 and a Reynolds number of $5.7 \times 10^6$ .....	79
Figure D.8 RC(4)-10 lift curve at Mach 0.44 and a Reynolds number of $3.8 \times 10^6$ .....	79
Figure D.9. RC(4)-10 lift curve at Mach 0.44 and a Reynolds number of $6.0 \times 10^6$ .....	80
Figure D.10. RC(4)-10 lift curve at Mach 0.49 and a Reynolds number of $3.8 \times 10^6$ .....	80
Figure D.11 RC(4)-10 lift curve at Mach 0.49 and a Reynolds number of $6.6 \times 10^6$ .....	81
Figure D.12 RC(4)-10 lift curve at Mach 0.54 and a Reynolds number of $7.0 \times 10^6$ .....	81
Figure D.13 RC(4)-10 lift curve at Mach 0.59 and a Reynolds number of $7.5 \times 10^6$ .....	82
Figure D.14 RC(4)-10 lift curve at Mach 0.69 and a Reynolds number of $8.3 \times 10^6$ .....	82
Figure D.15 RC(4)-10 lift curve at Mach 0.73 and a Reynolds number of $8.5 \times 10^6$ .....	83
Figure D.16 RC(4)-10 lift curve at Mach 0.78 and a Reynolds number of $8.8 \times 10^6$ .....	83
Figure D.17 RC(4)-10 drag bucket at Mach 0.34 and a Reynolds number of $3.9 \times 10^6$ .....	84
Figure D.18 RC(4)-10 drag bucket at Mach 0.34 and a Reynolds number of $4.8 \times 10^6$ .....	84
Figure D.19 RC(4)-10 drag bucket at Mach 0.37 and a Reynolds number of $3.8 \times 10^6$ .....	85
Figure D.20 RC(4)-10 drag bucket at Mach 0.39 and a Reynolds number of $3.8 \times 10^6$ .....	85
Figure D.21 RC(4)-10 drag bucket at Mach 0.39 and a Reynolds number of $5.4 \times 10^6$ .....	86
Figure D.22 RC(4)-10 drag bucket at Mach 0.42 and a Reynolds number of $3.8 \times 10^6$ .....	86
Figure D.23 RC(4)-10 drag bucket at Mach 0.42 and a Reynolds number of $5.7 \times 10^6$ .....	87
Figure D.24 RC(4)-10 drag bucket at Mach 0.44 and a Reynolds number of $3.8 \times 10^6$ .....	87
Figure D.25 RC(4)-10 drag bucket at Mach 0.44 and a Reynolds number of $6.0 \times 10^6$ .....	88
Figure D.26 RC(4)-10 drag bucket at Mach 0.49 and a Reynolds number of $3.8 \times 10^6$ .....	88
Figure D.27 RC(4)-10 drag bucket at Mach 0.49 and a Reynolds number of $6.6 \times 10^6$ .....	89
Figure D.28 RC(4)-10 drag bucket at Mach 0.54 and a Reynolds number of $7.0 \times 10^6$ .....	89
Figure D.29 RC(4)-10 drag bucket at Mach 0.59 and a Reynolds number of $7.5 \times 10^6$ .....	90
Figure D.30 RC(4)-10 drag bucket at Mach 0.63 and a Reynolds number of $7.9 \times 10^6$ .....	90
Figure D.31 RC(4)-10 drag bucket at Mach 0.69 and a Reynolds number of $8.3 \times 10^6$ .....	91
Figure D.32 RC(4)-10 drag bucket at Mach 0.73 and a Reynolds number of $8.5 \times 10^6$ .....	91
Figure D.33 RC(4)-10 drag bucket at Mach 0.78 and a Reynolds number of $8.8 \times 10^6$ .....	92
Figure E.1 SSC-A09, Run 60, Mach 0.399, Re $3.85 \times 10^6$ : lift coefficient versus $\alpha$ .....	93
Figure E.2 SSC-A09, Run 61, Mach 0.307, Re $4.29 \times 10^6$ : lift coefficient versus $\alpha$ .....	93
Figure E.3 SSC-A09, Run 63, Mach 0.5, Re $4.57 \times 10^6$ : lift coefficient versus $\alpha$ .....	94
Figure E.4 SSC-A09, Run 65, Mach 0.599, Re $5.16 \times 10^6$ : lift coefficient versus $\alpha$ .....	94
Figure E.5 SSC-A09, Run 68, Mach 0.603, Re $5.21 \times 10^6$ : lift coefficient versus $\alpha$ .....	95
Figure E.6 SSC-A09, Run 69, Mach 0.703, Re $5.73 \times 10^6$ : lift coefficient versus $\alpha$ .....	95
Figure E.7 SSC-A09, Run 70, Mach 0.804, Re $6.11 \times 10^6$ : lift coefficient versus $\alpha$ .....	96
Figure E.8 SSC-A09, Run 60, Mach 0.399, Re $3.85 \times 10^6$ : drag coefficient versus $\alpha$ .....	96
Figure E.9 SSC-A09, Run 61, Mach 0.307, Re $4.29 \times 10^6$ : drag coefficient versus $\alpha$ .....	97
Figure E.10 SSC-A09, Run 63, Mach 0.5, Re $4.57 \times 10^6$ : drag coefficient versus $\alpha$ .....	97
Figure E.11 SSC-A09, Run 65, $M = 0.599$ , $Re = 5.16 \times 10^6$ : drag coefficient versus $\alpha$ .....	98
Figure E.12 SSC-A09, Run 68, $M = 0.603$ , $Re = 5.21 \times 10^6$ : drag coefficient versus $\alpha$ .....	98
Figure E.13 SSC-A09, Run 69, $M = 0.703$ , $Re = 5.73 \times 10^6$ : drag coefficient versus $\alpha$ .....	99
Figure E.14 SSC-A09, Run 70, Mach 0.804, Re $6.11 \times 10^6$ : drag coefficient versus $\alpha$ .....	99
Figure E.15 SSC-A09, Run 60, $M = 0.399$ , $Re = 3.85 \times 10^6$ : $c_l$ vs $c_d$ .....	100
Figure E.16 SSC-A09, Run 61, $M = 0.307$ , $Re = 4.29 \times 10^6$ : $c_l$ vs $c_d$ .....	100

Figure E.17 SSC-A09, Run 63, $M = 0.5$ , $Re = 4.57 \times 10^6$ : $c_l$ vs $c_d$ .....	101
Figure E.18 SSC-A09, Run 65, Mach 0.599, $Re = 5.16 \times 10^6$ : $c_l$ vs $c_d$ .....	101
Figure E.19 SSC-A09, Run 68, $M = 0.603$ , $Re = 5.21 \times 10^6$ : $c_l$ vs $c_d$ .....	102
Figure E.20 SSC-A09, Run 69, $M = 0.703$ , $Re = 5.73 \times 10^6$ : $c_l$ vs $c_d$ .....	102
Figure E.21 SSC-A09, Run 70, $M = 0.804$ , $Re = 6.11 \times 10^6$ : $c_l$ vs $c_d$ .....	103
Figure E.22 SSC-A09, Run 60, $M = 0.399$ , $Re = 3.85 \times 10^6$ : $c_m$ versus $\alpha$ .....	103
Figure E.23 SSC-A09, Run 61, $M = 0.307$ , $Re = 4.29 \times 10^6$ : $c_m$ versus $\alpha$ .....	104
Figure E.24 SSC-A09, Run 63, $M = 0.5$ , $Re = 4.57 \times 10^6$ : $c_m$ versus $\alpha$ .....	104
Figure E.25 SSC-A09, Run 65, $M = 0.599$ , $Re = 5.16 \times 10^6$ : $c_m$ versus $\alpha$ .....	105
Figure E.26 SSC-A09, Run 68, $M = 0.603$ , $Re = 5.21 \times 10^6$ : $c_m$ versus $\alpha$ .....	105
Figure E.27 SSC-A09, Run 69, $M = 0.703$ , $Re = 5.73 \times 10^6$ : $c_m$ versus $\alpha$ .....	106
Figure E.28 SSC-A09, Run 70, $M = 0.804$ , $Re = 6.11 \times 10^6$ : $c_m$ versus $\alpha$ .....	106

## NOMENCLATURE

$a$	=	speed of sound, m/s
$C_p$	=	pressure coefficient
$C_f$	=	skin friction coefficient, $\tau/q$
$c$	=	Airfoil chord, m
$c_d$	=	section drag coefficient, $D/(0.5\rho V^2 c)$
$c_l$	=	section lift coefficient, $L/(0.5\rho V^2 c)$
$c_m$	=	section moment coefficient, $M_a/(0.5\rho V^2 c)$
$D$	=	section aerodynamic drag force, N/m
$g$	=	gravitational acceleration, $m/s^2$
$H$	=	shape factor, $\delta^2/\theta$
$L$	=	section aerodynamic lift force, N
$M$	=	Mach number
$M_a$	=	section aerodynamic pitching moment, N/m
$N$	=	amplification factor
$q$	=	dynamic pressure, $(0.5\rho V^2)$
$p$	=	static pressure, kPa
$R$	=	universal gas constant, $m/(s^2K)$
$R$	=	rotor radius, m
$Re$	=	Reynolds number
$Re/M$	=	Reynolds-Mach proportionality constant
$r$	=	rotor radial coordinate, m
$S$	=	shear correlation factor, $(\tau_w\theta)/\mu u_e$
$T$	=	absolute temperature, K
$t$	=	airfoil thickness, m
$u_\infty$	=	freestream velocity, m/s
$u_e$	=	velocity at the edge of the boundary layer, m/s
$V$	=	section resultant velocity, m/s
$y^+$	=	Dimensionless wall distance
$\alpha$	=	angle of attack, deg
$\delta$	=	velocity boundary layer thickness
$\delta^*$	=	displacement thickness
$\gamma$	=	specific heat ratio
$\mu$	=	dynamic viscosity, $(Ns)/m^2$
$\rho$	=	density, $kg/m^3$
$\nu$	=	kinematic viscosity, $m^2/s$
$\theta$	=	momentum thickness
$\tau$	=	shear stress
$\tau_w$	=	shear stress at the wall

# Chapter 1. Introduction

## 1.1. Airfoil Tables Overview

An airfoil is a two-dimensional cross-section of a blade or a wing. Airfoil geometries are selected for rotor blade and wing design based on desired aerodynamic characteristics that the airfoil possesses. Characteristics such as thickness, camber, and twist can achieve desired aerodynamic characteristics. These simple geometries are the heart of aerodynamic analyses, primarily because their aerodynamic performance qualities can communicate a lot about how a full-size aircraft will behave in flight. In the rotorcraft community, airfoil tables are the bread and butter of aerodynamicists specializing in computational fluid dynamics (CFD) and comprehensive analysis tools because they provide good approximations of full span aerodynamic behavior. Airfoil tables are a valuable asset to research and analysis efforts for the development of aircraft and rotorcraft. An airfoil table provides the sectional lift, sectional drag, and sectional moment coefficients for wing or blade cross-sectional profiles (or geometries), which provide an accurate approximation of an entire wing or blade's overall aerodynamic characteristics. These coefficients can be determined by an integrating pressure and shear stress distributions over the surface of an airfoil, and breaking these resultant forces down into lift, drag, and moment components [1]. The resultant forces acting on an airfoil are depicted in Figure 1.1.

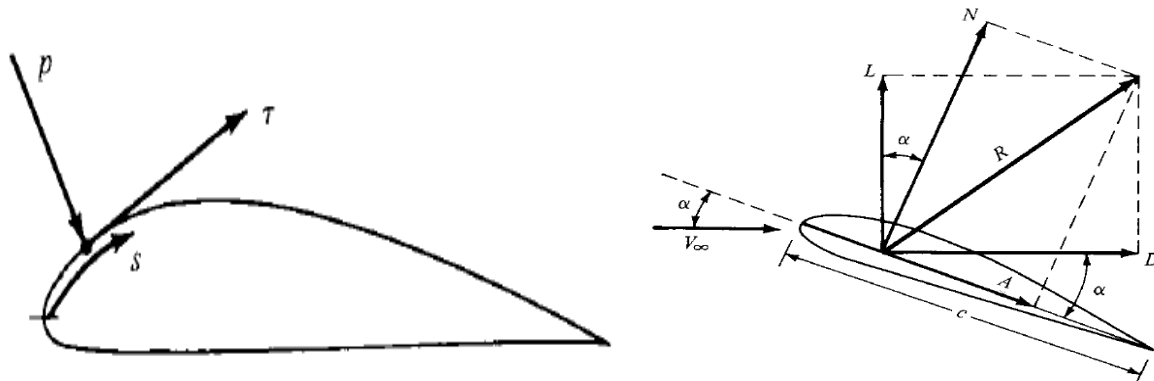


Figure 1.1. Aerodynamic forces acting on an airfoil. [1]

The diagram depicts an airfoil at an angle of attack ( $\alpha$ ) relative to a freestream velocity,  $v_\infty$ . The three forces acting on the airfoil are the lift, drag, and moment forces. A standard airfoil table in .c81 format provides the lift coefficients first, drag coefficients second, and the moment coefficients last as a converged value for a specific  $\alpha$ -Mach pair - meaning, for each  $\alpha$  and Mach number, there exists a specific lift, drag, or moment coefficient. Figure 1.2 provides an example of a partial \*.c81 airfoil table.

NACA 0012	11391165 947								
	0.	.20	.30	.40	.50	.60	.7	.75	.8
	.9	1.							
-180.	0.	0.	0.	0.	0.	0.	0.	0.	0.
	0.	0.							
-172.5	.78	.78	.78	.78	.78	.78	.78	.78	.78
	.78	.78							
-161.	.62	.62	.62	.62	.62	.62	.62	.62	.62
	.62	.62							
-147.	1.	1.	1.	1.	1.	1.	1.	1.	1.
	1.	1.							
-129.	1.	1.	1.	1.	1.	1.	1.	1.	1.
	1.	1.							
-49.	-1.18	-1.18	-1.18	-1.18	-1.18	-1.18	-1.18	-1.18	-1.18
	-1.18	-1.18							
-39.	-1.18	-1.18	-1.18	-1.18	-1.18	-1.18	-1.18	-1.18	-1.18
	-1.18	-1.18							
-21.	-.8	-.8	-.81	-.83	-.85	-.85	-.85	-.71	-.68
	-.64	-.64							
-16.5	-1.007	-1.007	-.944	-.96	-.965	-.965	-.965	-.795	-.76
	-.7	-.7							
-15.	-1.19	-1.19	-1.09	-1.055	-.99	-.98	-.98	-.83	-.79
	-.72	-.72							

Figure 1.2. Partial example of the standard 0012 airfoil table commonly used by NASA and industry. [2]

In Figure 1.2, the first row depicts the airfoil name and a sequence of numbers that will be explained shortly. The second and third rows in this case contain the Mach numbers. The left-hand column, beginning at -180 deg, indicates the  $\alpha$ . Each row up to 180 deg for each section contains an aerodynamic coefficient. In this case, we see the lift coefficients for a number of  $\alpha$ -Mach pairs. The sequence of numbers seen in Figure 1 indicate a FORTRAN formatted header of A28, 2X, 6I2, which indicates a 28-letter text string, 2 spaces, and 6 sets of two integers, describing the series of numbers that the number of  $\alpha$  and Mach numbers used to calculate the  $c_l$ ,  $c_d$ , and  $c_m$  of the airfoil. Table 1.1 provides details on what the first line of an airfoil table represents.

Table 1.1. Line 1 description for typical .c81 table.

NACA 0012	11391165 947
11	number of Mach points for the $c_l$
39	number of $\alpha$ points for the $c_l$
11	number of Mach points for the $c_d$
65	number of $\alpha$ points for the $c_d$
9	number of Mach points for the $c_m$
47	number of $\alpha$ points for the $c_m$

## 1.2. Rotorcraft Design Process

Typically, multiple airfoil tables are necessary to provide enough aerodynamic data for the entire span of a rotor blade. The airfoils are selected based on a specific location along the blade span, which can be called an airfoil station or radial station interchangeably. Generally, these airfoil stations possess distinct features that, when combined, provide an excellent approximation of a blade and its aerodynamic characteristics. Figure 1.3 depicts a simple example of a rotor blade, with three radial stations marked around the  $\frac{1}{4}$ -chord point.

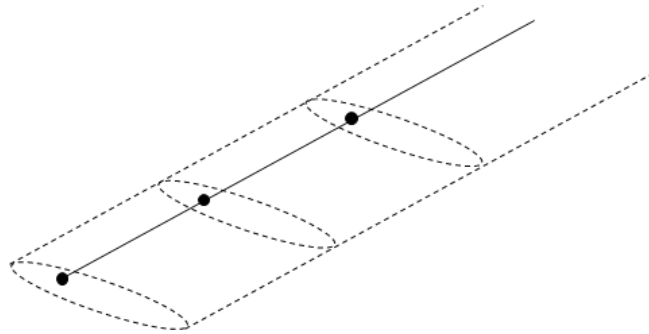


Figure 1.3. Rotor blade radial stations from the blade tip inward [2].

For conceptual design applications, the airfoil data is an input file for both comprehensive analysis tools and CFD. Comprehensive analysis tools, such as Comprehensive Hierarchical Aeromechanics Rotorcraft Model (CHARM) and Comprehensive Analytical Model of Rotorcraft Aerodynamics and Dynamics (CAMRAD II), use concepts such as lifting line theory (LL), blade element theory (BEM), vortex lattice/lifting methods (VLM), and wake analyses to provide an accurate overview of rotorcraft performance in wind tunnels or open air environments. These types of tools provide aeromechanical analysis of rotorcraft that support conceptual design efforts by modeling aerodynamics and dynamics (structural, multibody, interactional) of both isolated rotors and full-body conceptual designs [3,4]. In the design process, the airfoil tables are one of the first steps before moving on to design iterations. Airfoils are selected based on mission goals for maximum lift coefficients, desired lift-to-drag ratios (L/D), and their practicality for specific configurations. As mentioned previously, the quality of the airfoil table can have an impact on simulations and modeling of rotorcraft aerodynamics and dynamics in CFD and comprehensive analysis. For new designs, this process of airfoil analysis, comprehensive analysis, CFD, and control analysis can provide insights on design flaws and inspire modifications until performance is within desired limits. Figure 1.4 is a flow chart of how this rotorcraft design process works within NASA, with airfoil tables included in the blue box feeding into comprehensive analysis and NASA Design and Analysis of Rotorcraft (NDARC), and acoustics software programs.

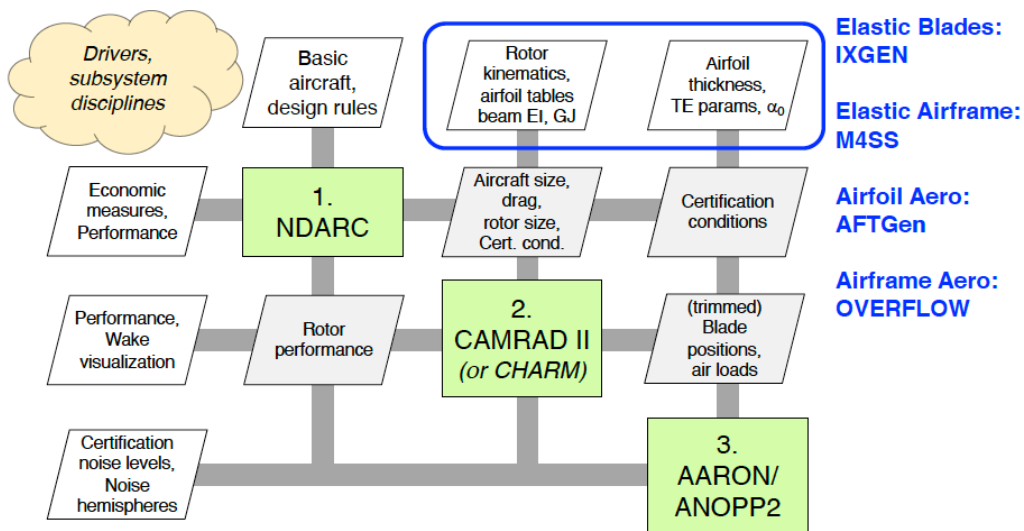


Figure 1.4. Rotorcraft design process in the NASA Aeromechanics Office [2].

Oftentimes, tools like CHARM, CAMRAD II, and CFD are used to generate pre-test predictions to provide a realistic idea of forces, moments, and interactional aerodynamics within a wind tunnel. Having good expectations for an upcoming wind tunnel test allows for mitigation of possible challenges during tests and/or a better understanding of how phenomena such as flow recirculation can cloud data collected. In addition, these programs provide validation for these codes and their ability to capture and compare well with experimental test data.

### 1.3. Legacy Airfoil Tables

Legacy airfoil tables are widely used and circulated within the rotorcraft community. Legacy airfoils include NACA 4-, 5-, and 6-series airfoils, which have served as benchmarks for checking experimental test setups in wind tunnels and simulation results [5]. However, one challenge is that occasionally, the original source of an airfoil table being circulated is not known, and therefore the fidelity of the values is uncertain. In addition, some circulated tables are a composite of multiple sources, including both measured and computed values.

### 1.4. Airfoil Selection

The airfoils selected for this study are relevant because there is a large amount of experimental data that can be used to evaluate simulation results, and additionally, the geometries are publicly available for use. Having accessible, validated airfoil tables for use in pre-test predictions, for both CFD and comprehensive analysis applications, will support design and analysis efforts of next-generation rotary wing concepts.

#### 1.4.1. NACA 0012

The NACA 0012 airfoil is a 4-series, symmetrical airfoil commonly used for aeronautics and wind turbine applications, likely due to its high L/D ratio in many flight conditions. The NACA 0012 airfoil has a wealth of legacy data, from 1939 to the present day, that provides aerodynamic coefficients across a large range of flow conditions.

One of the most well-known reports, frequently used as a reference in benchmark simulations, was written by W.J. McCroskey in 1987, and provides a comprehensive list of over 40 wind tunnel tests for the 0012 airfoil [6]. The goal of this report is to provide the reader with valuable feedback on the accuracy of these tests based on the facilities tested in, the  $\alpha$ -Mach ranges, and data reliability. This is intended to allow users to validate CFD simulations and pre-test predictions for wind tunnel tests, as well as provide a good comparison for experimental testing. Ultimately, McCroskey determines that data collected by Charles D. Harris in 1981 provides the most reliable results, cementing Harris' 0012 airfoil data as superior over the others with respect to lift and drag characteristics. The full .c81 table referenced in this report was developed by Davis [7] using a rotorcraft flight simulation program.

In 1981, Harris conducted 2D tests of the NACA 0012 airfoil in NASA Langley's 8-Foot Transonic Wind Tunnel [8]. This now defunct variable pressure, continuous flow wind tunnel was capable of varying Mach number (from 0.2 to 1.2), stagnation pressure (from 0.25 to 2 atm) and temperature, and humidity independently [9]. Tests covered Mach numbers from 0.3 to 0.86 at Reynolds number from  $3.0 \times 10^6$  through  $9.0 \times 10^6$  and fixed transition at 5% of the chord, with lift coefficients generated from close to zero up to maximum lift. The airfoil profile is included in Figure 1.5.



Figure 1.5. NACA 0012 symmetrical airfoil profile [8].

That same year, Caradonna and Tung performed hover performance studies of a untapered, untwisted rotor using a NACA 0012 airfoil. While their efforts to provide benchmark data for hover performance analysis, particularly to assist in the development of comprehensive analysis codes. Codes such as CHARM provide Caradonna and Tung hover performance results as a test case for new users to their code, which cements the value of using the NACA 0012 as a benchmark airfoil for airfoil table analyses. An airfoil table can be interchanged within a CHARM input file, for example. In a previous study, completed in 2019, ARC2D was used to generate a full  $\pm 180^\circ$  airfoil table with good agreement for airfoil table data, particularly at Mach numbers exceeding 0.3 in the linear  $\alpha$  range for sectional lift and drag coefficients [10].

Similar to the McCroskey, Harris, and Caradonna and Tung studies, Sheldahl and Klimas generated 0012 airfoil data (alongside similarly symmetric profiles such as the 0009, 0012H, and 0015) from 0 to  $180^\circ \alpha$  at Reynolds numbers from  $10^4$  to  $10^7$  [11]. Although the applications are for vertical axis wind turbines, the data may still be invaluable for comparison studies specific to rotors. Sheldahl and Klimas created four models from aluminum with 6-inch chords, with a blade span around 3 feet. The value in this specific test set is in its large  $\alpha$  range.

#### 1.4.2. RC(4)-10

The RC(4)-10 airfoil was one of a series designed at NASA’s Langley Research Center to advance airfoil concepts that optimize rotorcraft performance. In 1990, Noonan determined the sectional lift, drag, and moment coefficients for the RC(4)-10 and the RC(5)-10 airfoils and compared them against the baseline VR-7 airfoil. Wind tunnel testing was completed in NASA Langley’s 6-by 28-Inch Transonic Wind Tunnel (6x28TT) and the Low-Turbulence Pressure Tunnel for Mach numbers from 0.3 - 0.84 and 0.10 to 0.44, respectively. The stagnation pressure for the 6x28TT wind tunnel ranges from 30 to 90 psia. A majority of the RC(4)-10 data collected at a constant stagnation pressure of 60 psia, with Mach numbers from 0.34 to 0.49 also tested at stagnation pressures ranging from 48 to 36 psia. Summarized results of the wind tunnel test for the RC(4)-10, compared with the VR-7 airfoil, are provided in Table 1.2 [12]

Table 1.2. Summarized  $c_{lmax}$  and drag divergence values for the RC(4)-10 versus the VR-7 (where applicable) [12].

Airfoil	$c_{lmax}$ @ M = 0.2	$c_{lmax}$ @ M=0.34	$c_{lmax}$ @ M=0.42	drag divergence Mach #
RC(4)-10	1.74	1.57	1.42	0.74
VR-7		1.47	1.38	

The maximum lift coefficients are promising and meet design requirements, particularly for

airfoils that need to be within a region inboard of the rotor blade (in comparison to the SSC-A09, which is more for locations closer to the blade tip). A summary of the lift coefficients versus  $\alpha$  and the drag coefficients versus  $\alpha$  for the RC(4)-10 airfoil is shown in Figure 1.6 and Figure 1.7, respectively.

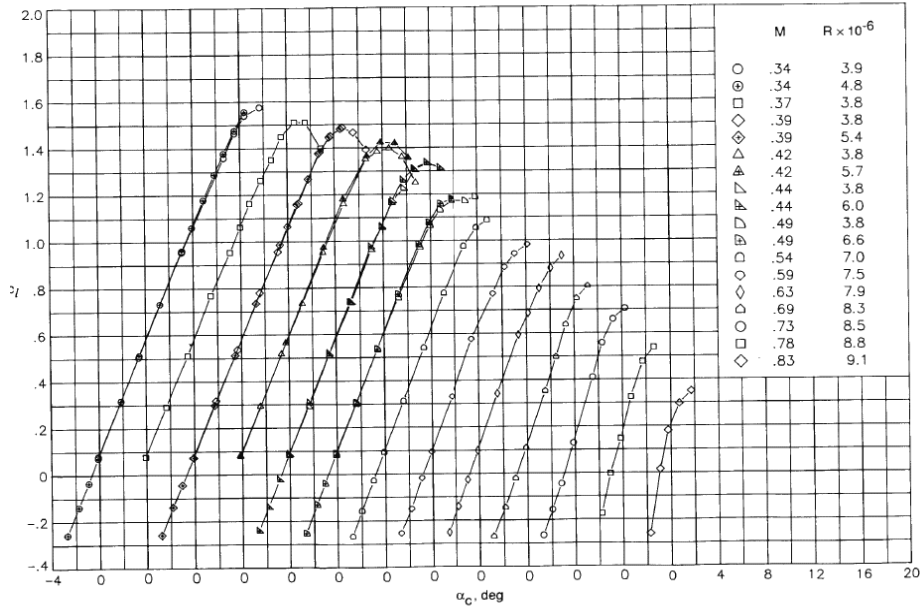


Figure 1.6. RC(4)-10 lift coefficient versus zero lift angle of attack, as compiled by Noonan [12].

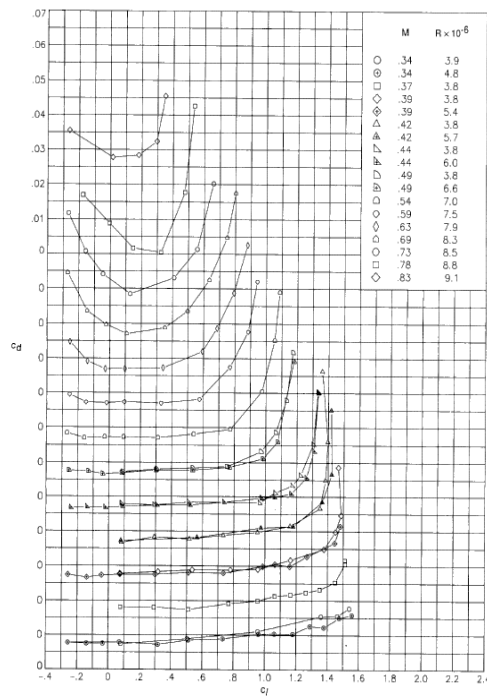


Figure 1.7. RC(4)-10 drag coefficient versus lift coefficient, as compiled by Noonan [12].

This report focuses on data collected in the 6x28TT wind tunnel. This test does not include corrections for wind tunnel sidewall boundary effects. For this reason, data collected in this tunnel tends to show a reduced maximum lift coefficient, with data lower by around 0.09, particularly at Mach 0.34.

A second comparative study in 1988 preceded Noonan’s analysis. In this case, Althoff compared the hover performance of small-scale rotors using a 0012 rotor and a second rotor incorporating the RC(4)-10, RC(5)-10, and the RC(8)-10 [13]. At the time of the test, the Noonan data was still being processed, so it provides insight into how the airfoils performed in hover tests prior to having detailed sectional aerodynamic coefficient analysis. Using two small scale rotors, Althoff proved that the advanced RC rotor resulted in better overall hover performance than the NACA 0012 rotor, as it produced higher thrust. Using blade element analysis in two codes, HOVER and LSAF, Althoff also determined that the RC rotor was more efficient.

### 1.4.3. SSC-A09

The SSC-A09 airfoil is a third-generation airfoil developed by Sikorsky Aircraft alongside other airfoils, with the design intention to improve upon the performance of earlier SC airfoils. The test program was a joint effort supported by both NASA Ames Research Center and Sikorsky Aircraft in 1984, with the SSC-A09 as developed as part of a series with the intention of reducing the drag divergence Mach number by a minimum of 0.03 [14]. The SSC-A09 was tested alongside a number of other transonic airfoils, as well as the UH-60A rotor SC1095 and SC1094R8 airfoils, in NASA Ames’s 11-Foot Transonic Wind Tunnel at Mach numbers from 0.3 to 1.07. Wind tunnel stagnation pressure was 1.0 and 1.4 atmospheres, with an average stagnation temperature of approximately 70°.

The SSC-A09 outperformed other airfoils with respect to maximum lift, particularly at higher Mach numbers between 0.5 and 0.74, with the overall maximum L/D values for the entire SSC-AXX family similarly exceeding other transonic airfoils developed. This performance quality likely resulted in further testing of the SSC-A09 with additions such as bumps and surface inconsistencies which would ultimately influence drag but provide insight into how surface defects or anomalies may influence performance. The end result of testing showed that the SSC-AXX series achieved their design goals with success. Wind tunnel test data was used to validate transonic airfoil analysis codes, particularly for pressure distribution, drag, lift, and pitching moments. Figure 1.8 provides the Reynolds Mach number relationship for each airfoil tested at both 1 atm and 1.4 atm, while Table 1.3 contains tabulated data of the maximum lift coefficient, drag divergence values, and characteristics of all airfoils studied in this test.

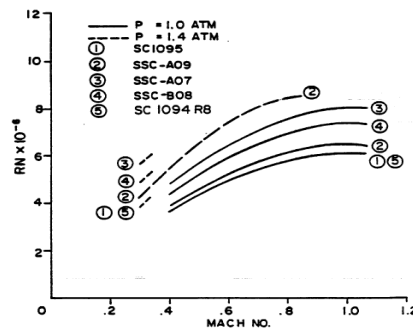


Figure 1.8. Re versus Mach for both 1 atm and 1.4 atm test conditions [14].

Table 1.3. Airfoil characteristics, plus  $c_{l_{max}}$  and drag divergence at zero lift, adapted from data in Flemming [14].

<b>SSC-A09, Configuration 2, 6-10*</b>	
Parameter	Value
Thickness Ratio, $t/c$	0.090
Chord, inches	17.290
feet	1.4408
meters	0.4392
$x/c$ for maximum thickness	0.38
$x/c$ for maximum camber	0.17
Model aspect ratio	7.63
Tunnel height/chord	7.63
Distance from trailing edge to wake rake, chords	1.86
$c_{L_{max}}$ @ $M = 0.3$	1.40
$c_{L_{max}}$ @ $M = 0.4$	1.24
$M_{DD}$ @ $C_L = 0$	0.833

\*Configuration 2 is clean SSC-A09 airfoil. Configurations 6-10 incorporate modifications to simulate deicing boots or abrasion strips (6 with step aft edge, 7 with faired aft edge), miniature pressure transducers (8), and contour bumps (9 and 10).

In 1985, the SSC-A09's aerodynamic qualities were assessed by Hicks and Collins in an effort to provide additional wind tunnel data that validated earlier tests and provided additional benchmark data to further assist in the development of comprehensive analysis and CFD codes [15]. Hicks and Collins manufactured three airfoil sections, the A-2 airfoil, the SSC-A09, and the SC105, out of stainless steel, with the SSC-A09 airfoil profile depicted in Figure 1.9.

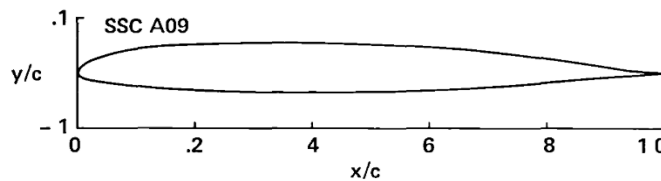


Figure 1.9. SC1095, A-2, and SSC-A09 airfoil contours [15].

Results in the Hicks study were quite comparable to Flemming, with an overall drag divergence Mach number higher than the SC1095, with good agreement between theoretical predictions and actual values for drag values, with attached flow resulting in the best correlation between theory and experiment. Although the SSC-A09 was not designed for improved pitching moment values, it performed better than the SC1095 airfoil in this regard.

Studies on the SSC-A09's performance characteristics have led to its serious consideration and modern-day comparative studies for its application in UAM technologies. In a recent effort by Murphy, Buning, and Simmons, development of a Rapid Aero Modeling (RAM) is being explored to quickly and accurately determine flight dynamics characteristics for use with eVTOL aircraft supporting UAM [16,17]. As designs evolve in complexity, RAM intends to fill a need for

modeling tools and computational efficiency that supports efforts to provide varying fidelity, from low to high, for a large array of eVTOL configurations. A flowchart of the RAM concept is shown in Figure 1.10.

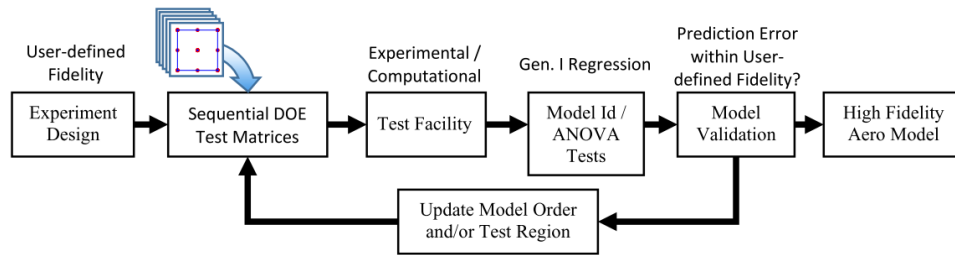


Figure 1.10. The RAM process, as provided by Murphy, Buning, and Simmons [16].

The SSC-A09 was selected for an airfoil study using RAM-C as a way to validate the algorithm’s capability for use in the rotorcraft design process. The Mach numbers selected are consistent with existing wind tunnel experiments completed at NASA Ames and Langley Research Centers, with an  $\alpha$  range from  $-20^\circ$  to  $20^\circ$ . RAM-C results are provided in Figure 1.11.

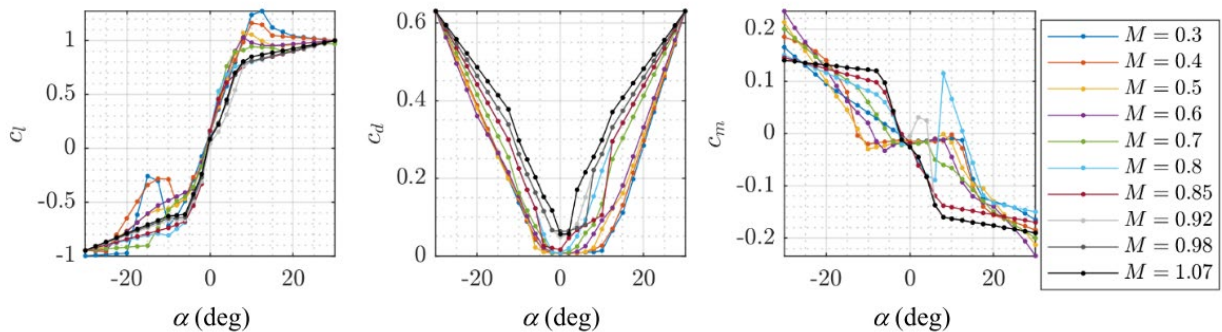


Figure 1.11. Sectional lift, drag, and moment coefficients for the SSC-A09 airfoil [17].

## 1.5. Applicability

For conventional Reynolds Number regimes, the 0012, SC1094R8, SC1095, SSC-A09, and RC(4)-10 have direct applicability for use in full-scale eVTOL analyses. Within the Aeromechanics Branch at NASA Ames Research Center, a number of reference models have been developed to meet the demand for UAM designs that meet FAA and industry air taxi requirements. Silva, Johnson, and Solis and published three concept vehicles that take into consideration payload, range, propulsion, and configurations [18]. Figure 1.12 provides an overview of the research areas that NASA is focusing on for the development of eVTOL aircraft.

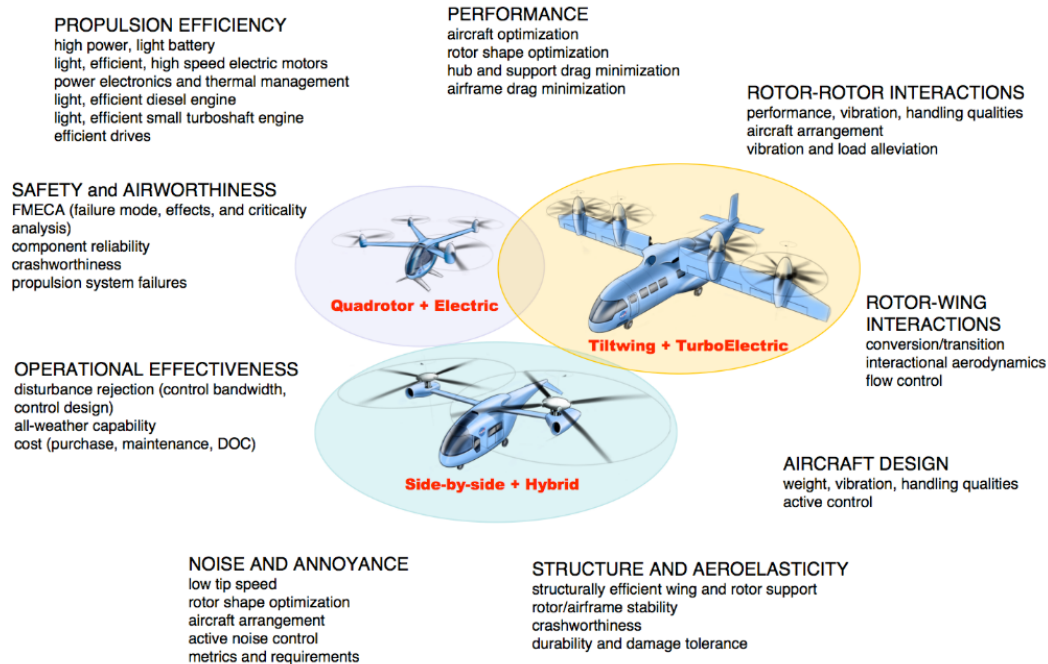


Figure 1.12. NASA research areas for the development of next generation, fully electric aircraft [18].

At this time, not many details exist on the airfoil selections for these designs, providing the airfoil aerodynamic coefficients and publishing them in the public domain, particularly for proprietary geometries, can allow more flexibility in the design process and complement existing data reports that provide details on overall hover or forward flight performance, without much discussion of the airfoil qualities.

### 1.5.1. Low Reynolds Number Applications

Although at this time, low Reynolds number analyses may not be possible within the timeline of this effort, it is important to touch on the value of these flow conditions and their applicability for small-scale and extraplanetary purposes. Low Reynolds number flight regimes are typically within the  $10^4$  to  $10^5$ . Drones tend to fly within this regime due to their small rotors, but the more interesting application in this study is the low Reynolds number flight of Ingenuity, the helicopter developed for, and currently flying in, the Martian atmosphere.

Koning, Romander, and Johnson completed an airfoil study of geometries that would perform well in a low-pressure environment, particularly in low Reynolds number flow (from  $10^3$  to  $10^5$ ) [19]. Using OVERFLOW to generate a full airfoil deck, Koning modeled a flat cambered plate in CAMRADII to determine its performance capabilities when compared with more conventional airfoil designs. Assuming a transition from laminar to turbulent flow, Koning performed a boundary layer study to better understand which flow conditions to use in his analysis, and thus justified the use of fully turbulent flow for his airfoil table generation. Ultimately, hover performance analyses resulted in an overall increase in thrust and figure of merit for a cambered flat plate versus a conventional airfoil, such as the airfoil use on Ingenuity.

## 1.6. Project Objective

The motivation for this study is to investigate the features and capability of AFTGen when coupled with XFOIL and OVERFLOW. The features of interest include the number of trailing edge points and clustering iterations, as well as a study of the effect of leading edge coordinate point density. The following sections will introduce the rotorcraft design process, discuss the NACA 0012, RC(4)-10, and SSC-A09 airfoils, provide information on the mathematical model incorporated into the flow solvers and the airfoil table generator tool, and compare the experimental lift, drag, and pressure coefficients with XFOIL and OVERFLOW calculations. Comparison of simulated results with well referenced historical data for comparison will provide a suitable foundation for the development of airfoil table best practices. The best practices documentation will provide researchers with guidance on how to generate airfoil tables for use with comprehensive analysis and CFD based on the flow regimes for eVTOL vehicle concepts.

### 1.6.1. Methodology

The benchmark data collected provides the operating conditions necessary for airfoil table generation. With these data in mind, it should be noted that typically, airfoil tables are generated within the linear operation range up to airfoil stall, around  $-20^\circ$  to  $20^\circ$   $\alpha$ , and populated beyond this  $\alpha$  range with existing test data for the NACA 0012, regardless of what the base airfoil table is. For every airfoil table generated, any  $\alpha$  value exceeding  $\pm 20^\circ$  will be blended with the standard legacy NACA 0012 airfoil table coefficients. The following define the approach to airfoil table generation:

#### 1. Reynolds and Mach Number Regimes:

- i. Sweep Mach number from 0 to 0.92 at angles of attack from 0 to  $\pm 20^\circ$ , depending on the range tested in benchmark experimental testing.
  - ii. Reynolds numbers will range from the order of  $10^5$  up an order of magnitude larger, in the  $10^6$  range. Reynolds number input is either in the form of:
    - a Reynolds-Mach number proportionality constant,  $Re/M$ , which allows for calculation of Reynolds number at any Mach number.
    - Individual Reynolds numbers, based on benchmark  $Re$  range.
2. **Airfoil Selection:** All airfoils used in the analysis will operate at Reynolds numbers relating to a desired flight regime based on wind tunnel data available for comparison with simulations completed in AFTGen. The airfoils of interest have been identified based on their applicability to electric vertical takeoff and landing (VTOL) aircraft.
  3. **Flow Conditions:** XFOIL will be run with AFTGen using viscous flow. Fully turbulent flow and transition flow will be utilized for the OVERFLOW flow solver. will be selected based on the Reynolds number.
  4. **Panel/Grid Parameters:** A number of different grid parameters will be adjusted in OVERFLOW, with a focus on comparison on the  $C_{l,max}$  region at a set range of angle of attack and Mach values.
    - **XFOIL:** XFOIL uses a panel approach using potential flow theory to solve for aerodynamic coefficients. Determine if increasing/decreasing panels influences results.

- **OVERFLOW:** An O-grid was selected because the airfoils of interest are imported into AFTGen with a blunt trailing edge.
    - **Trailing edge points:** explore how increasing the number of trailing edge points for the grid influences the flow for select  $\alpha$ -Mach pairs..
    - **Leading edge point clustering:** increase the number of leading edge points for the airfoil from the leading edge to about 15% chord on the upper and lower airfoil surfaces. Determine impact on simulations versus experimental data for select  $\alpha$ -Mach pairs.
    - **Clustering iterations:**
5. **Flow Solvers:** Using XFOIL and OVERFLOW, define the flow solvers' capability and accuracy when compared with experimental data. Determine solver limitations, compare computational expense versus end result. Tabulate flow parameters and settings implemented in each flow solver.

For the OVERFLOW solver, the Pleiades supercomputer at NASA Ames will be used to expedite airfoil table generation. Because of the pandemic, limited access to center resources is permitted, which stunts the capability to “farm” computers to run long  $\alpha$ -Mach sweeps for airfoils on existing workstations. This results in computational limitations, and for this reason, some time has been budgeted to achieve project goals within the time constraints of this project.

Once the airfoil tables have been generated, a quantitative analysis of the sectional lift, drag, and moment coefficients will be performed. A direct comparison of flow solver accuracy versus benchmark data will provide insight into which flow solver performs best and provides the best balance for airfoil table generation within a specific flow regime.

In future work, the best practices will result in a test matrix that encompasses all desired parameters, included grid size, computation time, angle of attack range, Mach number range, pressure, temperature, Reynolds number and/or Re/M value, flow conditions (turbulent, transition model, laminar), time steps, and other possible factors in computation accuracy and time. Computer specifications should also be recorded, as not all computers are capable of running refined grids.

## Chapter 2. Mathematical Model

In this study, multiple flow solvers will be used to compare the best methodology for generating an airfoil table. For this reason, an overview of the theory used to develop each solver is necessary to understand the differences in each code and its applicability for use in generating an airfoil table.

### 2.1. Boundary Layers

The Reynolds number of a flow is defined as the ratio between the internal forces and viscous forces, where equation 2.1 depicts the relationship between these forces in terms of density, velocity, reference length, and dynamic viscosity.

$$Re = \frac{\rho v l}{\mu} \tag{2.1}$$

A boundary layer forms when a layer of fluid flow (a thin layer at the surface of an airfoil, for example) experiences a rapid change in velocity and temperature. The key phenomena that boundary layers induce are flow turbulence, a wake influenced by flow separation, airfoil stall, and vorticity, which are determined by analyzing velocity, pressure, and heat distribution over the surface [1]. This data is valuable because it allows us to understand and calculate drag and heat transfer. The temperature and velocity profiles over a flat plate, as described in Anderson's Fundamentals of Aerodynamics, are depicted in Figure 2.1 [1].

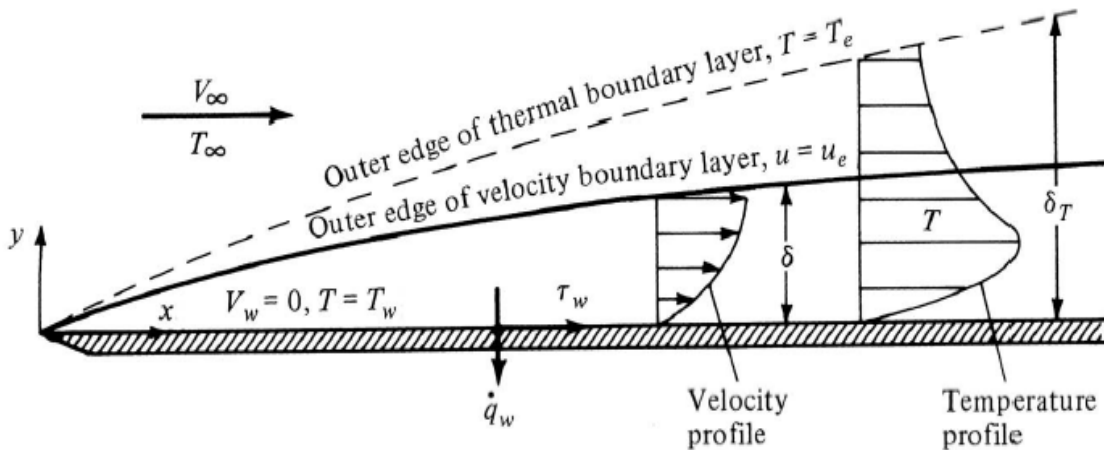


Figure 2.1. Boundary layer properties on a flat plate [1].

There are a few fundamental properties that define an airfoil are the boundary layer thickness  $\delta$ , displacement thickness  $\delta^*$ , thermal boundary layer thickness  $\delta_T$ , and momentum thickness  $\theta$ . Boundary layer thickness, displacement thickness and the momentum thickness can be calculated using equations 2.2, 2.3, and 2.4.

$$\delta(x) = \sqrt{\frac{12(\mu/\rho)x}{U_e}} \quad (2.2)$$

$$\delta^* = \int_0^{y_1} \left(1 - \frac{\rho u}{\rho_e u_e}\right) dy \quad (2.3)$$

$$\theta = \int_0^{y_1} \frac{\rho u}{\rho_e u_e} \left(1 - \frac{\rho u}{\rho_e u_e}\right) dy \quad (2.4)$$

To derive the boundary layer equations, there are a couple of relationships that can be kept in mind to simplify the physics and reduce Navier-Stokes momentum and energy equations. Firstly, the Navier-Stokes equations that govern continuity, x-momentum, y-momentum, and z-momentum are provided in equations 2.5, 2.6, 2.7, and 2.8.

$$\frac{\partial \rho}{\partial t} + u \frac{\partial \rho}{\partial x} + \rho \frac{\partial u}{\partial x} + v \frac{\partial \rho}{\partial y} + \rho \frac{\partial v}{\partial y} + w \frac{\partial \rho}{\partial z} + \rho \frac{\partial w}{\partial z} = 0 \quad (2.5)$$

$$\rho \left[ \frac{\partial u}{\partial t} + u \frac{\partial u}{\partial x} + v \frac{\partial u}{\partial y} + w \frac{\partial u}{\partial z} \right] = -\frac{\partial p}{\partial x} + \frac{\partial \tau_{xx}}{\partial x} + \frac{\partial \tau_{xy}}{\partial y} + \frac{\partial \tau_{xz}}{\partial z} + \rho f_x \quad (2.6)$$

$$\rho \left[ \frac{\partial v}{\partial t} + u \frac{\partial v}{\partial x} + v \frac{\partial v}{\partial y} + w \frac{\partial v}{\partial z} \right] = -\frac{\partial p}{\partial y} + \frac{\partial \tau_{xy}}{\partial x} + \frac{\partial \tau_{yy}}{\partial y} + \frac{\partial \tau_{yz}}{\partial z} + \rho f_y \quad (2.7)$$

$$\rho \left[ \frac{\partial w}{\partial t} + u \frac{\partial w}{\partial x} + v \frac{\partial w}{\partial y} + w \frac{\partial w}{\partial z} \right] = -\frac{\partial p}{\partial z} + \frac{\partial \tau_{xz}}{\partial x} + \frac{\partial \tau_{yz}}{\partial y} + \frac{\partial \tau_{zz}}{\partial z} + \rho f_z \quad (2.8)$$

The simplifications that can be kept in mind as boundary layer properties are explored are as follows:

1. y-momentum can be reduced to:  $\frac{\partial p}{\partial y} \approx 0$
2. Bernoulli's equation:  $U_e = \frac{dU_e}{dx} = -\frac{1}{\rho} \frac{dp}{dx}$
3. The boundary layer thickness is significantly smaller than the chord:  $\delta \ll \ll c$
4. When  $U_e$  is constant:  $\frac{d\theta}{dx} = \frac{C_f}{2}$

The skin friction coefficient is directly related to the shear stress, as shown in equation 2.9.

$$C_f = \frac{\tau_w}{0.5\rho U_e^2} \quad (2.9)$$

Using the boundary layer assumptions for steady state, the Navier-Stokes equations reduce down to equations 10 (continuity), 11 (x-momentum), and 12 (y-momentum), and the energy can be derived equation as depicted in equation 13 [1].

$$\frac{\partial(\rho u)}{\partial x} + \frac{\partial(\rho v)}{\partial y} = 0 \quad (2.10)$$

$$\rho u \frac{\partial u}{\partial x} + \rho v \frac{\partial u}{\partial y} = -\frac{dp_e}{dx} + \frac{\partial}{\partial y} \left( \mu \frac{\partial u}{\partial y} \right) \quad (2.11)$$

$$\frac{\partial p}{\partial y} = 0 \quad (2.12)$$

$$\rho u \frac{\partial h}{\partial x} + \rho v \frac{\partial h}{\partial y} = \frac{\partial}{\partial y} \left( k \frac{\partial T}{\partial y} \right) + u \frac{dp_e}{dx} + \mu \left( \frac{\partial u}{\partial y} \right)^2 \quad (2.13)$$

## 2.2. XFOIL Panel Methods

XFOIL, developed by Mark Drela at MIT, is a reliable tool for generating airfoil tables quickly, and is a valuable design tool for subcritical airfoils in both viscous and inviscid flows at low Reynolds numbers. To provide details on the foundation of the code, Drela's report *XFOIL: An Analysis and Design System for Low Reynolds Number Airfoils*, will be summarized.

The XFOIL code focuses on determining two-dimensional boundary layer aerodynamics for both inviscid and viscous flows. The XFOIL inviscid flow setting allows the code to discretize airfoil panels using a linear vorticity stream function distribution approach, while its viscous flow setting provides wake and boundary layer solutions using a two-equation integral boundary layer formulation. A user inputs an airfoil's two-dimensional coordinates, its flow conditions (inviscid/viscous, Reynolds number, Mach number, etc.), and the desired angle of attack range, and within minutes, the code produces a polar output file containing data on the pressure, lift, drag, and moment coefficients, in addition to the location of boundary layer transition from laminar to turbulent flow on the upper and lower surfaces of the airfoil. This is accomplished via a mixture of numerical methods, including potential flow theory, Karman-Tsien compressibility corrections,  $e^9$  amplification factors, and a Newton method. This combination of methods allows XFOIL to accurately capture boundary layer aerodynamics.

For inviscid boundary layer formulation, Drela uses a linear-vorticity stream function that enables the code to incorporate viscous effects and compatibility with a full-inverse and mixed-inverse modes [24]. By default, 160 panels are used to develop the flow over the airfoil. The panels can be increased to a maximum of 400. For both inviscid and viscous flow, Karman-Tsien compressibility corrections are made, and valid until the Mach number enters the transonic to supersonic regime. Drela states that this correction is determined from equations 2.14 and 2.15, with variables  $\lambda$  and  $\beta$  are defined in 2.16 and 2.17 [20].

$$C_P = \frac{C_{P_{inc}}}{\beta + \lambda(1 + \beta) \frac{C_{P_{inc}}}{2}} \quad (2.14)$$

$$q = \frac{q_{inc}(1 - \lambda)}{1 - \lambda\left(\frac{q}{q_\infty}\right)_{inc}^2} \quad (2.15)$$

$$\lambda = \frac{M_\infty^2}{(1 + \beta)^2} \quad (2.16)$$

$$\beta = \sqrt{1 - M_\infty^2} \quad (2.17)$$

When using the viscous flow setting, XFOIL's discretization of airfoil panels is determined using a linear vorticity distribution across an airfoil's panels, with the stream function in equation 18 summarizing the relationship between velocity components and vorticity source strength [20].

$$\psi(x, y) = u_\infty y - v_\infty x + \frac{1}{2\pi} \int \gamma(s) \ln r(s; x, y) ds + \frac{1}{2\pi} \int \sigma(s) \vartheta(ss; x, y) ds \quad (2.18)$$

Inviscid analyses in XFOIL assign a number of panel nodes  $N$ , a number of wake nodes  $N_w$ , node values  $\gamma_i$ , and a constant source strength  $\sigma_i$ . With panel nodes established, the airfoil geometry known, and the Kutta condition applied, XFOIL can solve for airfoil surface vorticity at each node. Figure 2.2 depicts the panel coordinate system used in XFOIL.

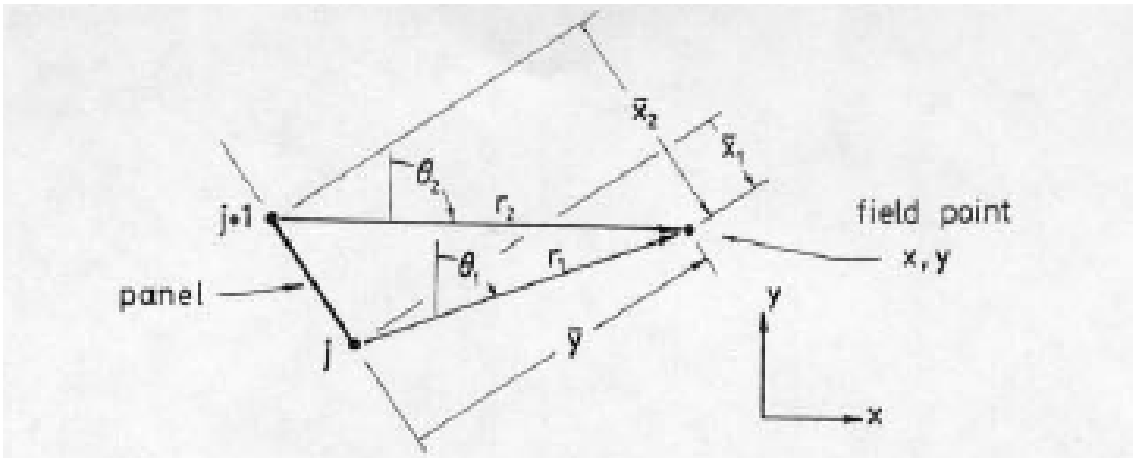


Figure 2.2. Panel coordinate system used in XFOIL [20].

A summary of XFOIL's numerical methods is provided by Silva, Avelino, and De-Lemos in which the viscous formulation governing equations (which are identical to the ISES code developed by Drela and Giles) allow for an improved calculation of base drag [20,21]. Drela provides equations 2.19 and 2.20 as the compressible integral momentum equation and the kinetic energy shape parameter equation.

$$\frac{C_f}{2} = \left[ \frac{d\theta}{d\xi} + (2 + H - M_e^2) \frac{\theta}{u_e} \frac{du_e}{d\xi} \right] \quad (2.19)$$

$$\theta \frac{dH^*}{d\xi} + (2H^{**} + H^*(1 - H)) \frac{\theta}{u_e} \frac{du_e}{d\xi} = 2C_D - H^* \frac{C_f}{2} \quad (2.20)$$

Ultimately, the stream function can be broken down into equation 2.21 to determine the velocity at the edge of the boundary layer,  $u_e$ , and used to solve for our momentum thickness, displacement thickness, and skin friction coefficient, as listed in equations 3 and 4 [21].

$$u_{e_i} = u_\infty \hat{n}_x - v_\infty \hat{n}_y + \sum_{j=1}^N c_{ij}^\gamma \gamma_j \sum_{j=1}^{N+N_w-1} c_{ij}^\sigma \sigma_j \quad (2.21)$$

### 2.3. OVERFLOW

OVERFLOW 2.3 is an implicit, time-marching, structured grid overset Navier Stokes code that is a product of decades of CFD iterations by Buning et. al [22]. When the code is coupled with AFTGen, default grid settings enable structured O-grids and C-grids for two-dimensional cases. Figure 2.3 depicts these grid configurations, where  $\eta$  represents the number of grid points in the normal direction (i.e, normal to the surface of the airfoil) and  $\xi$  represents the streamwise coordinate points (with the C-grid, this also includes grid points along the wake cut). The code also allows for use of both Pegasus 5 and Chimera Grid Tools to allow users to create and import overset grids.

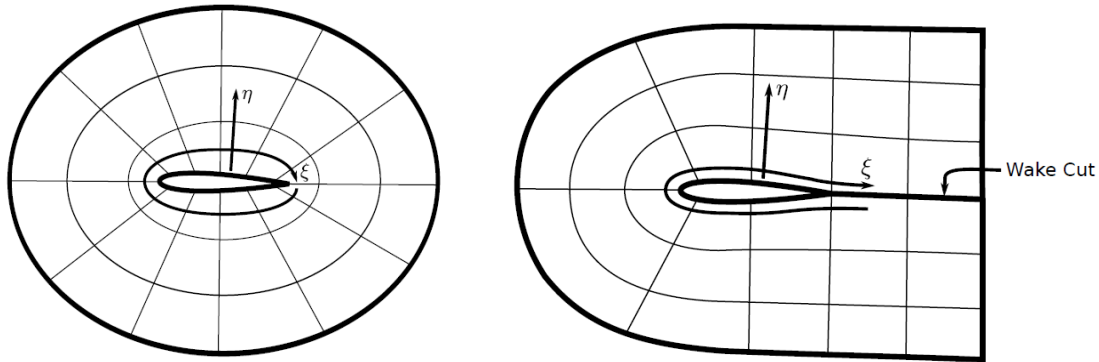


Figure 2.3. Simplification of structured O-grid and C-grid options in OVERFLOW [23].

AFTGen with OVERFLOW is capable of applying the following numerical schemes:

- I. Fully laminar.
- II. Fully turbulent Spalart-Allmaras.
- III. Spalart-Allmaras with Coder transition.
- IV. Spalart-Allmaras with Medida-Baeder transition.
- V. SST-2003 with Langtry-Menter transition.
- VI. Forced/fixed transition using transition list, array, or matrix input file.

Nichols, Tramel, and Buning summarize the Navier-Stokes equations in the simplified format shown in equation 22:

$$\frac{\partial \vec{q}}{\partial t} + \frac{\partial \vec{E}}{\partial \xi} + \frac{\partial \vec{F}}{\partial \eta} + \frac{\partial \vec{G}}{\partial \zeta} = 0 \quad (2.22)$$

In this simplification, the E, F, and G vectors represent the inviscid and viscous flow in the  $\xi$ ,  $\eta$ , and  $\zeta$  directions. The q vector is described by matrix 1 and comprises the computational cell volume as a factor of flow density  $\rho$  with the velocity vector components in the u, v, and w directions as well as the total energy  $e_0$  [22,24].

$$\vec{q} = \forall [\rho \quad \rho u \quad \rho v \quad \rho w \quad \rho e_0]^T \quad (1)$$

Nichols, Tramel, and Buning developed an algorithm for the two-equation k- $\omega$  and SST transport models and species equations. Figure 2.4 shows the transport equation used for these models.

$$\begin{aligned} \frac{\partial \rho s}{\partial t} + \frac{\partial \rho U s}{\partial \xi} + \frac{\partial \rho V s}{\partial \eta} + \frac{\partial \rho W s}{\partial \zeta} = & \frac{\partial}{\partial \xi} \left[ \left( \frac{\mu}{\sigma_L} + \frac{\mu_t}{\sigma_T} \right) (\xi_x^2 + \xi_y^2 + \xi_z^2) \frac{\partial s}{\partial \xi} \right] + \\ & \frac{\partial}{\partial \eta} \left[ \left( \frac{\mu}{\sigma_L} + \frac{\mu_t}{\sigma_T} \right) (\eta_x^2 + \eta_y^2 + \eta_z^2) \frac{\partial s}{\partial \eta} \right] + \frac{\partial}{\partial \zeta} \left[ \left( \frac{\mu}{\sigma_L} + \frac{\mu_t}{\sigma_T} \right) (\zeta_x^2 + \zeta_y^2 + \zeta_z^2) \frac{\partial s}{\partial \zeta} \right] + \\ & \frac{\partial}{\partial \xi} \left[ \left( \frac{\mu}{\sigma_L} + \frac{\mu_t}{\sigma_T} \right) (\xi_x \eta_x + \xi_y \eta_y + \xi_z \eta_z) \frac{\partial s}{\partial \eta} \right] + \frac{\partial}{\partial \xi} \left[ \left( \frac{\mu}{\sigma_L} + \frac{\mu_t}{\sigma_T} \right) (\xi_x \zeta_x + \xi_y \zeta_y + \xi_z \zeta_z) \frac{\partial s}{\partial \zeta} \right] + \\ & \frac{\partial}{\partial \eta} \left[ \left( \frac{\mu}{\sigma_L} + \frac{\mu_t}{\sigma_T} \right) (\xi_x \eta_x + \xi_y \eta_y + \xi_z \eta_z) \frac{\partial s}{\partial \xi} \right] + \frac{\partial}{\partial \eta} \left[ \left( \frac{\mu}{\sigma_L} + \frac{\mu_t}{\sigma_T} \right) (\eta_x \zeta_x + \eta_y \zeta_y + \eta_z \zeta_z) \frac{\partial s}{\partial \zeta} \right] + \\ & \frac{\partial}{\partial \zeta} \left[ \left( \frac{\mu}{\sigma_L} + \frac{\mu_t}{\sigma_T} \right) (\xi_x \zeta_x + \xi_y \zeta_y + \xi_z \zeta_z) \frac{\partial s}{\partial \xi} \right] + \frac{\partial}{\partial \zeta} \left[ \left( \frac{\mu}{\sigma_L} + \frac{\mu_t}{\sigma_T} \right) (\eta_x \zeta_x + \eta_y \zeta_y + \eta_z \zeta_z) \frac{\partial s}{\partial \eta} \right] + \\ & + \text{Source Terms} \end{aligned}$$

Figure 2.4. OVERFLOW transport equation with generalized  $\xi$ ,  $\eta$ , and  $\zeta$  coordinates [24].

The turbulence models of interest in this report include the fully turbulent (item II) and fully turbulent with Coder transition (item III). OVERFLOW's fully turbulent model incorporates the Spalart-Allmaras 1 equation model, which includes tripline specification (DDADI left-hand side)[24,25].

## Chapter 3. Computational Approach

### 3.1. AFTGen

Aerodynamic coefficients were generated using AFTGen for  $\pm 20$  deg angle of attack at Mach numbers ranging from 0.0 to 1.0 for the NACA 0012, 0.3 to 0.85 for the SSC-A09, and 0.37 to 0.9 for the RC(4)-10, with the Mach number and Reynolds numbers selected based on the Mach and Reynolds number ranges available in the experimental test data. AFTGen is a software tool developed by Sukra-Helitek that provides a GUI interface for XFOIL, MSES, ARC2D, UNS2D, and OVERFLOW [23]. AFTGen provides a user-friendly interface that supports a range of low-, mid-, and high-fidelity flow solvers to analyze single-element airfoil using a built-in grid generator. AFTGen also features a C81blender module that allows the user to combine partially populated airfoil tables in order of preference, resulting in a single airfoil table spanning full angle of attack and Mach values. The flow solvers of interest in this study are XFOIL and OVERFLOW as they represent low-fidelity and high-fidelity codes.

### 3.2. Primary Case Setup

Cases run on both XFOIL and OVERFLOW have overlapping inputs that will vary for each airfoil. For all airfoils,  $\alpha$  is swept from  $-20$  to  $+20$  deg in 1-deg increments to capture the linear angle of attack range as well as the stall region in which more complex phenomena, such as flow separation and transition, is experienced. Beyond this angle of attack range, a base NACA 0012 airfoil table, dubbed the legacy 0012 airfoil table (Appendix A), will be blended with the primary aerodynamic coefficients. The Mach number range is set to the range depicted in each primary benchmark. Flow conditions, similarly, correspond to wind tunnel test conditions. Table 3.1 details the inputs for each airfoil.

Table 3.1 Angle of attack, Mach number, and Reynolds number input range for each airfoil.

	<b>NACA 0012</b>	<b>SSC-A09</b>	<b>RC(4)-10</b>
Alpha Range	$\pm 20^\circ$	Various	$-4^\circ$ to $16^\circ$
Mach Range	0 to 1.0	0.3 - 0.9	0.3 - 0.9
Reynolds Number	$5.2 \times 10^6$ *	$3.85 \times 10^6$ - $6.07 \times 10^6$	$5.2 \times 10^6$ - $9.6 \times 10^6$

\* Reynolds-Mach proportionality constant,  $Re/M$

### 3.3. AFTGen with XFOIL Setup

XFOIL does not allow for a selection of a particular numerical scheme. The code automatically determines fixed transition locations upon the upper and lower surfaces of an airfoil. The selection of a grid, time grid, numerical scheme, and further, run control, thus, only applies to the use of OVERFLOW with AFTGen. XFOIL settings are shown in Table 3.2.

Table 3.2. XFOIL run control and boundary layer inputs.

<b>Setting</b>	<b>Input</b>
Flow type	Viscous
Delta alpha	1.0
Max Iterations	500
Number of Panels	400
Panel Bunching Parameter	1.0
Panel Density Ratio (TE/LE)	0.15
Amplification exponent (Ncrit)	9.0

The maximum number of panels is selected to better define the airfoil. A panel study was looked at to determine whether or not increasing paneling increased the accuracy of the results, and the answer is no - increasing panels did not increase coefficient accuracy. For some airfoils, it may be worth it to explore modifying the amplification exponent. The amplification exponent is the factor of the most amplified wind tunnel frequency and is a condition that can trigger laminar-turbulent flow transition. The default input is 9 and can vary based on conditions. For an airfoil tested in certain environments, Table 3.3 depicts the amplification factor, Ncrit, for various situations.

Table 3.3. Amplification factor for airfoil surface roughness in various conditions.

<b>Condition</b>	<b>Ncrit</b>
sailplane	12-14
motorglider	11-13
clean wind tunnel	10-12
average wind tunnel	9
dirty wind tunnel	4-8

### 3.4. AFTGen with OVERFLOW Setup

#### 3.4.1. 2D Grid

As described in section 3.1, an O-grid was selected based on the blunted trailing edge of each geometry. As multiple parameters are explored during the course of this study, standard AFTGen settings were selected for the grid. OVERFLOW simulations were run for  $\zeta = 201$  and  $\eta = 101$ . Other parameters, including the leading-edge profile, minimum points between corners, and clustering iterations are also explored, with all three traits influencing convergence. The maximum ratio of consecutive segments in the  $\xi$  direction, similarly called the stretching ratio, is left at 1.1, with layer spacing in the  $\eta$  is defined solely by the spacing at the airfoil ( $y^+$ ) outward, using the hyperbolic tangent. The overall domain radius of the grid is set to 50 chords. The  $y^+$  of the airfoil is kept at a default value of 1.0. Time permitting, additional cases using C-grids can be incorporated in this study to analyze the accuracy of sharp trailing edges versus experimental data and provide insight on the best methods for generating airfoil tables for sharp trailing edge airfoils. For C-grids, the default  $y^+$  value incorporated in AFTGen is 35. The relaxation factor, which applied to grid extrusion in the normal direction, is kept at 0.2, with a ramp distance, or the distance at which the relaxation factor reaches its value relative to the chord length of the airfoil, is similarly

left at its default value of 0.1 Table 3.4 summarizes the 2D grid settings used for AFTGen with OVERFLOW.

Table 3.4. Preliminary 2D grid inputs for AFTGen using the OVERFLOW solver.

<b>2D Grid Setting</b>	<b>Input</b>
Total Periodic Points	201
Total Normal Points	101
Maximum Stretching Ratio	1.1
Extrusion layer spacing mode	Hyperbolic Tangent
Quantities used to define layer spacing	Only y+
Domain radius (in chords)	50
y+ at airfoil	1.0

### 3.4.2. Time Grid

Modifying the time grid in AFTGen allows modification of OVERFLOW’s time integration scheme. AFTGen allows modification of subiterations per time step, maximum steady state time steps, as well as maximum time accurate and steady state time step sizes. In addition, an algorithm input allows the user to identify which time integration methodology is used. In this study, steady state switching to time accurate is selected, which allows a switch to time accurate integration if the steady state residuals begin to diverge. Time accurate time steps are scaled with Mach number using the relationship in equation 3.1 [22].

$$dt_{max} = \frac{dt_{max}}{\sqrt{M_{\infty}}} \quad (3.1)$$

In addition to time step considerations, the angle of attack that forces time accuracy can also be modified. These values were all left at default values except for the scaling of time steps as function of Mach number input. Table 3.5 details the Time Grid inputs for AFTGen with OVERFLOW.

Table 3.5. Time Grid settings for all airfoil cases.

<b>Parameter</b>	<b>Input</b>
Subiterations per time step	10
Algorithm	Steady State switching to Time Accurate
Maximum steady state time steps	50000
Scale maximum time accurate step with Mach number	Checked
Maximum time accurate step size	0.05
Maximum steady state time step size	1.0
Angle of attack (deg) to force time accuracy	10

### 3.4.3. Run Control Options

AFTGen with OVERFLOW allows a stacked approach for time steps that changes based on the grid, ranging from coarse to fine. This study used this grid sequencing approach, in addition to an

equal amount of time steps for every run. These values are left at default values, with the exception being the aerodynamic coefficients are brute force averaged if the case has not converged at the end of the overall time steps. Run control inputs are depicted in Table 3.6

Table 3.6. Default run control options in AFTGen with OVERFLOW.

<b>Parameter</b>	<b>Input</b>
Enable Grid Sequencing	checked
Steps for initial run (coarse grid)	2000
Steps for initial run (medium grid)	2000
Steps for initial run (fine grid)	1000
Number of steps per steady state run	250
Number of steps per time accurate run	250
Minimum runs	10
Maximum runs	50
Multigrid	checked
Maximum wall time	365 days
Force Average	checked
Minimum runs to force average	10

#### 3.4.4. Numerical Scheme

The fully turbulent flow selection uses OVERFLOW's NQT variable to 102, indicating that the solver will use the Spalart-Allmaras SA-neg-noft2 1-equation model (DDADI left-hand side). This model does not incorporate transition, nor does it include wall functions. This turbulence model is unique based on the manner in which it calculates to convergence - the equation at one point is not dependent on a converged solution of another point [25,26]. This model is governed by equation 3.2 [27]:

$$\frac{\partial \hat{\nu}}{\partial t} + u_j \frac{\partial \hat{\nu}}{\partial x_j} = c_{b1}(1 - c_{t3})\Omega \hat{\nu} + c_{w1} \left( \frac{\hat{\nu}}{d} \right)^2 + \frac{1}{\sigma} \left[ \frac{\partial}{\partial x_j} \left( (\nu + \hat{\nu} f_n) \frac{\partial \hat{\nu}}{\partial x_j} \right) + c_{b2} \frac{\partial \hat{\nu}}{\partial x_i} \frac{\partial \hat{\nu}}{\partial x_i} \right] \quad (3.2)$$

The second numerical scheme is the Spalart-Allmaras turbulence model with Coder SA\_AFT2017b transition. This scheme couples the negative Spalart-Allmaras turbulence model with a transition model that is able to sufficiently calculate the aerodynamic coefficients and boundary layer characteristics in laminar-turbulent transition conditions [28,29].

In addition to the flow type, OVERFLOW user inputs include a minimum and maximum Courant-Friedrichs-Lewy (CFL) number that can be used to assist in obtaining convergence. The CFL number can be calculated using equation 3.3 [30] [34].

$$C = u \frac{\Delta t}{\Delta x} \quad (3.3)$$

As a rule of thumb, the number of timesteps,  $\Delta t$ , impacts  $C$  directly; further,  $\Delta t$  should be selected to keep the CFL number equal to or less than 1. The default values in AFTGen are 0.25 and 5.0, and in this study, these will be left at default values.

Finally, AFTGen's numerical scheme includes second-order dissipation parameters. Second-order dissipation is artificial dissipation used by the solver to increase simulation stability and is by default scaled with the Mach number.

## Chapter 4. Results and Discussion

### 4.1. OVERFLOW Leading Edge Geometry Improvements

In this section, the number of coordinate points used for the initial geometry is explored, and the final grid is produced by resampling the coordinate points to produce the final grid. Coordinates for the NACA 0012 were obtained using published equations for the surface geometry, while the RC(4)-10 and SSC-A09 are only available as a limited set of coordinate points as obtained from the UIUC database [31]. The default NACA 0012 geometry includes approximately 400 coordinate points. In contrast, the RC(4)-10 and SSC-A09 geometry obtained from the UIUC database contain 83 and 131 coordinate points, respectively. Preliminary results using the OVERFLOW solver and the UIUC default profiles resulted in a coarser gridding around the leading edge, which in turn resulted in a large discrepancy between calculations and experimental data for all of the RC(4)-10 cases. To improve this gridding around the leading edge, the leading edge of these airfoils was refined using a MATLAB code that allowed more point clustering (using a number of points specified by the user) around the leading edge using a spline fit. Figure 4.1 shows the leading-edge density in the default and improved coordinate file for the RC(4)-10 airfoil. Figure 4.2 similarly compares the default coordinates with a denser leading-edge profile for the SSC-A09 airfoil.

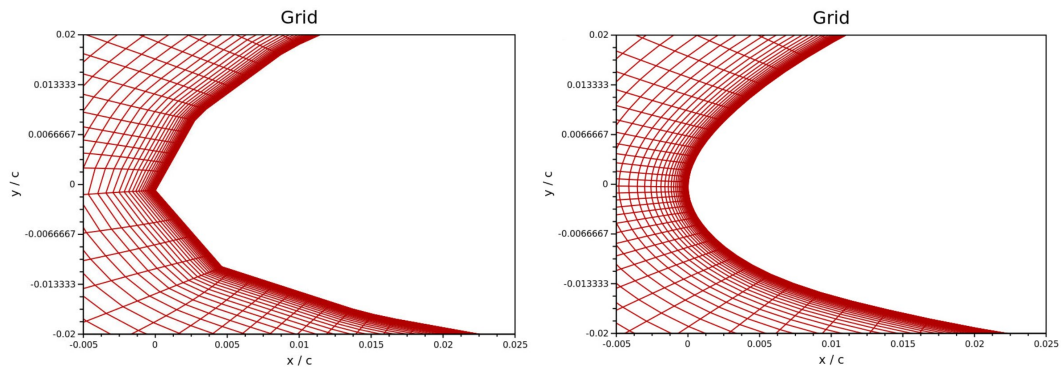


Figure 4.1. Close up of the leading edge of the RC(4)-10 airfoil; default coordinates (left) and the denser leading edge coordinates (right).

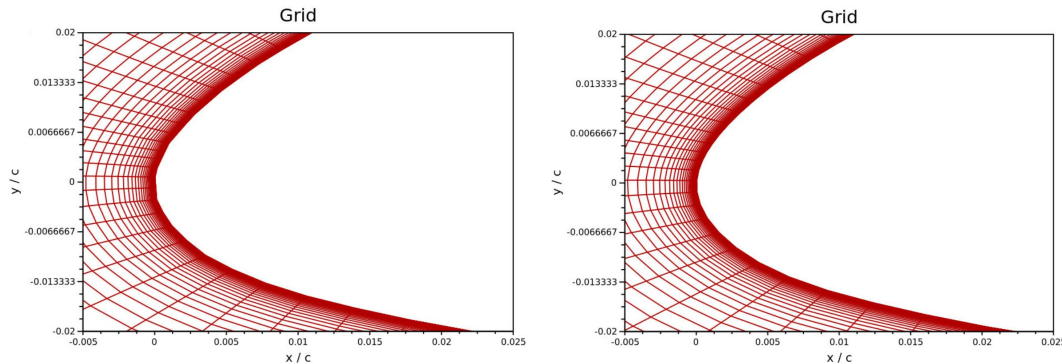


Figure 4.2. Close up of the leading edge of the SSC-A09 airfoil; default coordinates (left) and denser leading-edge coordinates (right).

The leading-edge points were refined for  $0 \leq x/c \leq 0.15$  for both the upper and lower surface. The original ( $x/c, y/c$ ) values were input into a MATLAB code which interpolated point by point to increase the number of points (equally spaced) for that specified section. This approach was particularly effective for the RC(4)-10, which yielded more accurate correlation with experimental data. The discrepancies, and possible explanations for these discrepancies, with respect to the SSC-A09 results are discussed in later sections.

## 4.2. OVERFLOW Trailing Edge and Clustering Iterations Study

Two secondary grid conditions of interest, the number of points across the blunt face of the trailing edge (TE) and the clustering iterations (CI), were varied to assess the impact on the OVERFLOW simulation correlation with experimental test data.

The number of trailing edge points are the number of points used along the blunt trailing edge of the geometry. The default value for these points is 3 for the OVERFLOW solver and can be increased as needed to improve refinement in this area. Increasing the trailing edge points can improve the resolution at the trailing edge, which can better resolve separated vortices and other flow phenomenon that may occur in this area. However, it should be noted that increasing the number of trailing edge points means a loss in resolution in other regions of the grid, as it counts toward the total number of periodic points used in grid generation.

AFTGen provides an option to increase the number of clustering iterations used for its grid generation. By definition, the number of clustering iterations indicates the number of total iterations used to cluster the grid points in the periodic ( $\zeta$ ) direction on the airfoil surface [23]. An iterative technique is used by AFTGen that results in point clustering along the airfoil surface. Table 4.1 summarizes the simulation inputs for the trailing edge and clustering iterations study.

Table 4.1. AFTGen inputs for the trailing edge and clustering iterations studies.

OVERFLOW   Fully Turbulent S-A Model			
Airfoil	NACA0012	RC(4)-10	SSC-A09
Re number	$5.2 \times 10^6$ *	$3.9 \times 10^6$ $3.8 \times 10^6$ $6 \times 10^6$ $7.9 \times 10^6$	$5.16 \times 10^6$
M	0.3, 0.4	0.37 to 0.9	0.599
$\alpha, \Delta 1^\circ$	$\pm 8^\circ$ to $17^\circ$	$-4^\circ$ to $16^\circ$	$-1^\circ$ to $20^\circ$
$\xi, \eta$ **	(201,101)	(201,101)	(201,101)
TE***, $\Delta 2$	3 to 41	3 to 41	3 to 41
CI, $\Delta 5K$	10K to 60K	10K to 60K	10K to 60K

\*  $Re/M$  – Reynolds Mach proportionality constant

\*\*number of points in normal and periodic direction

\*\*\*number of points across blunt trailing edge face

Trailing edge cases were run in the  $c_{l,max}$  range for the 0012 airfoil (8 - 17 deg angle of attack) at Mach numbers of 0.3 and 0.4 and Reynolds-Mach ( $Re/M$ ) proportionality constant of  $5.2 \times 10^6$ . For the RC(4)-10, cases were run for an angle of attack range of -4 - 16 deg for Mach numbers of 0.34, 0.37, 0.49, and 0.63 at respective Reynolds numbers of  $3.9 \times 10^6$ ,  $3.8 \times 10^6$ ,  $3.8 \times 10^6$ , and

$7.9 \times 10^6$ . These pairings were selected based on their correlation with experimental test data and to provide comparisons between XFOIL and OVERFLOW. The TE points included odd numbers only, with a step size of 2 points up until 41 total TE points. Figure 4.3 and Figure 4.4 show the TE point results for the 0012 at Mach number of 0.3 and 0.4.

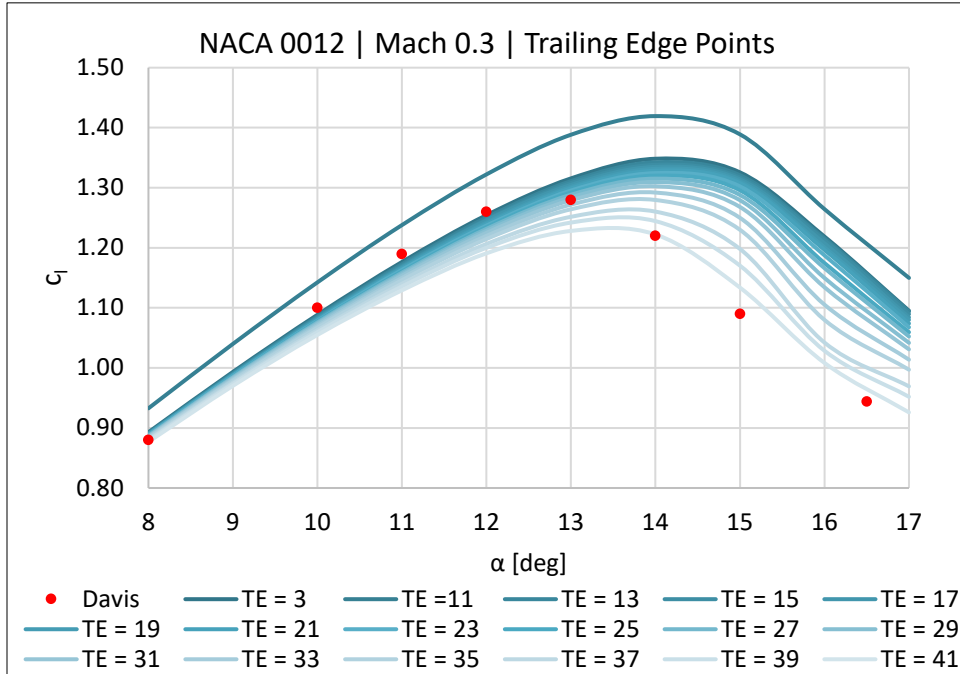


Figure 4.3. TE point change for the NACA 0012 at  $M = 0.3$  and  $Re/M = 5.2 \times 10^6$ .

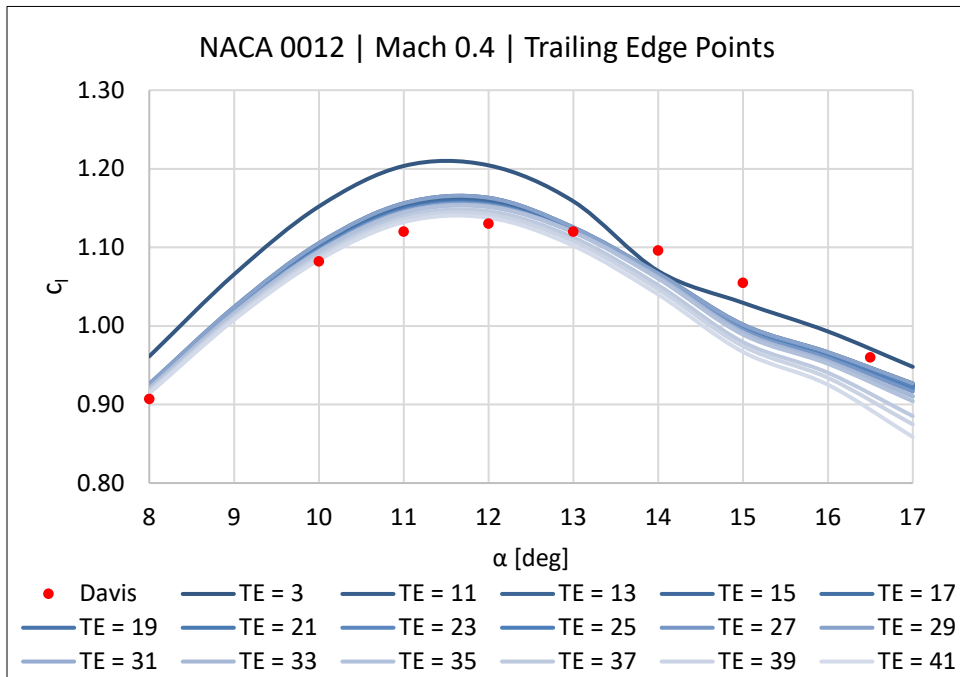


Figure 4.4. TE point change for the NACA 0012 at  $M = 0.4$  and  $Re/M = 5.2 \times 10^6$ .

Increasing the number of trailing edge points for both NACA 0012 cases results in the maximum lift coefficient approaching the value in the legacy airfoil table, depicted in red. However, neither of the cases result in a close comparison with the stall region of the airfoil. The maximum lift coefficient for the Mach 0.3 case seems to occur at a higher angle of attack than seen with the experimental test data. For the Mach 0.4 case, the correlation is marginally better, but still does not produce a result that matches the experimental data trend. This seems to be consistent with NACA 0012 results overall (discussed in later sections). Increasing beyond 11 TE points shows that the lift curve nearly converges to the same lift coefficient up to 33 TE points. Beyond this number of points, from 37 to 41, this same “convergence” trend is not seen. The increase in trailing edge point count seems to converge and show results that are nearly identical past a value of 33 TE points for the Mach 0.4 case. For subsequent NACA 0012 simulations, the trailing edge points was set to 33. A similar trailing edge study for the RC(4)-10 was completed, with results shown in Figure 4.5, Figure 4.6, and Figure 4.7.

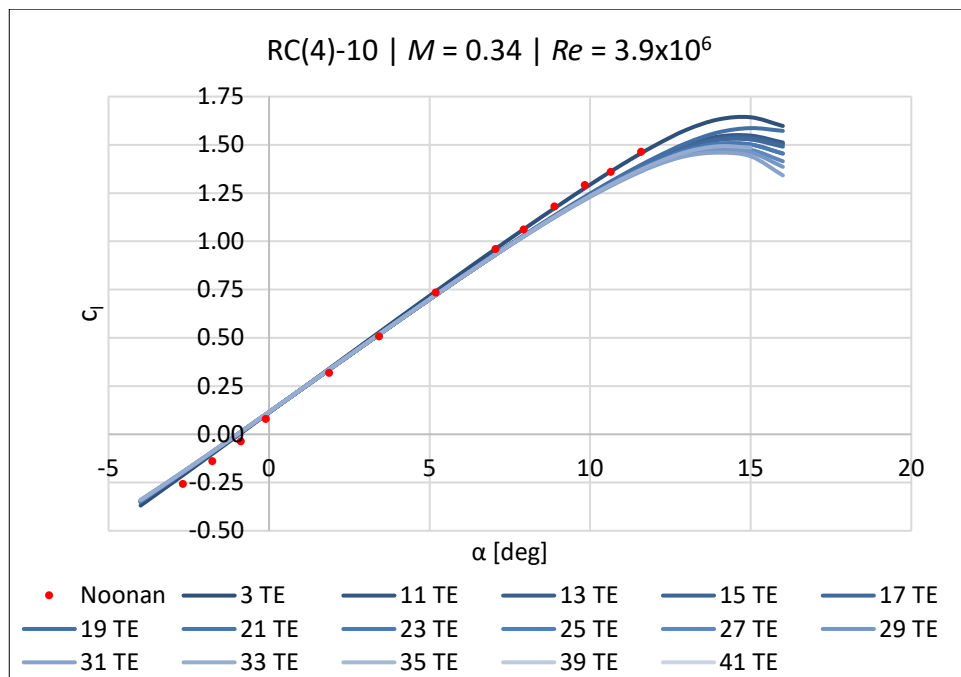


Figure 4.5. Lift coefficient versus  $\alpha$  for the RC(4)-10 airfoil at  $M = 0.34$  and  $Re = 3.9 \times 10^6$ .

For  $M = 0.34$  (Fig. 10), the RC(4)-10 correlation with the Noonan experimental data does not improve – in fact, at these Mach-Reynolds number values, the smallest value of TE (TE = 3) lies closest to the experimental data. However, for higher Mach numbers shown in Figure 4.6 and Figure 4.7, the opposite is true.

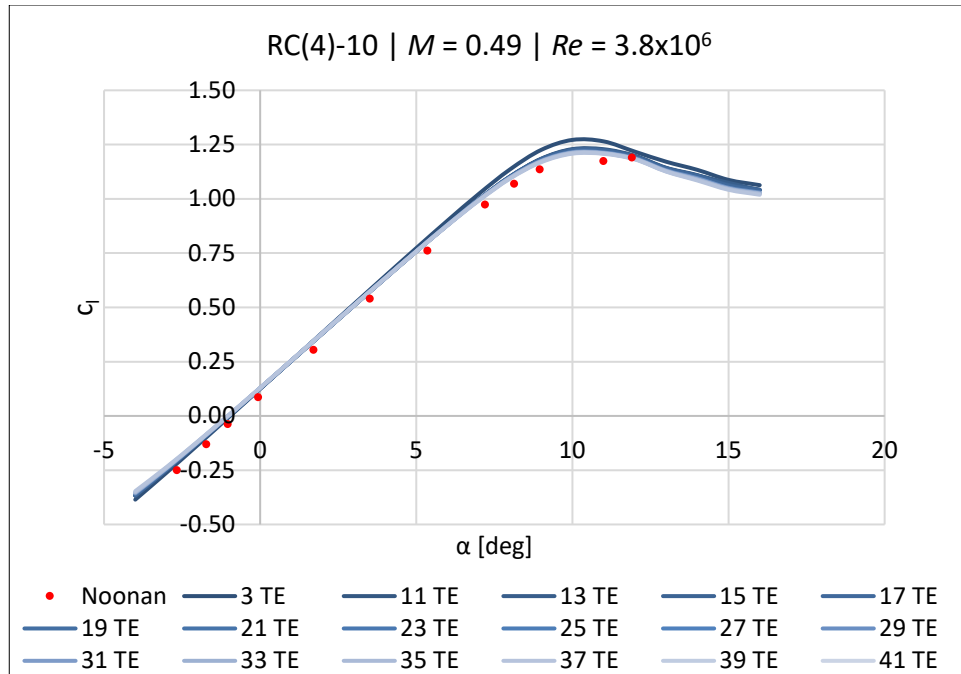


Figure 4.6. Lift coefficient versus  $\alpha$  for the RC(4)-10 airfoil at  $M = 0.49$  and  $Re = 3.8 \times 10^6$ .

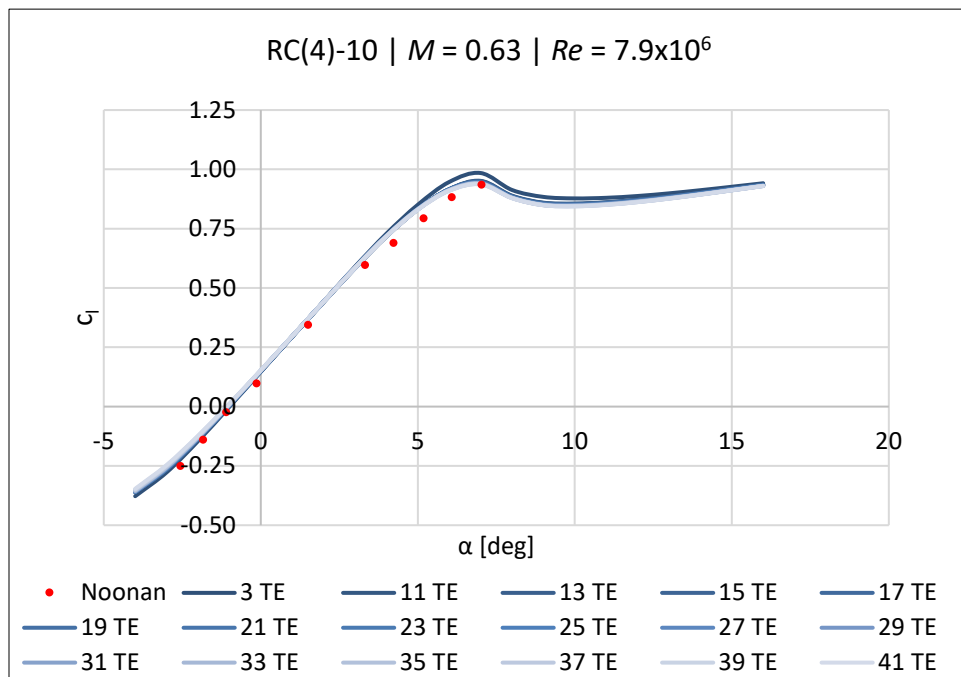


Figure 4.7. Lift coefficient versus  $\alpha$  for the RC(4)-10 airfoil at  $M = 0.63$  and  $Re = 7.9 \times 10^6$ .

Figure 4.6 and Figure 4.7 show that for higher Mach numbers, as the trailing edge grid density is increased, the curve approaches the experimental test data, correlating quite well in comparison. In Figure 4.7, increasing the value of TE converges to the same lift coefficient trend. Increasing the number of trailing edge points ultimately results in a lift curve that more closely aligns with experimental data. For this reason, a trailing edge clustering of 33 was selected for all three airfoils

(beyond this, the results appear to be very similar). With respect to both the 0012 and RC(4)-10, additional considerations are required to improve OVERFLOW results with experimental test data, the primary consideration being the manner with which AFTGen generates a grid for OVERFLOW. The grid generator may affect the overall quality of the grid used for the flow solver. Figure 4.8 depicts the overall grid for the RC(4)-10 airfoil for 11 trailing edge points and 33 trailing edge points.

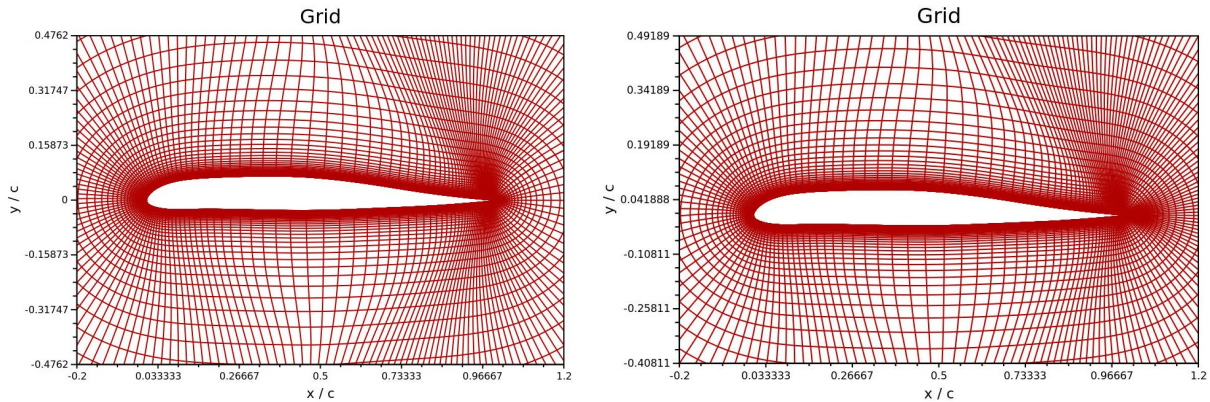


Figure 4.8. Effect on the overall RC(4)-10 grid for 11 TE points (top) and 33 TE points (bottom).

AFTGen’s default clustering iterations value is 10,000. The number of iterations was increased in increments of 5,000 up to 60,000. Figure 4.9 and Figure 4.10 show the change in section lift coefficient vs angle of attack plot with increasing clustering iterations for the NACA 0012 airfoil.

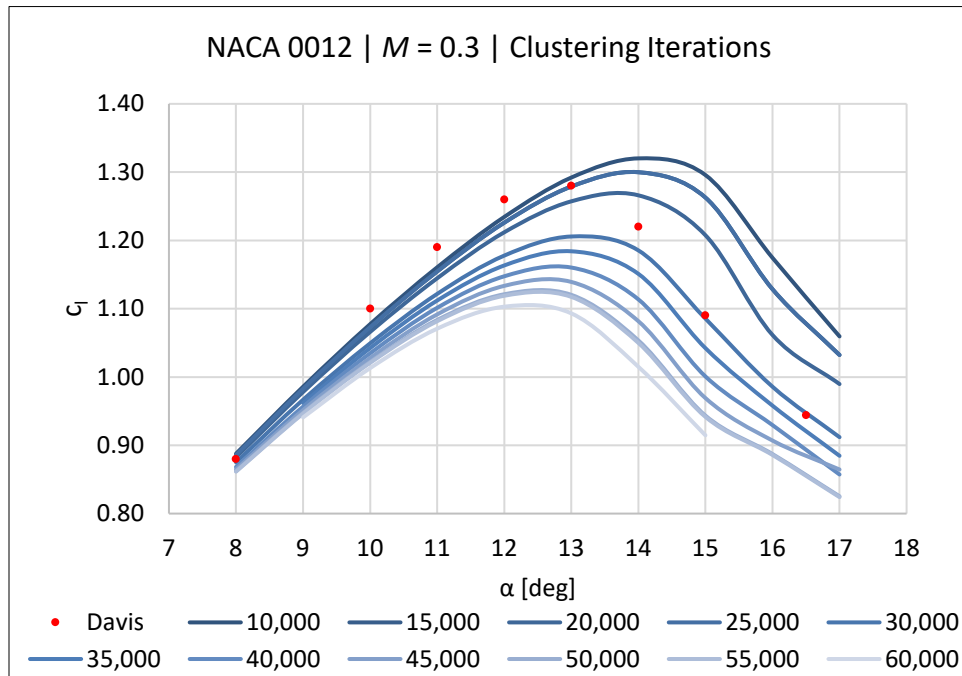


Figure 4.9. Change in CI for the NACA 0012 at  $M = 0.3$  and  $Re/M = 5.2 \times 10^6$ .

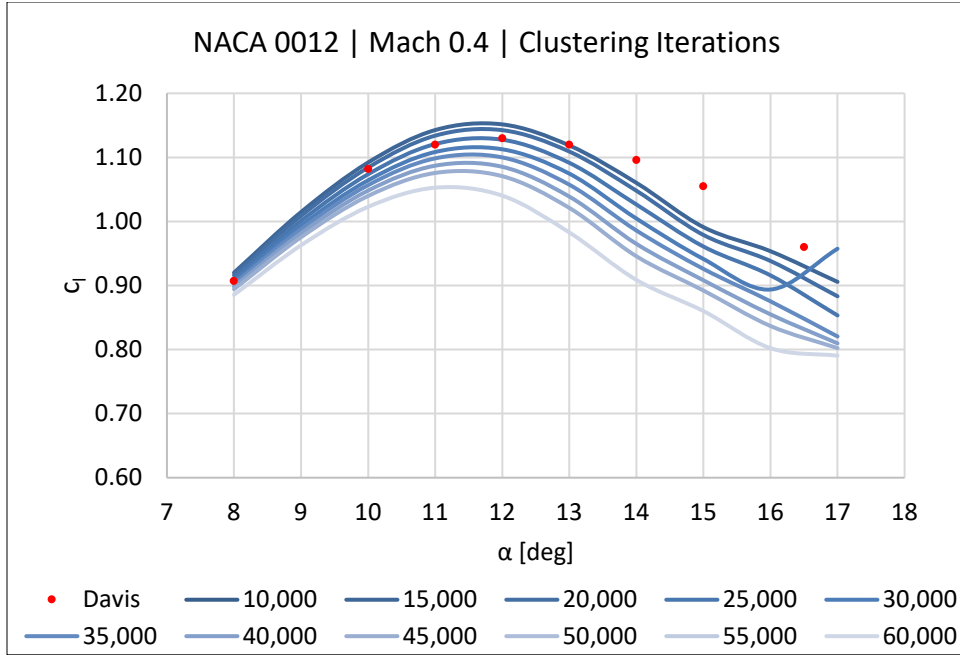


Figure 4.10. Change in  $C_l$  for the NACA 0012 at  $M = 0.4$  and  $Re/M = 5.2 \times 10^6$ .

While the clustering iterations seem to have no impact on accuracy when comparing simulations and experimental test data. Increasing the CI results in a worse correlation per 5,000 iterations. Increasing clustering iterations reduces the predicted maximum lift coefficient significantly, with no change in the end result's correlation with legacy 0012 airfoil table data. An investigation of the clustering iterations was performed for the RC(4)-10 and SSC-A09. Figure 4.11 and Figure 4.12 show the results of increasing clustering iterations at Mach 0.44 for the RC(4)-10 airfoil.

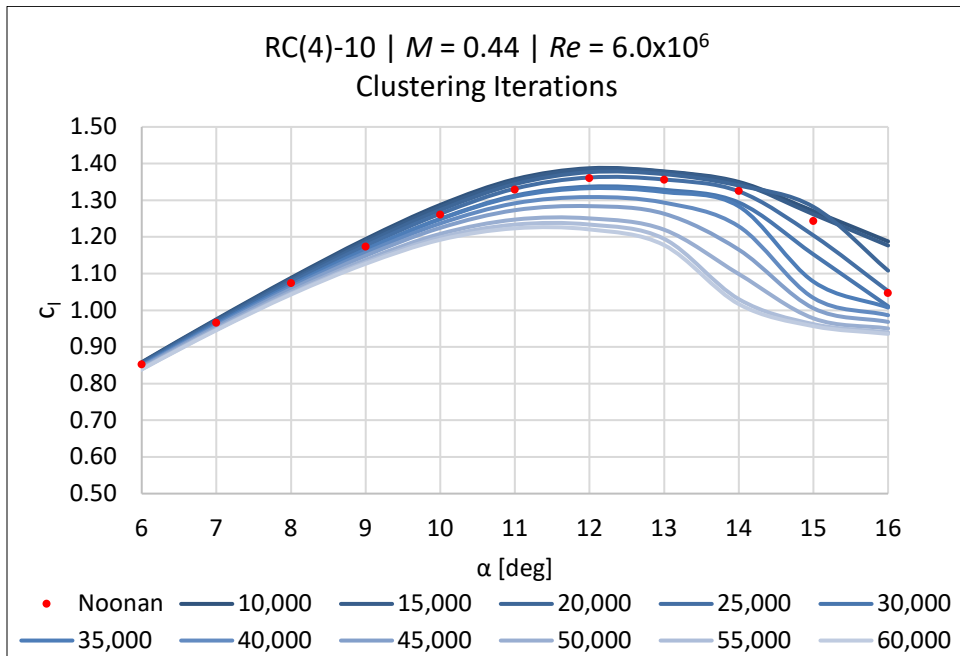


Figure 4.11. RC(4)-10 clustering iterations study at  $M = 0.44$  and  $Re = 6 \times 10^6$ ,  $c_l$  vs  $\alpha$ .

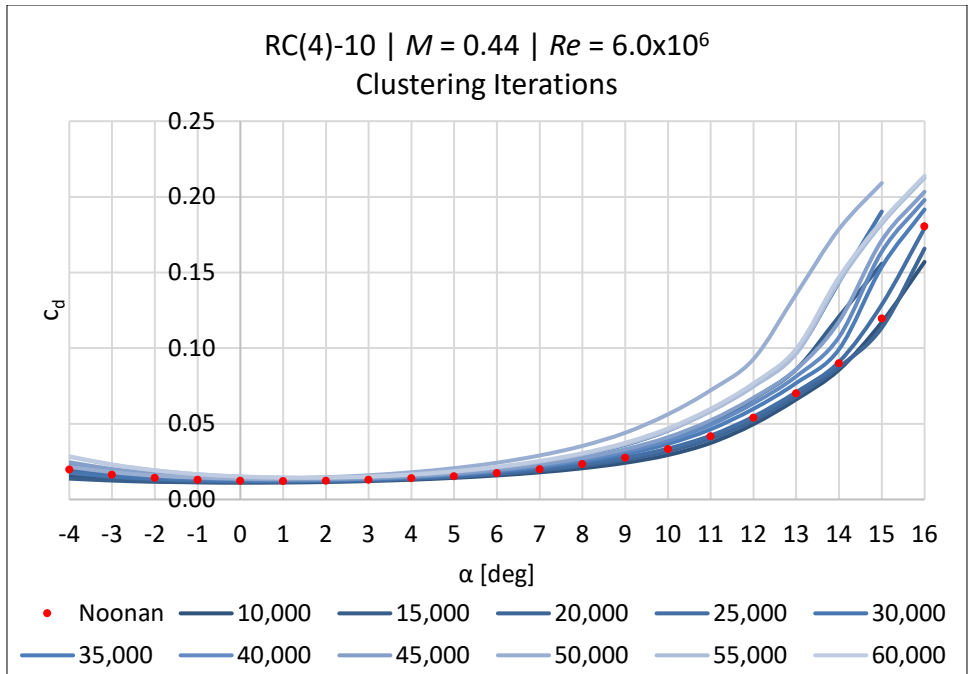


Figure 4.12. RC(4)-10 clustering iterations study at  $M = 0.44$  and  $Re = 6 \times 10^6$ ,  $c_d$  vs  $\alpha$ .

For the RC(4)-10 airfoil, a trend similar to the 0012 is seen, except at 20K CI, there is a fairly good approximation of both the section lift and section drag coefficients. As the clustering iterations increase, the accuracy with between the OVERFLOW results and the experimental data decreases. With increasing clustering iterations, the lift is consistently underpredicted and drag is consistently overpredicted after 20,000 clustering iterations. Figure 4.13 provides a close up of the leading edge of the RC(4)-10 airfoil with increasing clustering iterations.

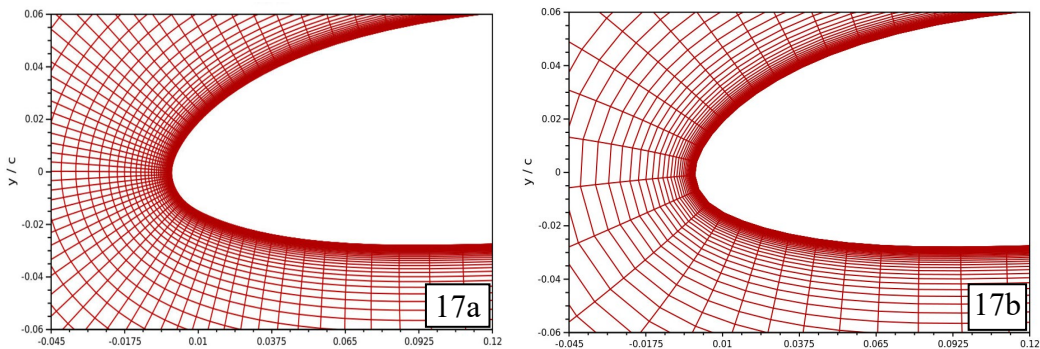


Figure 4.13. CI at the leading edge; 17a: 20K CI; 17b: 60K CI.

Up to 20K CI, there is a slight improvement to the grid at the leading edge. Beyond this, the grid seems to grow coarser as the number of clustering iterations increase. For both the NACA 0012 and the RC(4)-10 airfoils, the increase in clustering iterations results in a degradation of the lift curve slope. This trend also is seen when performing the same study with the SSC-A09 airfoil. Figure 4.14 and Figure 4.15 show the lift and drag coefficient versus angle of attack, with the experimental data not aligning as well with OVERFLOW simulations.

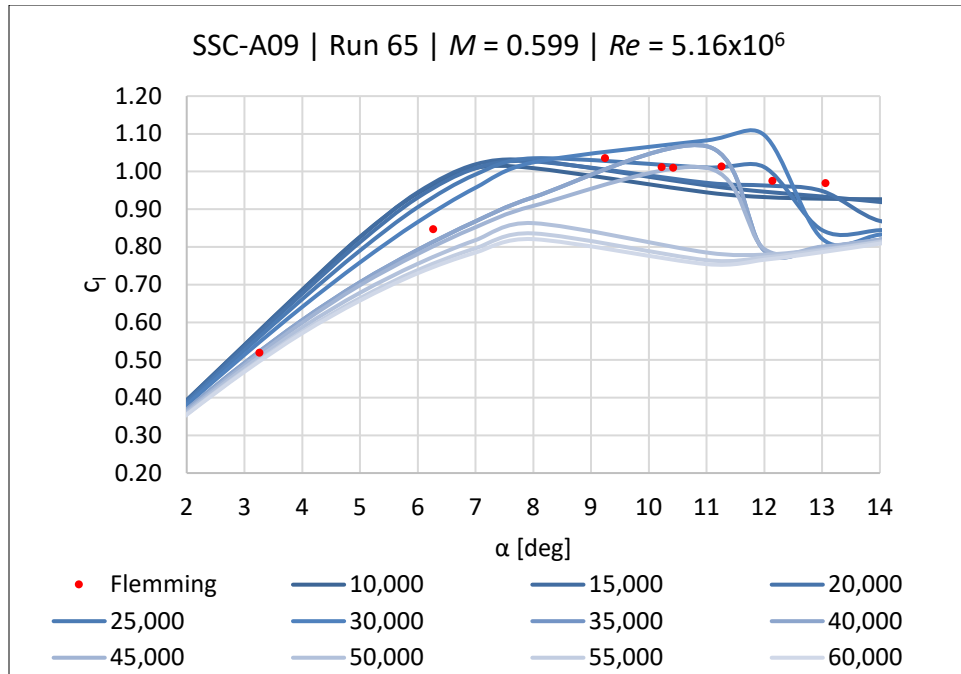


Figure 4.14. SSC-A09 CI study, Run 65 at  $M = 0.599$  and  $Re = 5.16 \times 10^6$ ,  $c_l$  vs  $\alpha$ .

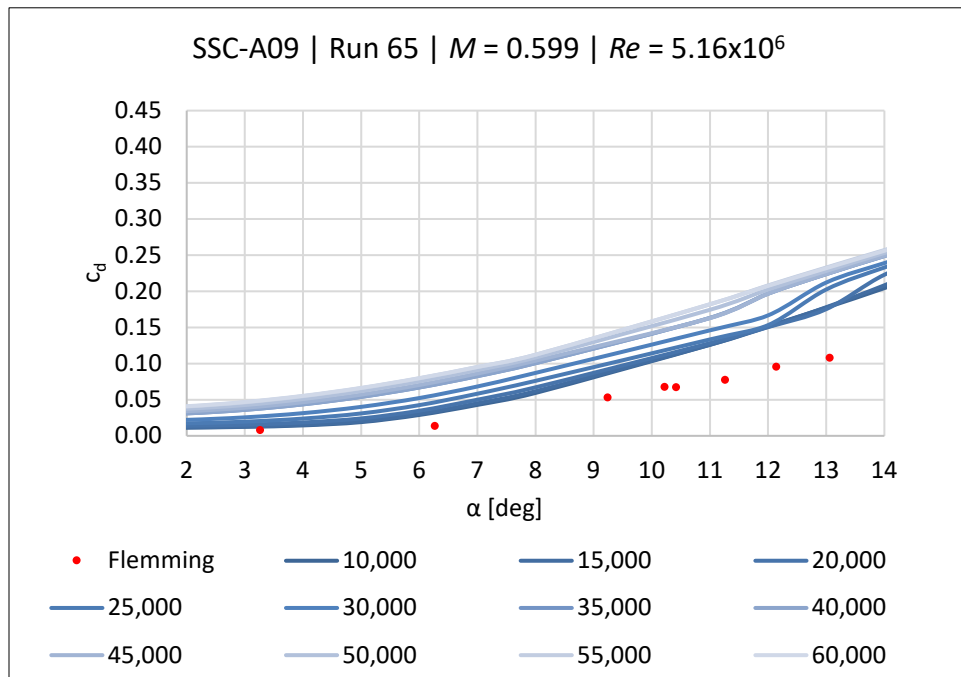


Figure 4.15. SSC-A09 CI study, Run 65 at  $M = 0.599$  and  $Re = 5.16 \times 10^6$ ,  $c_d$  vs  $\alpha$ .

The first few clustering iterations, from 5,000 to around 25,000, yield similar results with dramatic changes in the lift curve and the drag bucket with increasing iterations. The correlation is the worst for the SSC-A09 experimental and simulated data, and for this airfoil, the effect of increasing clustering iterations is inconclusive until further investigation can be performed.

### 4.3. XFOIL and OVERFLOW Results

The following sections present results generated using AFTGen with the XFOIL and OVERFLOW flow solvers. The NACA 0012, RC(4)-10, and SSC-A09 experimental data is compared against section lift and section drag coefficients calculated by XFOIL and OVERFLOW for a range of alpha-Mach pairs, discussed in more detail later. In addition, a comparison of the pressure coefficient for each airfoil is provided for validation of the computational approach used in this study.

The experimental pressure coefficient data in the NACA 0012 study originates from transition-free data as presented by Harris [8]. Section lift and drag coefficients originate from the Davis [7] produced airfoil table. The experimental section lift coefficient, section drag coefficient, and pressure coefficient distribution for the RC(4)-10 was digitized manually from data published by Noonan [12]. The SSC-A09 experimental data, as detailed by Flemming [14] was digitized from tabulated data on the pressure derived lift coefficient and wake rake derived drag coefficient, with the pressure data digitized manually from available pressure coefficient versus chord plots.

#### 4.3.1. NACA 0012

The NACA 0012 cases were run at a Reynolds-Mach proportionality constant of  $5.2 \times 10^6$ , which indicates that the Reynolds number is scaled with the Mach number. In essence, the  $Re/M$  input is the Reynolds number at Mach 1.0. The input Mach number in the simulation set is multiplied with this  $Re/M$  to determine the Reynolds number for each case in AFTGen [23]. Cases were run fully turbulent and using the Coder transition model in OVERFLOW. Cases were run at Mach numbers from 0.2 to 1.0 at 0.1 intervals, with additional individual Mach numbers of 0, 0.18, 0.28, 0.38, 0.48, 0.62, 0.72, 0.75, 0.77, 0.82, and 0.92 to provide a full range of comparison data for each aerodynamic coefficient. For clarity, the C81 table used most frequently does not provide aerodynamic coefficient data at the exact same Mach numbers and angle of attack range for each respective coefficient. The section lift coefficient has alpha-Mach pairs at 0 and 0.2 – 1.0 (intervals of 0.1), the section drag coefficient is determined for Mach numbers of 0, 0.18, 0.28, 0.38, 0.48, 0.62, 0.72, 0.77, 0.82, and 0.92, and the section moment coefficient listed at Mach numbers of 0, 0.2 – 1.0, and 0.75. To reflect this, the .c81 table generated for the 0012 incorporates the full Mach range (incorporating the range for each aerodynamic coefficient) and full  $-20^\circ$  to  $20^\circ$   $\alpha$  range, for a total of 2,583  $\alpha$ -Mach pairs. Appendix B contains the full range of plots generated from XFOIL (within the appropriate range) and OVERFLOW fully turbulent and transition cases. The Mach number, angle of attack range, and  $Re/M$  inputs are provided in Table 4.2.

Table 4.2. NACA 0012 AFTGen inputs for airfoil table generation in XFOIL and OVERFLOW.

Airfoil	$\alpha$ [deg]	$Re/M$	$M$
NACA 0012	$\pm 20^\circ$	$5.2 \times 10^6$	0.00, 0.18, 0.20, 0.28, 0.30, 0.38, 0.40, 0.48, 0.50, 0.60, 0.62, 0.70 0.72, 0.75, 0.77, 0.80, 0.82, 0.90, 0.92, 1.00

Figures C.1 through C.5 show the lift versus  $\alpha$  curve for Mach numbers 0.2 through 0.6. In Figures C.1 and C.2, XFOIL converged for the full  $\alpha$  range at Mach 0.2 and Mach 0.3, with the

section lift coefficient calculated slightly above the experimental data and the OVERFLOW predictions. At Mach 0.2, OVERFLOW's fully turbulent model aligns very well with the experimental data, and does a better job predicting the section lift coefficient in the stall region than the transition model does. The  $c_{l,max}$  is slightly underpredicted and occurs at a higher angle of attack. At Mach 0.3, OVERFLOW correlates very well with experimental data in the positive angle of attack range for both the fully turbulent and transition models, with the negative angles of attack underpredicting in comparison to the Davis data.

Figure C.3 shows convergence for XFOIL at  $-19^\circ$  to  $19^\circ$   $\alpha$  at Mach 0.4 and shows consistency with C.1 and C.2, with XFOIL results overpredicting the maximum lift coefficient. Figures C.4 and C.5 are at Mach numbers of 0.5 and 0.6. This Mach number regime can be challenging for XFOIL to calculate, particularly at higher angles of attack. This can be observed in Figures C.4 and C.5, where the capability of XFOIL dramatically reduces to a more limited  $\alpha$  range from  $-8^\circ$  to  $8^\circ$  at Mach 0.5 and  $-9^\circ$  to  $7^\circ$  at Mach 0.6. The OVERFLOW fully turbulent and transition results show very close predictions for  $c_{l,max}$  at Mach 0.4 and 0.5. At Mach 0.6, OVERFLOW's fully turbulent model overshoots the experimental data, with the fully turbulent and transition models not aligning particularly well beyond an alpha of  $\pm 8^\circ$ .

Beyond Mach 0.6, XFOIL was only able to converge for a limited range of angles of attack, and for this reason, Mach numbers beyond 0.6 are not depicted in Figures C.6 through C.10. In Figure C.6, the OVERFLOW models, similar to Figure C.5, show a distinct difference in predicted  $c_{l,max}$ . Further, the fully turbulent results don't align as closely in the linear angle of attack range. There appears to be a slight offset between the fully turbulent predictions and the transition model, as well as the experimental and XFOIL results. The cause for this discrepancy is unknown – all cases were run in the same simulation in AFTGen. Figures C.7 and C.8, at Mach 0.7 and 0.8, respectively, show very close predictions between the two OVERFLOW models. Figures C.9 and C.10 at Mach 0.9 and 1.0 show nearly identical predictions for the lift curve. For Figures C.5 through C.10 all show a difference in trends between simulated data and experimental data. It should be noted that the trend in the experimental data does not depict a conventional stall curve – instead, the 0012 experimental data set shows a much more gradual change in lift for angles of attack beyond 10 deg at Mach 0.4 and 0.5, with its peak shown at decreasingly small  $\alpha$  values as the Mach number increases.

The next data set of interest is the section drag coefficient versus angle of attack curves, shown in Figures C.11 through C.18. These plots show the predicted drag coefficient for Mach numbers at 0.18, 0.28, 0.38, 0.48, 0.62, 0.72, 0.77, and 0.82. XFOIL was able to converge up to Mach 0.62, and in all cases, tended to underpredict drag in the linear  $\alpha$  range. OVERFLOW, on the other hand, seems model calculates drag coefficients closer to the experimental data than the fully turbulent model can. OVERFLOW comes closest to the experimental results at Mach numbers from 0.38 through 0.62, with data and trends aligning fairly well. At Mach 0.72 and beyond, there is a difference in overall trend between simulated and experimental test results. The moment coefficient predictions, for both XFOIL and OVERFLOW, show the least agreement in overall data trends, shown in Figures C.19 through C.27.

Overall, for the NACA 0012 airfoil, XFOIL compares reasonably well with the experimental test data within the linear angle of attack range. This is expected, based on its limitations in the stall region for the airfoil. OVERFLOW shows good correlation with experimental data in this linear  $\alpha$  range as well as  $c_{l,max}$  up until Mach 0.5. At Mach 0.5 and beyond, the stall region from the experimental data shows a much more gradual decrease in lift than was expected, and for this

reason, the overall trends do not align well beyond the linear angle of attack range. This is an area of uncertainty that still needs to be investigated.

As a sanity check for the approach, an investigation into the pressure coefficient was completed. Unfortunately, the 0012 .c81 table referenced in this report, as provided by Davis, does not have a set of pressure data for comparison. For this reason, the Harris report was looked at for the relevant data as a sanity check. Only a handful of cases were run with the Harris testing conditions at a Reynolds number of  $3.0 \times 10^6$  and at an angle of attack close to  $0^\circ$  of  $-0.14^\circ$ . The Mach numbers selected were Mach 0.3 and 0.6 to have comparisons between incompressible and compressible flow. The cases selected were from the transition free model of the test, and because the airfoil is symmetric, it is not as straightforward to distinguish between the pressure across the upper and lower surface of the airfoil, as the data report's plots needed to be digitized for comparison.

Figure 4.16 and Figure 4.17 show the pressure coefficient versus chord curves, with the experimental data shown by the red icons, XFOIL shown in yellow, and OVERFLOW's fully turbulent results depicted by the blue curve.

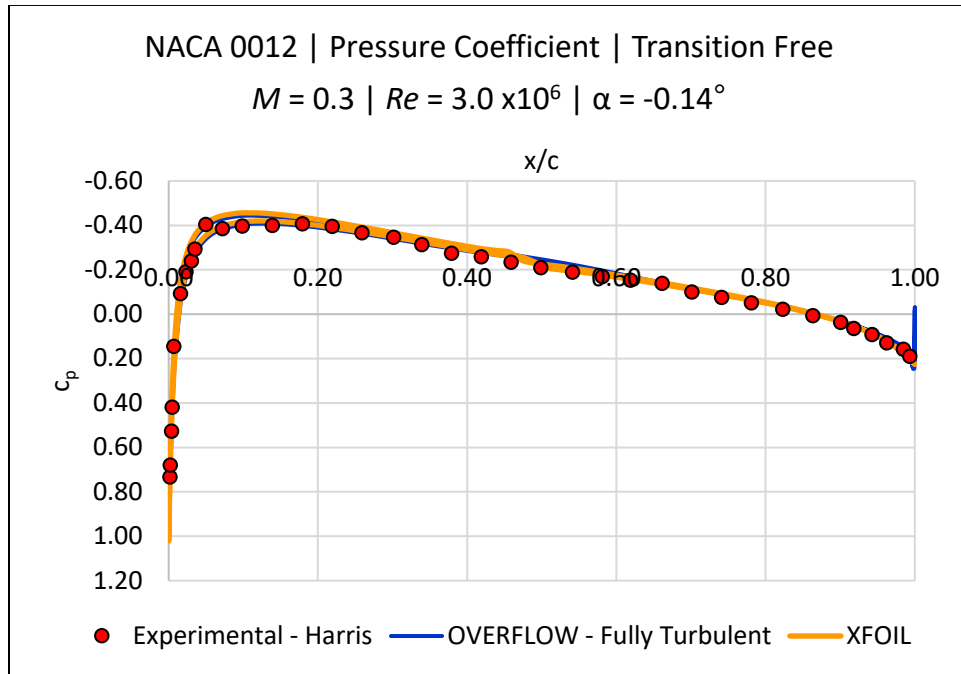


Figure 4.16.  $C_p$  vs  $x/c$  for the NACA 0012 airfoil at Mach 0.3. Digitized from Figure 40a [8].

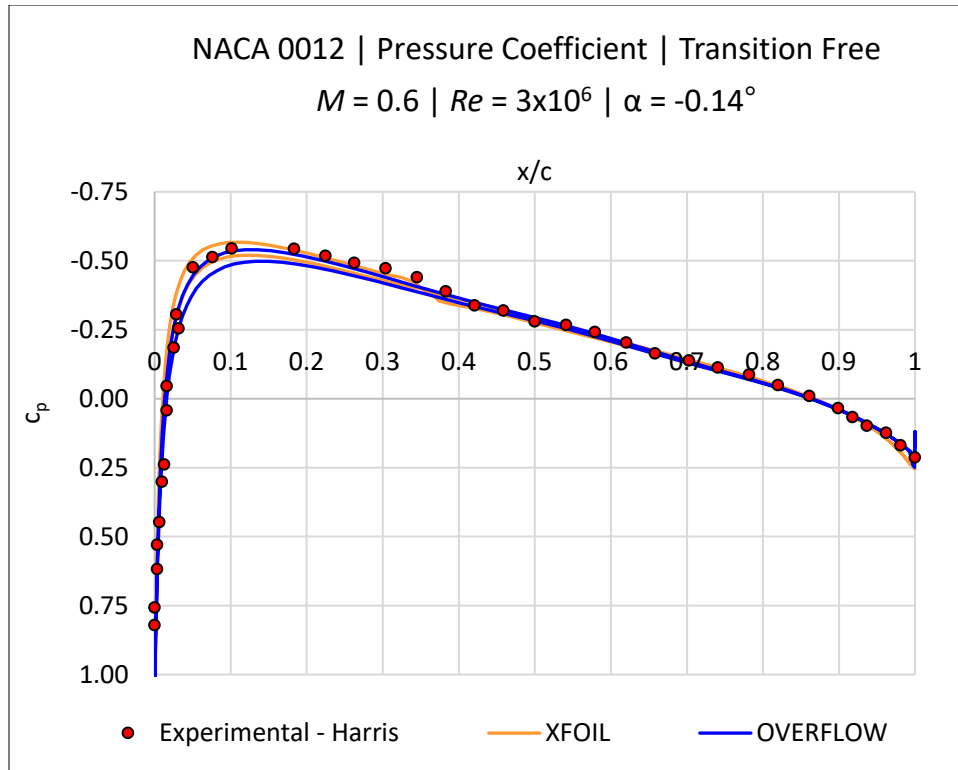


Figure 4.17.  $C_p$  vs  $x/c$  for the NACA 0012 airfoil at Mach 0.6. Experimental data digitized from Figure 40e [8].

The Reynolds-Mach pair at Mach 0.3 shows excellent agreement between the test data and OVERFLOW results, while XFOIL overpredicts the pressure coefficient (and thus, the lift coefficient). The agreement between OVERFLOW and the test data is quite good for these Mach-Reynolds pairs, although OVERFLOW overpredicts the lift coefficient at the leading edge. There is also a sharp spike in  $C_p$  at the trailing edge, suggesting that perhaps the resolution overall at the leading and trailing edges could be improved to better capture aerodynamic effects. The fact that the OVERFLOW fully turbulent cases align well with the experimental data shows that the approach for generating the aerodynamic coefficients was valid. After comparing these plots, the flow was visualized in Fieldview to generate the velocity and pressure contours. Figure 4.18 depicts the Fieldview contours for OVERFLOW's fully turbulent model at Mach 0.3, with the pressure set as the scalar and the velocity as the vector. Figure 4.19 depicts the Fieldview contours at Mach 0.3 with the velocity vectors displayed, with Mach number as the scalar value used for the color contours.

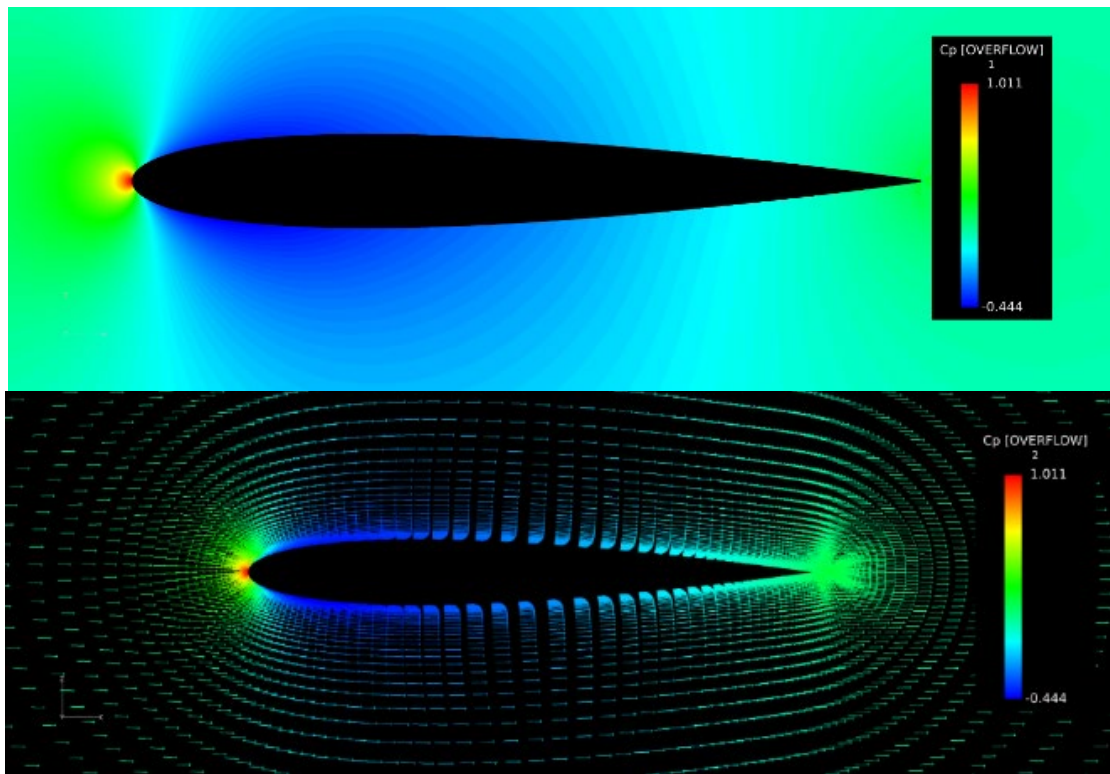


Figure 4.18. Pressure coefficient contour and vector plots at Mach 0.3 for the NACA 0012.

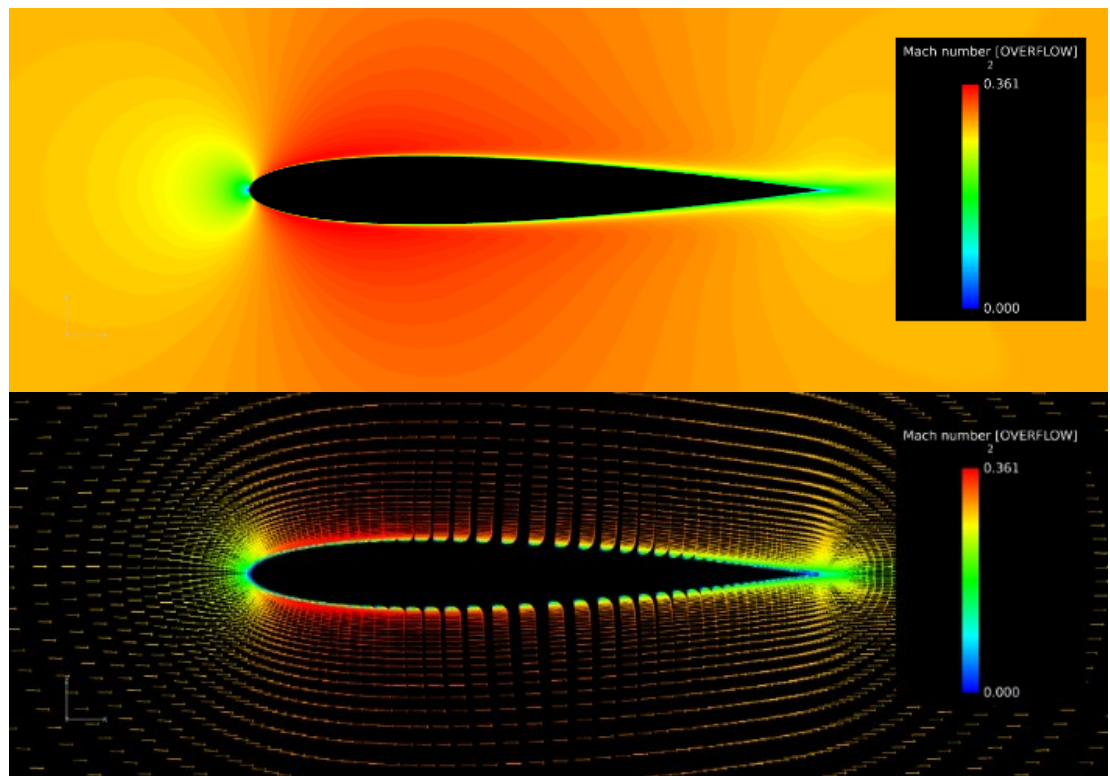


Figure 4.19. Mach contour and vector plots at Mach 0.3 for the NACA 0012.

The stagnation point at the leading edge of the airfoil shows a calculated pressure coefficient value of 1.011. In Figure 4.16, the Harris data showed a peak  $C_P$  around 0.7, which is overall lower than is shown in the OVERFLOW results. The pressure coefficient can be calculated directly using relationships between stagnation pressure, Mach number, and specific heat ratio, depicted in equation 4.1 as used for incompressible flow [32]:

$$C_P = \frac{P - P_\infty}{\frac{1}{2} \rho_\infty v_\infty^2} \quad (4.1)$$

Equation 4.1 can be further simplified into equation 4.2.

$$C_P = \frac{P - P_\infty}{\frac{1}{2} \rho_\infty v_\infty^2} \rightarrow \frac{P_\infty \left( \frac{P_0}{P_\infty} - 1 \right)}{\frac{1}{2} \gamma P_\infty M_\infty^2} \rightarrow \frac{2 \left( \frac{P_0}{P_\infty} - 1 \right)}{\gamma M_\infty^2} \rightarrow C_P = \frac{2}{\gamma M_\infty^2} \left( \frac{P_0}{P_\infty} - 1 \right) \quad (4.2)$$

Where  $p_0$  is the total pressure and  $p_\infty$  is the static freestream pressure. Using equation 25, the calculated stagnation pressure coefficient is 1.023. This shows that at this Mach number, OVERFLOW slightly underpredicts the pressure coefficient at the stagnation point.

Figure 4.20 shows the Fieldview generated contours at Mach 0.6 for OVERFLOW's fully turbulent model. In Figure 4.20, the pressure set as the scalar and the velocity as the vector.

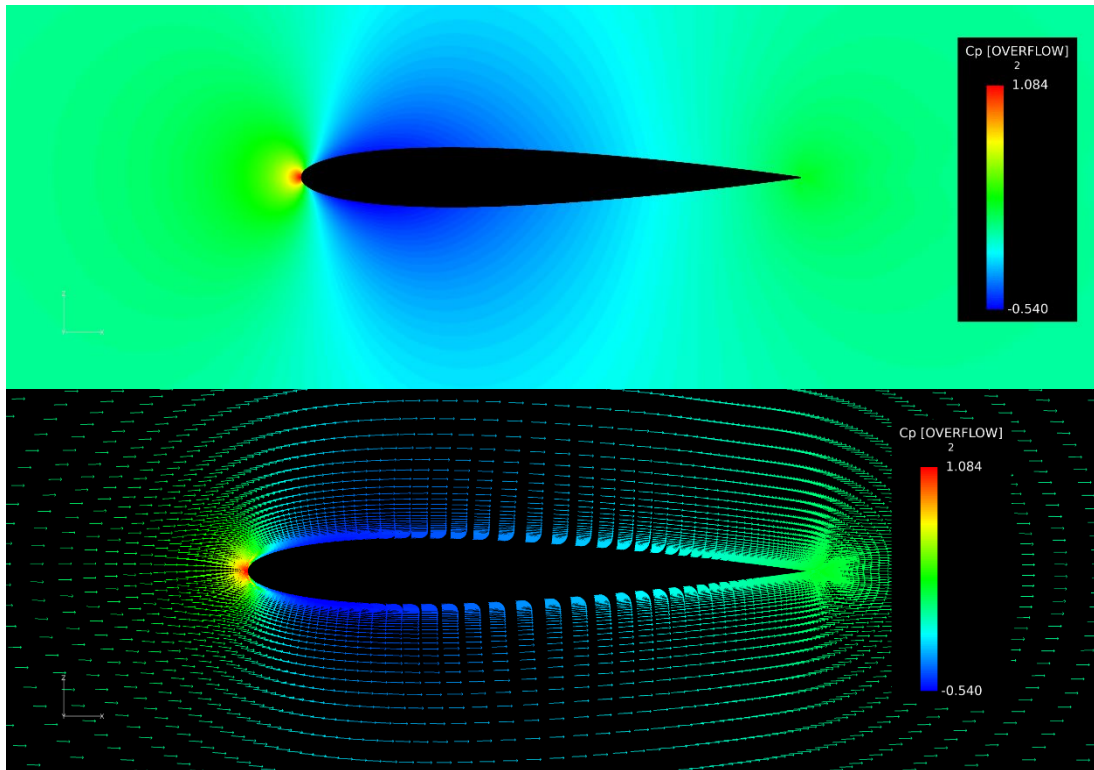


Figure 4.20. Pressure coefficient contour and vector plots at Mach 0.6 for the NACA 0012.

The contours above show the pressure distribution across the airfoil surface, with the pressure gradient shown in the bottom image of Figure 4.20. No adverse pressure gradient is shown, indicating at this Mach number and angle of attack, no flow separation occurs (which is not surprising). Using equation 25, the pressure coefficient can be calculated and compared with experimental and simulated results. The Harris data provides a pressure coefficient of 0.88 at the leading edge, OVERFLOW calculates the stagnation pressure coefficient as 1.084. For comparison, the pressure coefficient is again calculated using the formula for pressure coefficient at the stagnation point, however with equation 4.3, which is valid for compressible flow [35]:

$$C_P = \frac{2}{\gamma M_\infty^2} \left[ \left( 1 + \frac{\gamma-1}{2} M_\infty^2 \right)^{\frac{\gamma}{\gamma-1}} - 1 \right] \quad (4.3)$$

Using the above formula, the pressure coefficient at Mach 0.6 was determined to be 1.093. OVERFLOW again underpredicts the pressure. The full list of calculated stagnation pressure coefficients is included in Table 4.3.

Table 4.3. Calculated stagnation pressure coefficients at all Mach numbers for the NACA 0012 airfoil.

<b>Mach Number</b>	<b>C<sub>P,stag</sub></b>
0.10	1.0025
0.18	1.0081
0.20	1.0100
0.28	1.0197
0.30	1.0226
0.38	1.0365
0.4	1.0406
0.48	1.0587
0.50	1.0638
0.60	1.0928
0.62	1.0993
0.70	1.1278
0.72	1.1355
0.75	1.1476
0.77	1.1560
0.80	1.1691
0.82	1.1781
0.90	1.2171
0.92	1.2275
1.0	1.2722

### 4.3.2. RC(4)-10

The RC(4)-10 airfoil simulations were run for fewer  $\alpha$ -Mach pairs, with the details on angle of attack, Mach number, and Reynolds number included in Table 4.4.

Table 4.4. RC(4)-10 primary inputs for XFOIL and OVERFLOW.

<b>Simulation #</b>	<b><math>\alpha</math> range</b>	<b>Mach Number</b>	<b>Reynolds Number</b>
1	-4° to 16° ( $\Delta 1^\circ$ )	0.34	$3.9 \times 10^6$
2	-4° to 16° ( $\Delta 1^\circ$ )	0.34	$4.8 \times 10^6$
3	-4° to 16° ( $\Delta 1^\circ$ )	0.37	$3.8 \times 10^6$
4	-4° to 16° ( $\Delta 1^\circ$ )	0.39	$3.8 \times 10^6$
5	-4° to 16° ( $\Delta 1^\circ$ )	0.39	$5.4 \times 10^6$
6	-4° to 16° ( $\Delta 1^\circ$ )	0.42	$3.8 \times 10^6$
7	-4° to 16° ( $\Delta 1^\circ$ )	0.42	$5.7 \times 10^6$
8	-4° to 16° ( $\Delta 1^\circ$ )	0.44	$3.8 \times 10^6$
9	-4° to 16° ( $\Delta 1^\circ$ )	0.44	$6.0 \times 10^6$
10	-4° to 16° ( $\Delta 1^\circ$ )	0.49	$3.8 \times 10^6$
11	-4° to 16° ( $\Delta 1^\circ$ )	0.49	$6.6 \times 10^6$
12	-4° to 16° ( $\Delta 1^\circ$ )	0.59	$7.0 \times 10^6$
13	-4° to 16° ( $\Delta 1^\circ$ )	0.63	$7.9 \times 10^6$
14	-4° to 16° ( $\Delta 1^\circ$ )	0.69	$8.3 \times 10^6$
15	-4° to 16° ( $\Delta 1^\circ$ )	0.73	$8.5 \times 10^6$
16	-4° to 16° ( $\Delta 1^\circ$ )	0.78	$8.8 \times 10^6$

For ease of description, the simulations will be referred to by the simulation number provided in Table 10. Sims 1, 3, 4, 6, 8, 10, and 12-16 were run at a constant stagnation pressure of 60 psia while Sims 2, 5, 7, 9, and 11 were based on experimental data at stagnation pressures ranging from 48 to 36 psia. All experimental data for comparison was digitized manually to capture a good estimate of the points for lift and drag coefficients. For this dataset, the moment coefficients have not yet been explored. All of the plots for the RC(4)-10 airfoil are collected in Appendix C.

The lift coefficient versus  $\alpha$  curve for sims 1, 2, 3, 4, 5, 6, and 7 are depicted in Figures D.1 through D.7, with experimental data shown in red, XFOIL in orange, OVERFLOW fully turbulent in blue, and OVERFLOW transition in green. In all of these simulations, there is good agreement between XFOIL and OVERFLOW in the linear angle of attack range, specifically at low Mach numbers, which is expected. However, there is an offset seen between the two solvers at negative angles of attack and at  $\alpha$ 's usually right around  $5^\circ$ , with this offset occurring sooner at high Mach numbers approaching XFOIL's convergence capability. In all simulations, XFOIL overshoots the maximum lift coefficient, with the most accurate estimates seen at the lower angles of attack (0.34 and 0.37). As the Mach number increases, the discrepancy between XFOIL calculations, OVERFLOW, and experimental data increases. Sims 1 and 2 show that both OVERFLOW models slightly underpredict the lift coefficient – granted, the experimental data set does not provide a maximum lift coefficient, but the trend suggests a peak slightly greater than what is shown by the OVERFLOW transition model. Sims 3, 4, 5, 6, and 7 show OVERFLOW's transition model capturing the experimental data more accurately than XFOIL or the fully turbulent model. However, the transition model slightly overpredicts the maximum lift coefficient, while the

fully turbulent model consistently underpredicts the maximum lift coefficient. Figures D.8 through D.13 show the XFOIL and OVERFLOW results for Sims 8 through 13. At these Mach numbers, XFOIL continues to overpredict lift, while the OVERFLOW fully turbulent and transition model results align very closely with one another as well as the experimental test data. The exception of Sim 9 at Mach 0.49, which shows that both models underpredict lift beyond  $9^\circ \alpha$ . For Sims 8 and 10.13, the experimental and OVERFLOW lift curves are in good agreement. At Mach 0.69, 0.73, and 0.78, shown in Figures D.14 through D.16, the experimental data set is more limited. However, the trends show an offset in the linear  $\alpha$  range between OVERFLOW results and the experimental data for the  $\alpha$ - $c_l$  data available. OVERFLOW's fully turbulent and transition models are nearly identical for the simulation at Mach 0.69. However, at Mach 0.73 and 0.78, the transition model overshoots the experimental lift coefficient more than the fully turbulent model does.

The next set of data included in Appendix C visualizes the drag polar for the airfoil, with the digitized Noonan data depicted by the red icons, XFOIL in orange, OVERFLOW fully turbulent in blue, and OVERFLOW transition in green. Figures D18 through D-32 compare the Noonan digitized data with XFOIL results (within its Mach number limits) and OVERFLOW results (both fully turbulent and transition models). XFOIL correlates best with the test data at Mach numbers below 0.4. At Mach 0.34 (Figures D-16 and D-17), the experimental data shows the same trend and lies fairly close to the XFOIL curve, with XFOIL slightly underpredicting the drag overall. At higher angles of attack and as Mach number increases beyond Mach 0.34, XFOIL (as mentioned earlier in this section) tends to overpredict drag. This trend is shown in all drag polars, with the largest discrepancies seen as the Mach number approaches transonic conditions. This is not surprising, as XFOIL is not designed to analyze flow at transonic speeds. At Mach numbers from 0.34 through 0.44, fully turbulent simulations overpredict drag, while the transition model results match up quite well in the linear  $\alpha$  range, with some discrepancy in drag seen as the curve approaches maximum lift. At Mach numbers at 0.49 and above, the fully turbulent and transition results (Figures D-25 through D-31) show nearly identical trends. For the Mach numbers, the fully turbulent results are consistent in overpredicting drag slightly. However, for the most part, the experimental curves align well with results from both flow types, with transition tending to lie closer to Noonan's test data.

In an effort to better understand the flow, a study of the pressure coefficient was completed. First, the stagnation pressure coefficient was calculated using equation 4.3, applicable for compressible flow as described in section 4.3. Because there are a large number of results, only three Mach-Reynolds pairs were selected based on available pressure coefficient data in Noonan's NASA/TN: simulation 2, at Mach 0.34 and Reynolds number  $4.8 \times 10^6$ ; simulation 9, at Mach 0.44 and Reynolds number  $6.0 \times 10^6$ ; and finally, simulation 12, at Mach 0.59 and Reynolds number  $7.0 \times 10^6$ . The Noonan plots were digitized using an online web plotting tool, as data in table/excel format were not available. Figure 4.21, Figure 4.22, and Figure 4.23 display experimental data against simulated results for Mach 0.34, 0.44, and 0.59 at respective Reynolds numbers of  $4.8 \times 10^6$ ,  $6.0 \times 10^6$ , and  $7.0 \times 10^6$ .

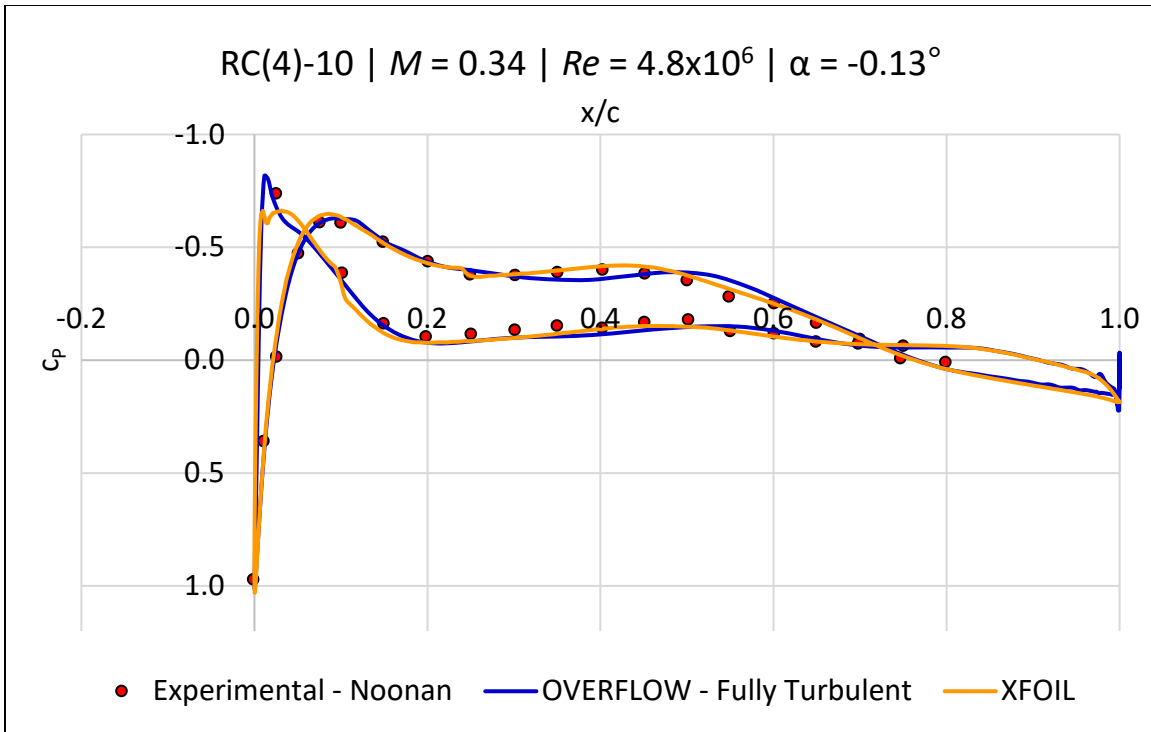


Figure 4.21.  $C_p$  vs  $x/c$  for the RC(4)-10 airfoil at Mach 0.34, Reynolds  $4.8 \times 10^6$ . Experimental data digitized from Figure 24a [13].

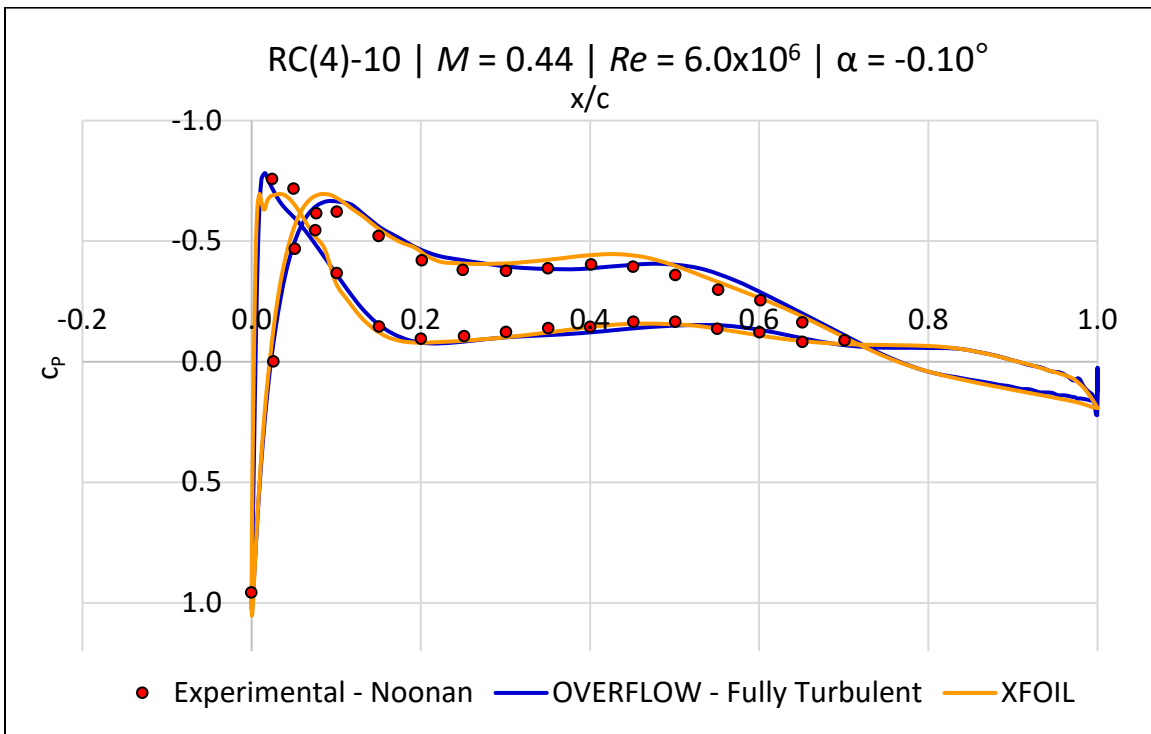


Figure 4.22.  $C_p$  vs  $x/c$  for the RC(4)-10 airfoil at Mach 0.44, Reynolds  $6.0 \times 10^6$ . Experimental data digitized from Figure 24b [13].

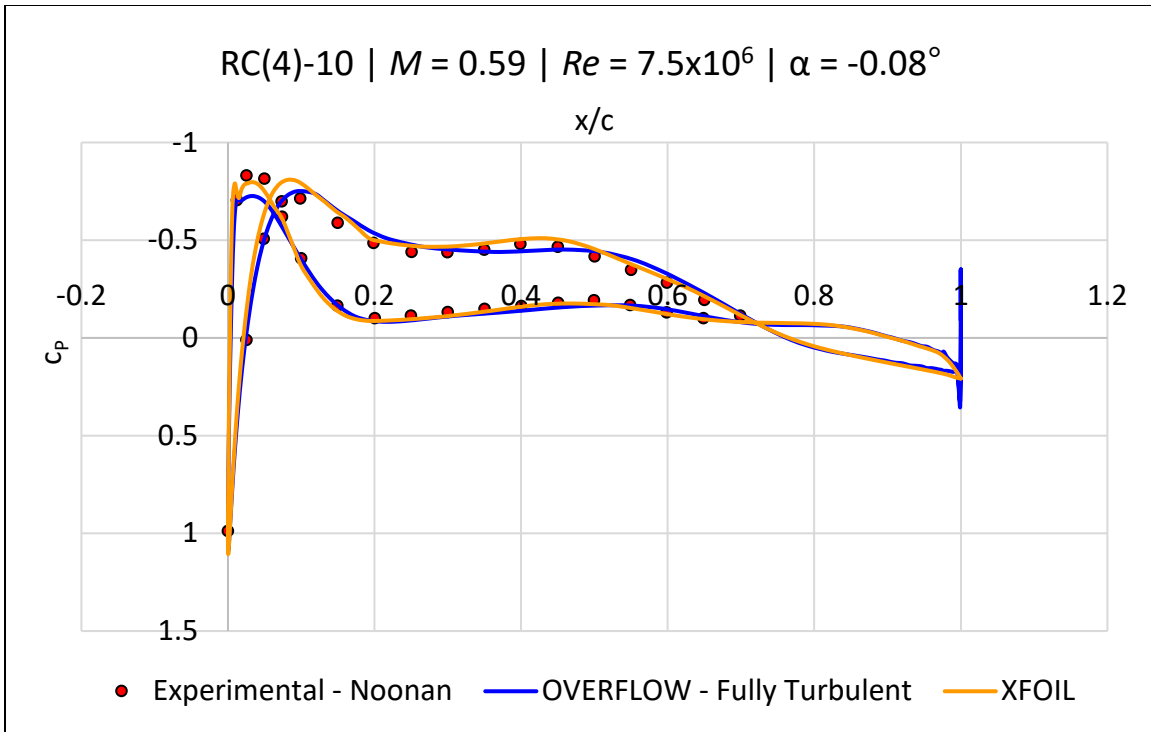


Figure 4.23.  $C_p$  vs  $x/c$  for the RC(4)-10 airfoil at Mach 0.59, Reynolds  $7.5 \times 10^6$ . Experimental data digitized from Figure 24e [13].

These plots were created to show the pressure coefficient at an angle of attack as close as possible to  $0^\circ$  to compare with the hand calculated stagnation pressure coefficient. As a refresher, equation 4.3 was used to calculate the stagnation pressure coefficient. Table 4.5 lists the stagnation pressure coefficient calculated for the RC(4)-10 at all tested/simulated Mach numbers.

Table 4.5. Calculated stagnation pressure coefficients at all Mach numbers for the RC(4)-10 airfoil.

Mach Number	$C_{P, \text{stag}}$
0.34	1.0291
0.37	1.0346
0.39	1.0385
0.42	1.0447
0.49	1.0613
0.54	1.0747
0.59	1.0897
0.63	1.1027
0.69	1.1240
0.73	1.1395
0.78	1.1603
0.83	1.1827

The calculated value provides a way to check the OVERFLOW, XFOIL, and experimental data results for the stagnation pressure coefficient. Once the calculations were completed, the OVERFLOW results were visualized in Fieldview to both show the pressure and velocity contours and show where the stagnation point is located, as well as the calculated pressure coefficient at that point. Figure 4.24, Figure 4.25, and Figure 4.26 show the pressure and Mach contours for the Reynolds-Mach pairs of interest.

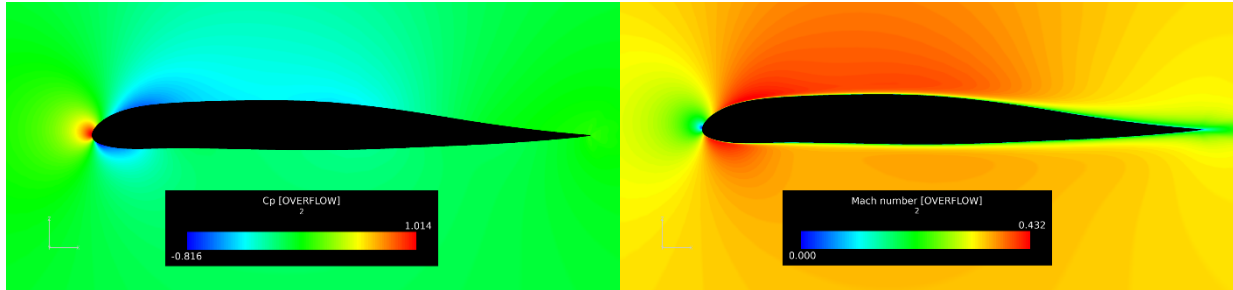


Figure 4.24. Pressure coefficient and Mach number contours for the RC(4)-10 airfoil at Mach 0.34 and a Reynolds number of  $4.8 \times 10^6$ .

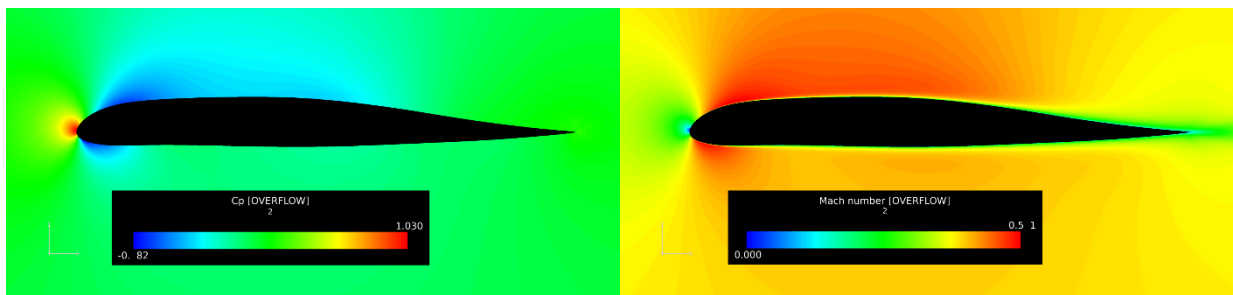


Figure 4.25. Pressure coefficient and Mach number contours for the RC(4)-10 airfoil at Mach 0.44 and a Reynolds number of  $6.0 \times 10^6$ .

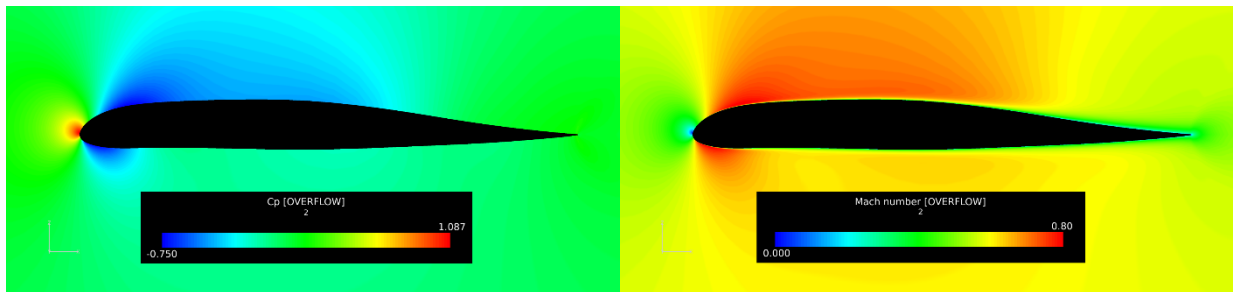


Figure 4.26. Pressure coefficient and Mach number contours for the RC(4)-10 airfoil at Mach 0.59 and a Reynolds number of  $7.5 \times 10^6$ .

At Mach 0.34, the pressure coefficient is calculated by hand to be approximately 1.03, with the experimental data approximately 0.97. OVERFLOW predicts a stagnation pressure coefficient of 1.013, and XFOIL determines the closest to the hand calculated value with a stagnation  $C_p$  of 1.03. At Mach 0.44, the hand calculated Mach number is approximately 1.06 and the experimental data is estimated to be around 0.96. OVERFLOW predicts the stagnation pressure coefficient as 1.03. XFOIL determines the pressure coefficient at 1.053, again calculating the pressure more

accurately than the higher fidelity solver. At Mach 0.59, the hand calculation is 1.0897 and the estimated pressure coefficient is around 0.99. OVERFLOW predicts the maximum pressure coefficient at 1.087, while XFOIL slightly overpredicts it at 1.106.

The first thing to note is that the experimental data pressure coefficient is an estimate – the report plots were not clear in this region. In all analyses (lift, drag, and pressure), there is an unknown error percentage based on digitizing the original plots by hand. In general, XFOIL does a very good job with its pressure coefficient calculations across the chord of the airfoil, with its primary failing being the leading edge overprediction and overall overestimate of the lift coefficient with rising angle of attack.

#### 4.3.3. SSC-A09

The SSC-A09 lift curve, drag polars, and moment curves are contained in Appendix D. Section lift coefficient versus  $\alpha$  is shown in Figures E.1 through E.7, section drag coefficient versus  $\alpha$  in Figures E.8 through E.14, section lift coefficient versus section drag coefficient in Figures E.15 through E.21, and finally the section moment coefficient versus  $\alpha$  is visualized in Figures E.22 through E.28. In all Figures, red represents experimental data from the Flemming report, orange represents XFOIL, blue indicates OVERFLOW’s fully turbulent model, and green indicates OVERFLOW’s Coder transition model. The run number, total pressure  $p_0$ , angle of attack, Mach number, and Reynolds number are shown in Table 4.6 below.

Table 4.6. SSC-A09 primary inputs for XFOIL and OVERFLOW.  
Total pressure is included for completeness.

Run #	$p_0$ [atm]	$\alpha$ range	Mach Number	Reynolds Number
60	1.0	-1° to 7° ( $\Delta 1^\circ$ )	0.399	$3.85 \times 10^6$
61	1.4	0° to 16° ( $\Delta 1^\circ$ )	0.307	$4.29 \times 10^6$
63	1.0	-6° to 20° ( $\Delta 1^\circ$ )	0.500	$4.57 \times 10^6$
65	1.0	-5° to 14° ( $\Delta 1^\circ$ )	0.599	$5.16 \times 10^6$
68	1.0	-1° to 16° ( $\Delta 1^\circ$ )	0.603	$5.21 \times 10^6$
69	1.0	-4° to 12° ( $\Delta 1^\circ$ )	0.703	$5.73 \times 10^6$
70	1.0	-4° to 9° ( $\Delta 1^\circ$ )	0.804	$6.11 \times 10^6$

The experimental test data was plotted using the available tabulated data in the report, with two sets of aerodynamic coefficients provided for use. Flemming provides pressure derived lift, drag, and moment coefficients, as well as the balance derived lift, drag, and moment coefficients. The only coefficients of interest, and as such, discussed in this report, are the pressure derived aerodynamic coefficients. Similarly, only configuration 2 SSC-A09 cases are considered, with configuration 2 described as the clean airfoil configuration in the wind tunnel test. This analysis for this airfoil will primarily discuss the lift curves and drag polars – however, the moment curves are still included in Appendix D for future exploration.

Figure E.1 shows the lift curve for Run 60. This was a limited  $\alpha$  run and only includes the linear  $\alpha$  range. Normally, this would suggest that there would be good agreement between the simulations and experimental test data, but for this airfoil, this is consistently not the case. In Run 61, XFOIL underpredicts lift below an angle of attack of 1.5 deg, but overestimates the lift beyond 2.5°, leaving a limited region where there is some overlap between XFOIL calculations and experimental test data. With respect to the OVERFLOW results, the fully turbulent and transition

models overlap XFOIL results from  $-1$  to  $1.5^\circ$  but underestimates the lift coefficient in this range. Beyond an angle of attack of  $2.5^\circ$ , the OVERFLOW models predict very similar lift coefficients, but overpredict the values recorded in the wind tunnel test. This can be seen much more clearly on the drag polar in Figure D.15. The drag polar shows that the fully turbulent model significantly overpredicts drag, while the XFOIL and transition model show drag and lift calculations more in the ballpark of the experimental data, although with not much commonality in curve trends.

Figures E.2. and E. 9 detail the lift curves and drag buckets for Run 61 test data and simulations. The primary difference in this data set is that the total pressure in the wind tunnel is different than the other runs included in this report. With respect to the lift curve, XFOIL and both OVERFLOW models agree on an underpredicted lift coefficient below an angle of attack of 2 deg. Above 2.5 deg, XFOIL and OVERFLOW no longer share agreement with one another, and although both overpredict the lift coefficient past this angle of attack. The most notable thing, however, is that the fully turbulent and transition models substantially underpredict lift. The maximum lift coefficient predicted by OVERFLOW is around 1.05, with XFOIL predicting 1.59 and the experimental data pressure derived maximum lift at 1.394. With respect to the drag polar in Figure E.19, there is good agreement between 0 to 4 deg angle of attack for experimental, XFOIL, and OVERFLOW. Beyond this angle of attack, XFOIL tends to overpredict lift and underpredict drag. OVERFLOW's transition model calculates drag more reasonably, at least within the 0 to 4 deg angle of attack range. The fully turbulent model overpredicts drag by an order of magnitude and underpredicts lift, as seen in the lift curve described earlier.

A notable difference between this run and others is that using a smoothed airfoil profile with 200 leading edge points resulted in a lower predicted maximum lift than using the original unsmoothed profile. Additionally, the Mach number used in this run is 0.307, which is slightly higher than the standard range for incompressible flow. However, in this regime, the best course of action would have been to consider OVERFLOW's low Mach number preconditioning algorithm. At low speeds, the solver takes significantly longer to converge to steady state, so a low Mach preconditioning algorithm can achieve improved convergence by equilibrating the eigenvalues calculated for the Euler equations and ensuring that the eigenvalues all have the same order of magnitude [33]. This is a possible limitation of using the AFTGen interface instead of running the solver directly, as there does not appear to be information on how to improve convergence at low Mach numbers using the interface. This concept needs to be investigated further and included in future research.

Figures E.3 and E.10 show the test data lift and drag curves plotted against simulated data for Run 63, at Mach 0.5 and a Reynolds number of  $4.57 \times 10^6$ . For this run, the lift curve shows that both XFOIL and OVERFLOW underpredict lift below an angle of attack around 1 deg, with XFOIL showing a greater discrepancy in lift compared with the OVERFLOW cases. Beyond this same angle of attack, the opposite is true – the lift curve is overpredicted, with XFOIL showing a greater discrepancy in lift than the fully turbulent and transition models. OVERFLOW calculates the maximum lift coefficient around the same angle of attack range, while an earlier stall condition, and thus, maximum lift coefficient, is predicted by XFOIL. The maximum lift coefficient predicted by the experimental data, XFOIL, OVERFLOW's fully turbulent model, and OVERFLOW's transition model are 1.121, 1.3132, 1.1719, and 1.1941. With respect to the drag curve, XFOIL aligns fairly well with experimental data from  $-4$  to 4 deg angle of attack. For the most part, it appears that the XFOIL and experimental curve share a trend as well. The OVERFLOW fully turbulent and transition models are close in value and nearly identical in trend until the angle of attack approaches stall conditions. For the most part, drag is overpredicted by both models, while

XFOIL slightly overpredicts in the linear region (from -2 to 5 deg) and overpredicts drag from 5 deg to 18 deg.

Runs 65, 68, 69, and 70 have comparative lift curves shown in Figures E.4, E.5, E.6, and E.7, with drag curves shown in Figures E.11, E.12, E.13 and E.14. XFOIL is not accounted for in these runs do to the very limited number of  $\alpha$ -Mach pairs it was able to converge. For most of these runs, there is an overall weak comparison between the simulated data and the experimental test data, with a consistent trend of OVERFLOW underpredicting the lift for negative angles of attack, and overpredicting the lift at angles of attack beyond 1 deg (or -1 deg, in the case on Run 70). Runs 65, 69, and 70 show the fully turbulent model overpredicting drag, with the transition model similarly overpredicting drag, with the exception of a small region in the linear alpha range, where the minimum drag coefficient for the transition model is very close to what is derived in the experimental data set. A full summary of the experimental and simulated results is in Table 4.7.

Table 4.7. Summary of maximum lift and minimum drag coefficients for the SSC-A09 airfoil results.

<b>Run 60   Mach 0.399   Reynolds Number 3.85x10<sup>6</sup></b>		
<b>Data Set</b>	<b>C<sub>l,max</sub></b>	<b>C<sub>d,min</sub></b>
Experiment	0.7800	0.0066
XFOIL	0.9287	0.0051
OVERFLOW – Fully Turbulent	0.9154	0.0119
OVERFLOW – Coder Transition	0.9200	0.0061
<b>Run 61   Mach 0.307   Reynolds Number 4.29x10<sup>6</sup></b>		
<b>Data Set</b>	<b>C<sub>l,max</sub></b>	<b>C<sub>d,min</sub></b>
Experiment	1.3430	0.0071
XFOIL	1.5904	0.0049
OVERFLOW – Fully Turbulent	1.0379	0.0122
OVERFLOW – Coder Transition	1.0389	0.0066
<b>Run 63   Mach 0.5   Reynolds Number 4.57x10<sup>6</sup></b>		
<b>Data Set</b>	<b>C<sub>l,max</sub></b>	<b>C<sub>d,min</sub></b>
Experiment	1.1210	0.0071
XFOIL	1.3132	0.0052
OVERFLOW – Fully Turbulent	1.1719	0.0114
OVERFLOW – Coder Transition	1.1941	0.0056
<b>Run 65   Mach 0.599   Reynolds Number 5.16x10<sup>6</sup></b>		
<b>Data Set</b>	<b>C<sub>l,max</sub></b>	<b>C<sub>d,min</sub></b>
Experiment	1.0250	0.0074
XFOIL	1.1421	0.0054
OVERFLOW – Fully Turbulent	1.0072	0.0113
OVERFLOW – Coder Transition	1.0438	0.0055
<b>Run 68   Mach 0.603   Reynolds Number 5.21x10<sup>6</sup></b>		
<b>Data Set</b>	<b>C<sub>l,max</sub></b>	<b>C<sub>d,min</sub></b>
Experiment	1.0180	0.0072
OVERFLOW – Fully Turbulent	1.0025	0.0113
OVERFLOW – Coder Transition	1.0451	0.0055

Table 4.5. continued

<b>Run 69   Mach 0.703   Reynolds Number 5.73x10<sup>6</sup></b>		
<b>Data Set</b>	<b>C<sub>l,max</sub></b>	<b>C<sub>d,min</sub></b>
Experiment	0.8790	0.0073
OVERFLOW – Fully Turbulent	0.9873	0.0118
OVERFLOW – Coder Transition	1.0611	0.0061
<b>Run 70   Mach 0.804   Reynolds Number 6.11x10<sup>6</sup></b>		
<b>Data Set</b>	<b>C<sub>l,max</sub></b>	<b>C<sub>d,min</sub></b>
Experiment	0.6650	0.0008
OVERFLOW – Fully Turbulent	1.0875	0.0130
OVERFLOW – Coder Transition	1.1418	0.0081

As performed for the other two airfoils, a stagnation pressure coefficient study was performed to compare the pressure coefficient calculations between the experimental dataset and the various flow solvers. Equations 4.2 and 4.3 were used to calculate the pressure coefficient, with the corresponding run numbers, Mach numbers, and stagnation pressure coefficients tabulated in Table 4.8.

Table 4.8. SSC-A09 hand calculated pressure coefficients at the stagnation point.

<b>Run Number</b>	<b>Mach Number</b>	<b>C<sub>p, stag</sub></b>
60	0.399	1.0403
61	0.307	1.0238
63	0.500	1.0639
65	0.599	1.0925
68	0.603	1.0938
69	0.703	1.1289
70	0.804	1.1708

The data set studied did not provide a close to zero angle of attack, so instead, plots from the Flemming report are digitized as available and applicable to the datasets with the most reasonable data correlation. Pressure plots for Run 60 and Run 65 were digitized using an online web plotting tool. XFOIL and OVERFLOW calculations were performed for the corresponding test angle of attack. Figure 4.27 provides the experimental, XFOIL calculated, and OVERFLOW calculated pressure coefficients and Figure 4.28 visualizes the pressure and Mach contours for Run 60 at Mach 0.399 for the SSC-A09 airfoil.

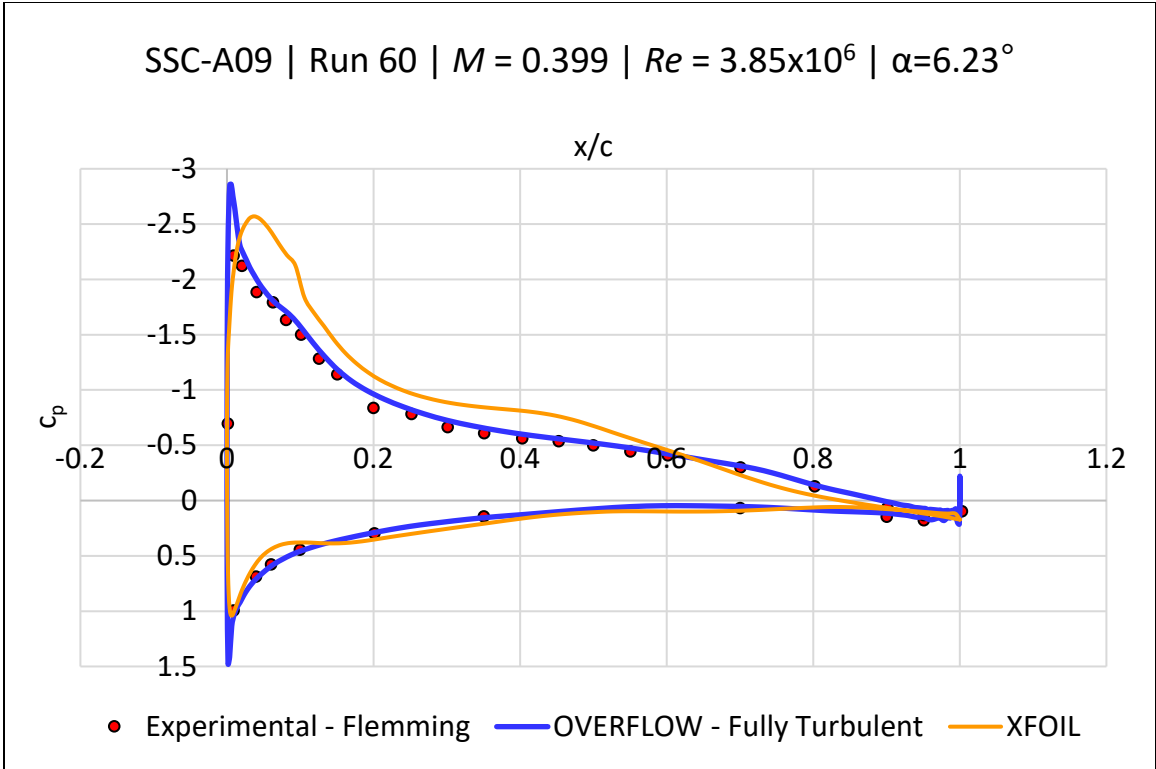


Figure 4.27. SSC-A09 pressure coefficient plot for Run 60.

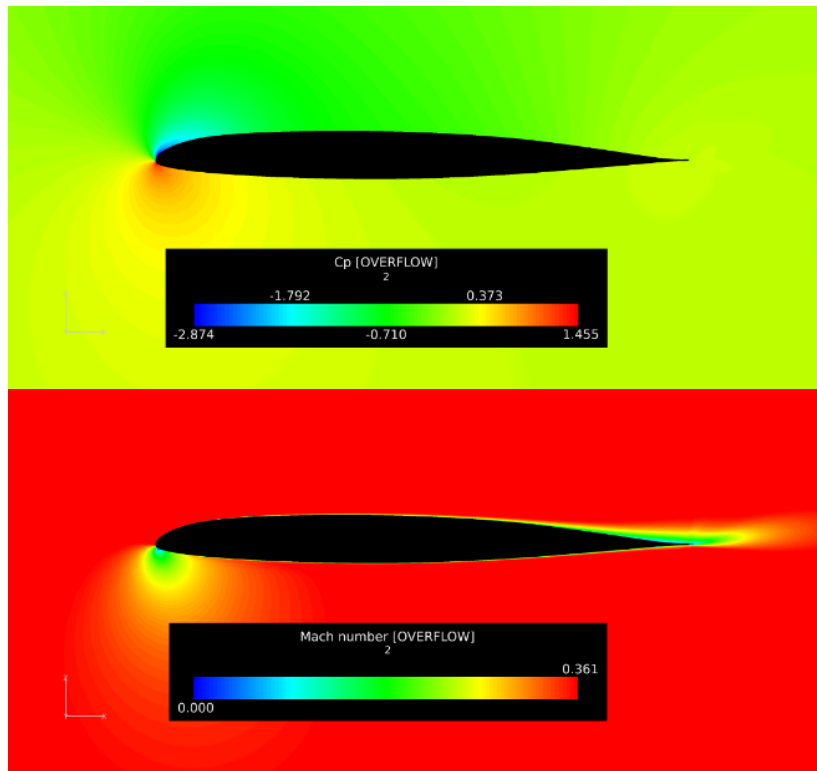


Figure 4.28. Pressure and Mach contour for the SSC-A09 airfoil, Run 60.

Figure 4.29 provides the experimental, XFOIL calculated, and OVERFLOW calculated pressure coefficients, Figure 4.30 visualizes the pressure contours, and Figure 4.31 visualizes the Mach contours for Run 65 at Mach 0.599 for the SSC-A09 airfoil.

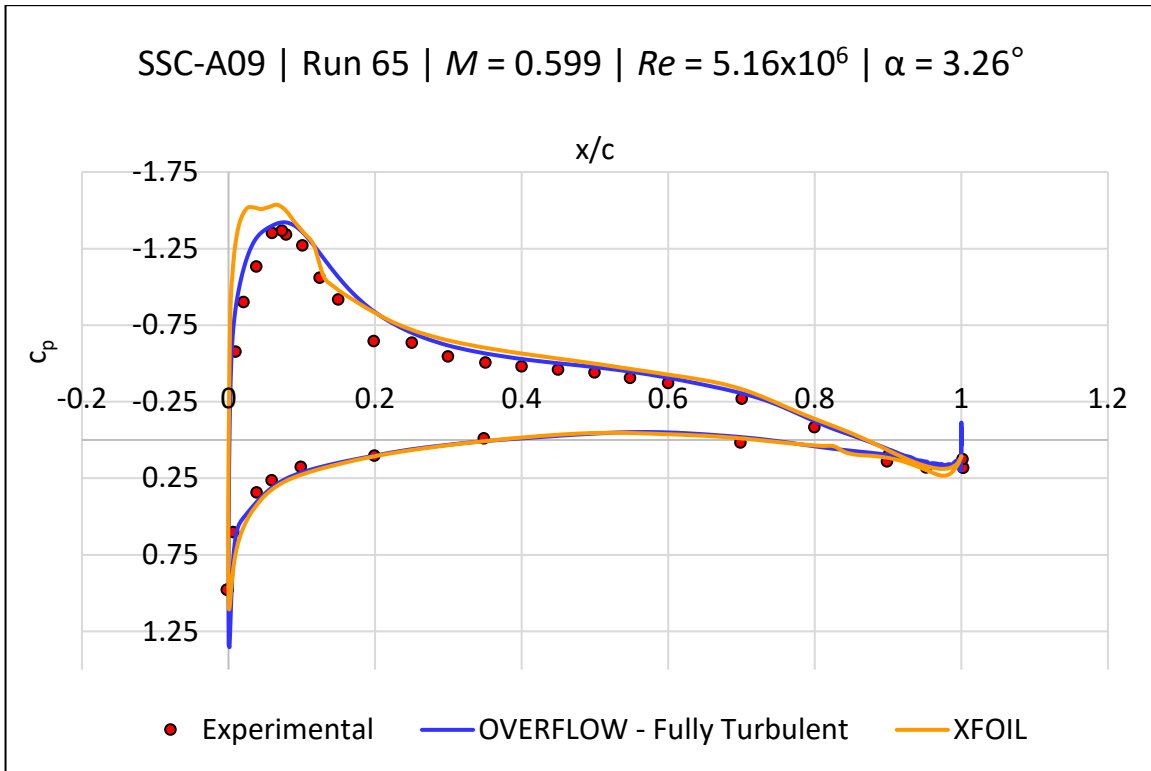


Figure 4.29. SSC-A09 pressure coefficient plot for Run 65.

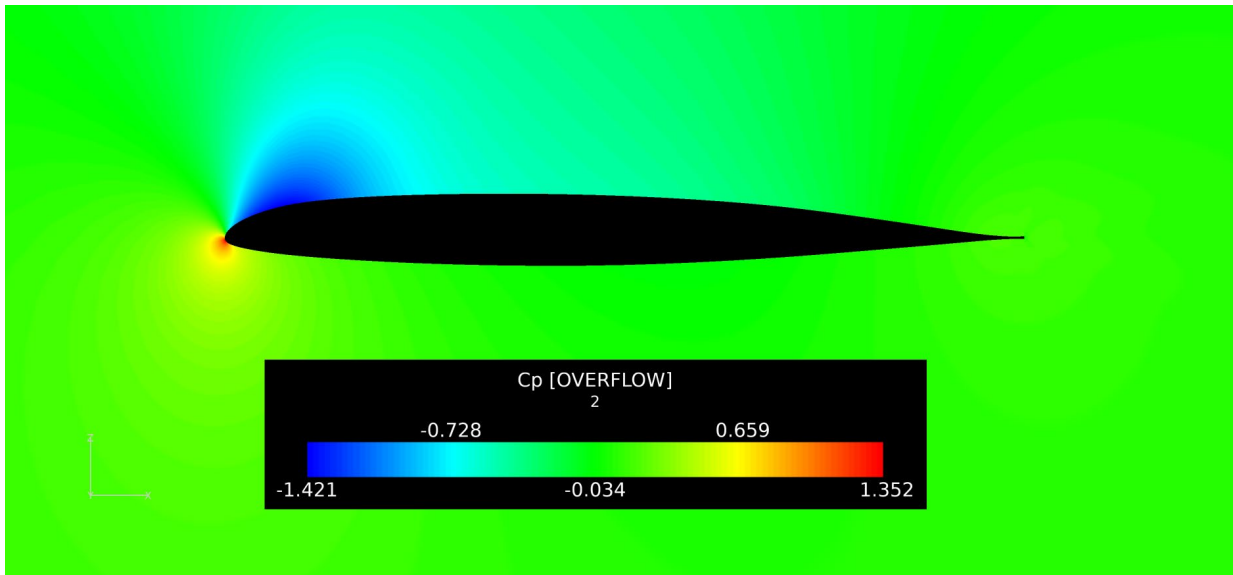


Figure 4.30. Pressure coefficient contour for the SSC-A09 airfoil, Run 60.

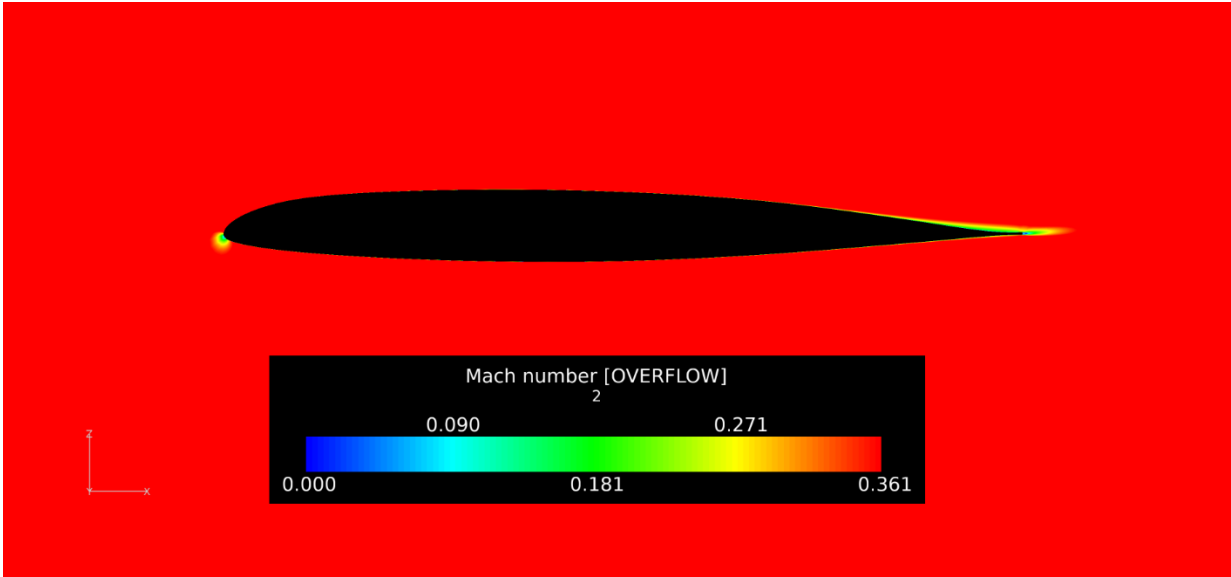


Figure 4.31. Mach number contour for the SSC-A09 airfoil, Run 60.

For Run 60, the experimental data's pressure coefficient at the leading edge can be estimated at 1. XFOIL calculates the pressure coefficient at approximately 1.04. OVERFLOW overestimates this value at 1.455. Figure 4.27 shows that OVERFLOW's fully turbulent model overpredicted the pressure coefficient, while XFOIL is reasonably close to the experimental data. However, OVERFLOW correlates extremely well with the experimental pressure coefficient, matching the trend nearly identically aside from the stagnation pressure and trailing edge. XFOIL's pressure coefficient trend is not nearly as accurate. It's possible that not enough iterations were run for the dataset, although the total iterations were set to 500 for the angle of attack. The discrepancy is primarily seen on the upper airfoil surface.

For Run 65, the experimental data set has an estimated leading edge pressure coefficient of 1, with XFOIL overpredicting the pressure coefficient at 1.1. OVERFLOW overpredicts the pressure coefficient as 1.35. In general, the trend for the OVERFLOW results is close to the experimental data set, with the pressure slightly underestimated on the upper airfoil. XFOIL shows a significant underestimate of the pressure curve at its peak, and a distinct different in trend until about 20% of the airfoil chord.

Overall, the SSC-A09 XFOIL and OVERFLOW results do not compare well with the experimental dataset, even considering the exploration of improvements to simulation approach with respect to clustering iterations, trailing edge points, and improvements in geometry. The likely cause is the grid itself is not refined enough. An individual grid study for the SSC-A09 airfoil was performed for future use in later iterations of this project, which will ultimately produce a best practices guide for airfoil table generation. Figure 4.32 shows the results for the SSC-A09 grid resolution study to improve future analyses in XFOIL.

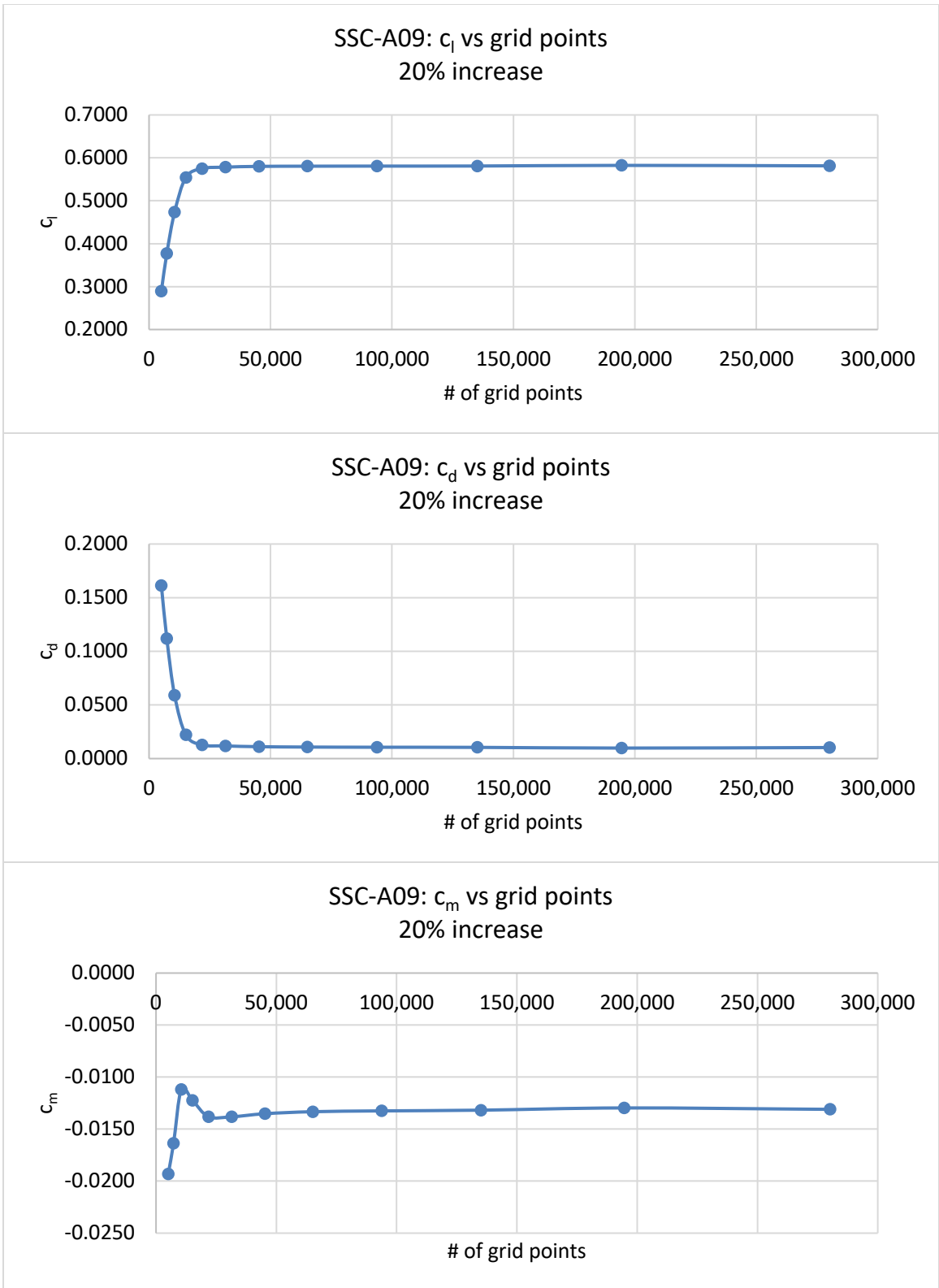


Figure 4.32 SSC-A09 grid resolution study, with a 20% increase in grid size.

This grid resolution study used a slow increment in grid size to see how close the drag count could reach convergence. In this study, the value appears to be converged in the graph, but in actuality, the drag value is still not consistent to within one drag count. For future investigations, this study should be revisited and extended, as the computation limitations with respect to time did not allow for full investigative studies of the grid after exploring other features such as the trailing edge spacing, clustering iterations, and leading edge profile resolution influence.

The grid is not the only culprit for the discrepancy in simulated and experimental data. Flemming describes an issue with the original SSC-A09 model, in which bolthead stresses required the leading edge to rotate slightly upward to minimize load. In addition, modifications in the form of out-of-contour bumps were added to the model for a small range of Mach number and angle of attack values. It would be worthwhile to explore the additional SSC-A09 tests and attempt to account for the angle change at the leading edge as well as the surface roughness added by the protuberances on the surface.

## Chapter 5. Conclusion

One of the major takeaways from this study is the limitations of XFOIL. XFOIL is only valid for subsonic flows, so cannot accurately model transonic flow due to phenomenon like shocks that may occur. XFOIL is also limited in angle of attack range and cannot accurately model stall and post-stall conditions, because it is an inviscid flow solver and cannot calculate viscous drag. The results are consistent in nearly every case run with XFOIL, where the linear range is generally predicted well and the lift coefficient is overpredicted as the stall angle of attack approaches (with the exception being the generally poor correlation with most of the SSC-A09 cases). XFOIL, however, runs in seconds on a desktop computer. OVERFLOW is limited at low Mach numbers, and appears to perform best at Mach numbers of 0.4 and above. The exploration of airfoil table generation using XFOIL and OVERFLOW yielded moderately successful results for the NACA 0012 airfoil table, reasonably good results for the RC(4)-10 results, and questionable results for the SSC-A09. The SSC-A09 XFOIL and OVERFLOW results do not compare well with the experimental dataset, even considering the exploration of improvements to simulation approach with respect to clustering iterations, trailing edge points, and improvements in geometry. An individual grid study for the SSC-A09 airfoil was performed for future use of this research project, which will further contribute to a best practice guide for airfoil table generation.

Another consideration is that this investigation focused on the capability of the XFOIL and OVERFLOW solvers using features built-in to AFTGen, with the takeaways from the study as follows:

1. Ensure the leading-edge profile of the airfoil is sufficiently defined.
  - a) If using AFTGen, consider that the grid generator may not refine the imported geometry adequately, so using additional points around the leading edge is helpful.
  - b) Use a spline to add more points around the leading edge of the airfoil, up to 15%, on the upper and lower surfaces. This improved the overall correlation between experimental data and simulations for the RC(4)-10 airfoil.
2. For OVERFLOW, ensure a blunt trailing edge contains enough points to define the grid in that region.
  - a) A minimum of 11 trailing edge points should be used, per suggestions by Allan, Buning, and Romander (Oct. 2021)
  - b) The trailing edge points are airfoil dependent – an independent study per airfoil is recommended.
3. For OVERFLOW, Clustering iterations study is optional
  - a) Increasing the clustering iterations showed no marked improvement in results for the 0012 and SSC-A09 airfoils, but 20,000 clustering iterations resulted in a small increase in accuracy for the RC(4)-10.
4. Visualize the flow
  - a) When possible, ensure that the pressure and Mach contours display reasonable results – contours should appear smooth and realistic for the conditions.
5. Perform independent studies for each airfoil, as there is not a one-size-fits-all grid.

## Chapter 6. Future Work

A number of other features can be explored in the future to improve experimental and simulated data correlation. Considerations for future work include the following:

1. Complete a study of  $N_{crit}$  values in XFOIL.
2. Import a grid for use in AFTGen and compare the AFTGen-generated grid and imported grid, focusing on grid point distribution around regions of high curvature.
3. Complete a study of higher Reynolds number airfoils, such as the SC1095 and SC1094R8 using similar and/or improved methodologies.
4. Explore the maximum stretching ratio of grid points and its effect on AFTGen's grid generator.
5. Research low Mach preconditioning and improve OVERFLOW results at lower Mach numbers.
6. Complete a study of low Reynolds number airfoils, for use with UAVs and airfoils used in low atmospheric conditions.

Although a best practice guide for airfoil table generation has not yet been developed, this present work is one of many projects that will be used toward that goal. A series of studies will need to be completed to improve OVERFLOW results, and a more in-depth exploration of XFOIL will provide a better understanding of its limitations and capabilities. Using both solvers in tandem for specific Mach-alpha combinations can improve efficiency in generating airfoil tables.

## References

- [1] Anderson, J. D. *Fundamentals of Aerodynamics*. McGraw Hill, 2007.
- [2] Yamauchi, G. K., Kallstrom, K., and Kuang, W. Airfoil Performance Tool. NASA Ames Research Center, , 2020.
- [3] Wachspress, D. Comprehensive Hierarchical Aeromechanics Rotorcraft Model. <https://continuum-dynamics.com/product/>. Accessed Jun. 25, 2021.
- [4] Johnson, W. Comprehensive Analytical Model of Rotorcraft Aerodynamics and Dynamics. <http://www.johnson-aeronautics.com/CAMRADII.html>. Accessed Jun. 25, 2021.
- [5] Von Doenhoff, Albert E.; Abbott, I. *Theory of Wing Sections*. McGraw-Hill, New York, 1949.
- [6] McCroskey, W. J. *A Critical Assessment of Wind Tunnel Results for the NACA 0012 Airfoil*. 1987.
- [7] Davis, J. M., Bennet, R., and Blankenship, B. *Rotorcraft Flight Simulation with Aeroelastic Rotor and Improved Aerodynamic Representation. Volume 1: Engineers Manual*. 1974.
- [8] Harris, C. D. *NASA Technical Memorandum 81927, Two-Dimensional Aerodynamic Characteristics of the NACA 0012 Airfoil in the Langley 8 Foot Transonic Pressure Tunnel*. Hampton, Virginia, 1981.
- [9] Brooks, C. W., Harris, C. D., and Reagon, P. G. *NASA/TP-3437: The NASA Langley 8-Foot Transonic Pressure Tunnel Calibration*. Hampton, Virginia.
- [10] Kallstrom, K. *C81Gen Validation for Rotorcraft Comprehensive Analyses with CHARM*. Moffett Field, CA, 2019.
- [11] Sheldahl, R. E., and Klimas, P. C. *Aerodynamic Characteristics of Seven Symmetrical Airfoil Sections Through 180-Degree Angle of Attack for Use in Aerodynamic Analysis of Vertical Axis Wind Turbines*. 1981.
- [12] Noonan, K. W. *NASA Technical Memorandum 4264: Aerodynamic Characteristics of a Rotorcraft Airfoil Designed for the Tip Region of a Main Rotor Blade*. 1991.
- [13] Althoff, S. L. *NASA/TP-2832: Effect of Advanced Rotorcraft Airfoil Sections on the Hover Performance of a Small-Scale Rotor Model*. 1988.
- [14] Flemming, R. J. *An Experimental Evaluation of Advanced Rotorcraft Airfoils in the NASA Ames Eleven-Foot Transonic Wind Tunnel*. Moffett Field, CA, 1984.
- [15] Hicks, R. M., and Collins, L. J. *NASA/TM-86719: An Evaluation of Three Helicopter Rotor Sections*. 1985.
- [16] Murphy, P. C., Hatke, D. B., Aubuchon, V. V., Weinstein, R., and Busan, R. C. Preliminary Steps in Developing Rapid Aero Modeling Technology. 2020.
- [17] Murphy, P. C., Buning, P. G., and Simmons, B. M. Rapid Aero Modeling for Urban Air Mobility Aircraft in Computational Experiments. 2021.
- [18] Johnson, W., Silva, C., and Solis, E. "Concept Vehicles for VTOL Air Taxi Operations." *Proceedings of the AHS International Technical Meeting on Aeromechanics Design for Transformative Vertical Flight 2018*, 2018.
- [19] Koning, W. J. F., Romander, E. A., and Johnson, W. Low Reynolds Number Airfoil Evaluation for the Mars Helicopter Rotor. No. 2018-May, 2018.
- [20] Drela, M. XFOIL: An Analysis and Design System for Low Reynolds Number Airfoils. *Low Reynolds Number Aerodynamics*. 12. [http://link.springer.com/chapter/10.1007/978-3-642-84010-4\\_1](http://link.springer.com/chapter/10.1007/978-3-642-84010-4_1).
- [21] Silva, D., Avelino, M., and De-Lemos, M. "Numerical Study of the Airflow around the Airfoil S1223." *II Congresso Nacional de Engenharia Mecânica*, 2002.

- [22] Nichols, R; Buning, P. “User’s Manual for OVERFLOW 2.3.” 2021.
- [23] Sukra Helitek Inc. OVERFLOW Module for AFTGen Application User Manual.
- [24] Nichols, R. H., Tramel, R. W., and Buning, P. G. “Solver and Turbulence Model Upgrades to OVERFLOW 2 for Unsteady and High-Speed Applications.” *Collection of Technical Papers - AIAA Applied Aerodynamics Conference*, Vol. 1, No. June, 2006, pp. 91–124. <https://doi.org/10.2514/6.2006-2824>.
- [25] Spalart, P. R., Allmaras, S. R., and Reno, J. “One-Equation Turbulence Model for Aerodynamic Flows.” *30th Aerospace Sciences Meeting & Exhibit*, 1992, p. 23.
- [26] Allmaras, S.R.; Spalart, P. R. Modifications and Clarifications for the Implementation of the Spalart-Allmaras Turbulence Model. *ICCFD7-1902*.
- [27] Rumsey, C. Langley Research Center Turbulence Modeling Resource. <https://turbmodels.larc.nasa.gov/spalart.html>.
- [28] Coder, J. G. Enhancements of the Amplification Transport Transition Modeling Framework. 2017.
- [29] Coder, James G., Pulliam, Thomas H., Jensen, J. C. Contribution to HiLiftPW-3. 2018.
- [30] Courant, R.; Friedrichs, K.; Lewy, H. “On the Partial Difference Equations of Mathematical Physics.” *IBM Journal of Research and Development*, Vol. 11, No. 2, 1967, pp. 215–234. <https://doi.org/10.1147/rd.112.0215>.
- [31] Selig, M. UIUC Airfoil Data Site. *online*. [https://m-selig.ae.illinois.edu/ads/coord\\_database.html](https://m-selig.ae.illinois.edu/ads/coord_database.html).
- [32] Anderson, J. D. *Introduction to Flight*. McGraw Hill, 1989.
- [33] Jespersen, D., Pulliam, T., and Buning, P. “Recent Enhancements to Overflow.” *35th Aerospace Sciences Meeting and Exhibit*, No. January, 1997. <https://doi.org/10.2514/6.1997-644>.

## Appendix A - NACA 0012 Airfoil Table

NACA 0012		11391165 947										
	0	0.2	0.3	0.4	0.5	0.6	0.7	0.75	0.8	0.9	1	
-180	0	0	0	0	0	0	0	0	0	0	0	
-172.5	0.78	0.78	0.78	0.78	0.78	0.78	0.78	0.78	0.78	0.78	0.78	0.78
-161	0.62	0.62	0.62	0.62	0.62	0.62	0.62	0.62	0.62	0.62	0.62	
-147	1	1	1	1	1	1	1	1	1	1	1	
-129	1	1	1	1	1	1	1	1	1	1	1	
-49	-1.18	-1.18	-1.18	-1.18	-1.18	-1.18	-1.18	-1.18	-1.18	-1.18	-1.18	
-39	-1.18	-1.18	-1.18	-1.18	-1.18	-1.18	-1.18	-1.18	-1.18	-1.18	-1.18	
-21	-0.8	-0.8	-0.81	-0.83	-0.85	-0.85	-0.85	-0.71	-0.68	-0.64	-0.64	
-16.5	-1.007	-1.007	-0.944	-0.96	-0.965	-0.965	-0.965	-0.795	-0.76	-0.7	-0.7	-0.7
-15	-1.19	-1.19	-1.09	-1.055	-0.99	-0.98	-0.98	-0.83	-0.79	-0.72	-0.72	
-14	-1.333	-1.333	-1.22	-1.096	-1	-0.97	-0.97	-0.84	-0.805	-0.73	-0.73	
-13	-1.334	-1.334	-1.28	-1.12	-1	-0.96	-0.96	-0.85	-0.815	-0.735	-0.735	
-12	-1.255	-1.255	-1.26	-1.13	-1	-0.947	-0.94	-0.85	-0.82	-0.74	-0.74	
-11	-1.161	-1.161	-1.19	-1.12	-0.994	-0.93	-0.923	-0.85	-0.81	-0.74	-0.74	
-10	-1.055	-1.055	-1.01	-1.082	-0.985	-0.91	-0.9	-0.845	-0.805	-0.73	-0.73	
-8	-0.844	-0.844	-0.88	-0.907	-0.922	-0.87	-0.84	-0.82	-0.77	-0.695	-0.695	
-6	-0.633	-0.633	-0.66	-0.684	-0.741	-0.77	-0.75	-0.77	-0.72	-0.593	-0.593	
-4	-0.422	-0.422	-0.44	-0.456	-0.494	-0.544	-0.578	-0.627	-0.603	-0.396	-0.396	
-2	-0.211	-0.211	-0.22	-0.228	-0.247	-0.272	-0.313	-0.35	-0.395	-0.2	-0.2	
0	0	0	0	0	0	0	0	0	0	0	0	
2	0.211	0.211	0.22	0.228	0.247	0.272	0.313	0.35	0.395	0.2	0.2	
4	0.422	0.422	0.44	0.456	0.494	0.544	0.578	0.627	0.603	0.396	0.396	
6	0.633	0.633	0.66	0.684	0.741	0.77	0.75	0.77	0.72	0.593	0.593	
8	0.844	0.844	0.88	0.907	0.922	0.87	0.84	0.82	0.77	0.695	0.695	
10	1.055	1.055	1.1	1.082	0.985	0.91	0.9	0.845	0.805	0.73	0.73	
11	1.161	1.161	1.19	1.12	0.994	0.93	0.923	0.85	0.81	0.74	0.74	
12	1.255	1.255	1.26	1.13	1	0.947	0.94	0.85	0.82	0.74	0.74	
13	1.334	1.334	1.28	1.12	1	0.96	0.96	0.85	0.815	0.735	0.735	
14	1.333	1.333	1.22	1.096	1	0.97	0.97	0.84	0.805	0.73	0.73	
15	1.19	1.19	1.09	1.055	0.99	0.98	0.98	0.83	0.79	0.73	0.73	
16.5	1.007	1.007	0.944	0.96	0.965	0.965	0.965	0.795	0.76	0.7	0.7	
21	0.8	0.8	0.81	0.83	0.85	0.85	0.85	0.71	0.68	0.64	0.64	
39	1.18	1.18	1.18	1.18	1.18	1.18	1.18	1.18	1.18	1.18	1.18	
49	1.18	1.18	1.18	1.18	1.18	1.18	1.18	1.18	1.18	1.18	1.18	
129	-1	-1	-1	-1	-1	-1	-1	-1	-1	-1	-1	
147	-1	-1	-1	-1	-1	-1	-1	-1	-1	-1	-1	
161	-0.62	-0.62	-0.62	-0.62	-0.62	-0.62	-0.62	-0.62	-0.62	-0.62	-0.62	
172.5	-0.78	-0.78	-0.78	-0.78	-0.78	-0.78	-0.78	-0.78	-0.78	-0.78	-0.78	-0.78
180	0	0	0	0	0	0	0	0	0	0	0	
0	0.18	0.28	0.38	0.48	0.62	0.72	0.77	0.82	0.92	1		
-180	0.022	0.022	0.022	0.022	0.022	0.022	0.022	0.022	0.022	0.022	0.022	
-175	0.062	0.062	0.062	0.062	0.062	0.062	0.062	0.062	0.062	0.062	0.062	
-170	0.132	0.132	0.132	0.132	0.132	0.132	0.132	0.132	0.132	0.132	0.132	

-165	0.242	0.242	0.242	0.242	0.242	0.242	0.242	0.242	0.242	0.242	0.242
-160	0.302	0.302	0.302	0.302	0.302	0.302	0.302	0.302	0.302	0.302	0.302
-140	1.042	1.042	1.042	1.042	1.042	1.042	1.042	1.042	1.042	1.042	1.042
-120	1.652	1.652	1.652	1.652	1.652	1.652	1.652	1.652	1.652	1.652	1.652
-110	1.852	1.852	1.852	1.852	1.852	1.852	1.852	1.852	1.852	1.852	1.852
-100	2.022	2.022	2.022	2.022	2.022	2.022	2.022	2.022	2.022	2.022	2.022
-90	2.022	2.022	2.022	2.022	2.022	2.022	2.022	2.022	2.022	2.022	2.022
-80	1.962	1.962	1.962	1.962	1.962	1.962	1.962	1.962	1.962	1.962	1.962
-70	1.842	1.842	1.842	1.842	1.842	1.842	1.842	1.842	1.842	1.842	1.842
-60	1.662	1.662	1.662	1.662	1.662	1.662	1.662	1.662	1.662	1.662	1.662
-50	1.392	1.392	1.392	1.392	1.392	1.399	1.392	1.392	1.392	1.392	1.392
-30	0.562	0.562	0.562	0.562	0.562	0.562	0.562	0.562	0.562	0.562	0.562
-21	0.332	0.332	0.332	0.332	0.332	0.332	0.332	0.332	0.332	0.342	0.342
-16	0.155	0.155	0.181	0.207	0.235	0.257	0.274	0.292	0.305	0.342	0.342
-15	0.102	0.102	0.148	0.181	0.209	0.233	0.252	0.271	0.282	0.298	0.298
-14	0.038	0.038	0.099	0.146	0.18	0.212	0.233	0.249	0.26	0.293	0.293
-13	0.0264	0.0264	0.0455	0.094	0.148	0.191	0.216	0.231	0.239	0.272	0.292
-12	0.022	0.022	0.03	0.06	0.111	0.164	0.198	0.211	0.22	0.252	0.291
-11	0.0196	0.0196	0.0232	0.038	0.078	0.135	0.17	0.192	0.202	0.232	0.275
-10	0.0174	0.0174	0.0189	0.0259	0.053	0.105	0.145	0.176	0.186	0.213	0.254
-9	0.0154	0.0154	0.0159	0.0187	0.0351	0.077	0.122	0.159	0.172	0.199	0.232
-8	0.0138	0.0138	0.0138	0.0147	0.022	0.053	0.101	0.14	0.155	0.183	0.214
-7	0.0122	0.0122	0.0122	0.0123	0.0141	0.035	0.082	0.111	0.139	0.169	0.192
-6	0.011	0.011	0.011	0.011	0.011	0.0212	0.0615	0.082	0.12	0.14	0.17
-5	0.01	0.01	0.01	0.01	0.01	0.0132	0.038	0.054	0.088	0.111	0.14
-4	0.0093	0.0093	0.0093	0.0093	0.0093	0.01	0.0167	0.03	0.0575	0.095	0.112
-3	0.0088	0.0088	0.0088	0.0088	0.0088	0.009	0.0102	0.0175	0.0355	0.086	0.102
-2	0.0085	0.0085	0.0085	0.0085	0.0085	0.0085	0.0086	0.0117	0.024	0.081	0.098
-1	0.0083	0.0083	0.0083	0.0083	0.0083	0.0083	0.0083	0.0091	0.0175	0.078	0.096
0	0.008	0.008	0.008	0.008	0.008	0.008	0.008	0.008	0.0137	0.078	0.095
1	0.0083	0.0083	0.0083	0.0083	0.0083	0.0083	0.0083	0.0091	0.0175	0.078	0.096
2	0.0085	0.0085	0.0085	0.0085	0.0085	0.0085	0.0086	0.0117	0.024	0.081	0.098
3	0.0088	0.0088	0.0088	0.0088	0.0088	0.009	0.0102	0.0175	0.0355	0.086	0.102
4	0.0093	0.0093	0.0093	0.0093	0.0093	0.01	0.0167	0.03	0.0575	0.095	0.112
5	0.01	0.01	0.01	0.01	0.01	0.0132	0.038	0.054	0.088	0.111	0.14
6	0.011	0.011	0.011	0.011	0.011	0.0212	0.0615	0.082	0.12	0.14	0.17
7	0.0122	0.0122	0.0122	0.0123	0.0141	0.035	0.082	0.111	0.139	0.169	0.192
8	0.0138	0.0138	0.0138	0.0147	0.022	0.053	0.101	0.14	0.155	0.183	0.214
9	0.0154	0.0154	0.0159	0.0187	0.0351	0.077	0.122	0.159	0.172	0.199	0.232
10	0.0174	0.0174	0.0189	0.0259	0.053	0.105	0.145	0.176	0.186	0.213	0.254
11	0.0196	0.0196	0.0232	0.038	0.078	0.135	0.17	0.192	0.202	0.232	0.275
12	0.022	0.022	0.03	0.06	0.111	0.164	0.198	0.211	0.22	0.252	0.291
13	0.0264	0.0264	0.0455	0.094	0.148	0.191	0.216	0.231	0.239	0.272	0.292
14	0.038	0.038	0.099	0.146	0.18	0.212	0.233	0.249	0.26	0.293	0.293
15	0.102	0.102	0.148	0.181	0.209	0.233	0.252	0.271	0.282	0.298	0.298
16	0.155	0.155	0.181	0.207	0.235	0.257	0.274	0.292	0.305	0.342	0.342
21	0.332	0.332	0.332	0.332	0.332	0.332	0.332	0.332	0.332	0.342	0.342
30	0.562	0.562	0.562	0.562	0.562	0.562	0.562	0.562	0.562	0.562	0.562
50	1.392	1.392	1.392	1.392	1.392	1.392	1.392	1.392	1.392	1.392	1.392
60	1.662	1.662	1.662	1.662	1.662	1.662	1.662	1.662	1.662	1.662	1.662
70	1.842	1.842	1.842	1.842	1.842	1.842	1.842	1.842	1.842	1.842	1.842

80	1.962	1.962	1.962	1.962	1.962	1.962	1.962	1.962	1.962	1.962	1.962
90	2.022	2.022	2.022	2.022	2.022	2.022	2.022	2.022	2.022	2.022	2.022
100	2.022	2.022	2.022	2.022	2.022	2.022	2.022	2.022	2.022	2.022	2.022
110	1.852	1.852	1.852	1.852	1.852	1.852	1.852	1.852	1.852	1.852	1.852
120	1.652	1.652	1.652	1.652	1.652	1.652	1.652	1.652	1.652	1.652	1.652
140	1.042	1.042	1.042	1.042	1.042	1.042	1.042	1.042	1.042	1.042	1.042
160	0.302	0.302	0.302	0.302	0.302	0.302	0.302	0.302	0.302	0.302	0.302
165	0.242	0.242	0.242	0.242	0.242	0.242	0.242	0.242	0.242	0.242	0.242
170	0.132	0.132	0.132	0.132	0.132	0.132	0.132	0.132	0.132	0.132	0.132
175	0.062	0.062	0.062	0.062	0.062	0.062	0.062	0.062	0.062	0.062	0.062
180	0.022	0.022	0.022	0.022	0.022	0.022	0.022	0.022	0.022	0.022	0.022

	0.2	0.3	0.4	0.5	0.6	0.7	0.75	0.8	0.9		
-180	0	0	0	0	0	0	0	0	0		
-170	0.4	0.4	0.4	0.4	0.4	0.4	0.4	0.4	0.4		
-165	0.3	0.3	0.3	0.3	0.3	0.3	0.3	0.3	0.3		
-160	0.3	0.3	0.3	0.3	0.3	0.3	0.3	0.3	0.3		
-135	0.5	0.5	0.5	0.5	0.5	0.5	0.5	0.5	0.5		
-90	0.5	0.5	0.5	0.5	0.5	0.5	0.5	0.5	0.5		
-30	0.174	0.184	0.196	0.214	0.235	0.25	0.264	0.277	0.298		
-23	0.112	0.118	0.128	0.144	0.157	0.171	0.183	0.206	0.232		
-16	0.073	0.078	0.086	0.097	0.108	0.117	0.137	0.176	0.2		
-15	0.054	0.065	0.073	0.084	0.097	0.111	0.133	0.173	0.195		
-14	0	0.027	0.054	0.068	0.086	0.103	0.127	0.167	0.189		
-13	0	0.0015	0.025	0.05	0.074	0.093	0.122	0.163	0.184		
-12	0	0	0.002	0.03	0.06	0.083	0.116	0.157	0.176		
-11	0	0	-0.003	0.014	0.046	0.074	0.108	0.149	0.17		
-10	0	0	-0.0015	0.002	0.032	0.065	0.1	0.142	0.163		
-9	0	0	0	-0.003	0.016	0.054	0.089	0.132	0.154		
-8	0	0	0	-0.004	0.005	0.041	0.082	0.123	0.145		
-7	0	0	0	0	-0.004	0.0275	0.072	0.1125	0.136		
-6	0	0	0	0	-0.003	0.016	0.0625	0.1	0.125		
-4	0	0	0	0	0	0.005	0.04	0.076	0.102		
-3	0	0	0	0	0	-0.0025	0.026	0.0665	0.087		
-2	0	0	0	0	0	0	0.013	0.053	0.07		
-1	0	0	0	0	0	0	0.0035	0.033	0.045		
0	0	0	0	0	0	0	0	0	0		
1	0	0	0	0	0	0	-0.003	5 -.033	-0.045		
2	0	0	0	0	0	0	-0.013	-0.053	-0.07		
3	0	0	0	0	0	0.0025	-0.026	-0.0665	-0.087		
4	0	0	0	0	0	-0.005	-0.04	-0.076	-0.102		
6	0	0	0	0	0.003	-0.016	-0.062	5 -.1	-0.125		
7	0	0	0	0	0.004	-0.0275	-0.072	-0.1125	-0.136		
8	0	0	0	0.004	-0.005	-0.041	-0.082	-0.123	-0.145		
9	0	0	0	0.003	-0.016	-0.054	-0.089	-0.132	-0.154		
10	0	0	0.0015	-0.002	-0.032	-0.065	-0.1	-0.142	-0.163		
11	0	0	0.003	-0.014	-0.046	-0.074	-0.108	-0.149	-0.17		
12	0	0	-0.002	-0.03	-0.06	-0.083	-0.116	-0.157	-0.176		
13	0	-0.0015	-0.025	-0.05	-0.074	-0.093	-0.122	-0.163	-0.184		
14	0	-0.027	-0.054	-0.068	-0.086	-0.103	-0.127	-0.167	-0.189		
15	-0.054	-0.065	-0.073	-0.084	-0.097	-0.111	-0.133	-0.173	-0.195		

16	-0.073	-0.078	-0.086	-0.097	-0.108	-0.117	-0.137	-0.176	-0.2
23	-0.112	-0.118	-0.128	-0.144	-0.157	-0.171	-0.183	-0.206	-0.232
30	-0.174	-0.184	-0.196	-0.214	-0.235	-0.25	-0.264	-0.277	-0.298
90	-0.5	-0.5	-0.5	-0.5	-0.5	-0.5	-0.5	-0.5	-0.5
135	-0.5	-0.5	-0.5	-0.5	-0.5	-0.5	-0.5	-0.5	-0.5
160	-0.3	-0.3	-0.3	-0.3	-0.3	-0.3	-0.3	-0.3	-0.3
165	-0.3	-0.3	-0.3	-0.3	-0.3	-0.3	-0.3	-0.3	-0.3
170	-0.4	-0.4	-0.4	-0.4	-0.4	-0.4	-0.4	-0.4	-0.4
180	0	0	0	0	0	0	0	0	0
5200000.	0.								

standard C81 table

## Appendix B - NACA 0012 XFOIL and OVERFLOW Results

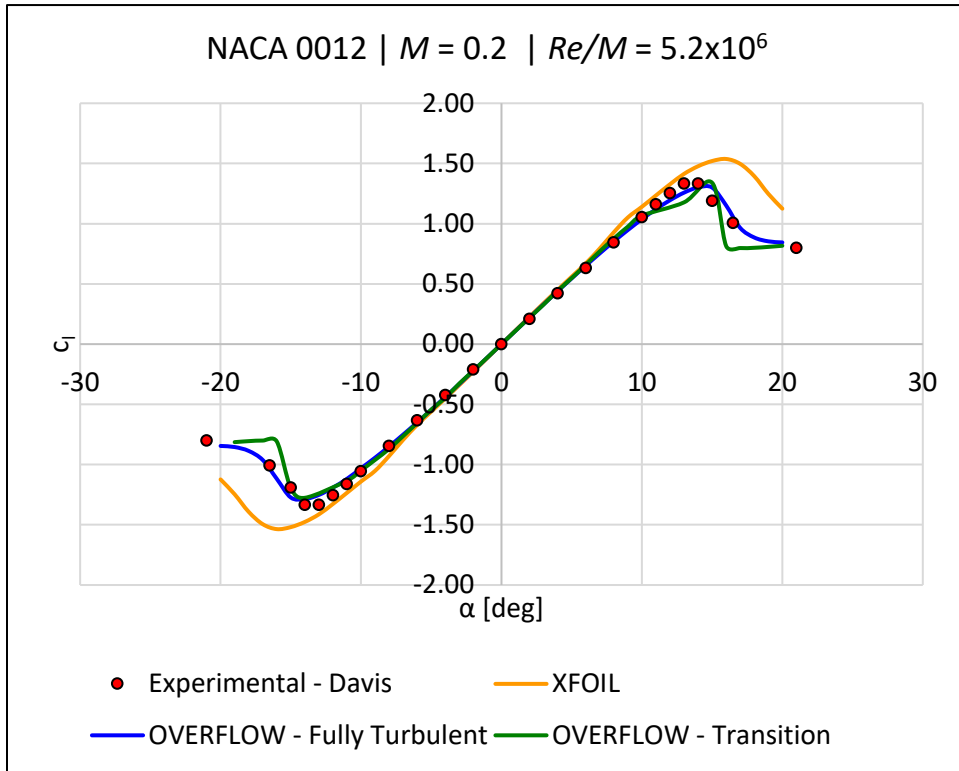


Figure B.1 NACA 0012 lift curve at Mach 0.2.

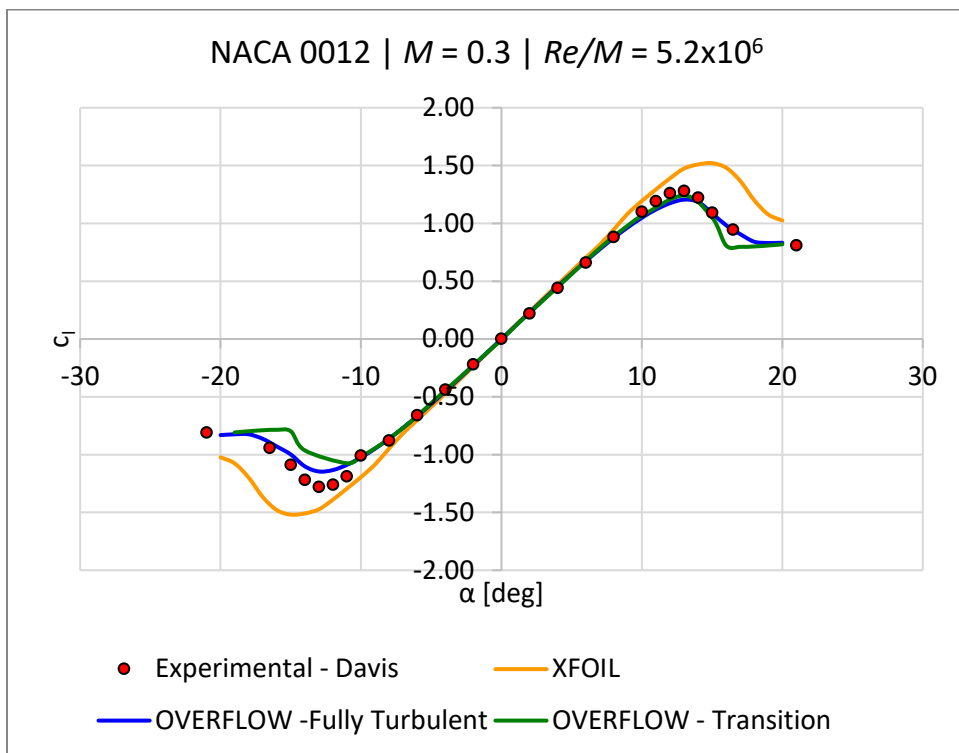


Figure B.2 NACA 0012 lift curve at Mach 0.3.

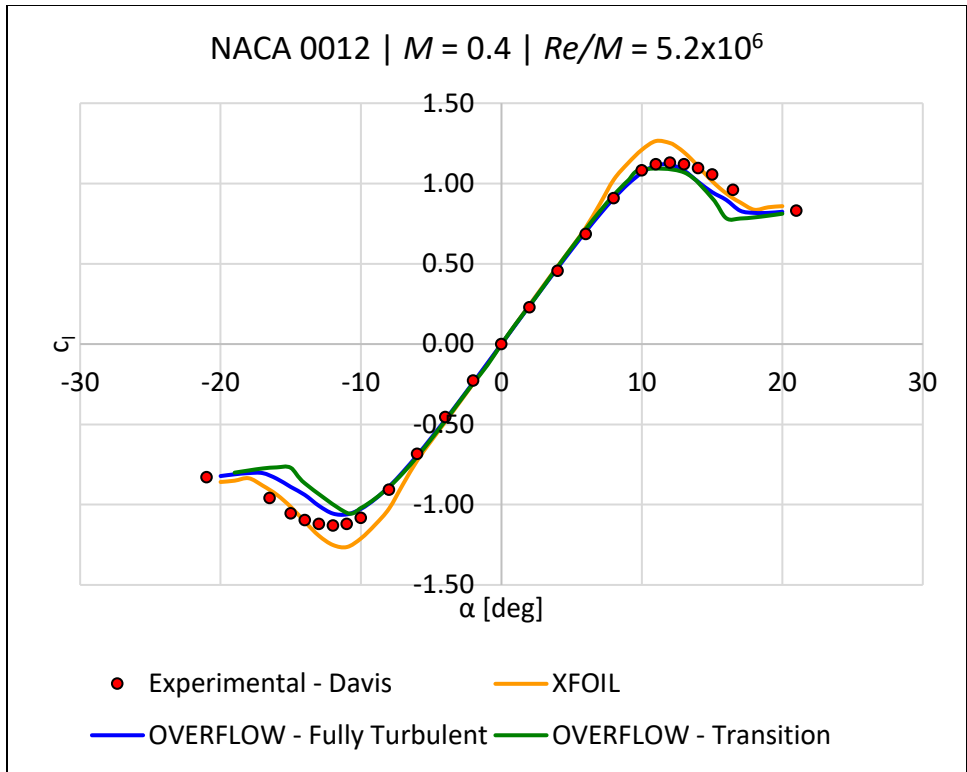


Figure B.3 NACA 0012 lift curve at Mach 0.4.

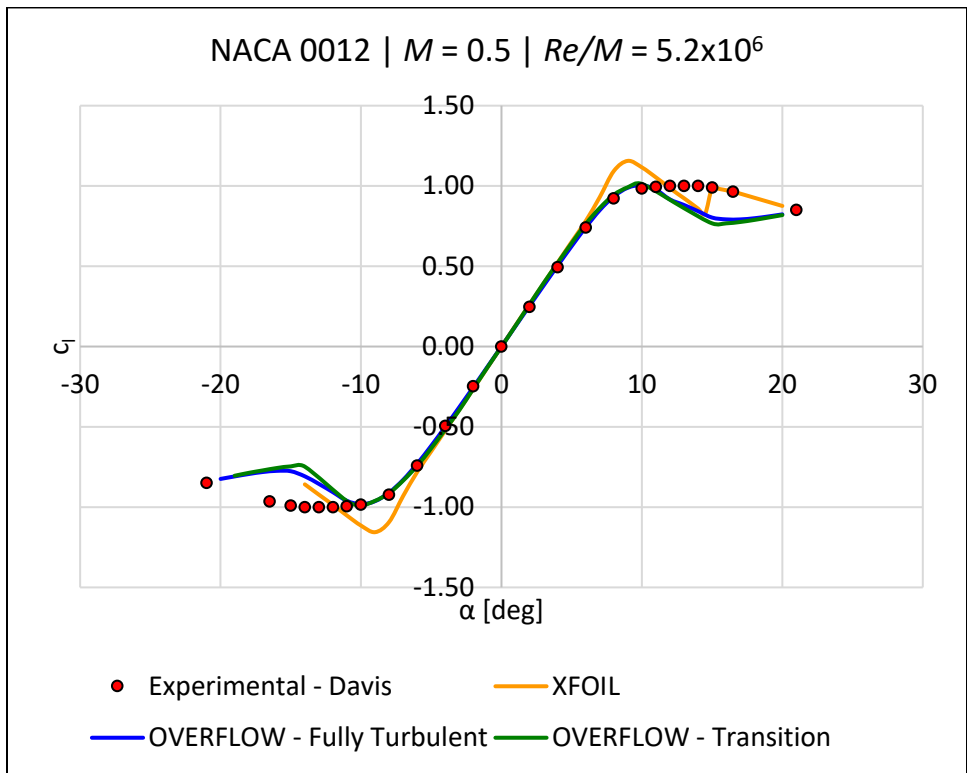


Figure B.4. NACA 0012 lift curve at Mach 0.5.

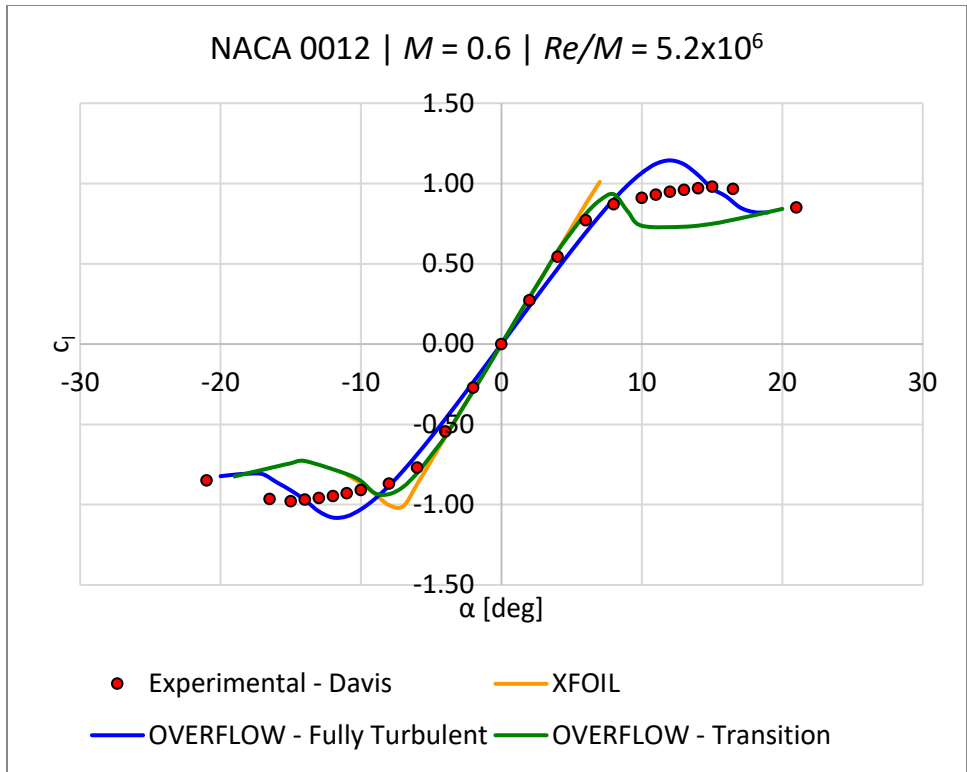


Figure B.5 NACA 0012 lift curve at Mach 0.6.

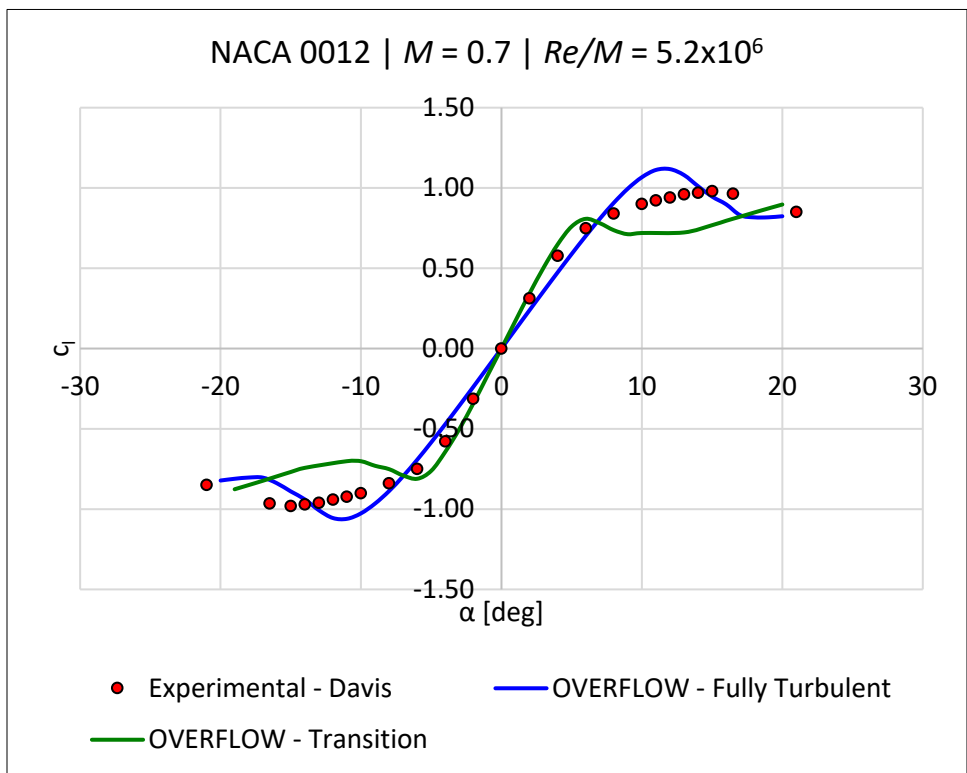


Figure B.6 NACA 0012 lift curve at Mach 0.7.

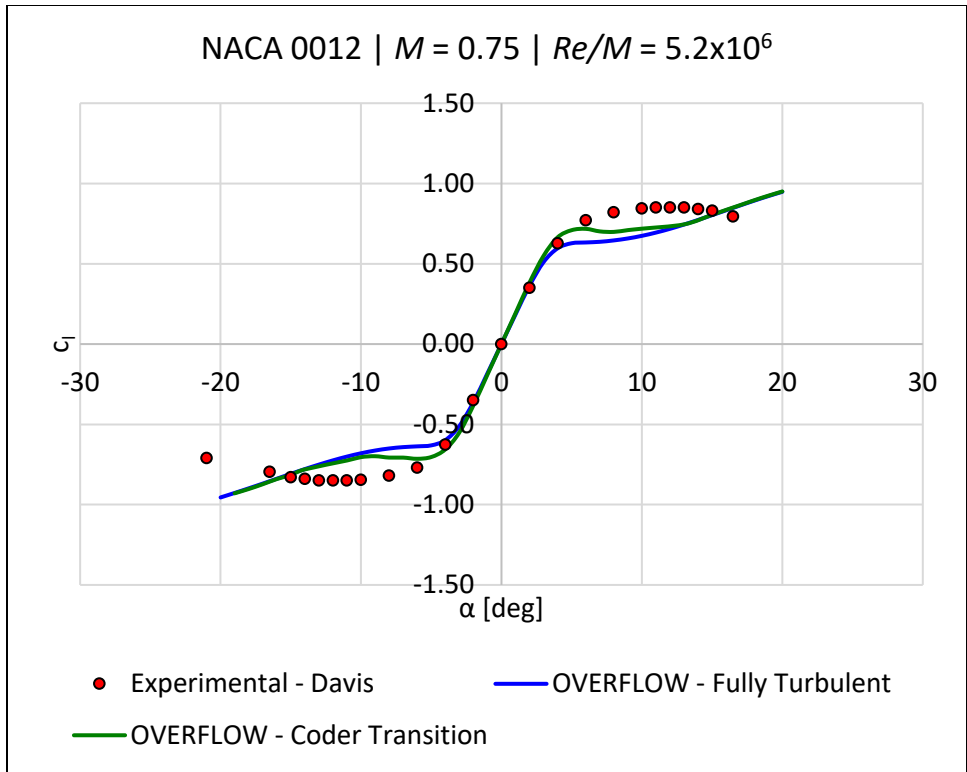


Figure B.7 NACA 0012 lift curve at Mach 0.75.

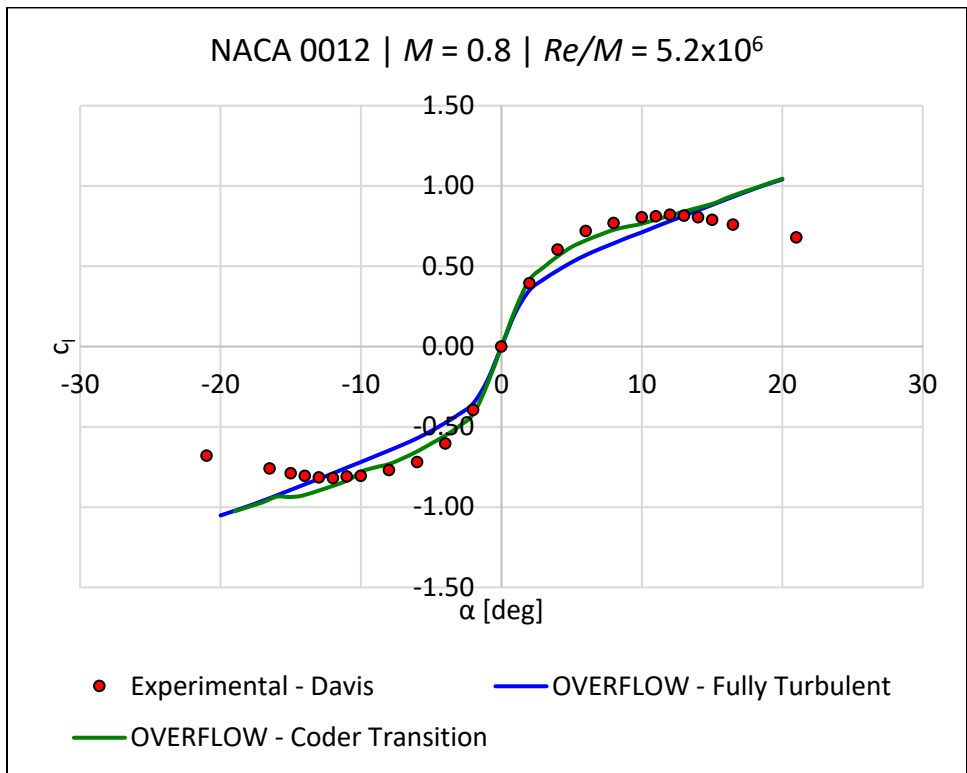


Figure B.8 NACA 0012 lift curve at Mach 0.8.

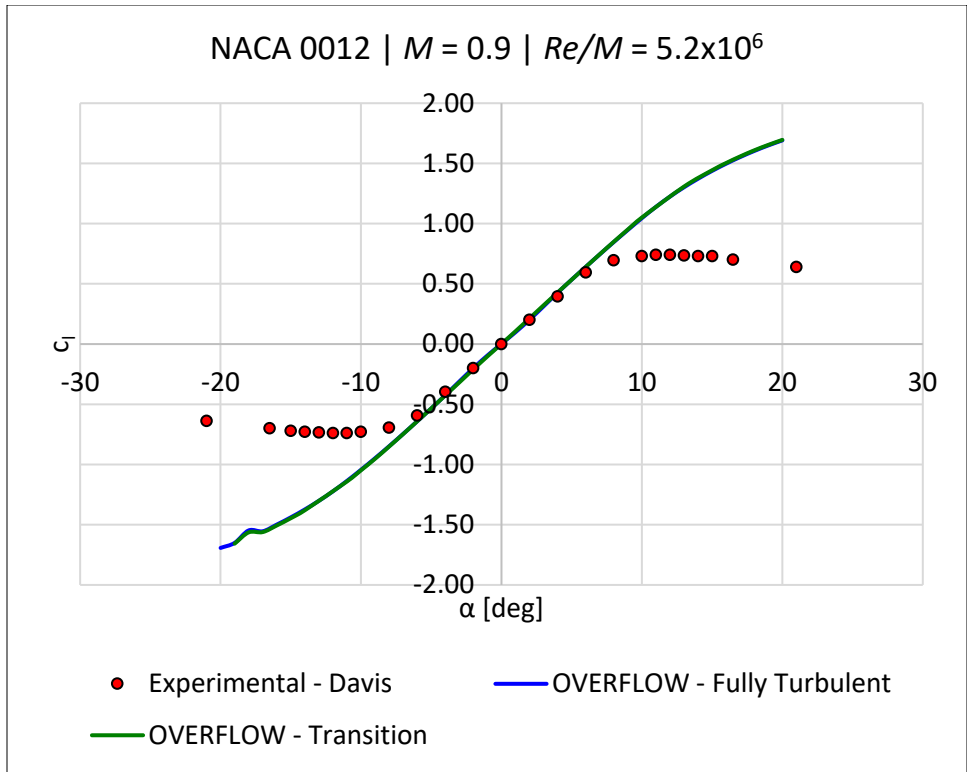


Figure B.9. NACA 0012 lift curve at Mach 0.9.

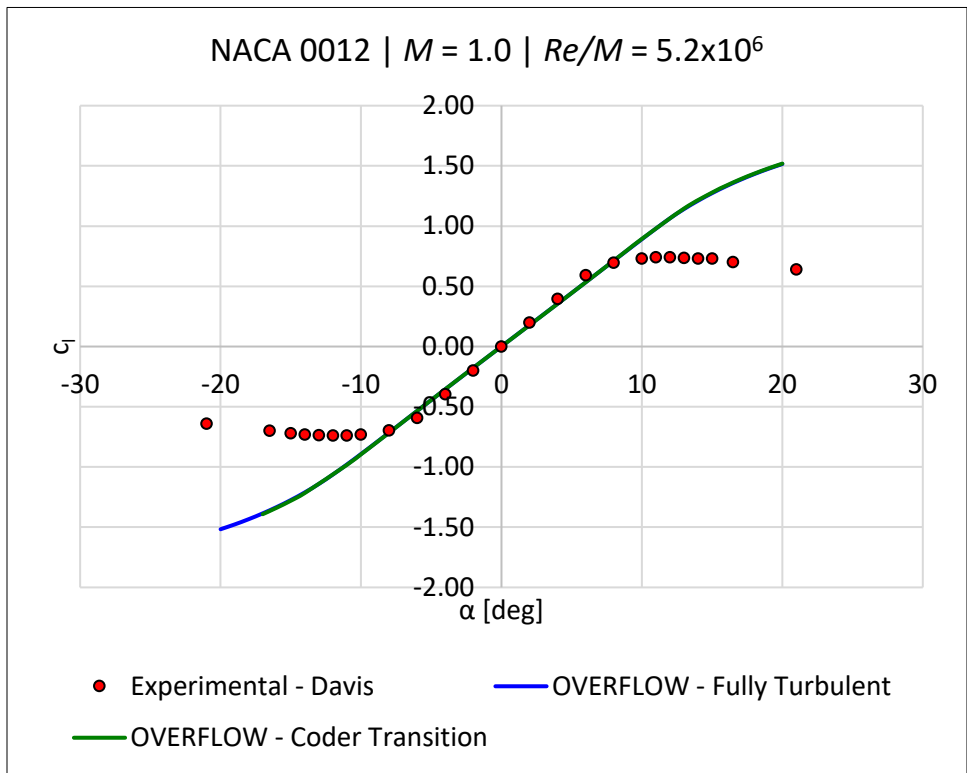


Figure B.10 NACA 0012 lift curve at Mach 1.0.

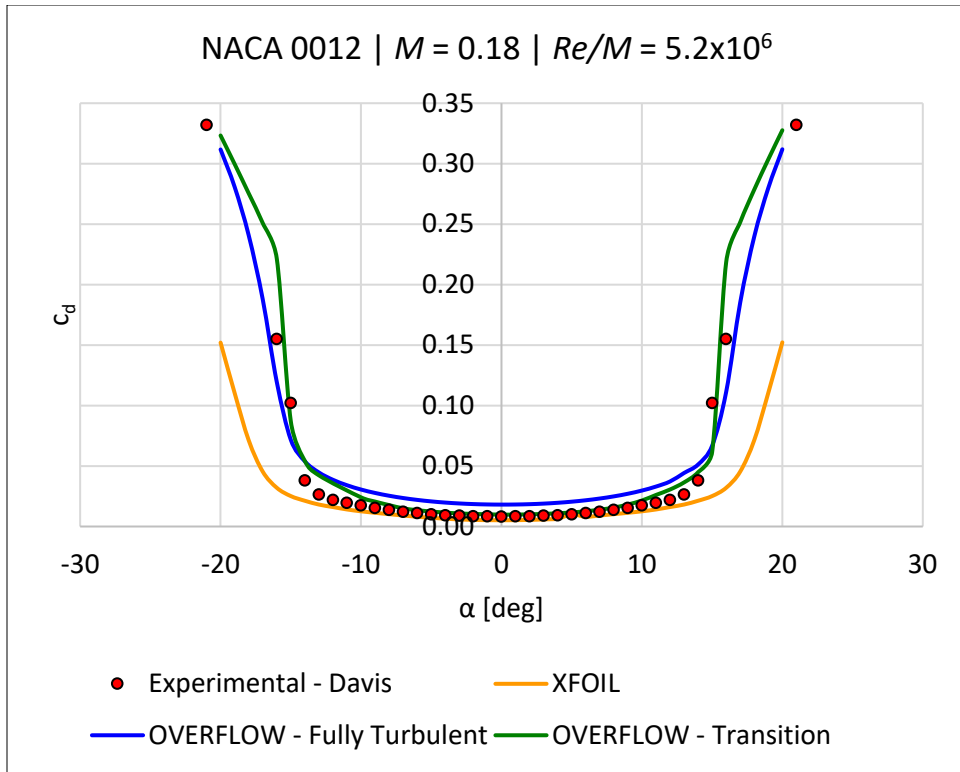


Figure B.11 NACA 0012 drag bucket at Mach 0.18.

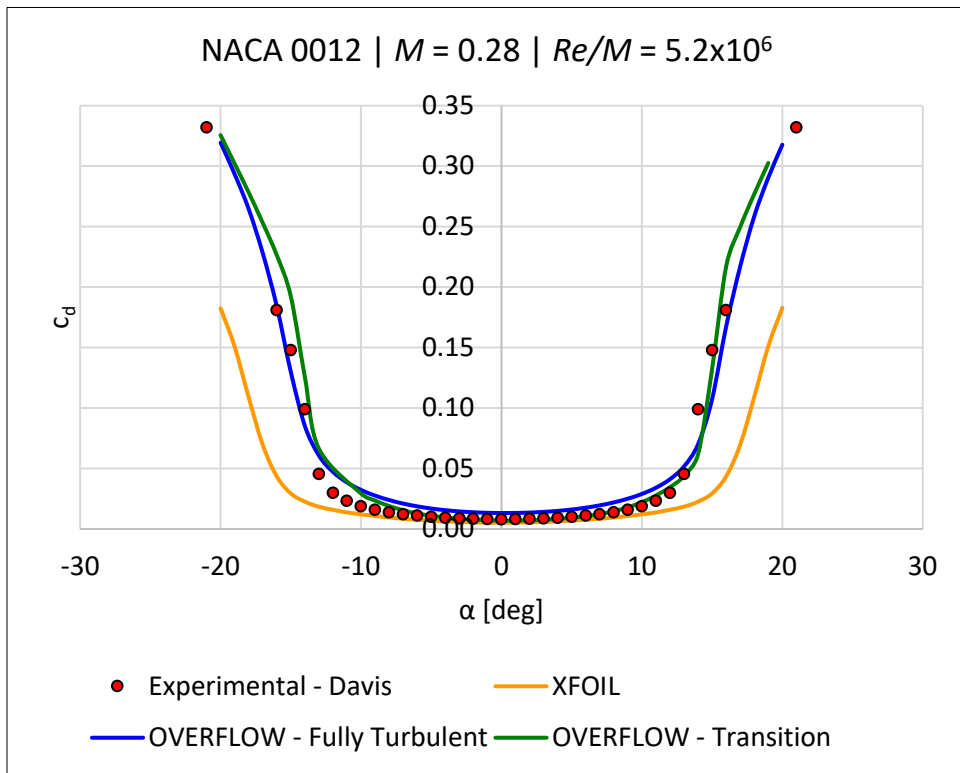


Figure B.12 NACA 0012 drag bucket at Mach 0.28.

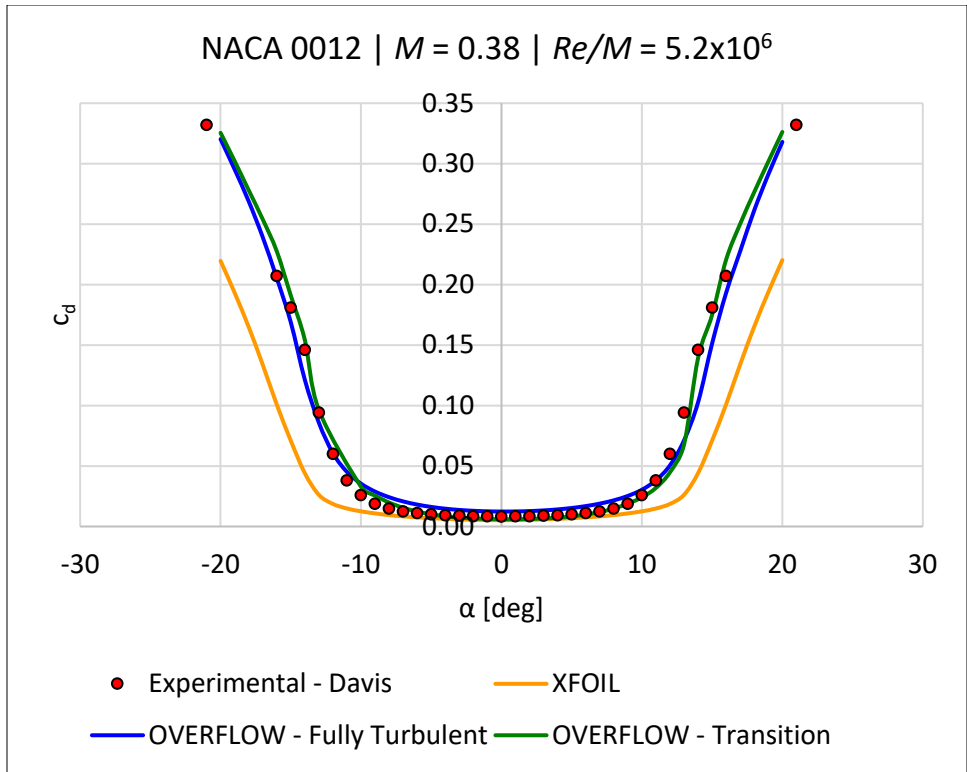


Figure B.13 NACA 0012 drag bucket at Mach 0.38.

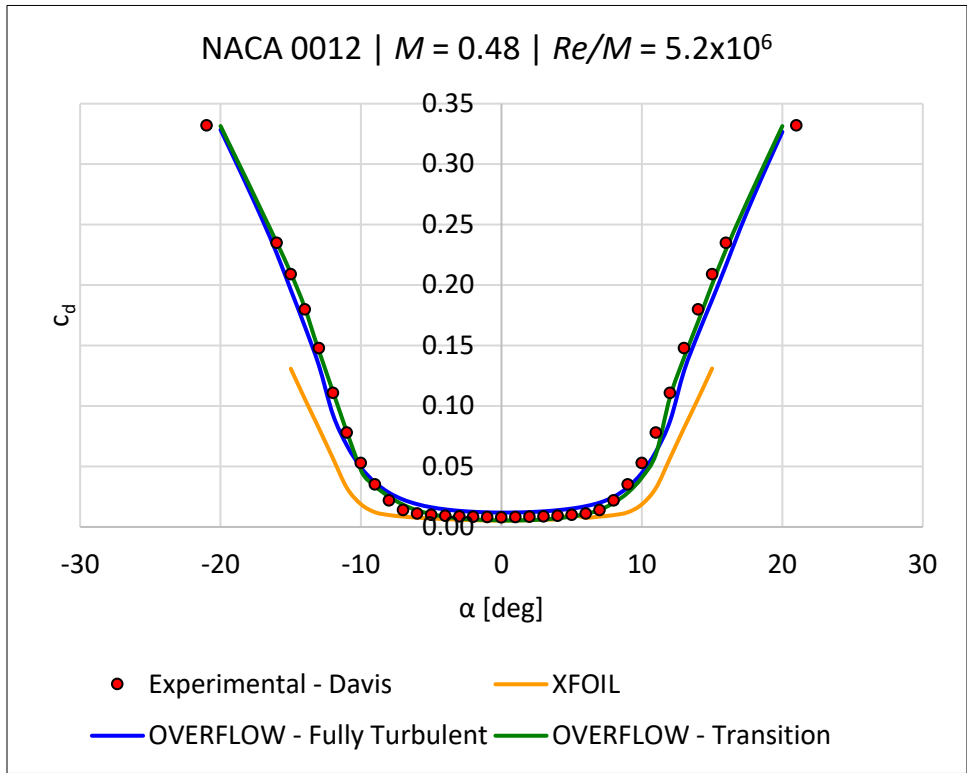


Figure B.14 NACA 0012 drag bucket at Mach 0.48.

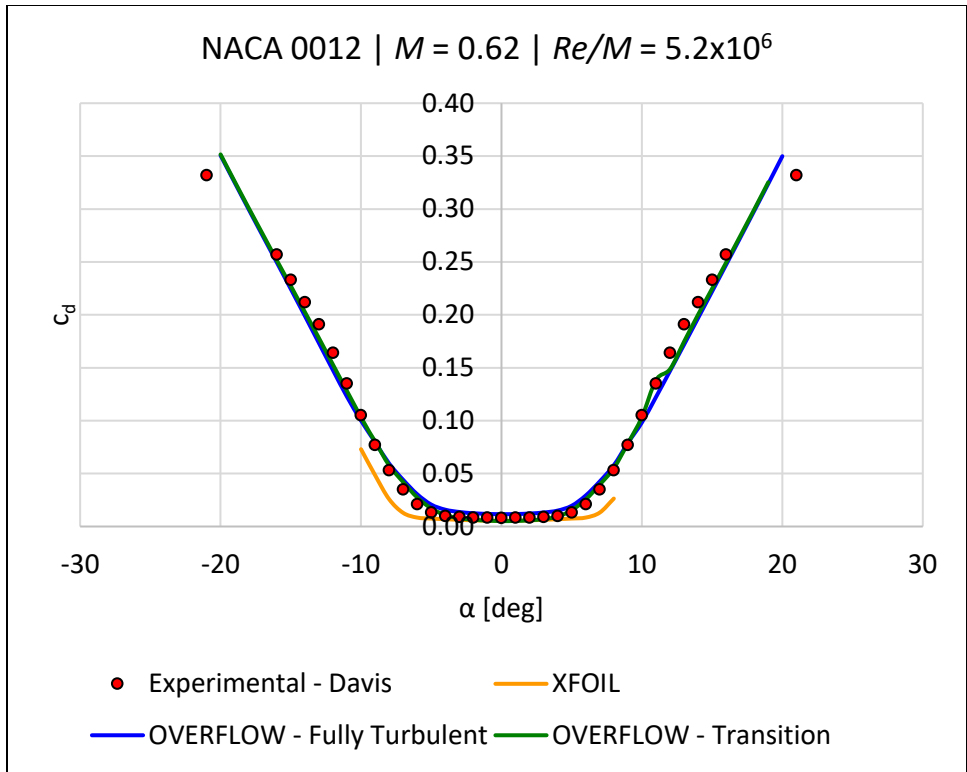


Figure B.15 NACA 0012 drag bucket at Mach 0.62.

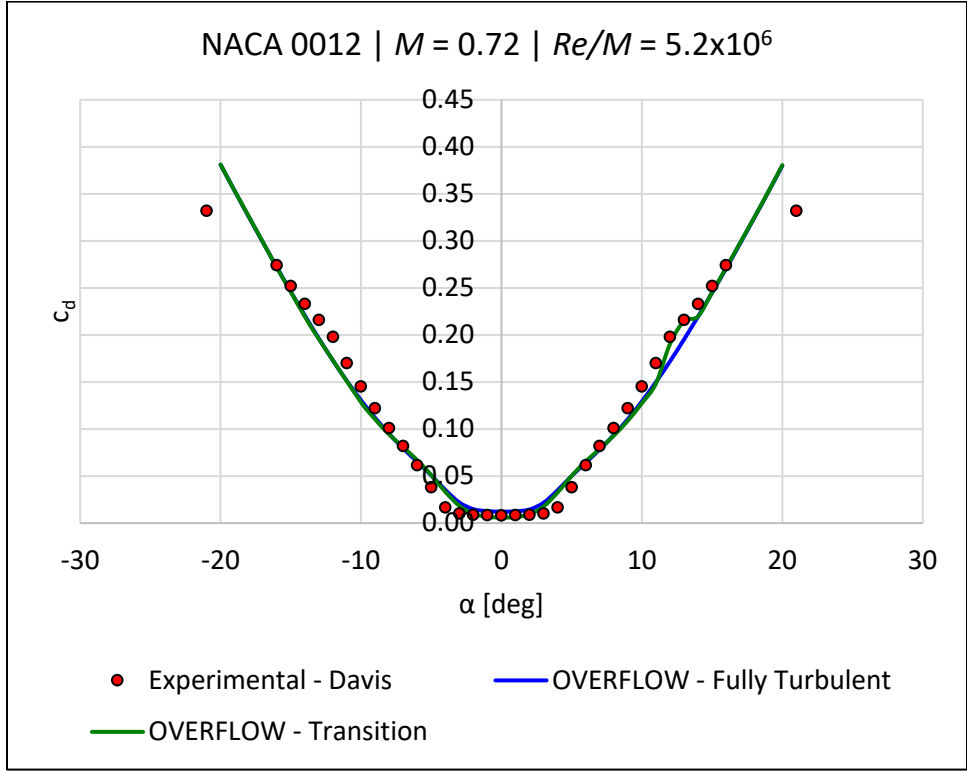


Figure B.16 NACA 0012 drag bucket at Mach 0.72.

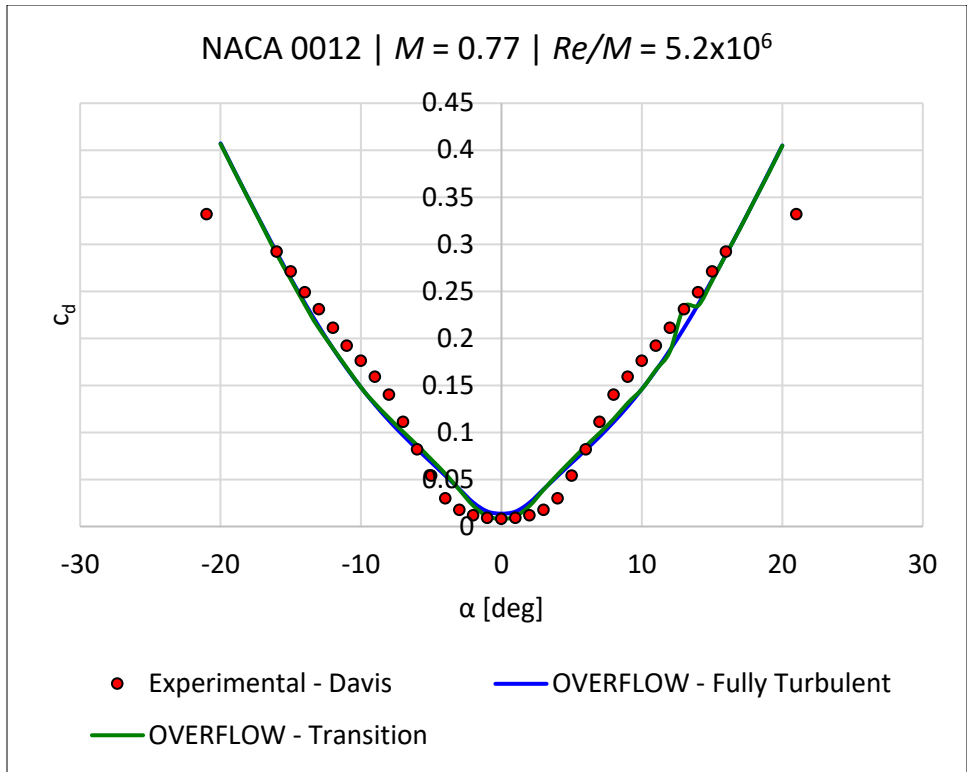


Figure B.17 NACA 0012 drag bucket at Mach 0.77.

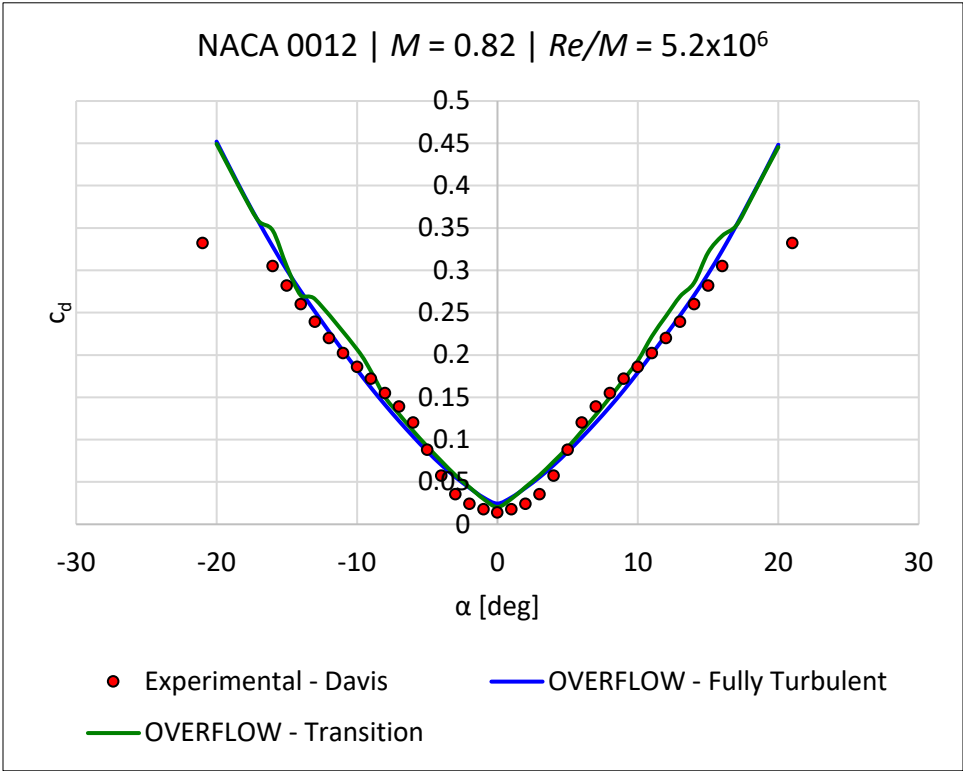


Figure B.18 NACA 0012 drag bucket at Mach 0.82.

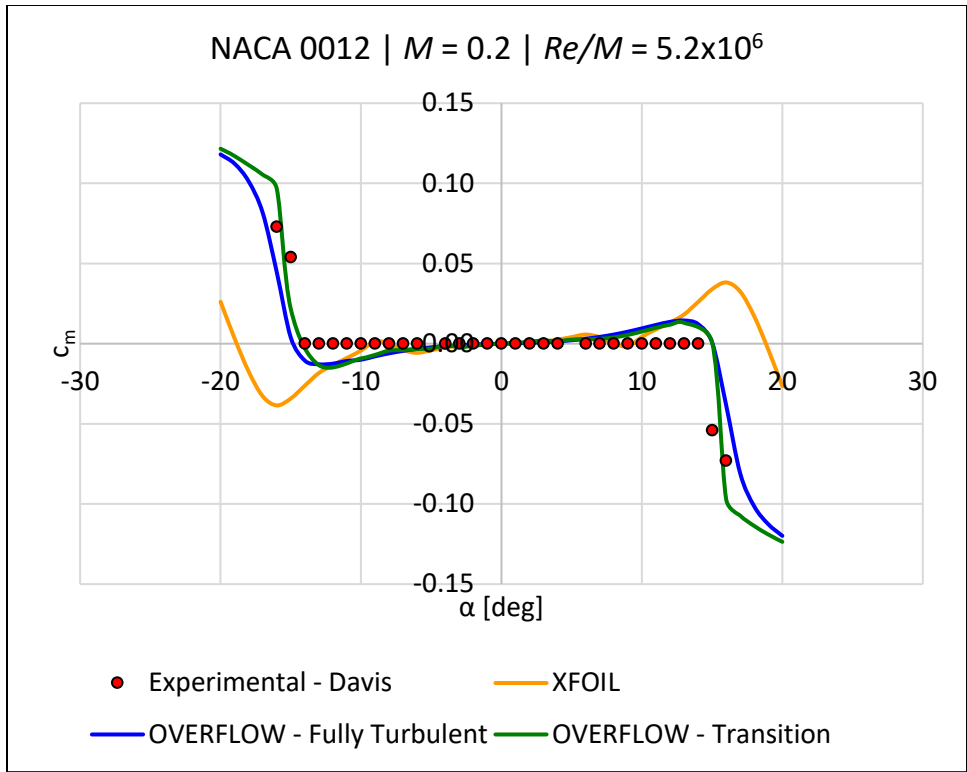


Figure B.19 NACA 0012 moment coefficient versus  $\alpha$  at Mach 0.2.

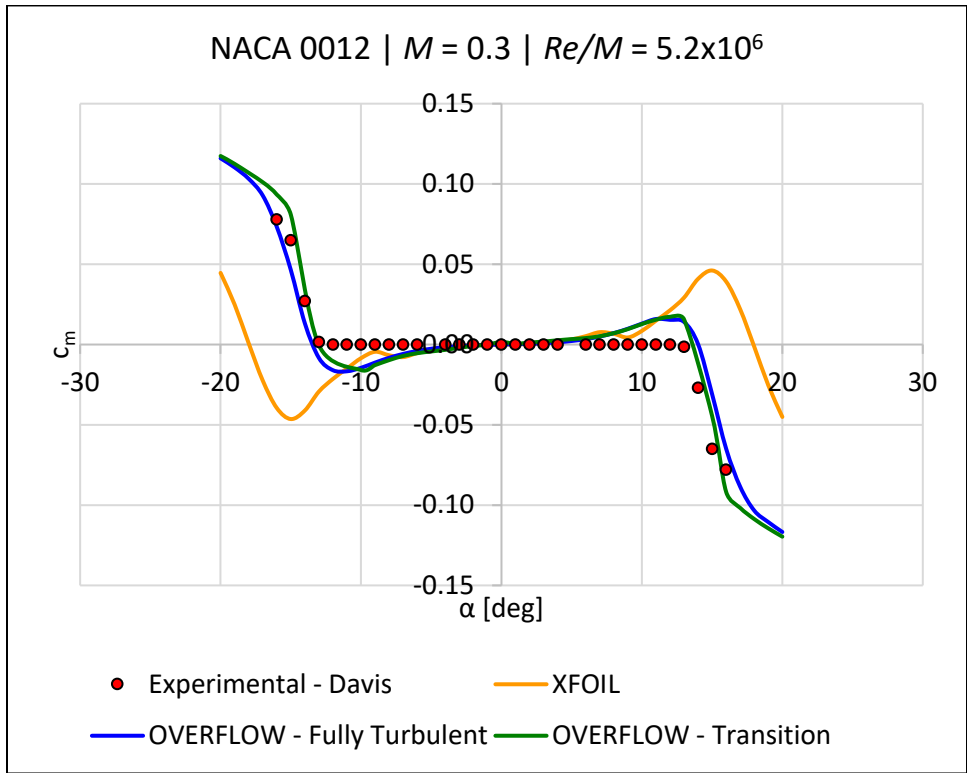


Figure B.20 NACA 0012 moment coefficient versus  $\alpha$  at Mach 0.3.

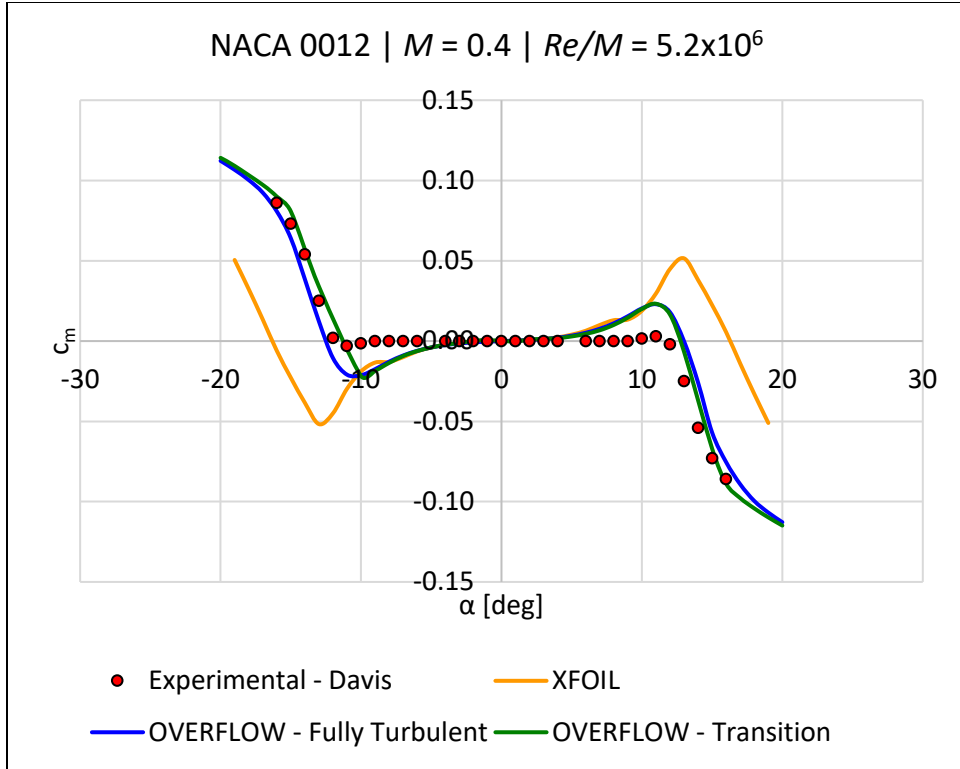


Figure B.21 NACA 0012 moment coefficient versus  $\alpha$  at Mach 0.4.

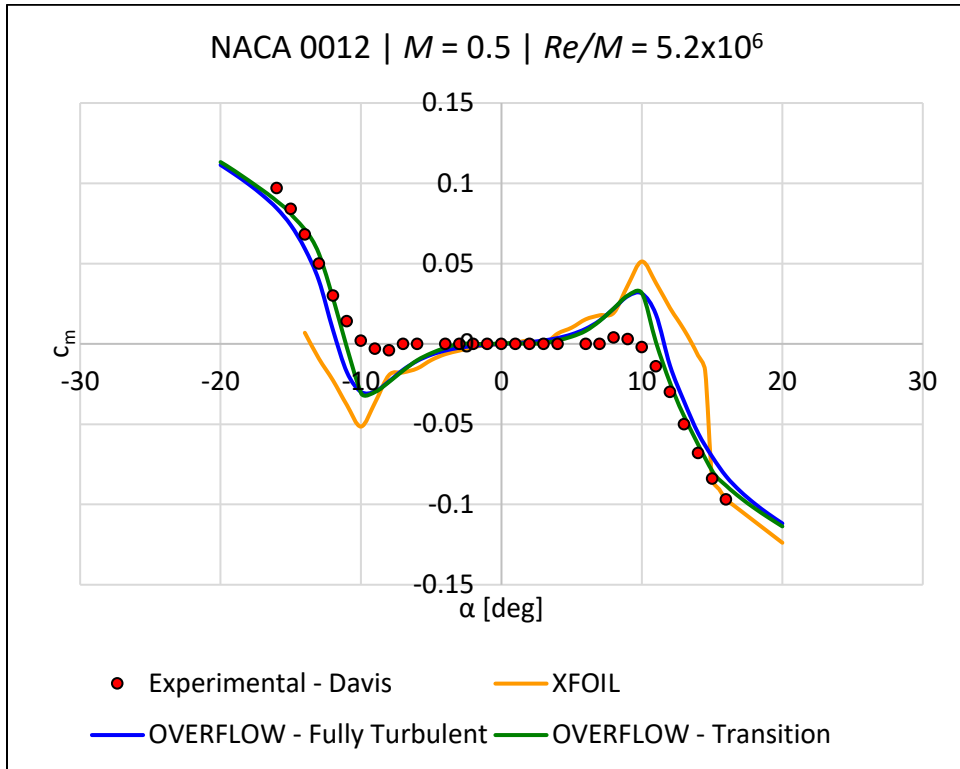


Figure B.22 NACA 0012 moment coefficient versus  $\alpha$  at Mach 0.5.

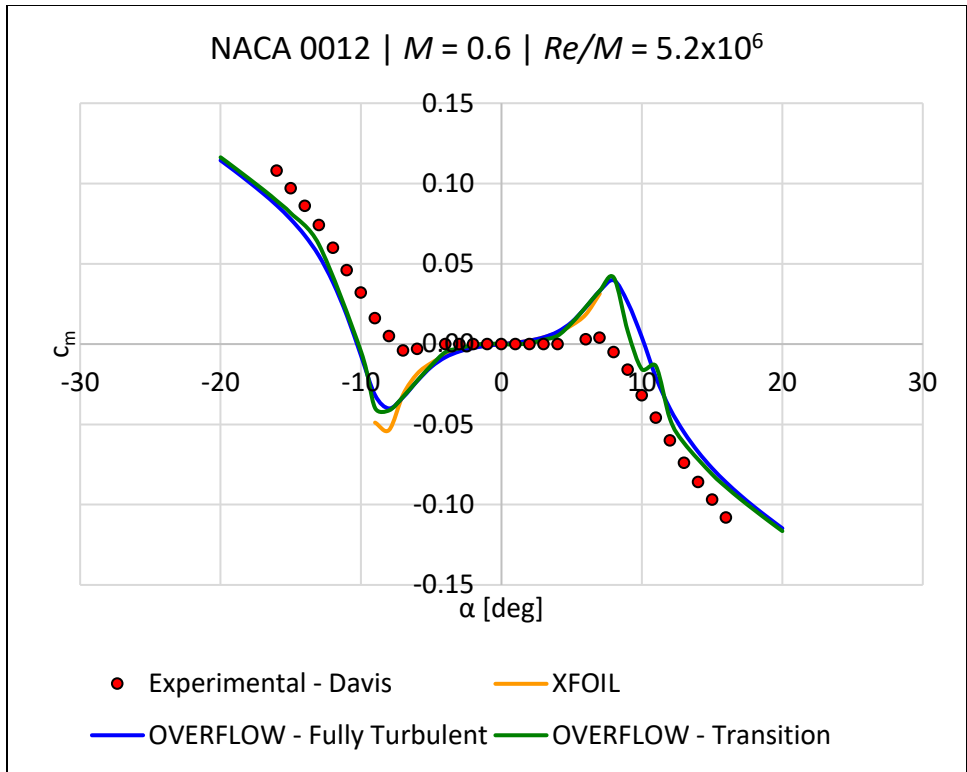


Figure B.23 NACA 0012 moment coefficient versus  $\alpha$  at Mach 0.6.

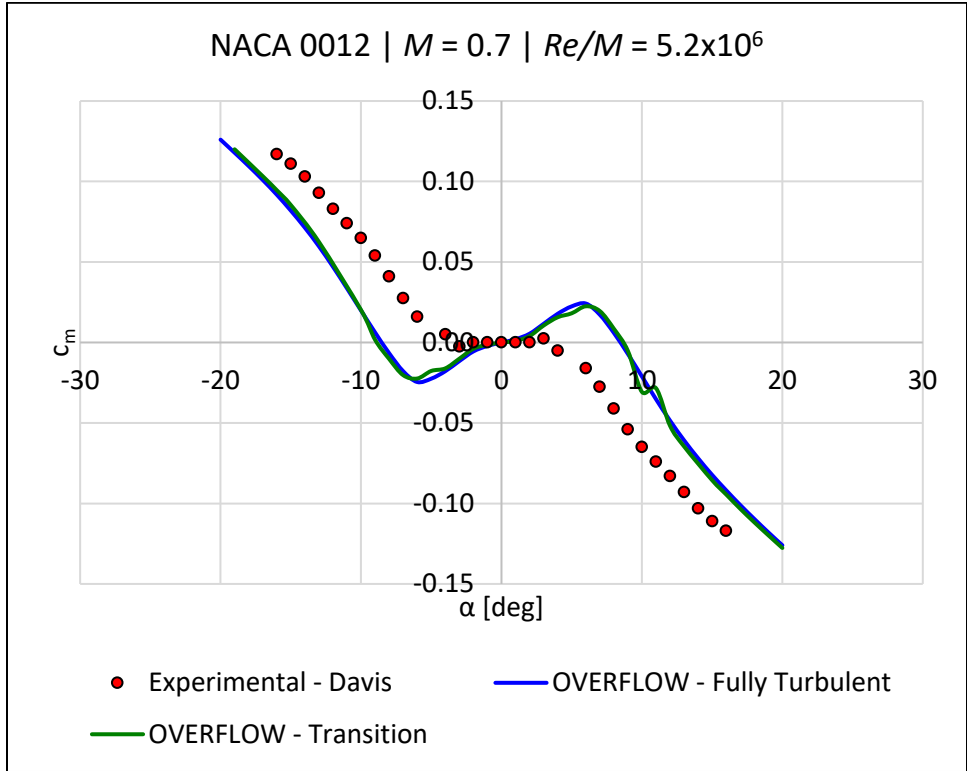


Figure B.24 NACA 0012 moment coefficient versus  $\alpha$  at Mach 0.7.

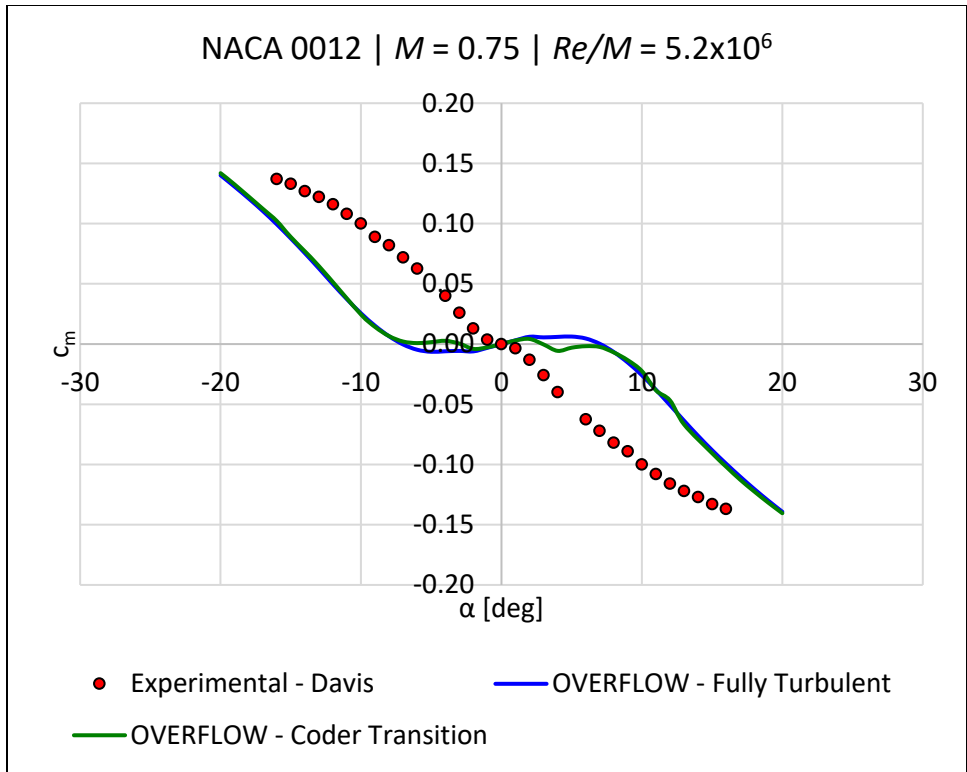


Figure B.25 NACA 0012 moment coefficient versus  $\alpha$  at Mach 0.75.

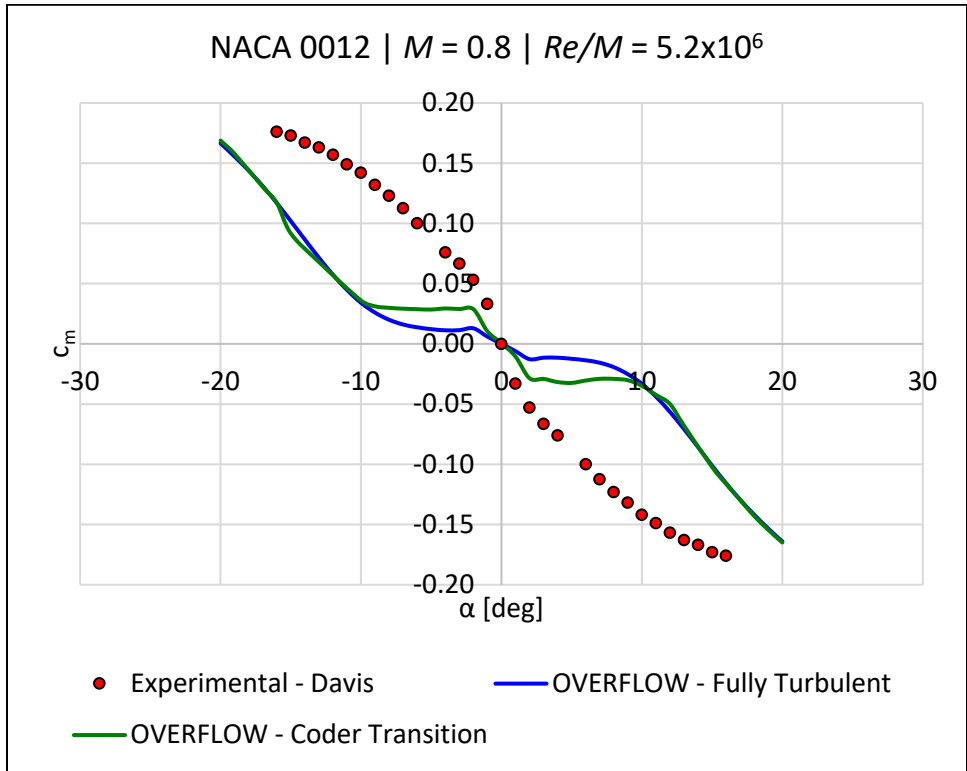


Figure B.26 NACA 0012 moment coefficient versus  $\alpha$  at Mach 0.8.

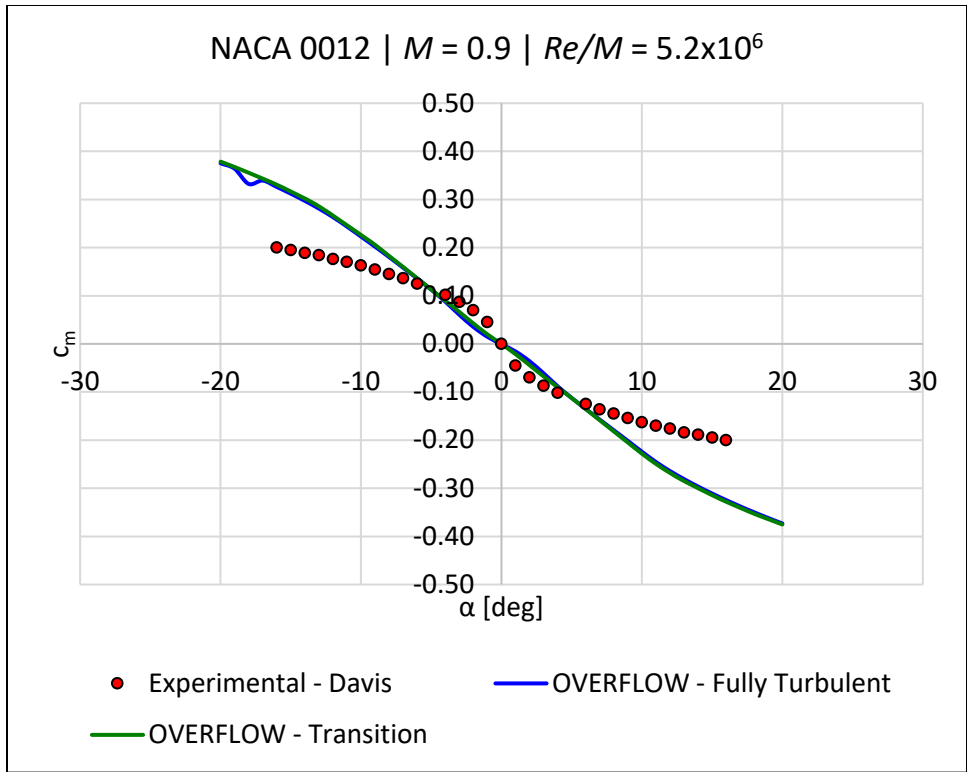


Figure B.27 NACA 0012 moment coefficient versus  $\alpha$  at Mach 0.9.

## Appendix C - RC(4)-10 XFOIL and OVERFLOW Results

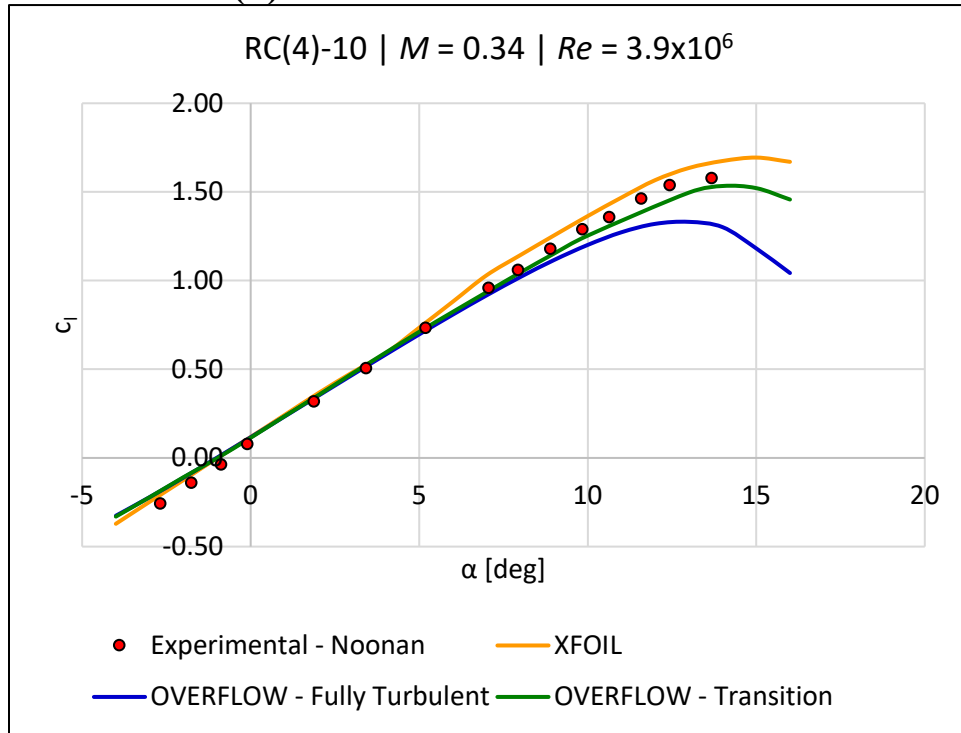


Figure C.1 RC(4)-10 lift curve at Mach 0.34 and a Reynolds number of  $3.9 \times 10^6$ .

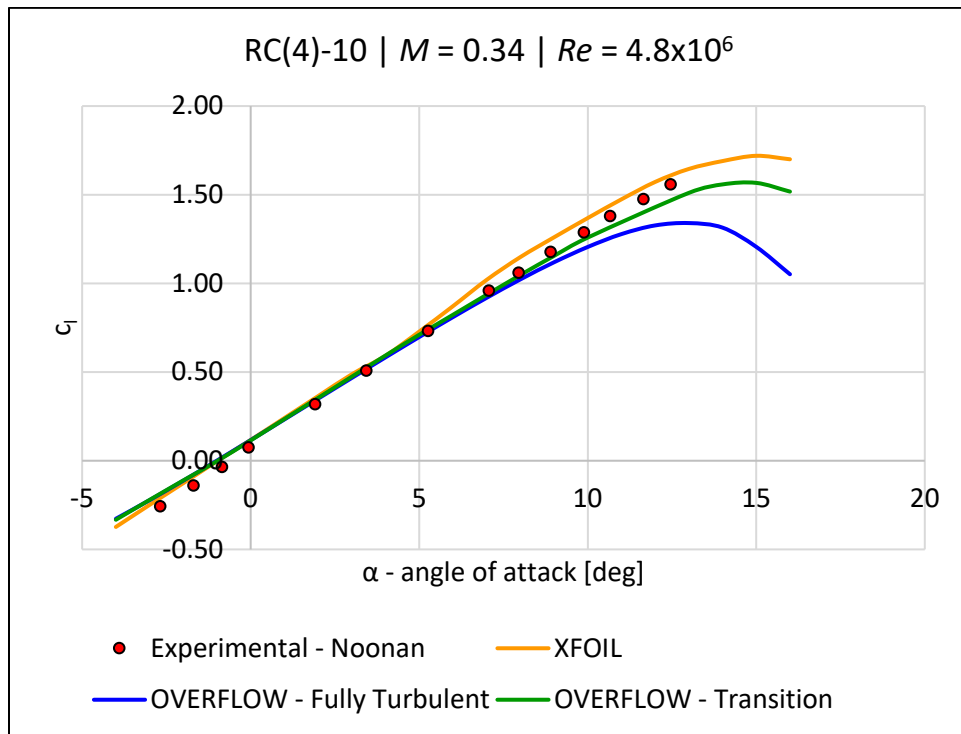


Figure C.2 RC(4)-10 lift curve at Mach 0.34 and a Reynolds number of  $4.8 \times 10^6$ .

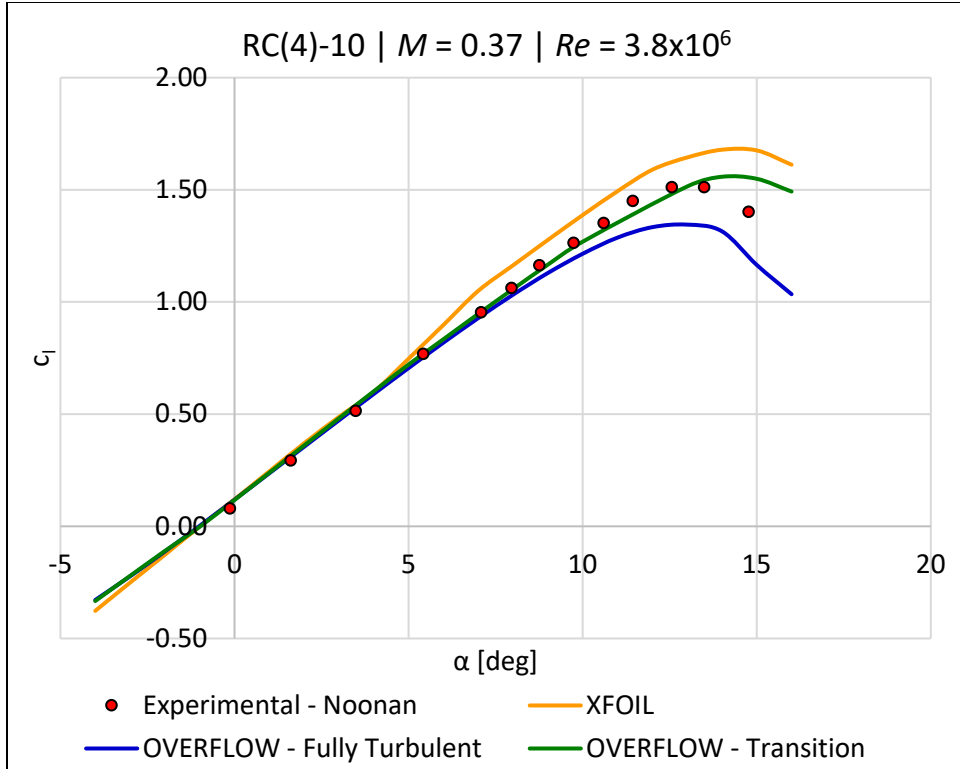


Figure C.3 RC(4)-10 lift curve at Mach 0.37 and a Reynolds number of  $3.8 \times 10^6$ .

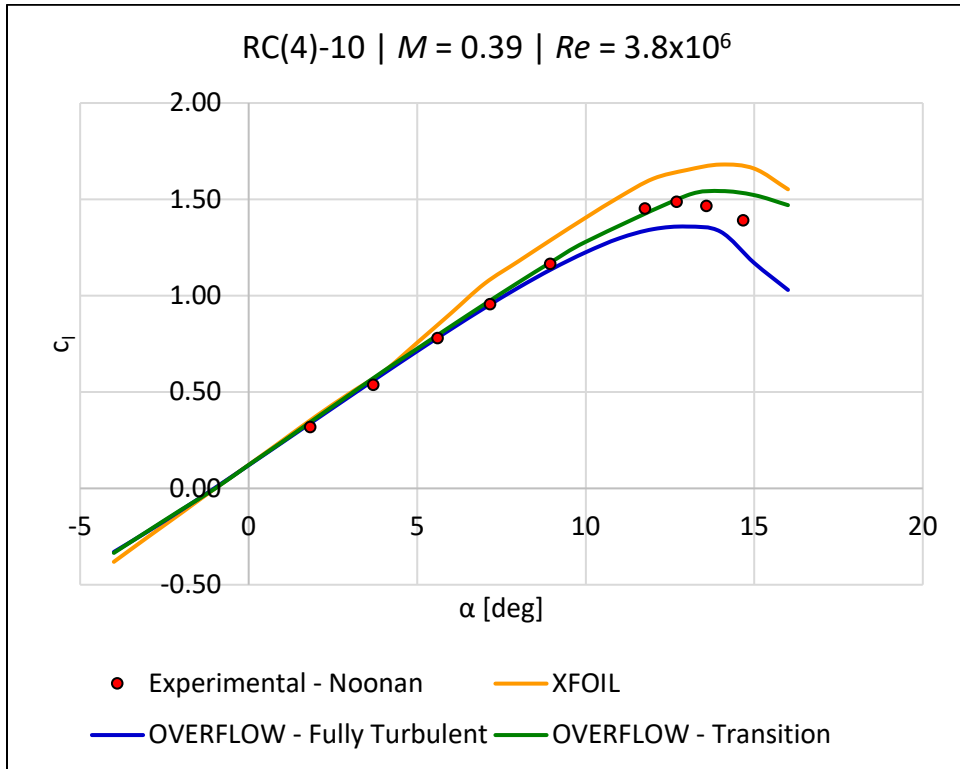


Figure C.4 RC(4)-10 lift curve at Mach 0.39 and a Reynolds number of  $3.8 \times 10^6$ .

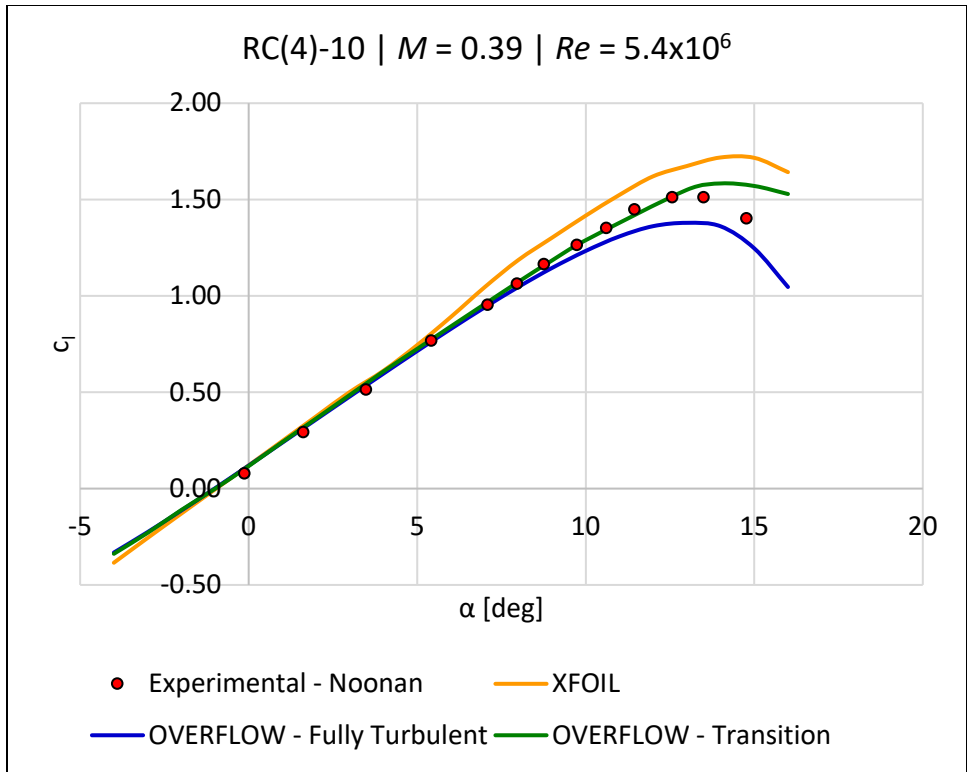


Figure C.5 RC(4)-10 lift curve at Mach 0.39 and a Reynolds number of  $5.4 \times 10^6$ .

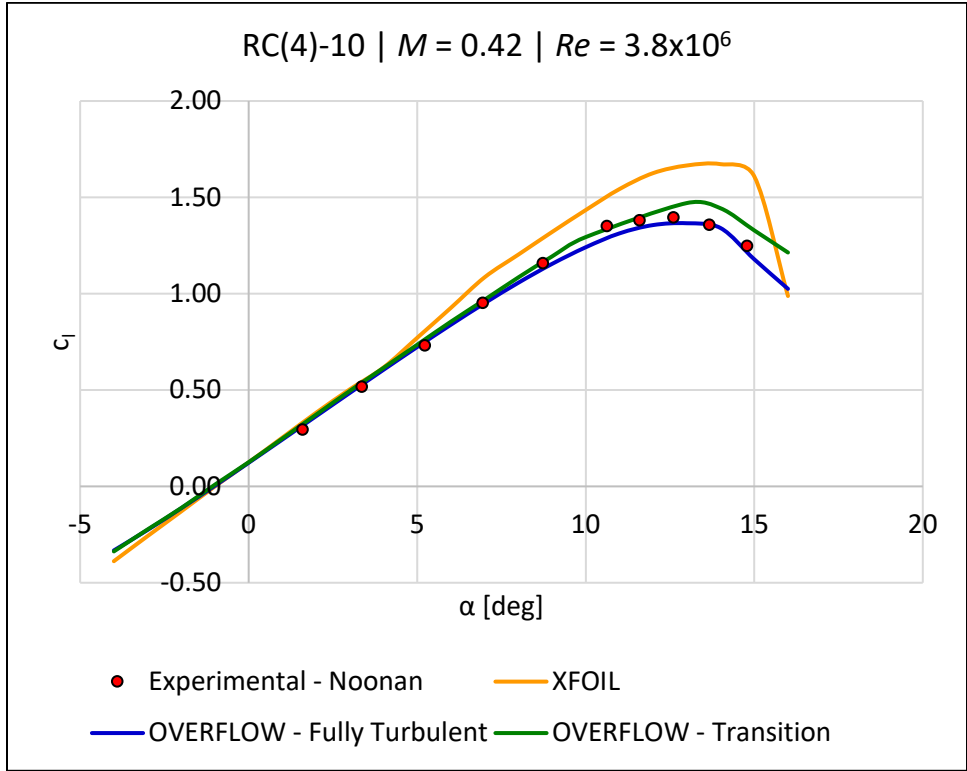


Figure C.6 RC(4)-10 lift curve at Mach 0.42 and a Reynolds number of  $3.8 \times 10^6$ .

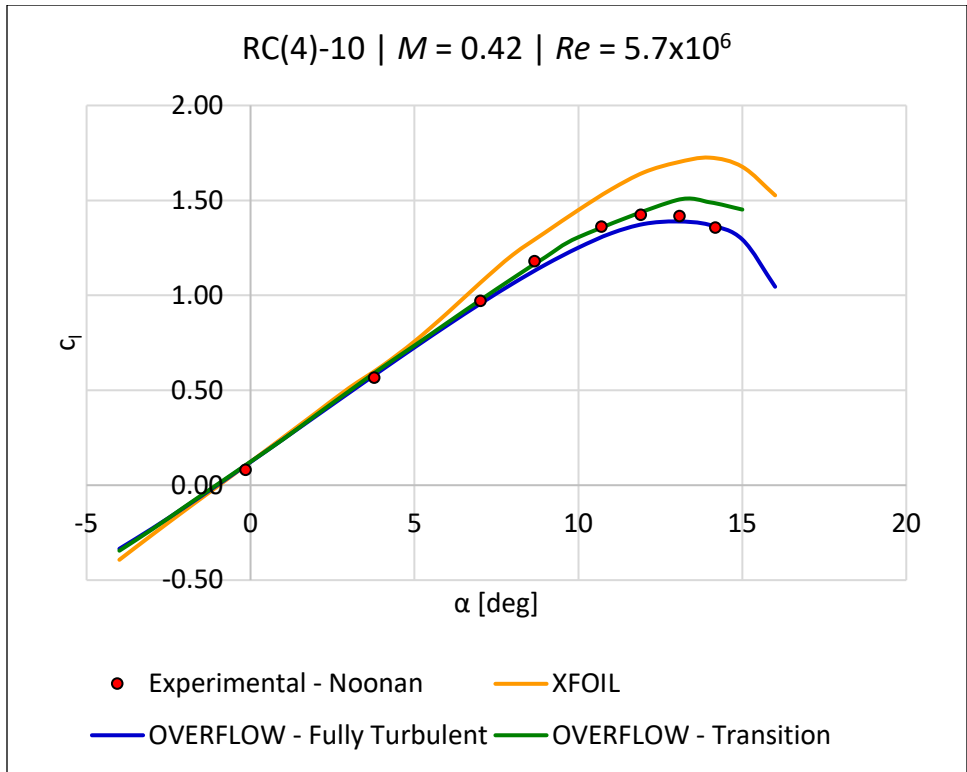


Figure C.7 RC(4)-10 lift curve at Mach 0.42 and a Reynolds number of  $5.7 \times 10^6$ .

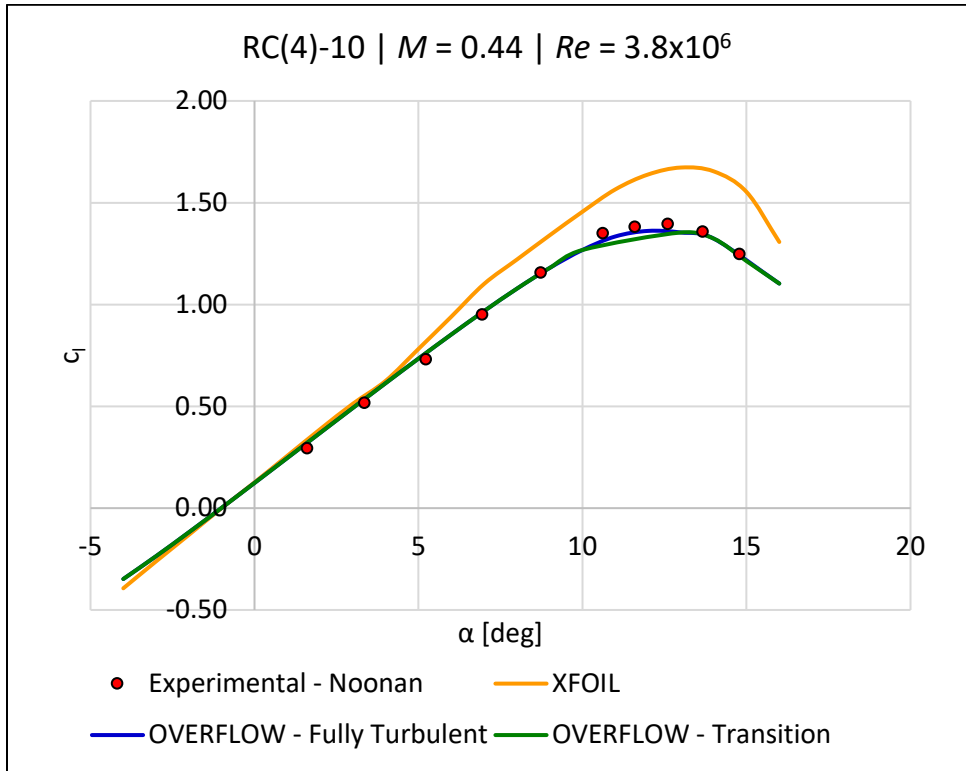


Figure C.8 RC(4)-10 lift curve at Mach 0.44 and a Reynolds number of  $3.8 \times 10^6$ .

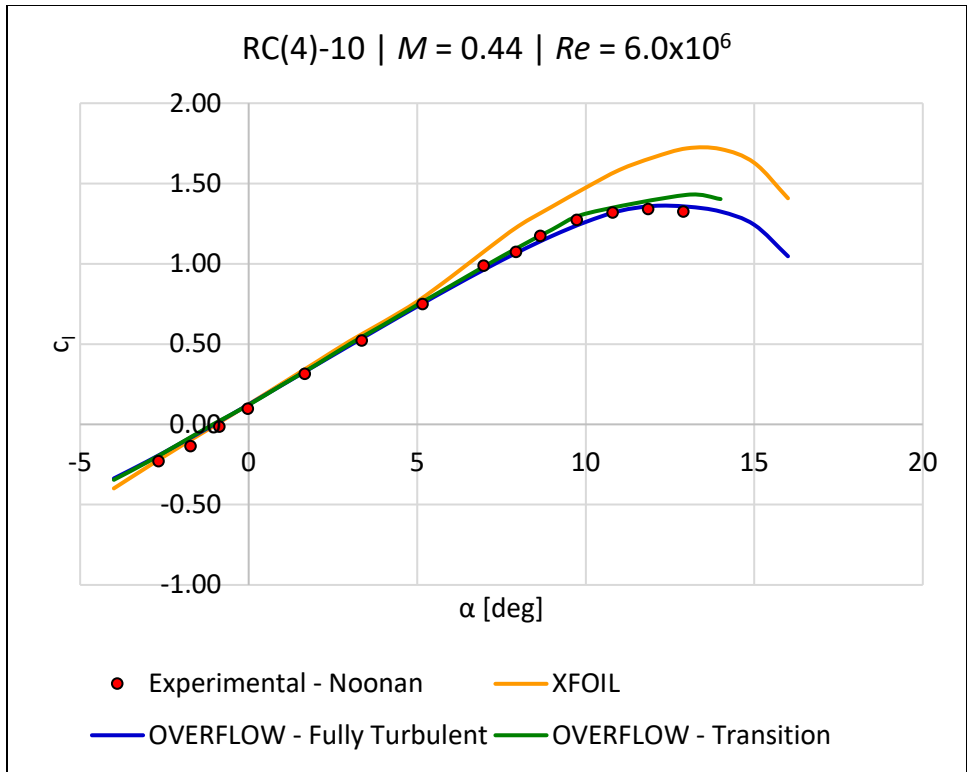


Figure C.9. RC(4)-10 lift curve at Mach 0.44 and a Reynolds number of  $6.0 \times 10^6$ .

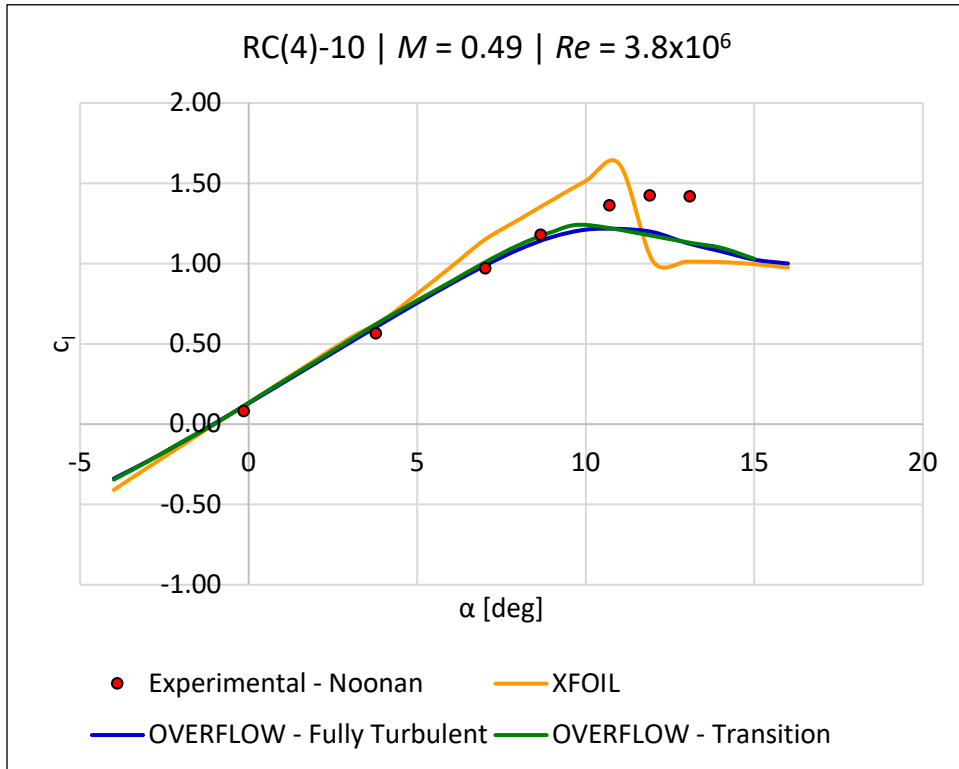


Figure C.10. RC(4)-10 lift curve at Mach 0.49 and a Reynolds number of  $3.8 \times 10^6$ .

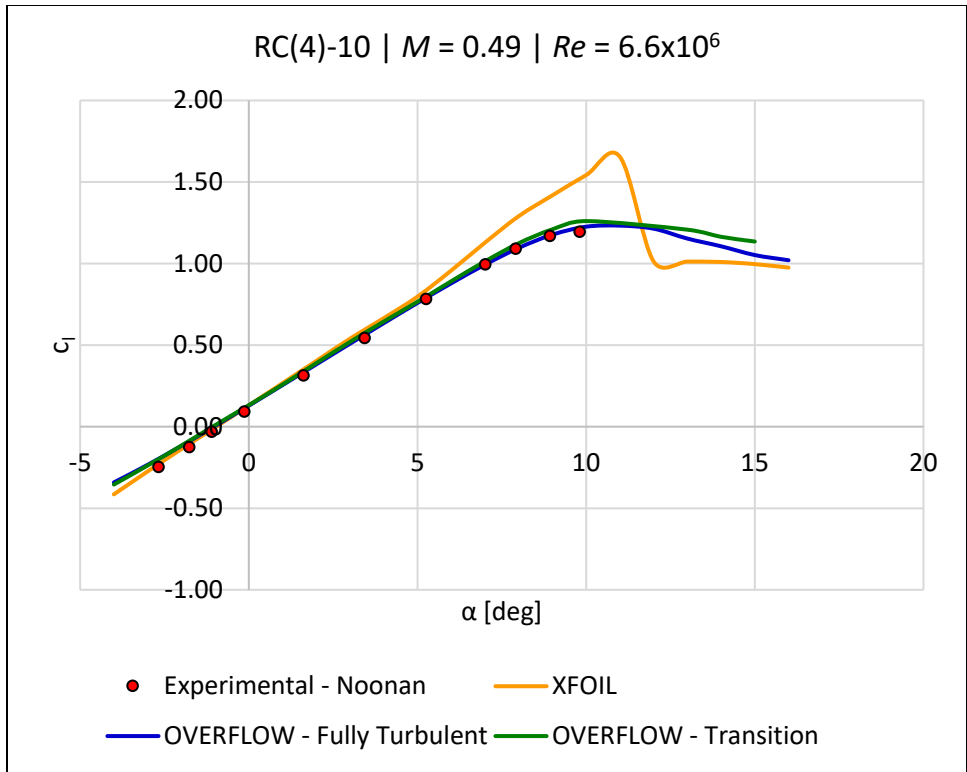


Figure C.11 RC(4)-10 lift curve at Mach 0.49 and a Reynolds number of  $6.6 \times 10^6$ .

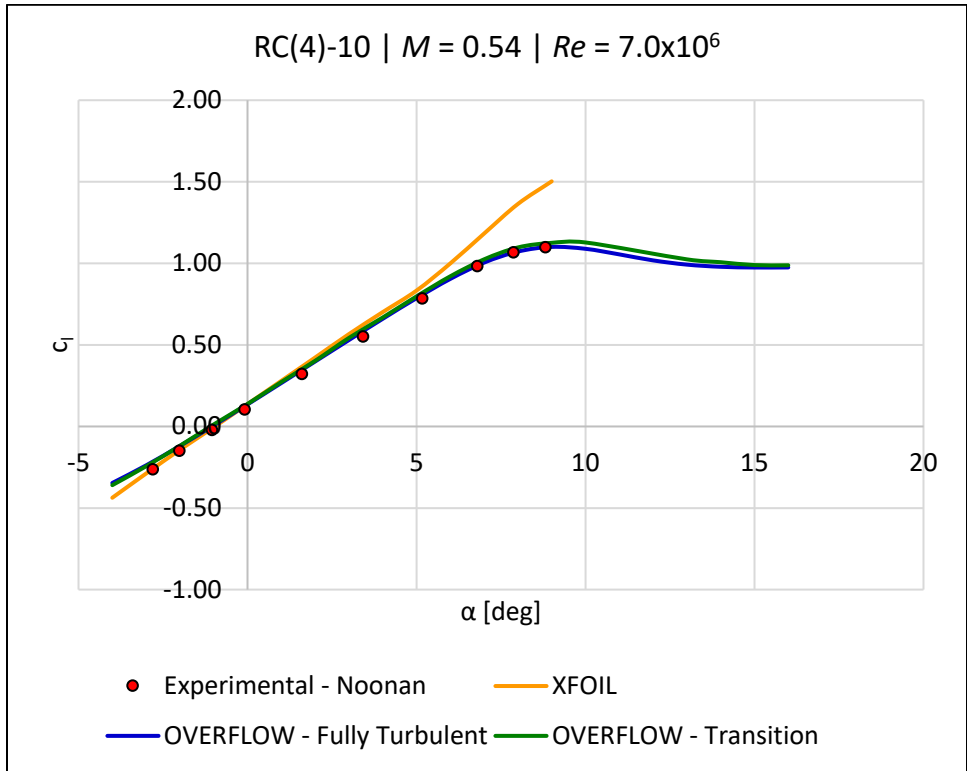


Figure C.12 RC(4)-10 lift curve at Mach 0.54 and a Reynolds number of  $7.0 \times 10^6$ .

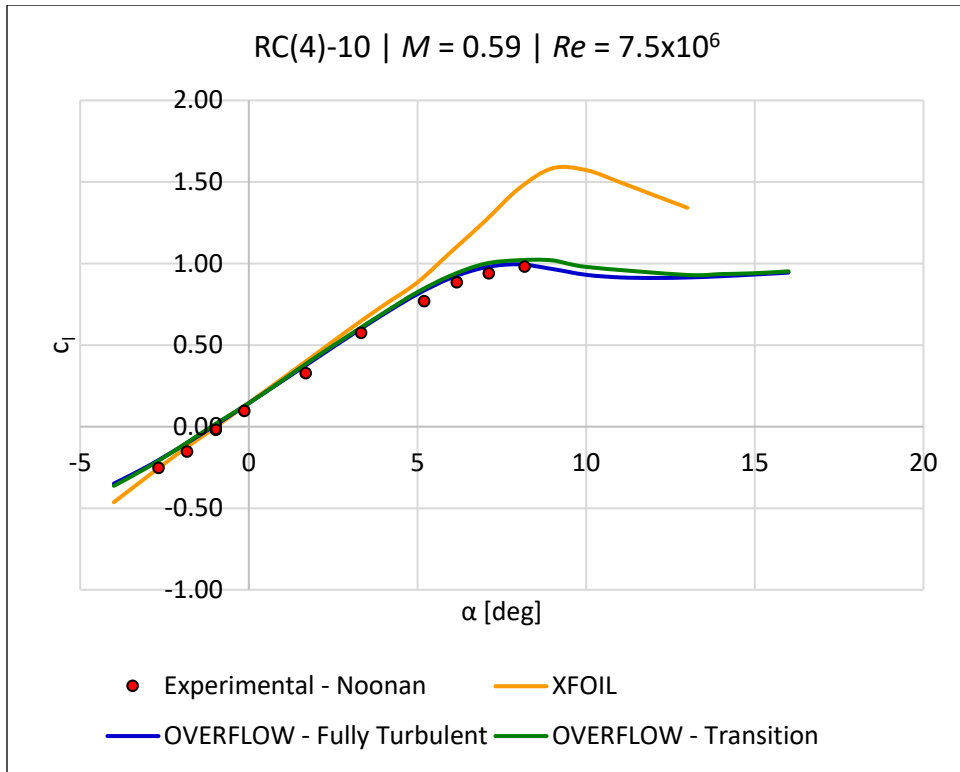


Figure C.13 RC(4)-10 lift curve at Mach 0.59 and a Reynolds number of  $7.5 \times 10^6$ .

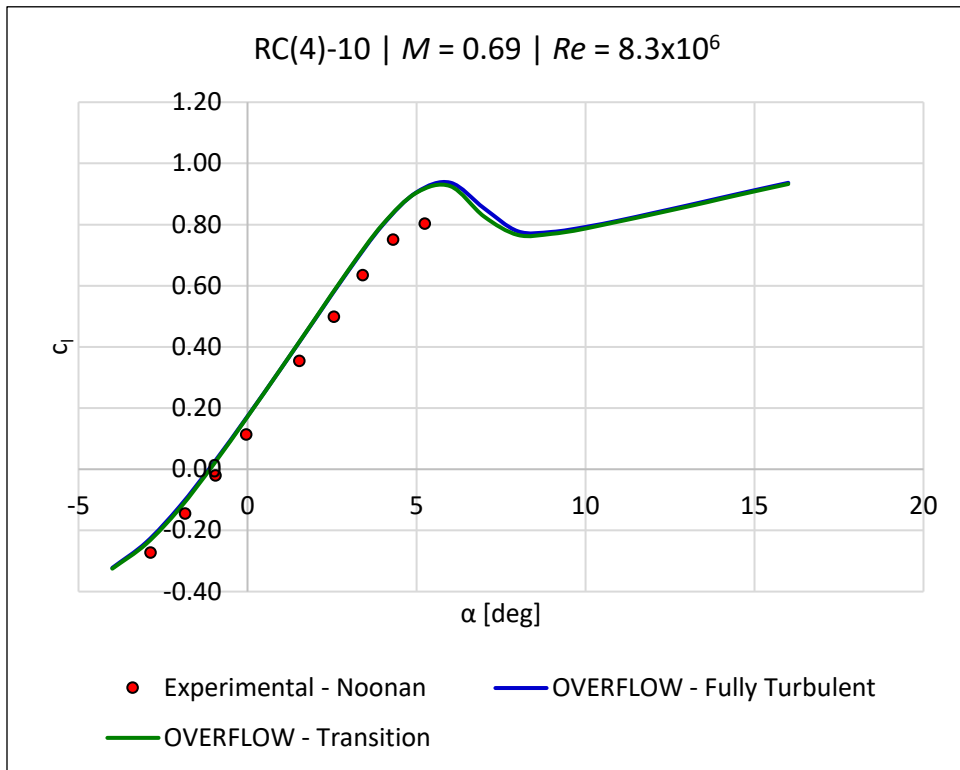


Figure C.14 RC(4)-10 lift curve at Mach 0.69 and a Reynolds number of  $8.3 \times 10^6$ .

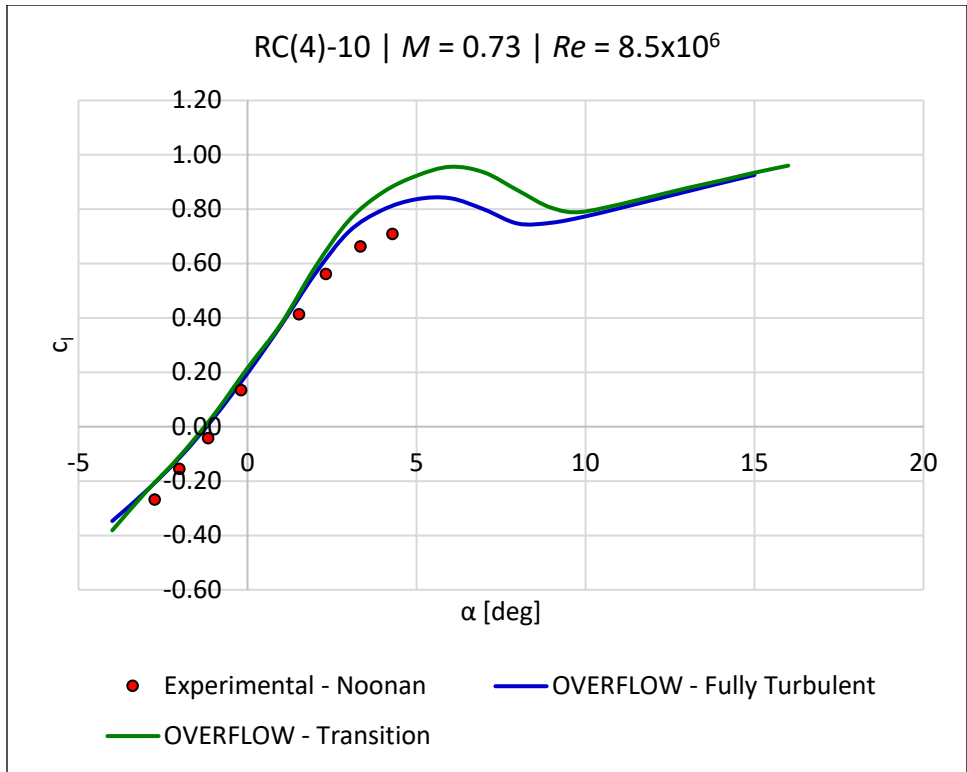


Figure C.15 RC(4)-10 lift curve at Mach 0.73 and a Reynolds number of  $8.5 \times 10^6$ .

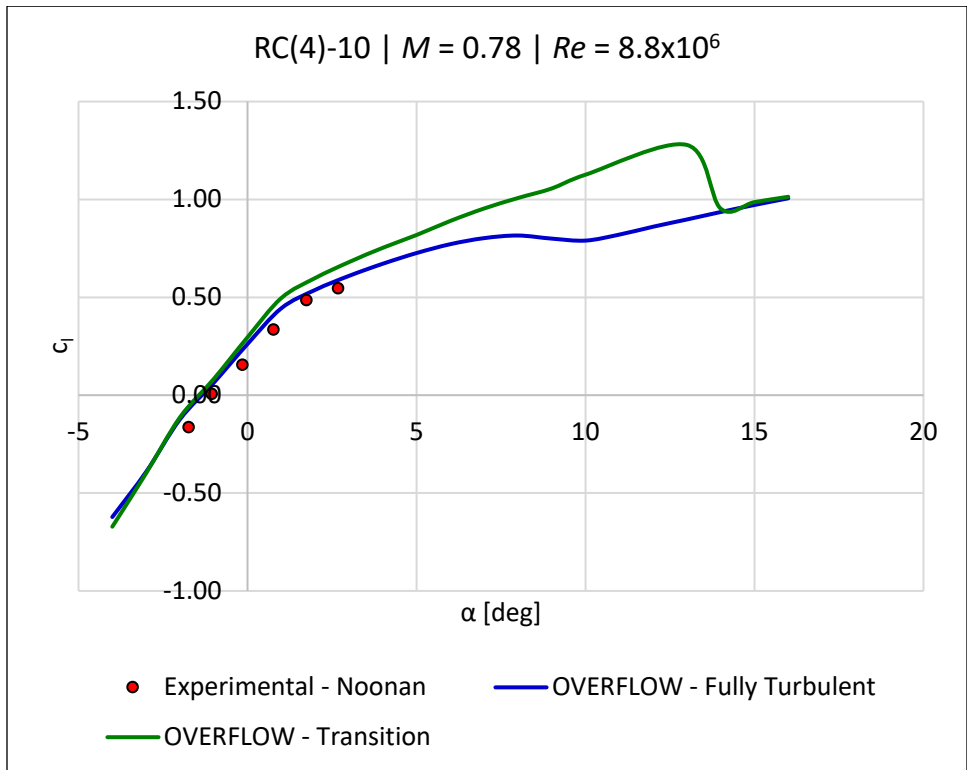


Figure C.16 RC(4)-10 lift curve at Mach 0.78 and a Reynolds number of  $8.8 \times 10^6$ .

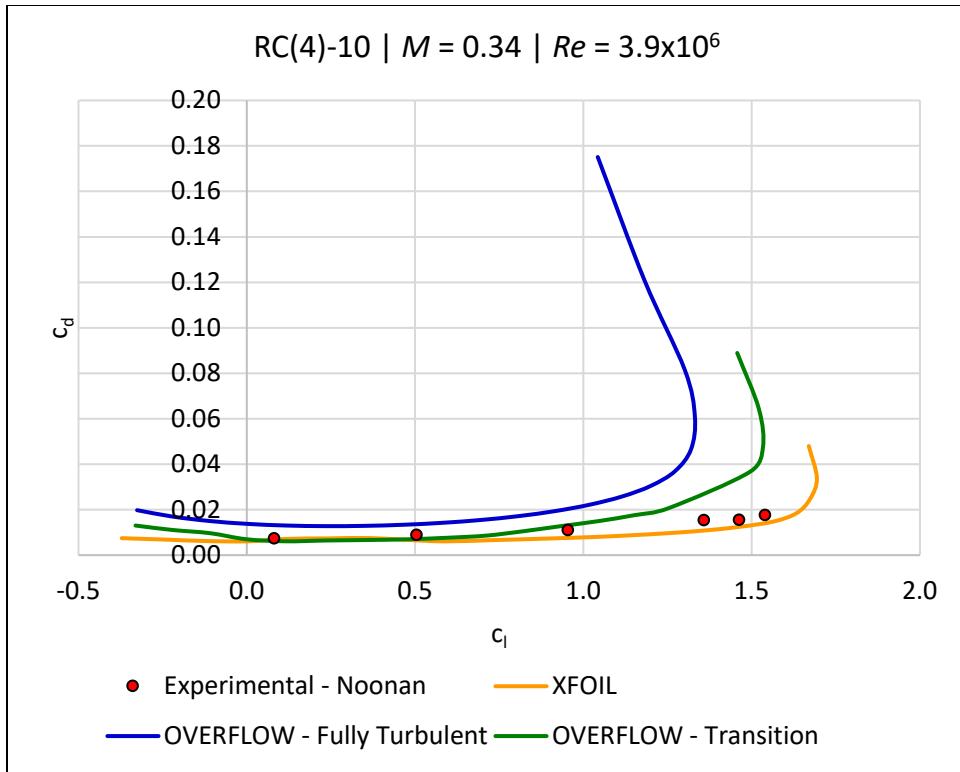


Figure C.17 RC(4)-10 drag bucket at Mach 0.34 and a Reynolds number of  $3.9 \times 10^6$ .

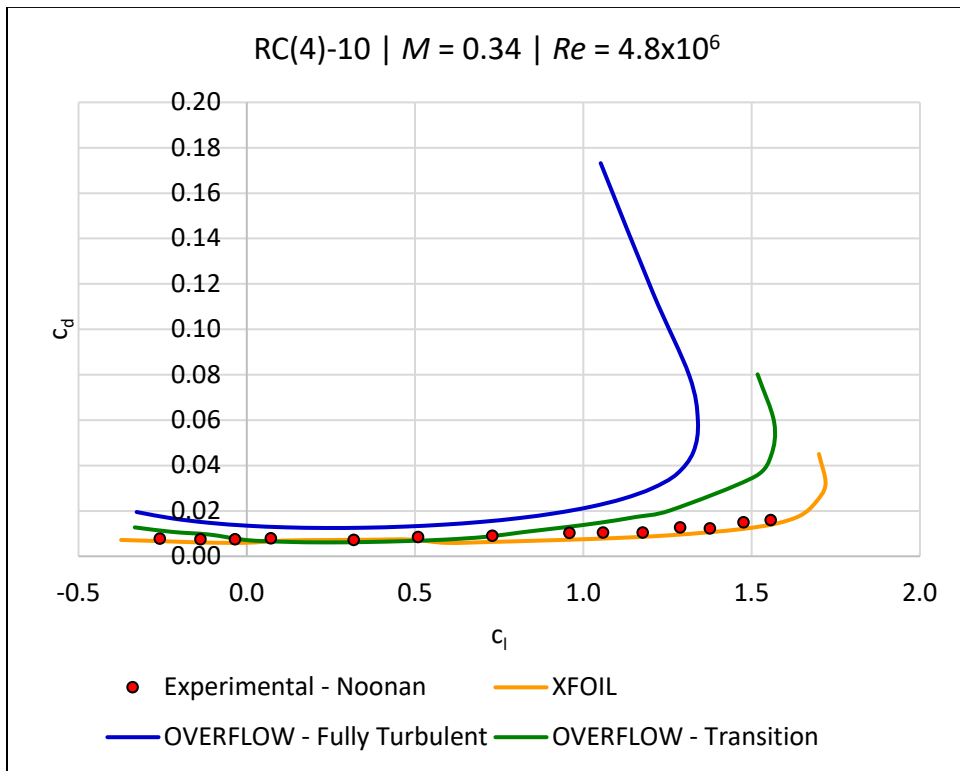


Figure C.18 RC(4)-10 drag bucket at Mach 0.34 and a Reynolds number of  $4.8 \times 10^6$ .

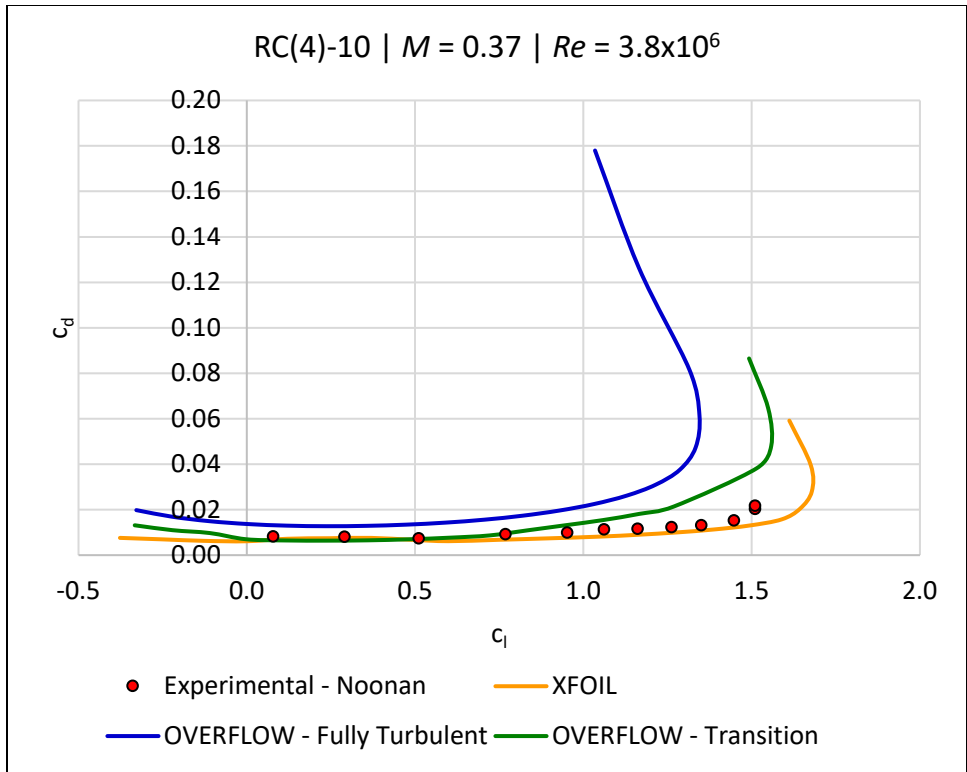


Figure C.19 RC(4)-10 drag bucket at Mach 0.37 and a Reynolds number of  $3.8 \times 10^6$ .

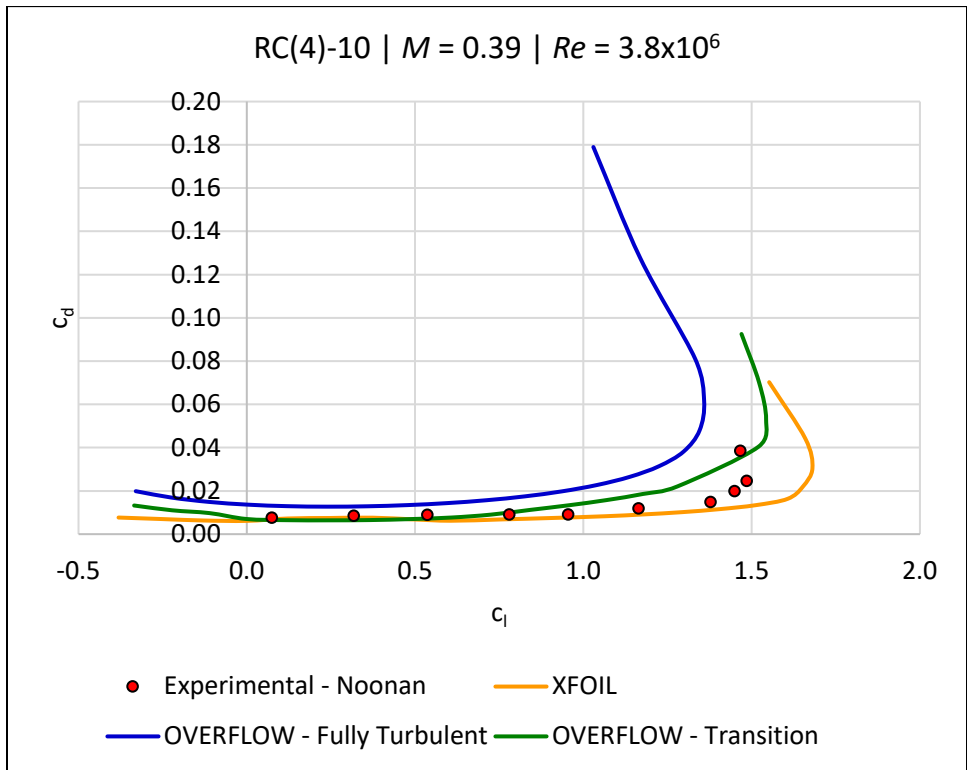


Figure C.20 RC(4)-10 drag bucket at Mach 0.39 and a Reynolds number of  $3.8 \times 10^6$ .

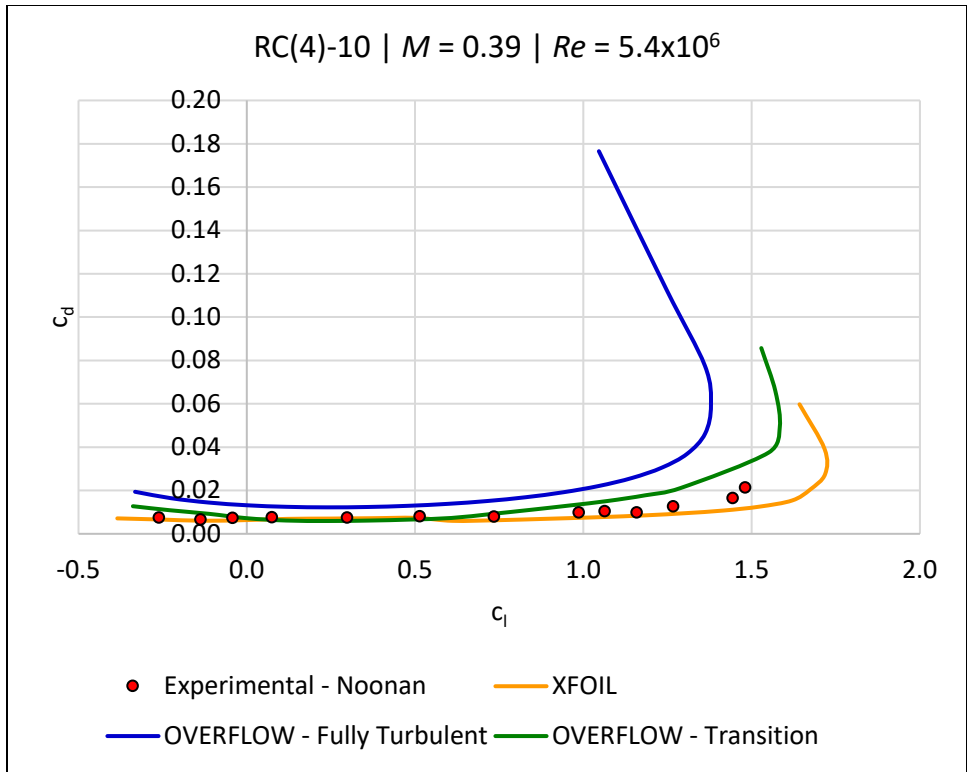


Figure C.21 RC(4)-10 drag bucket at Mach 0.39 and a Reynolds number of  $5.4 \times 10^6$ .

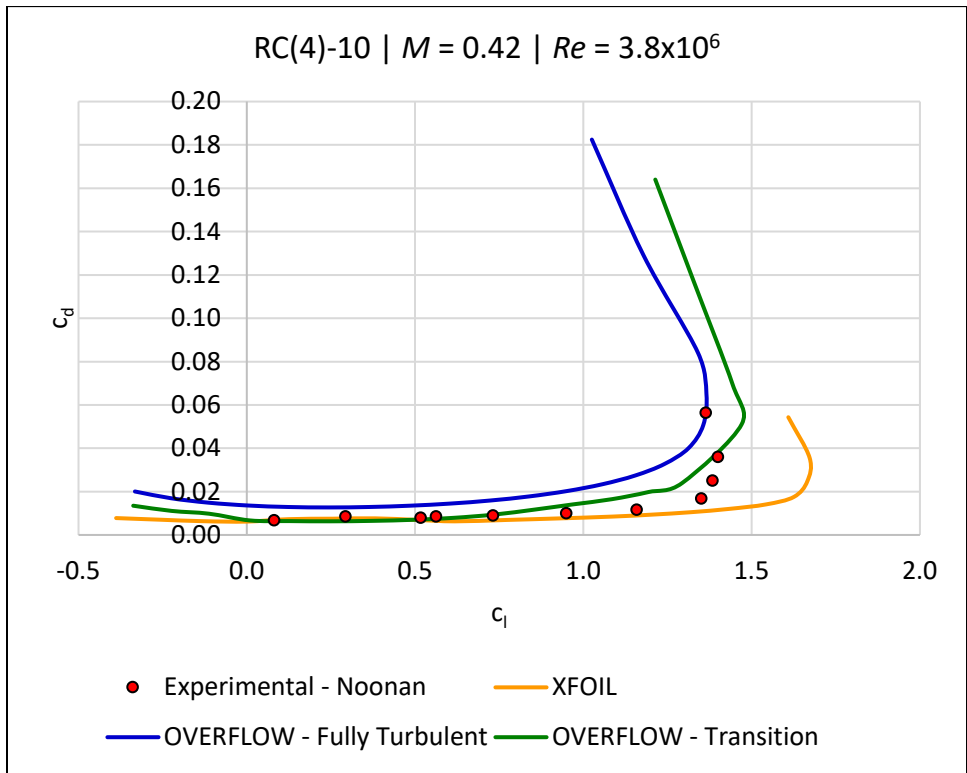


Figure C.22 RC(4)-10 drag bucket at Mach 0.42 and a Reynolds number of  $3.8 \times 10^6$ .

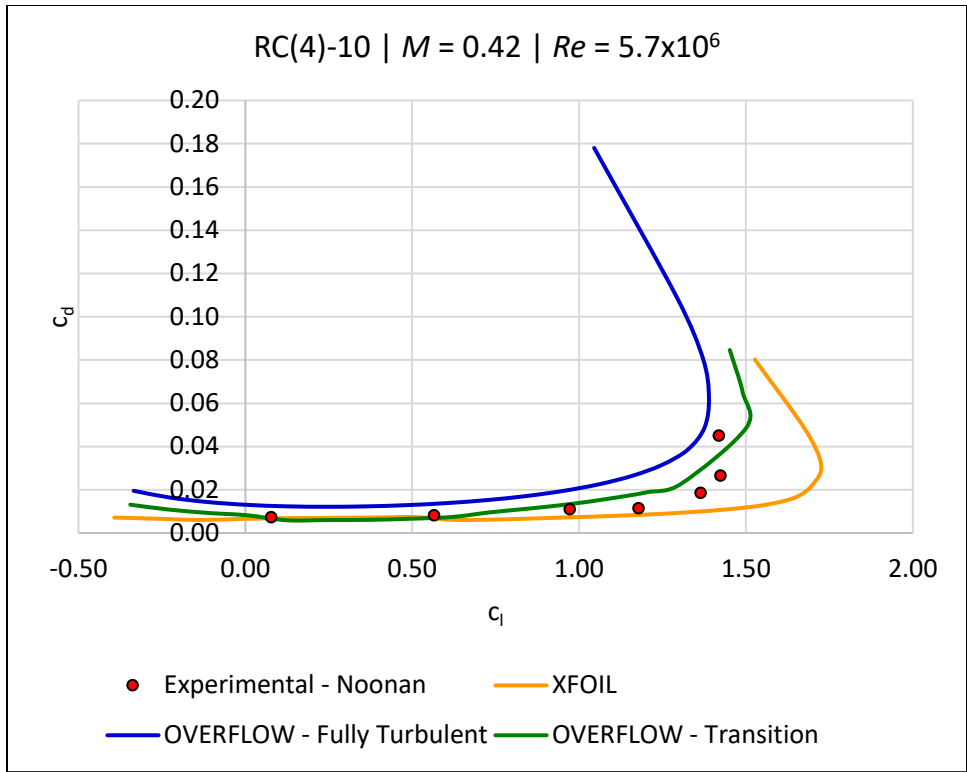


Figure C.23 RC(4)-10 drag bucket at Mach 0.42 and a Reynolds number of  $5.7 \times 10^6$ .

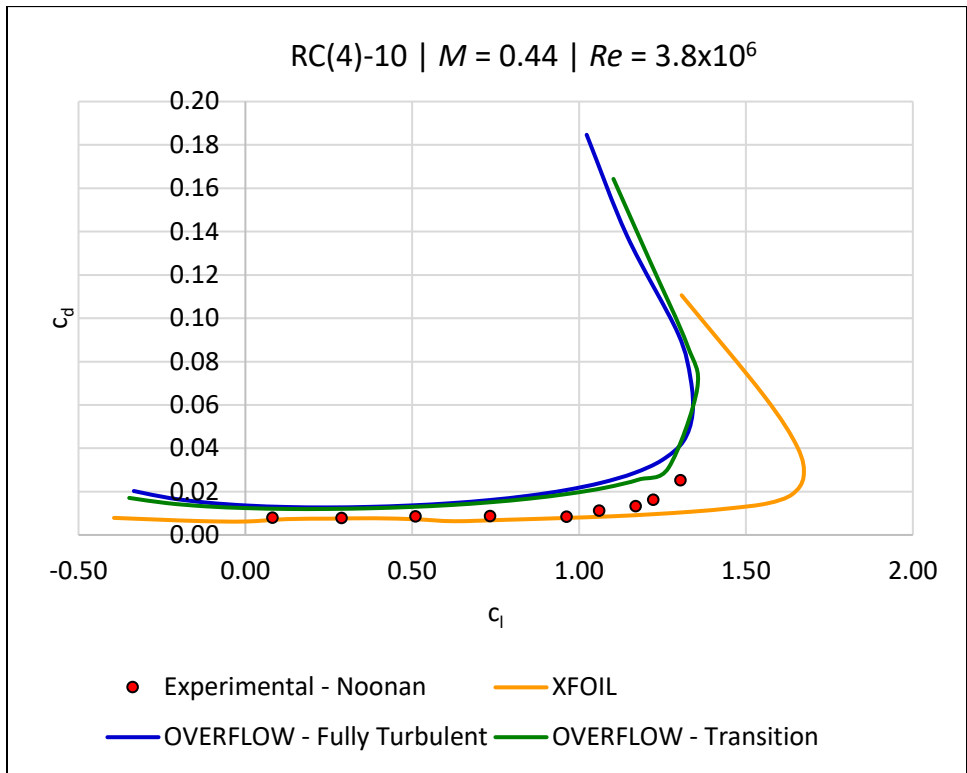


Figure C.24 RC(4)-10 drag bucket at Mach 0.44 and a Reynolds number of  $3.8 \times 10^6$ .

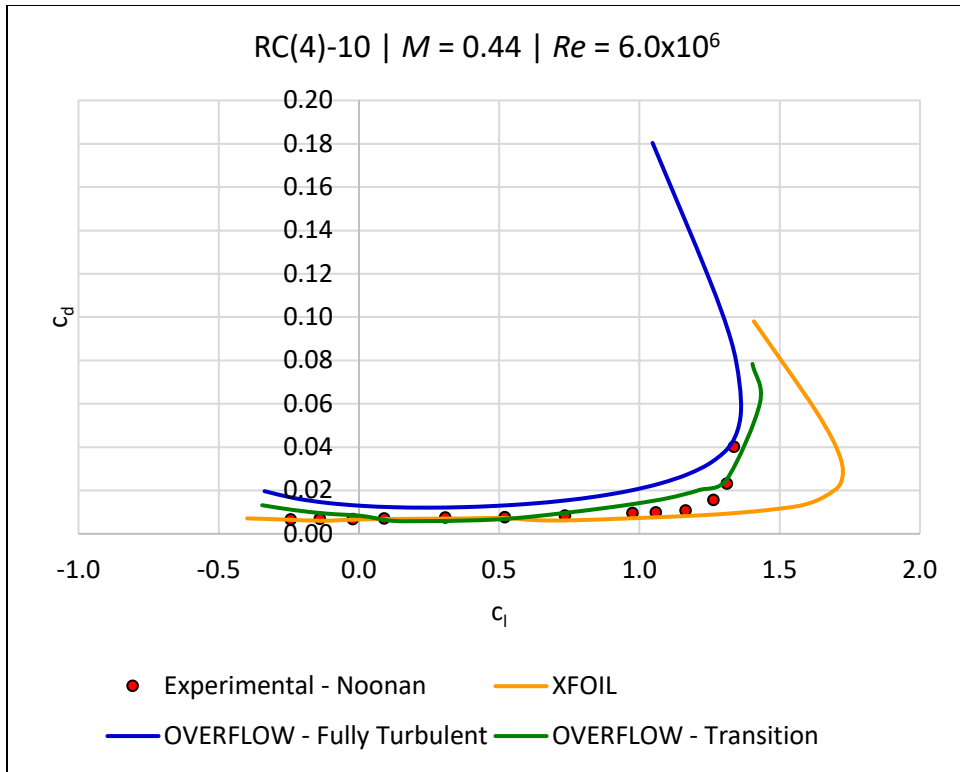


Figure C.25 RC(4)-10 drag bucket at Mach 0.44 and a Reynolds number of  $6.0 \times 10^6$ .

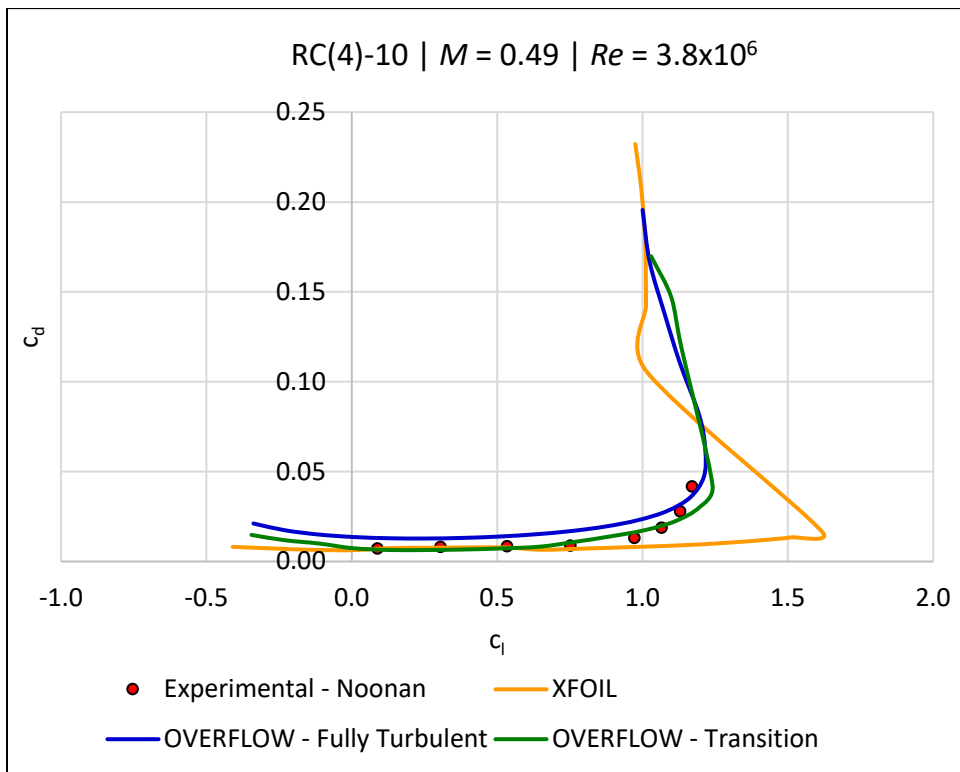


Figure C.26 RC(4)-10 drag bucket at Mach 0.49 and a Reynolds number of  $3.8 \times 10^6$ .

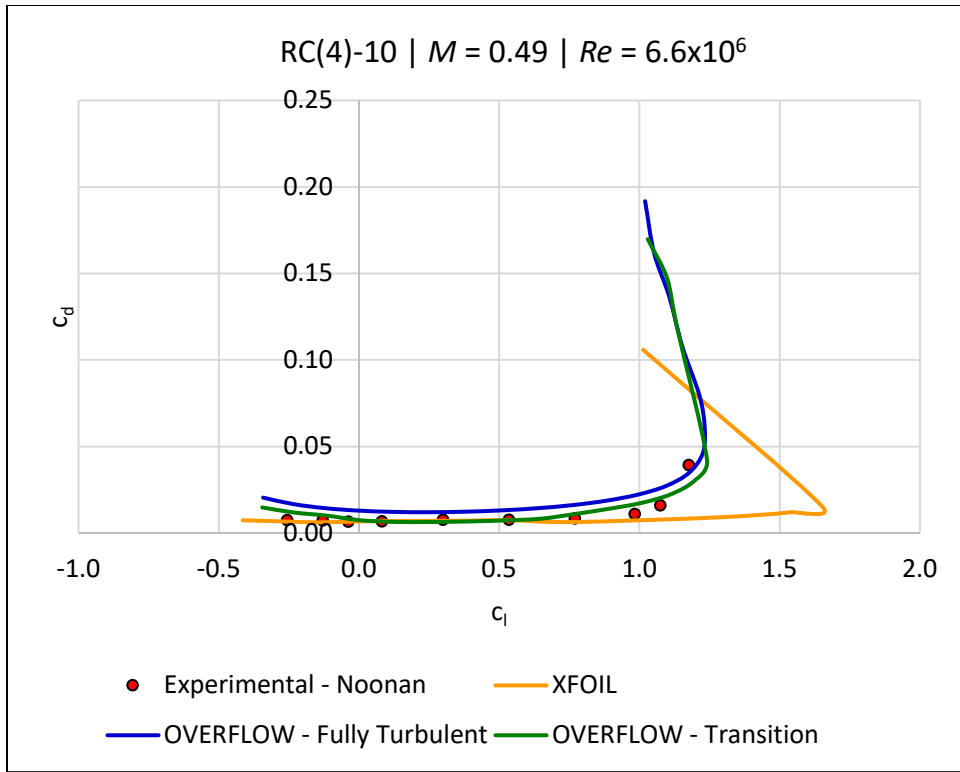


Figure C.27 RC(4)-10 drag bucket at Mach 0.49 and a Reynolds number of  $6.6 \times 10^6$ .

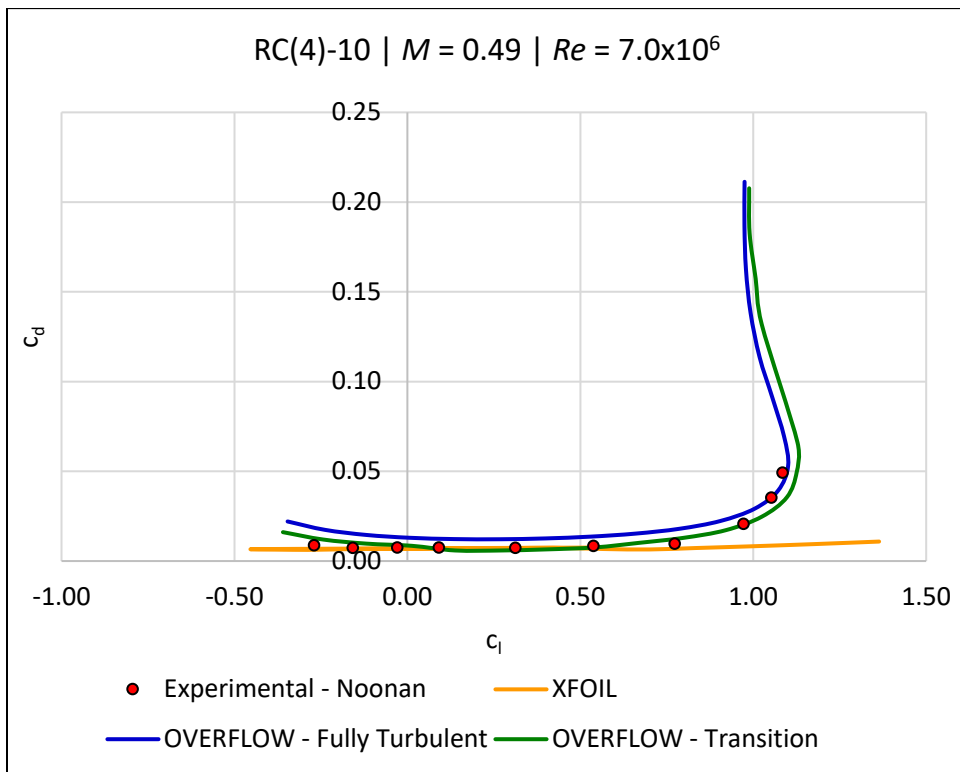


Figure C.28 RC(4)-10 drag bucket at Mach 0.54 and a Reynolds number of  $7.0 \times 10^6$ .

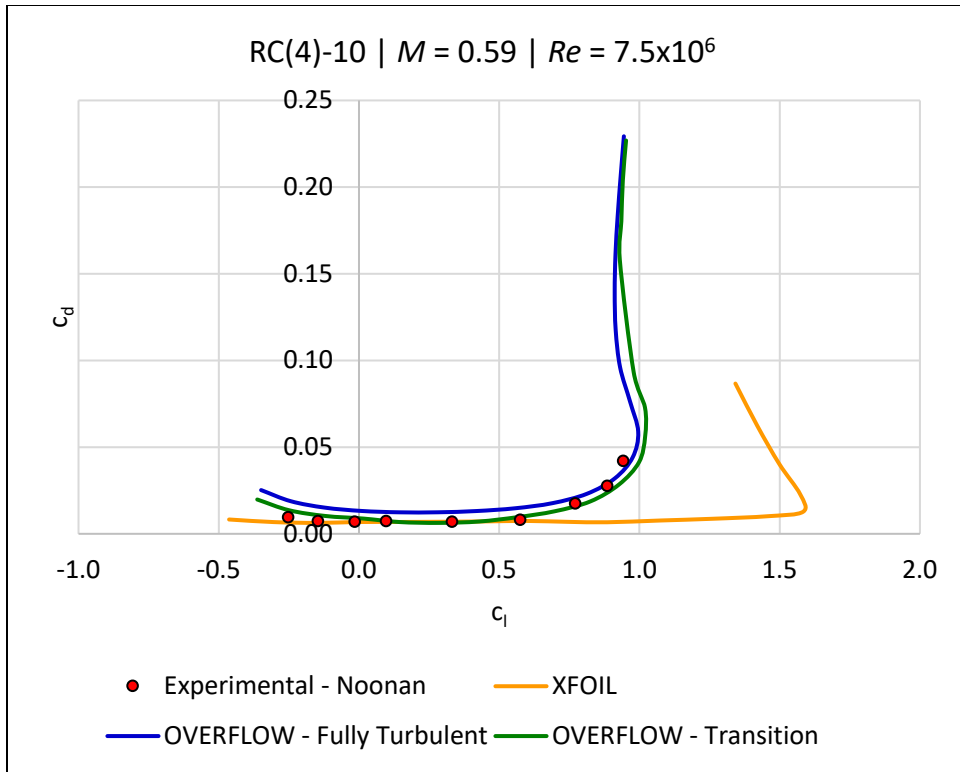


Figure C.29 RC(4)-10 drag bucket at Mach 0.59 and a Reynolds number of  $7.5 \times 10^6$ .

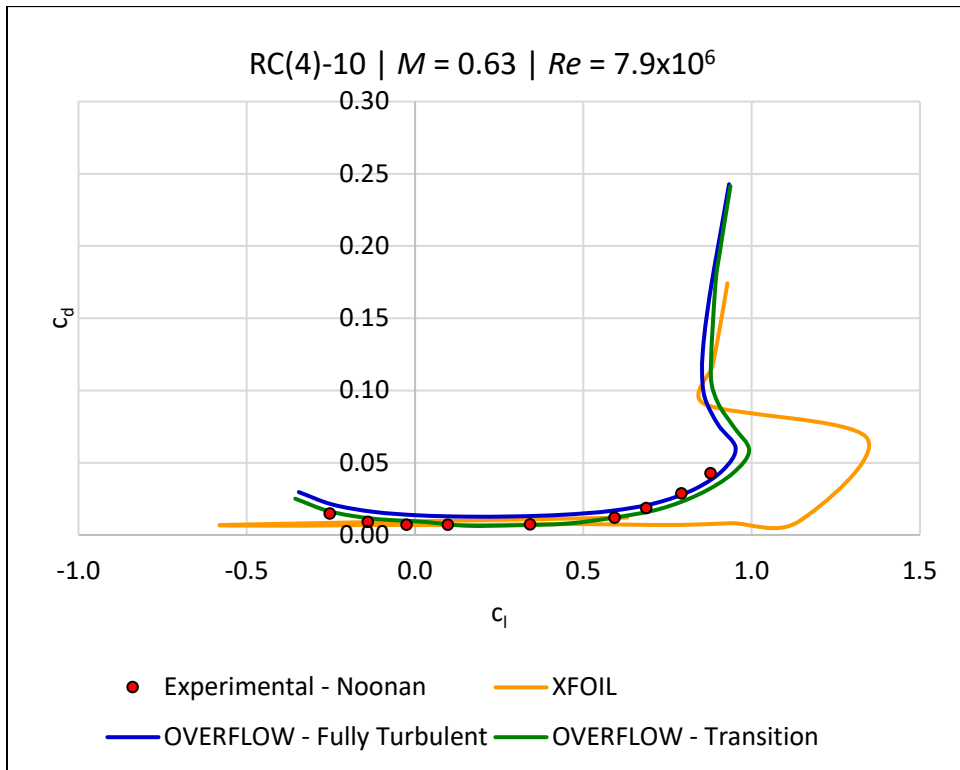


Figure C.30 RC(4)-10 drag bucket at Mach 0.63 and a Reynolds number of  $7.9 \times 10^6$ .

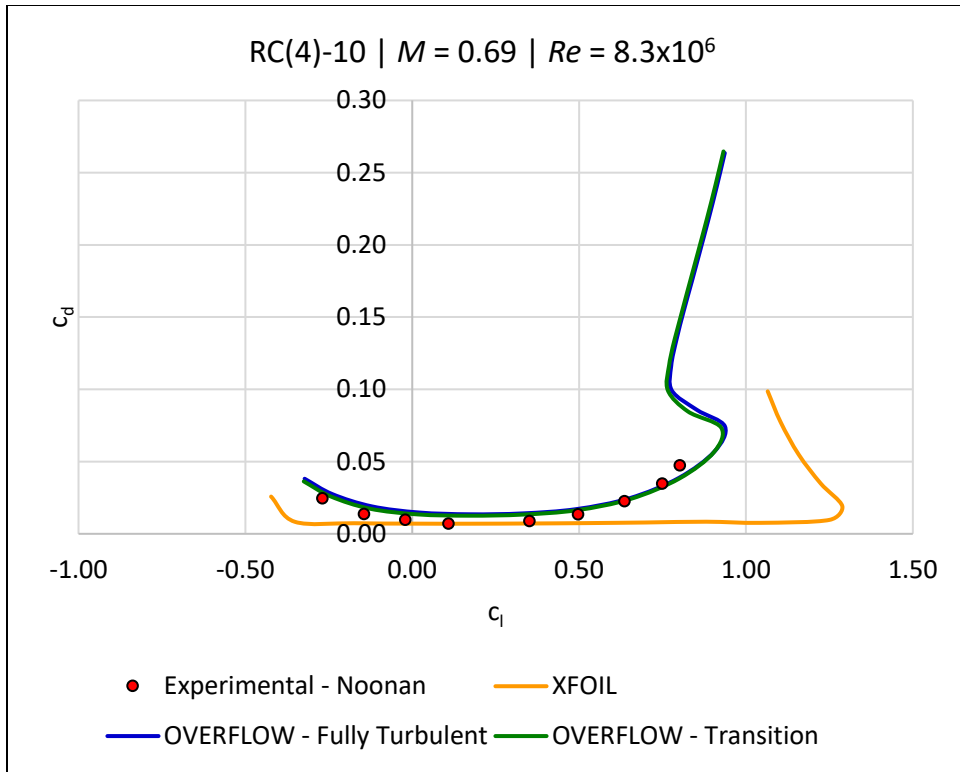


Figure C.31 RC(4)-10 drag bucket at Mach 0.69 and a Reynolds number of  $8.3 \times 10^6$ .

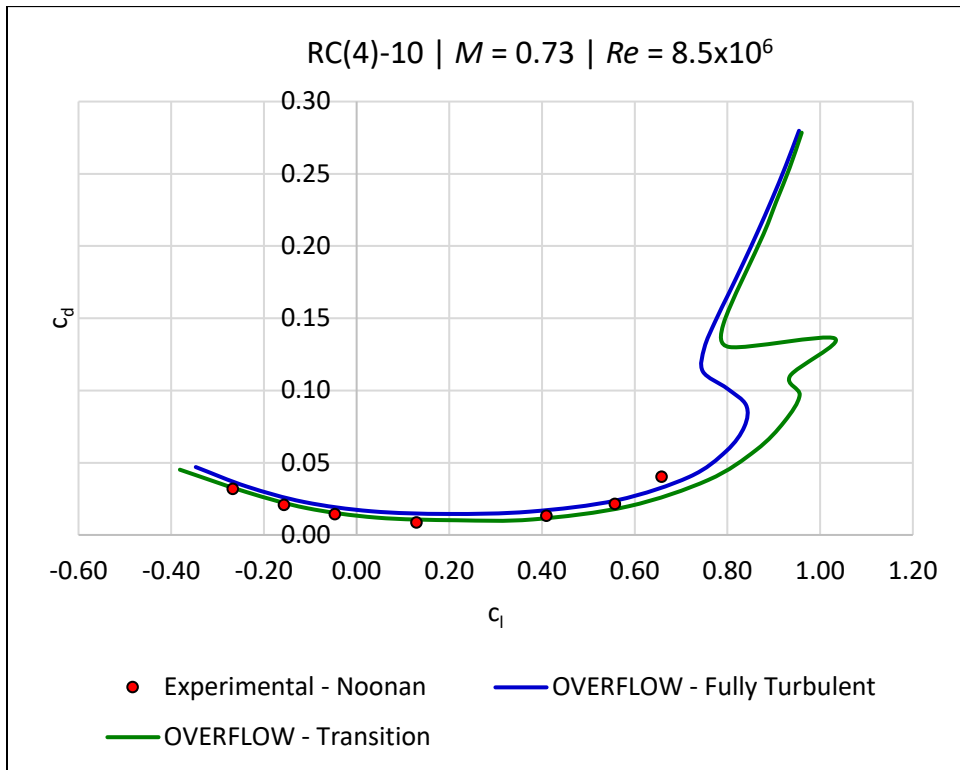


Figure C.32 RC(4)-10 drag bucket at Mach 0.73 and a Reynolds number of  $8.5 \times 10^6$ .

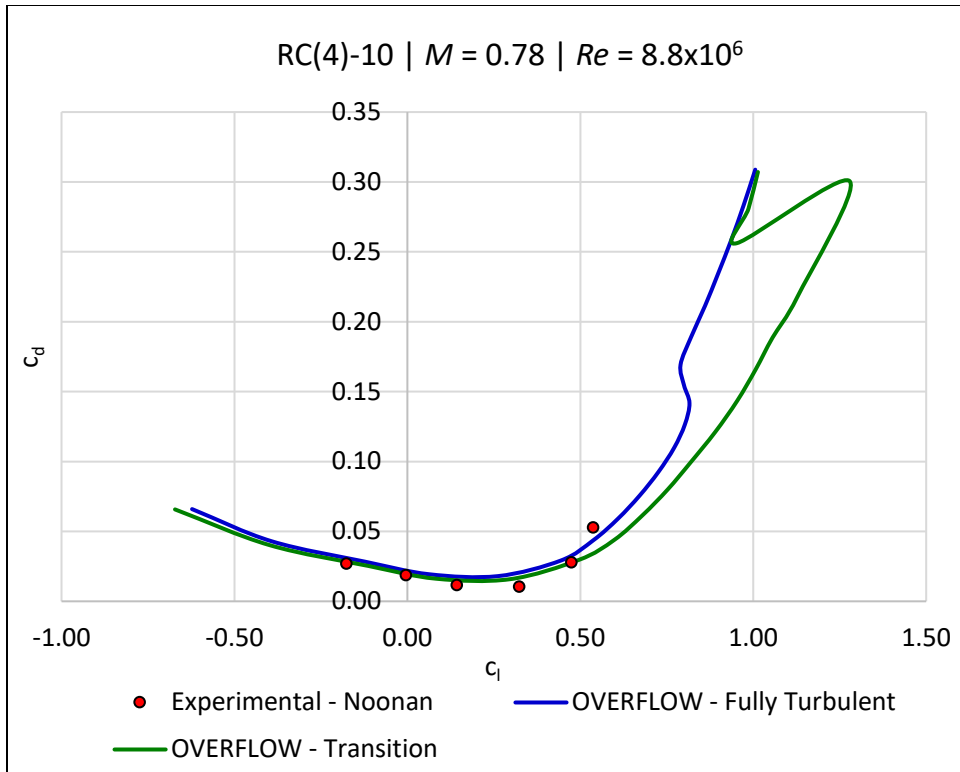


Figure C.33 RC(4)-10 drag bucket at Mach 0.78 and a Reynolds number of  $8.8 \times 10^6$ .

## Appendix D - SSC-A09 XFOIL and OVERFLOW Results

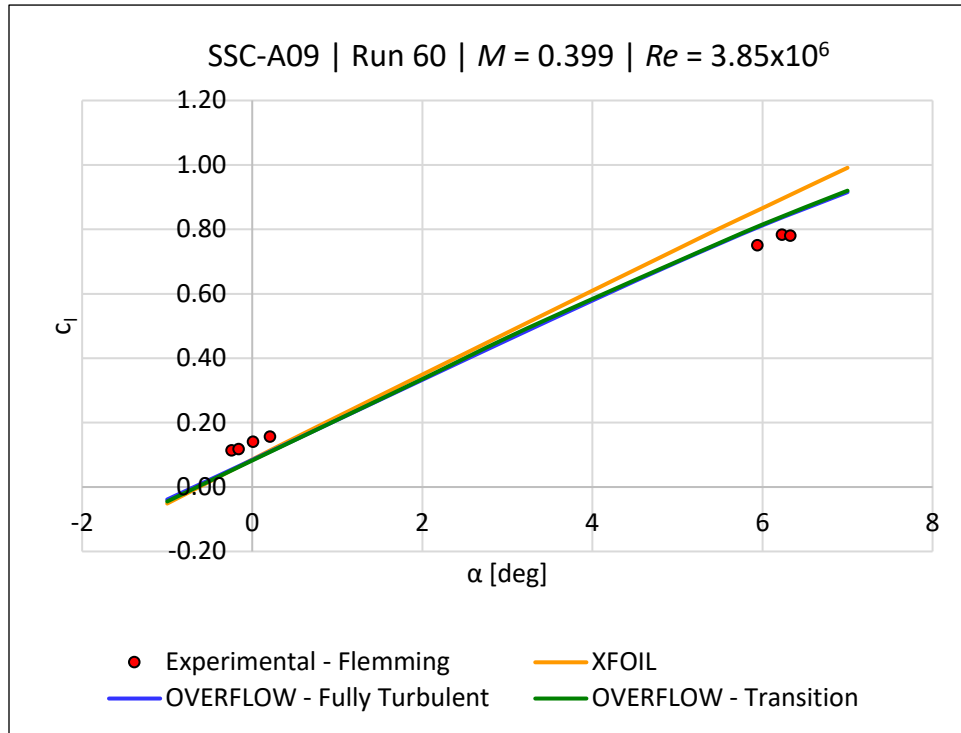


Figure D.1 SSC-A09, Run 60, Mach 0.399,  $Re\ 3.85 \times 10^6$ : lift coefficient versus  $\alpha$ .



Figure D.2 SSC-A09, Run 61, Mach 0.307,  $Re\ 4.29 \times 10^6$ : lift coefficient versus  $\alpha$ .

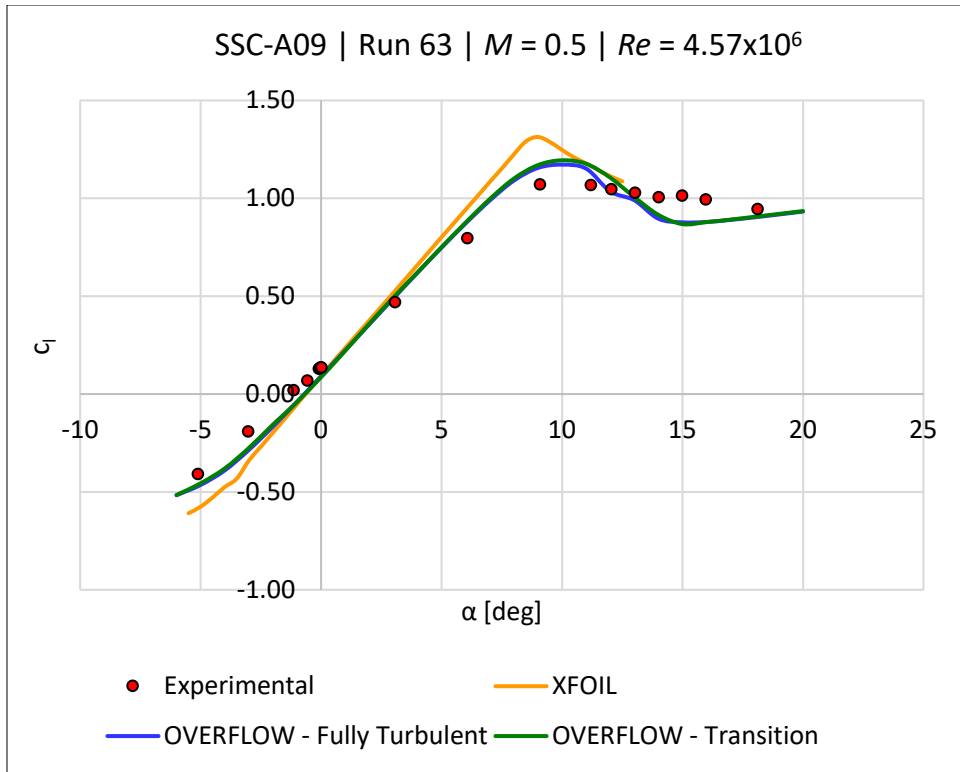


Figure D.3 SSC-A09, Run 63, Mach 0.5,  $Re\ 4.57 \times 10^6$ : lift coefficient versus  $\alpha$ .

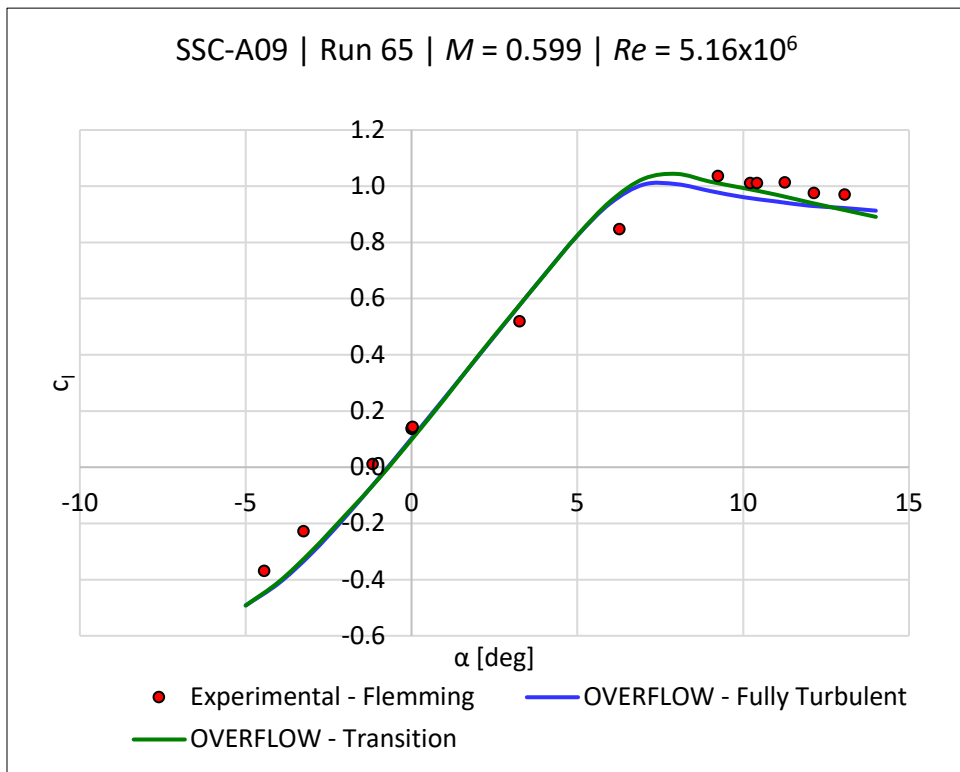


Figure D.4 SSC-A09, Run 65, Mach 0.599,  $Re\ 5.16 \times 10^6$ : lift coefficient versus  $\alpha$ .

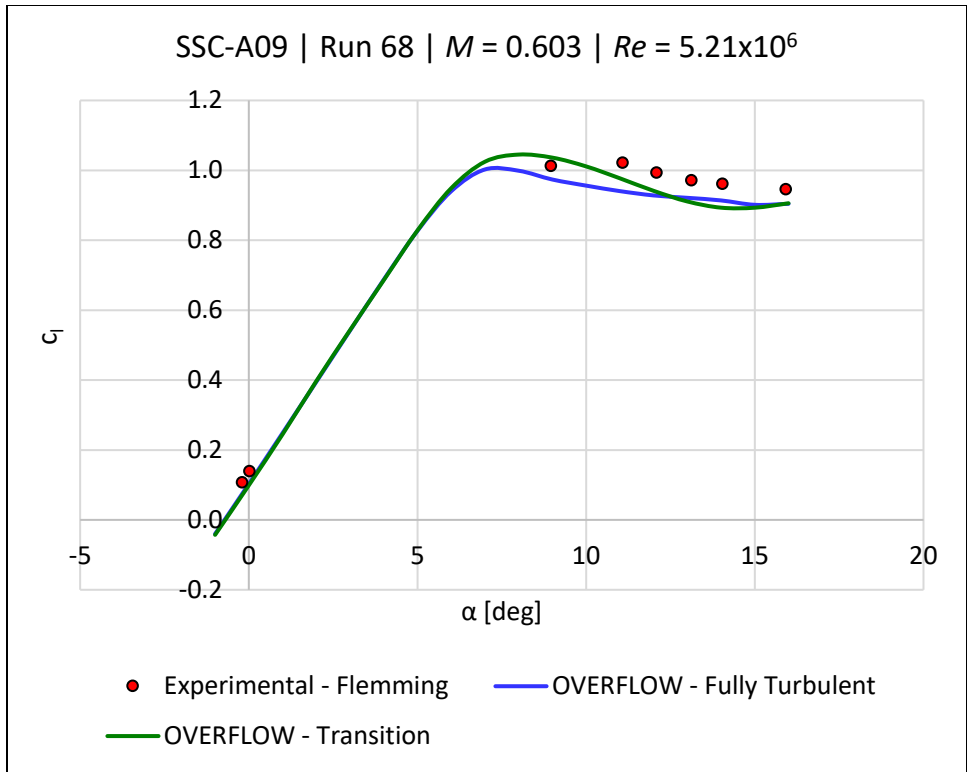


Figure D.5 SSC-A09, Run 68, Mach 0.603,  $Re\ 5.21 \times 10^6$ : lift coefficient versus  $\alpha$ .

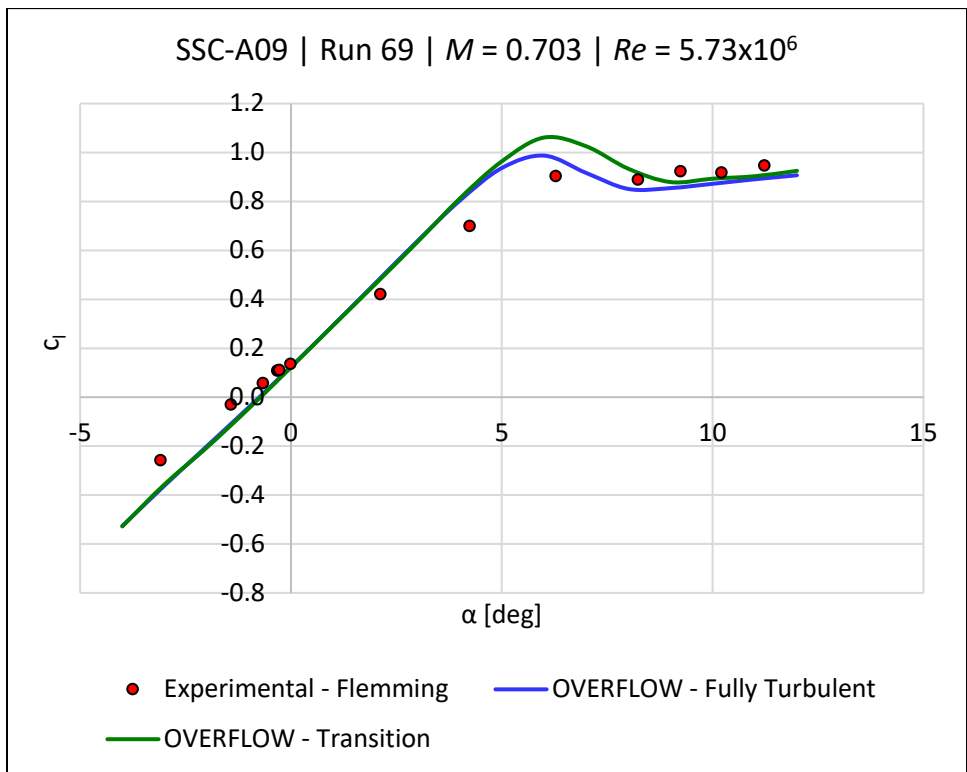


Figure D.6 SSC-A09, Run 69, Mach 0.703,  $Re\ 5.73 \times 10^6$ : lift coefficient versus  $\alpha$ .

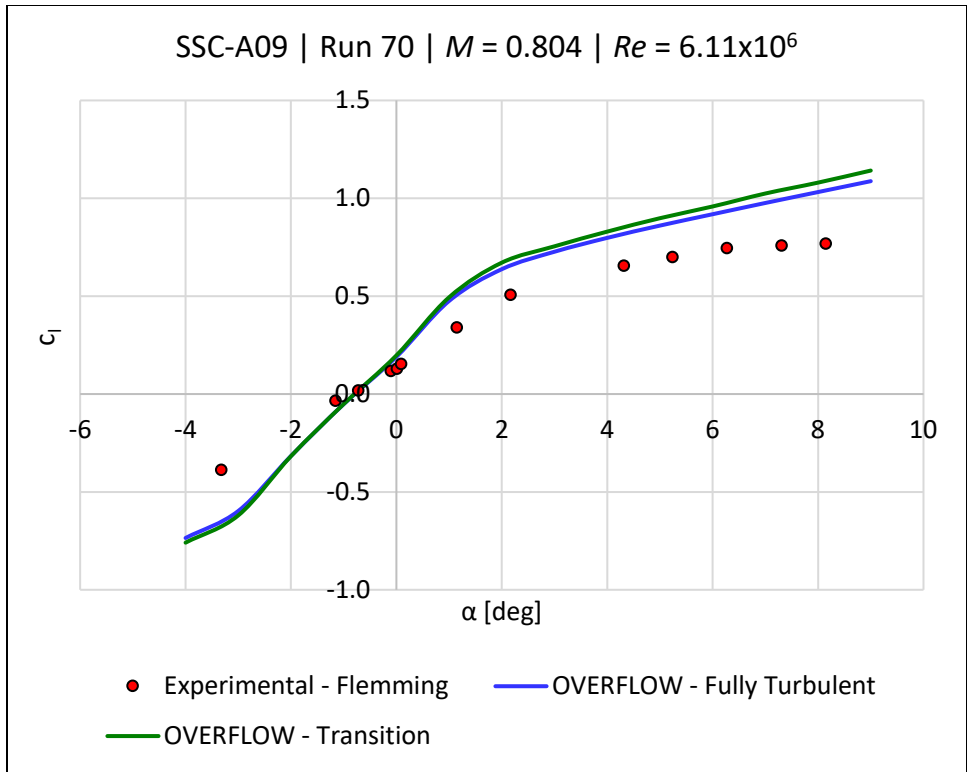


Figure D.7 SSC-A09, Run 70, Mach 0.804,  $Re\ 6.11 \times 10^6$ : lift coefficient versus  $\alpha$ .

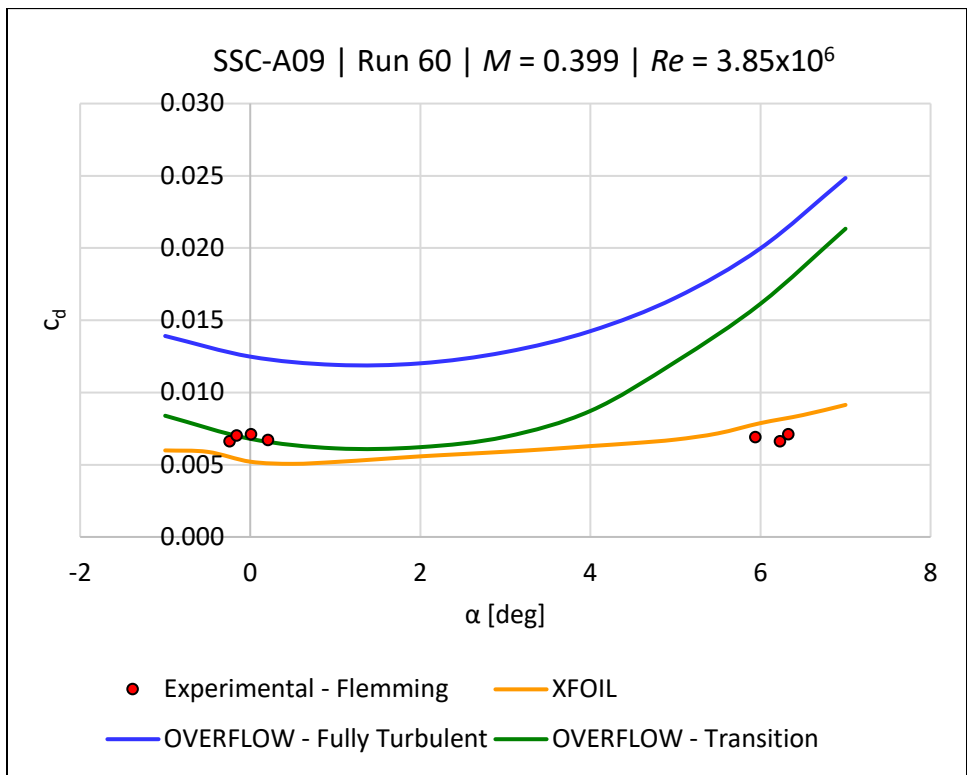


Figure D.8 SSC-A09, Run 60, Mach 0.399,  $Re\ 3.85 \times 10^6$ : drag coefficient versus  $\alpha$ .

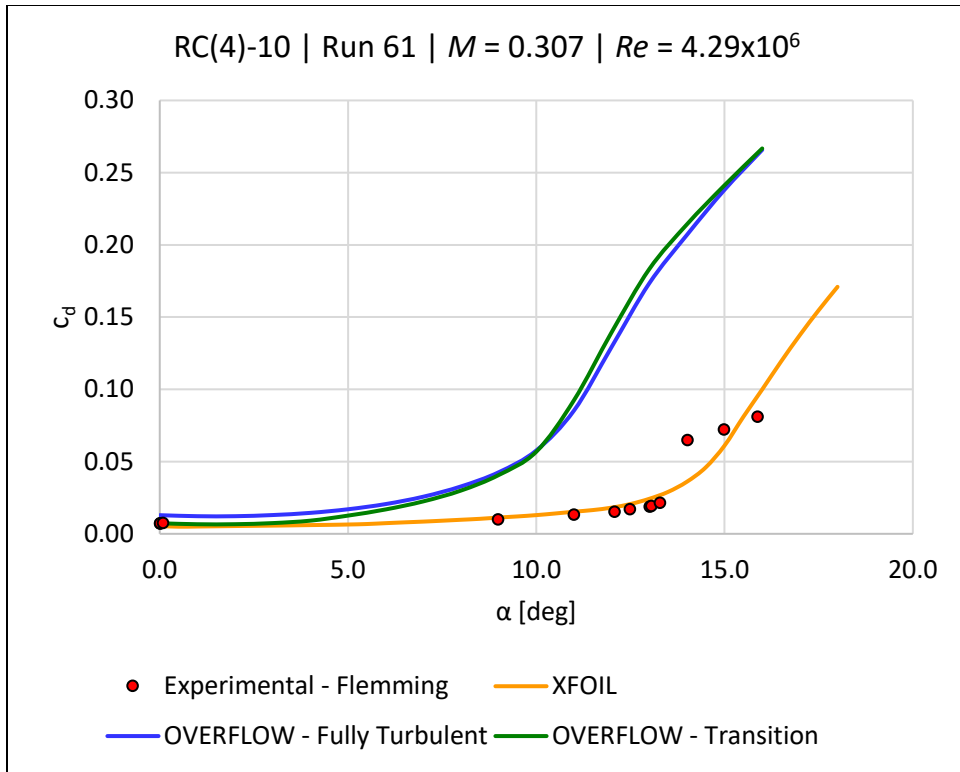


Figure D.9 SSC-A09, Run 61, Mach 0.307,  $Re\ 4.29 \times 10^6$ : drag coefficient versus  $\alpha$ .

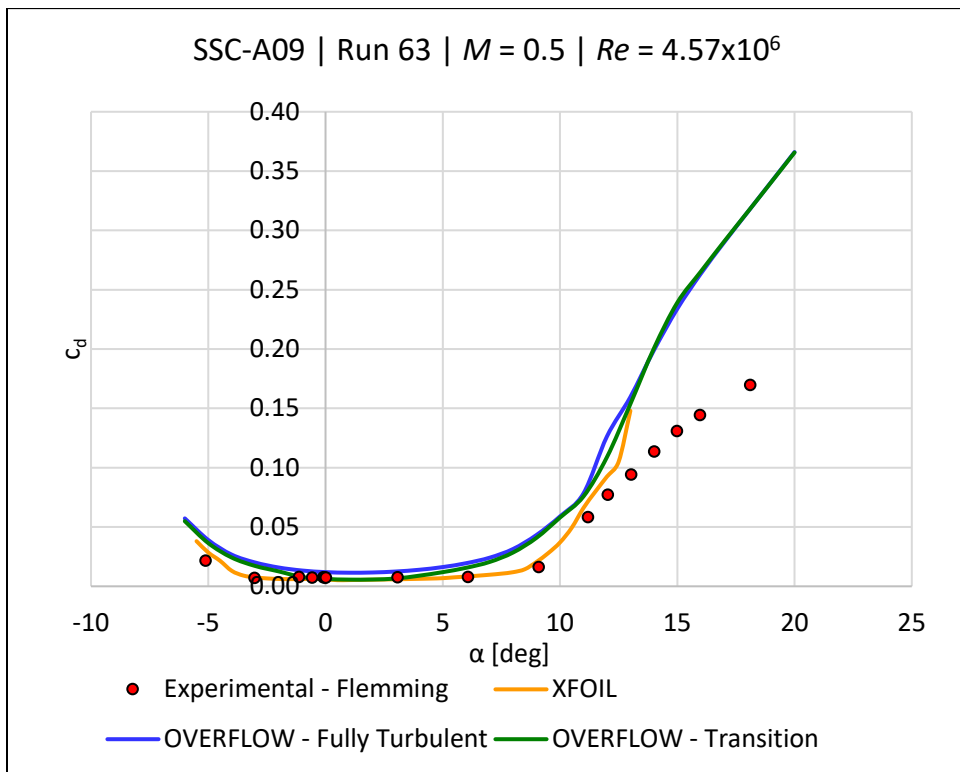


Figure D.10 SSC-A09, Run 63, Mach 0.5,  $Re\ 4.57 \times 10^6$ : drag coefficient versus  $\alpha$ .

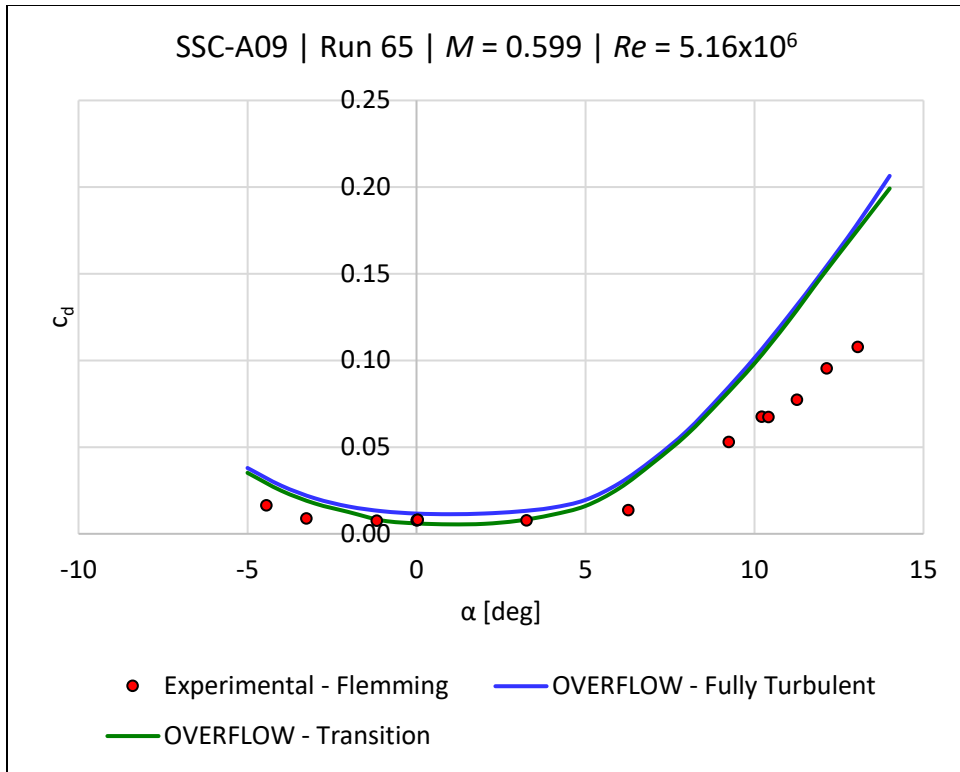


Figure D.11 SSC-A09, Run 65,  $M = 0.599$ ,  $Re = 5.16 \times 10^6$ : drag coefficient versus  $\alpha$ .

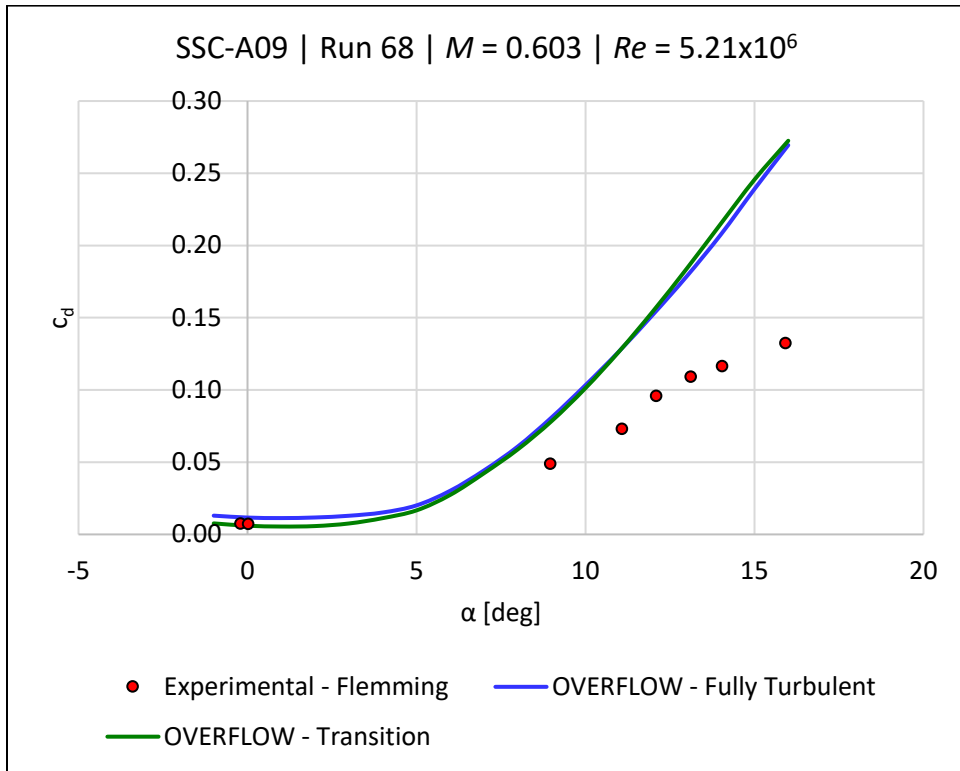


Figure D.12 SSC-A09, Run 68,  $M = 0.603$ ,  $Re = 5.21 \times 10^6$ : drag coefficient versus  $\alpha$ .

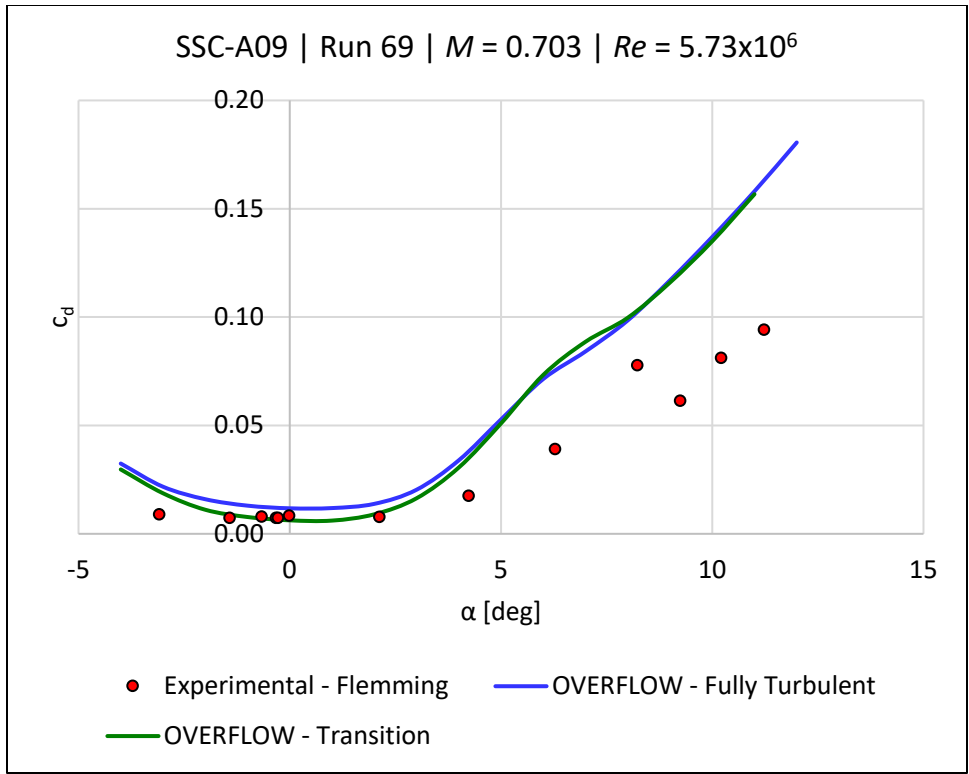


Figure D.13 SSC-A09, Run 69,  $M = 0.703$ ,  $Re = 5.73 \times 10^6$ : drag coefficient versus  $\alpha$ .

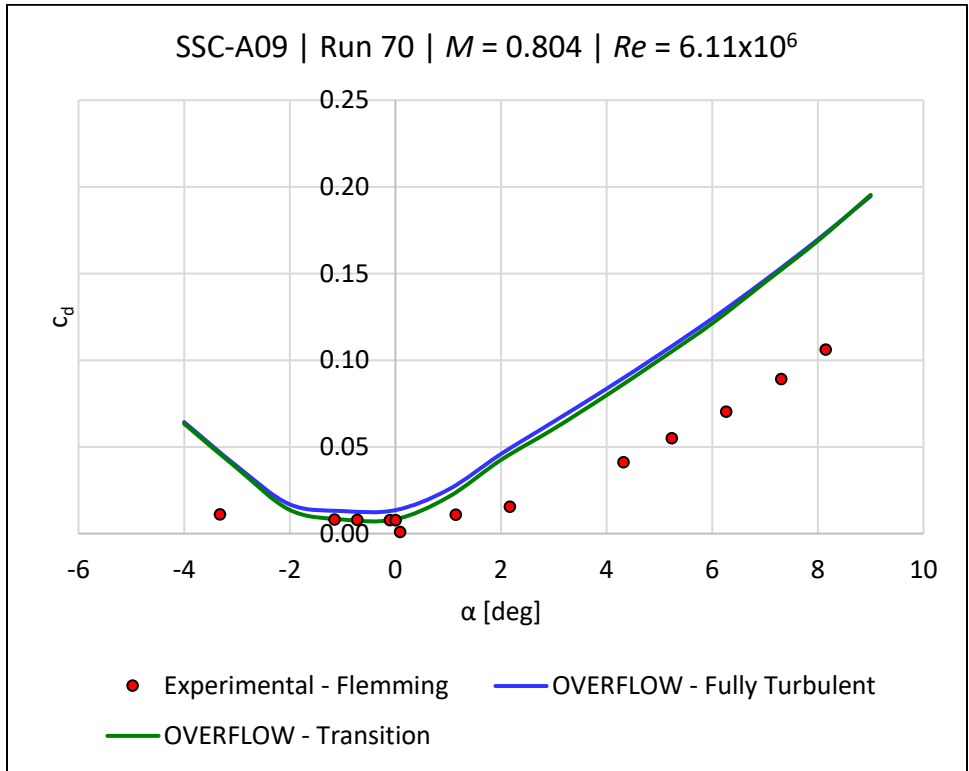


Figure D.14 SSC-A09, Run 70, Mach 0.804,  $Re = 6.11 \times 10^6$ : drag coefficient versus  $\alpha$ .

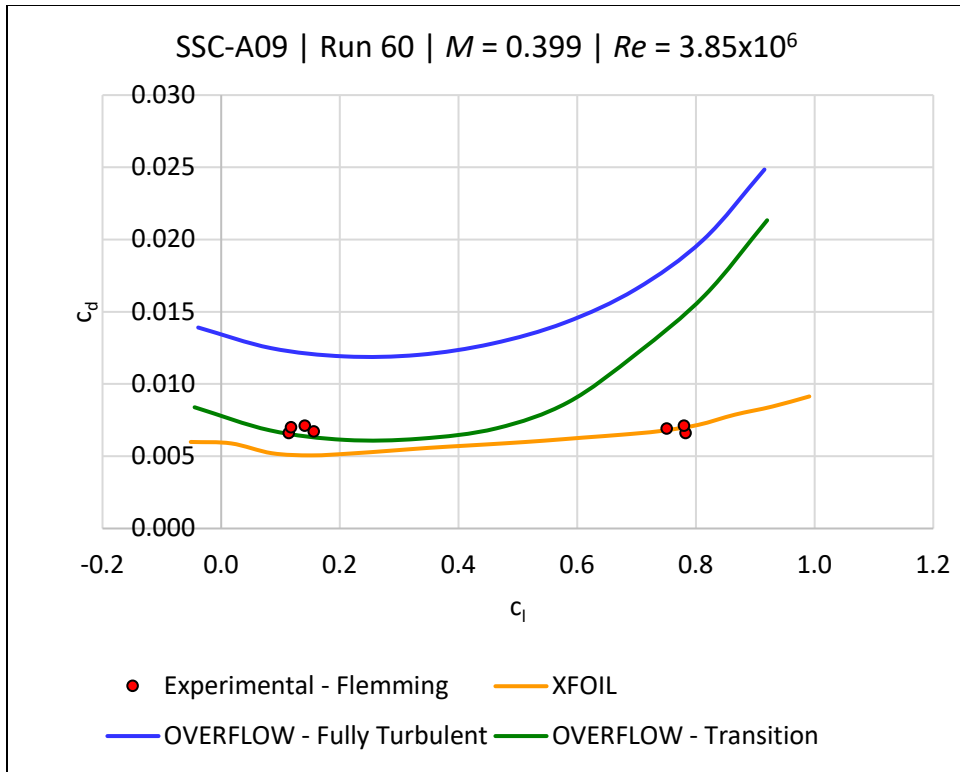


Figure D.15 SSC-A09, Run 60,  $M = 0.399$ ,  $Re = 3.85 \times 10^6$ :  $c_l$  vs  $c_d$ .

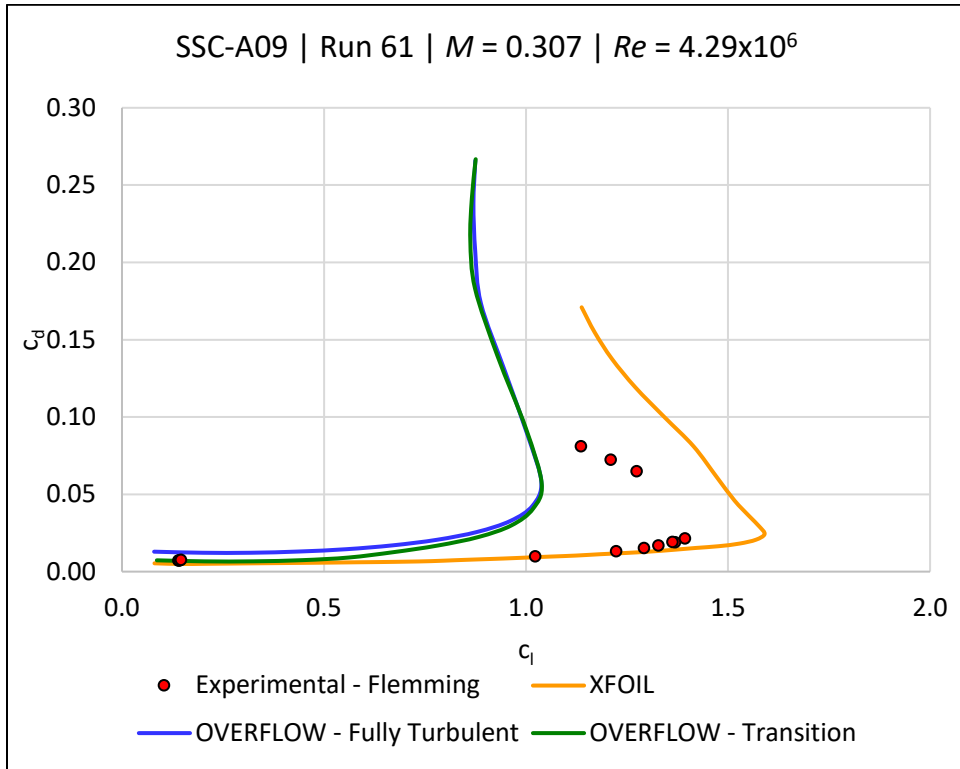


Figure D.16 SSC-A09, Run 61,  $M = 0.307$ ,  $Re = 4.29 \times 10^6$ :  $c_l$  vs  $c_d$ .

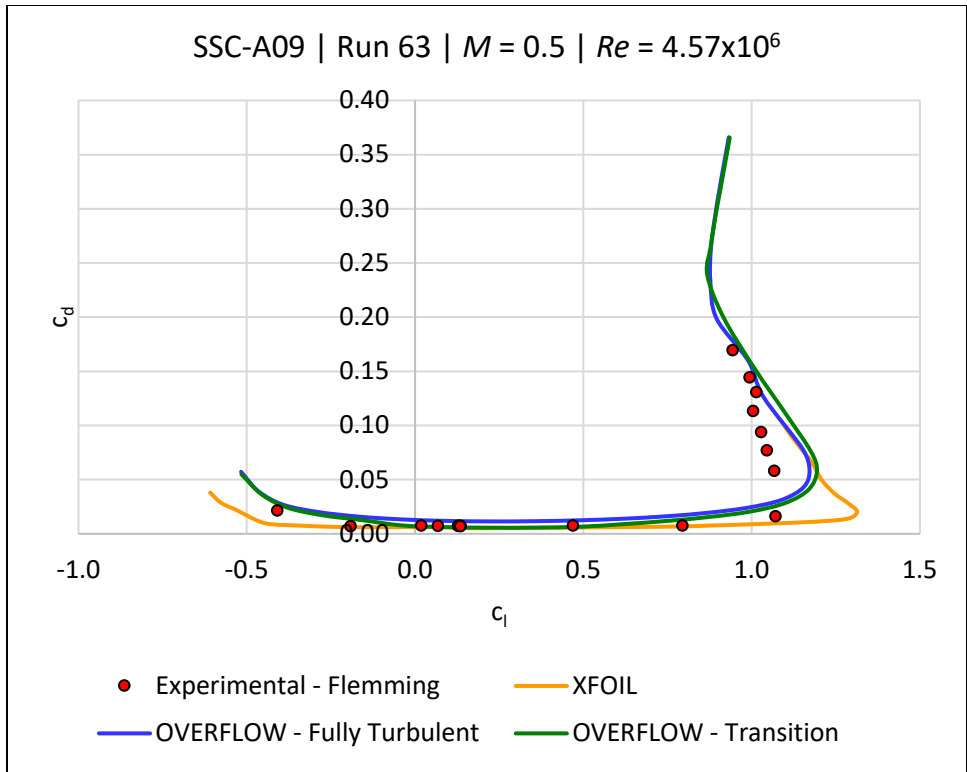


Figure D.17 SSC-A09, Run 63,  $M = 0.5$ ,  $Re = 4.57 \times 10^6$ :  $c_l$  vs  $c_d$ .

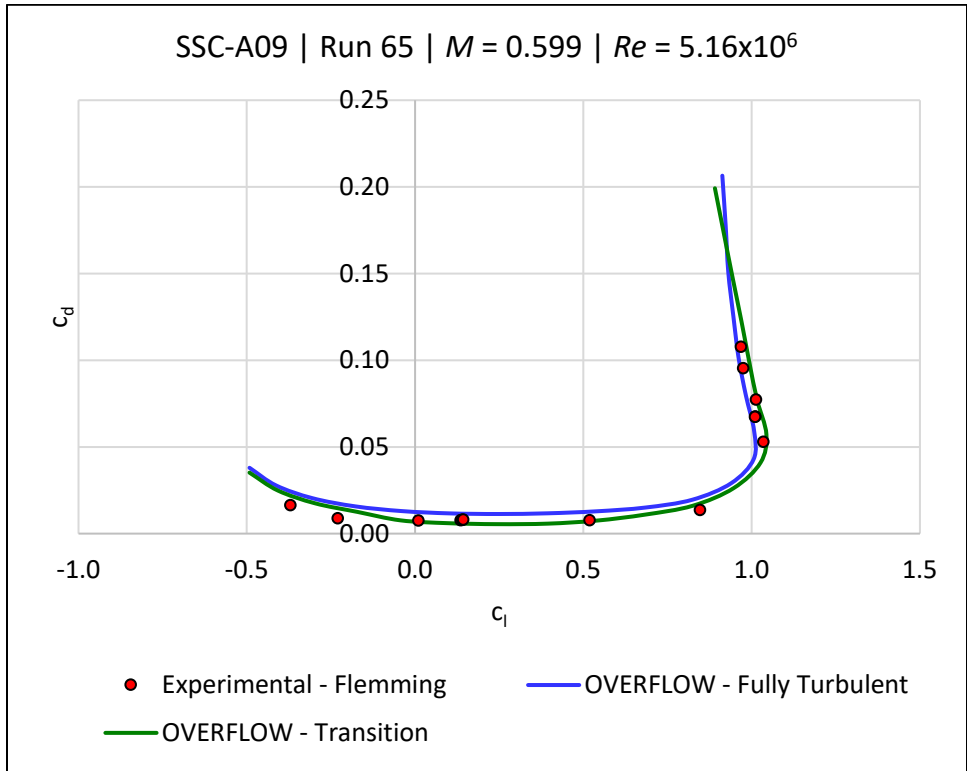


Figure D.18 SSC-A09, Run 65, Mach 0.599,  $Re = 5.16 \times 10^6$ :  $c_l$  vs  $c_d$ .

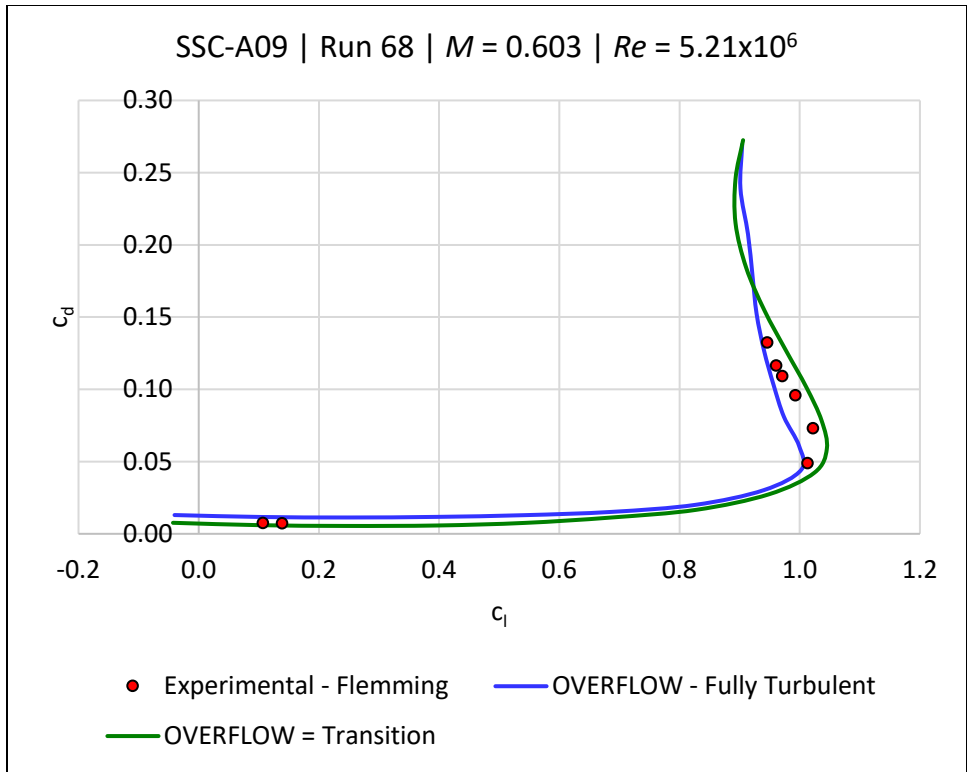


Figure D.19 SSC-A09, Run 68,  $M = 0.603$ ,  $Re = 5.21 \times 10^6$ :  $c_l$  vs  $c_d$ .

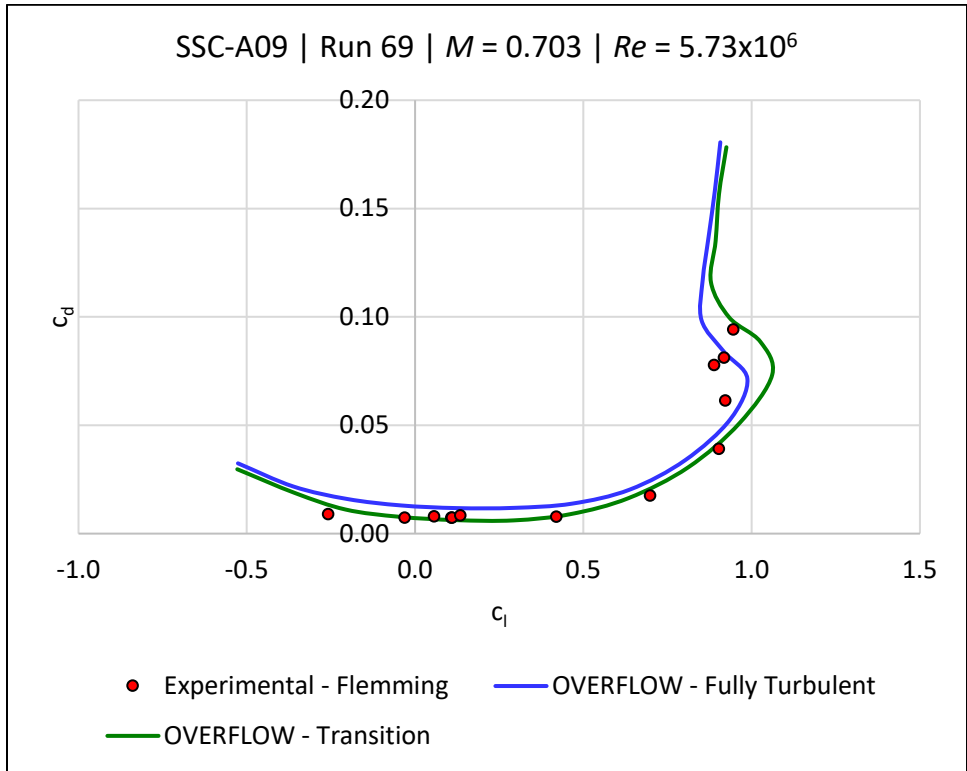


Figure D.20 SSC-A09, Run 69,  $M = 0.703$ ,  $Re = 5.73 \times 10^6$ :  $c_l$  vs  $c_d$ .

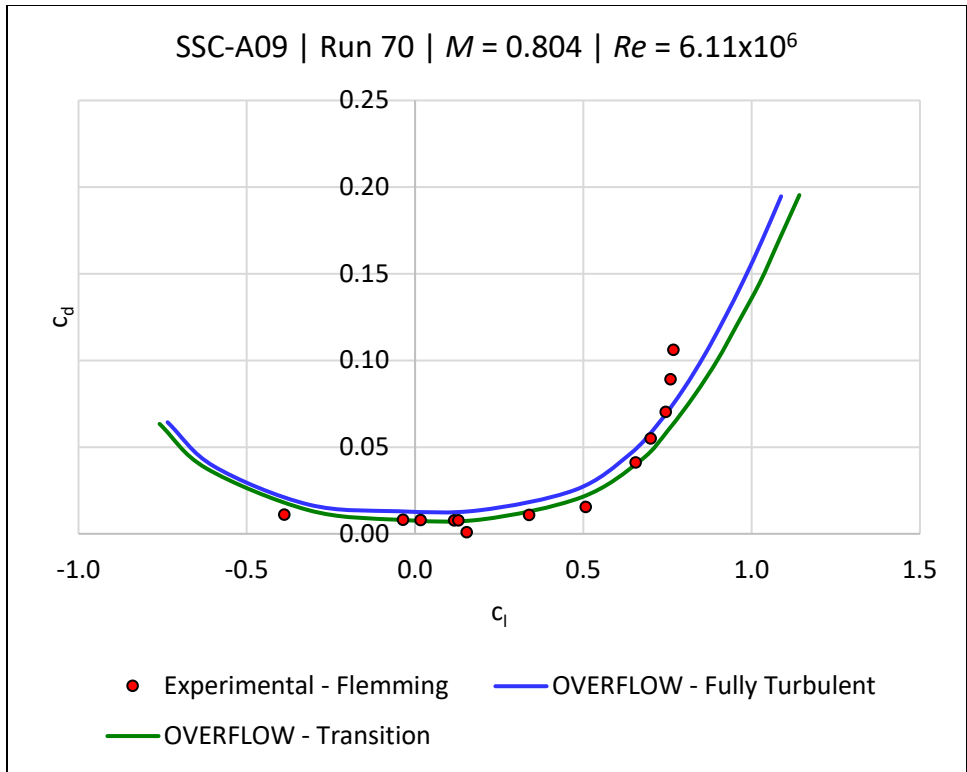


Figure D.21 SSC-A09, Run 70,  $M = 0.804$ ,  $Re = 6.11 \times 10^6$ :  $c_l$  vs  $c_d$ .

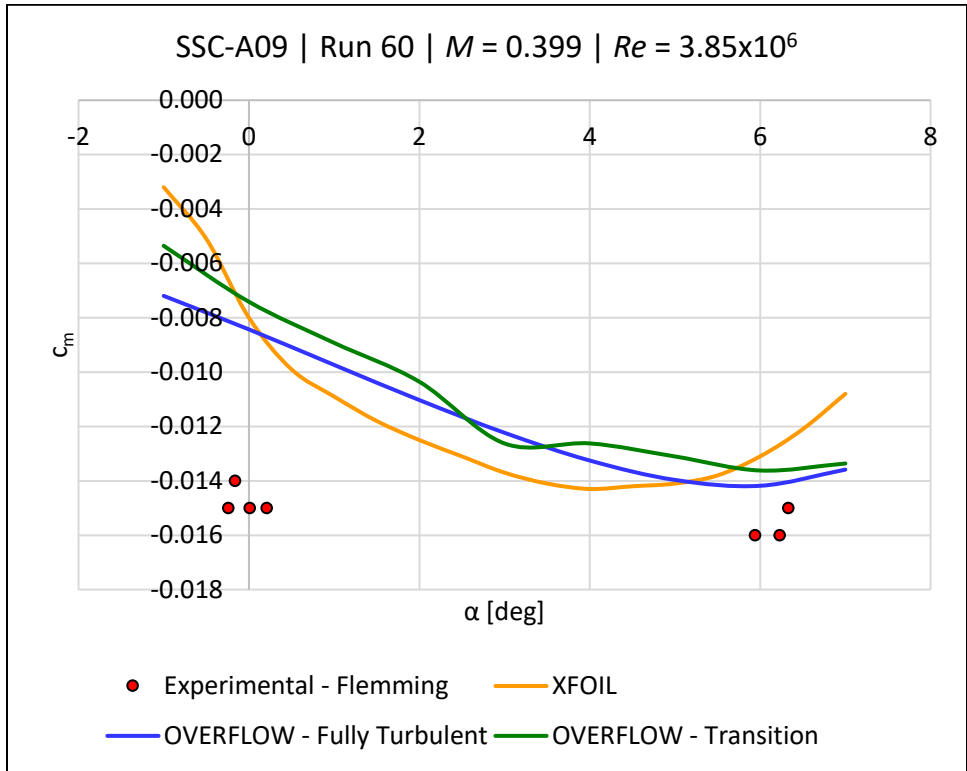


Figure D.22 SSC-A09, Run 60,  $M = 0.399$ ,  $Re = 3.85 \times 10^6$ :  $c_m$  versus  $\alpha$ .

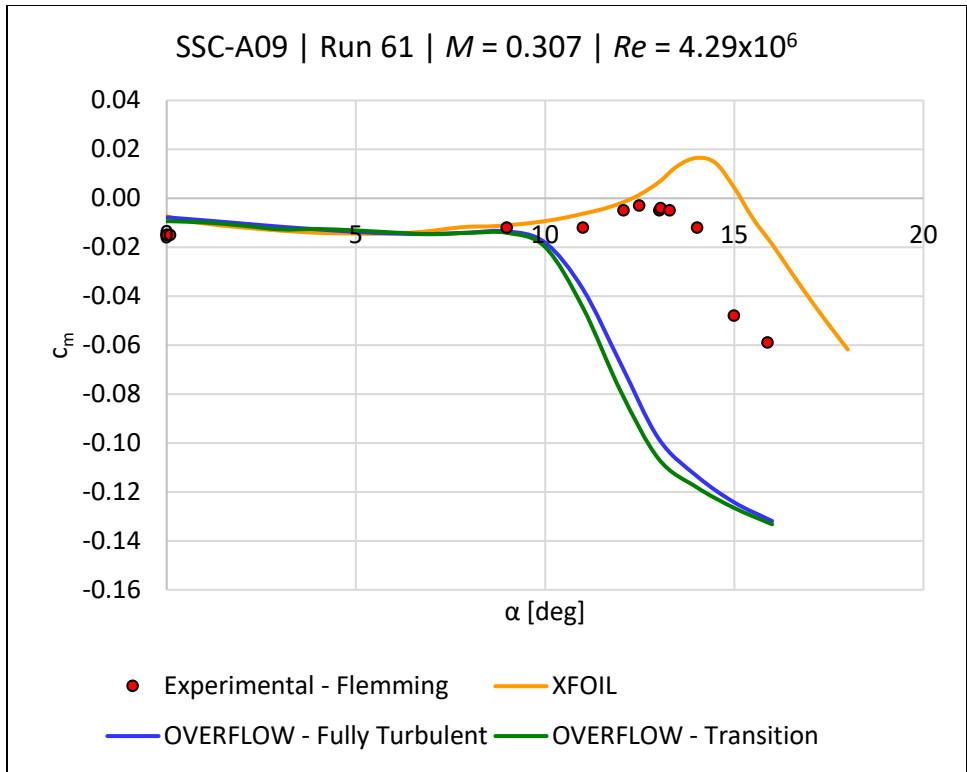


Figure D.23 SSC-A09, Run 61,  $M = 0.307$ ,  $Re = 4.29 \times 10^6$ :  $c_m$  versus  $\alpha$ .

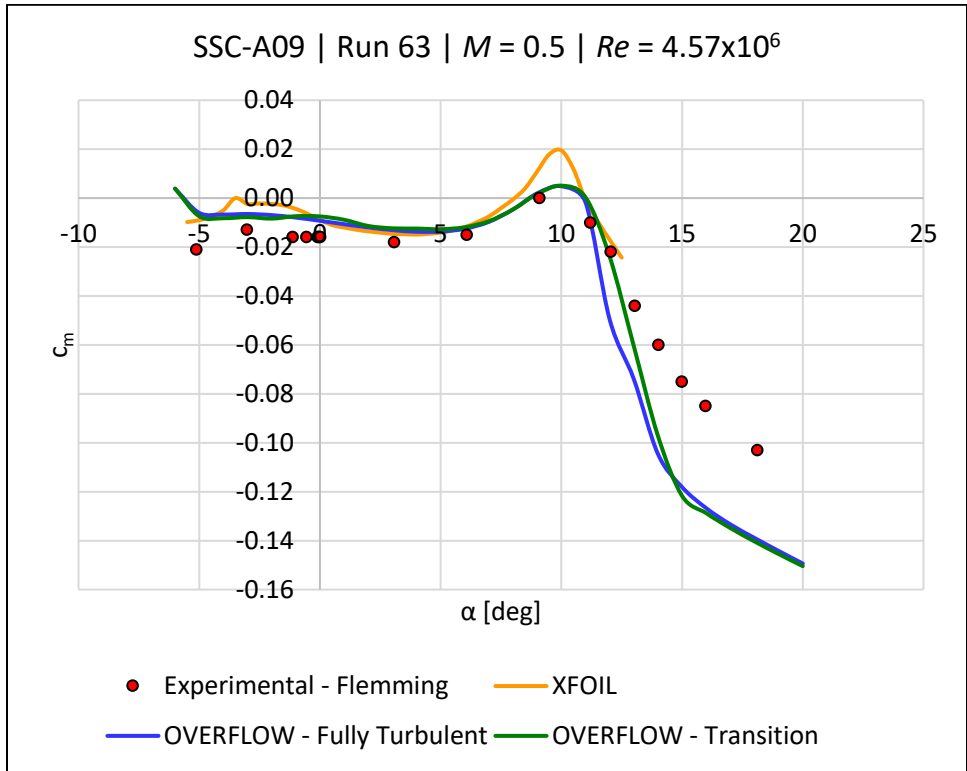


Figure D.24 SSC-A09, Run 63,  $M = 0.5$ ,  $Re = 4.57 \times 10^6$ :  $c_m$  versus  $\alpha$ .

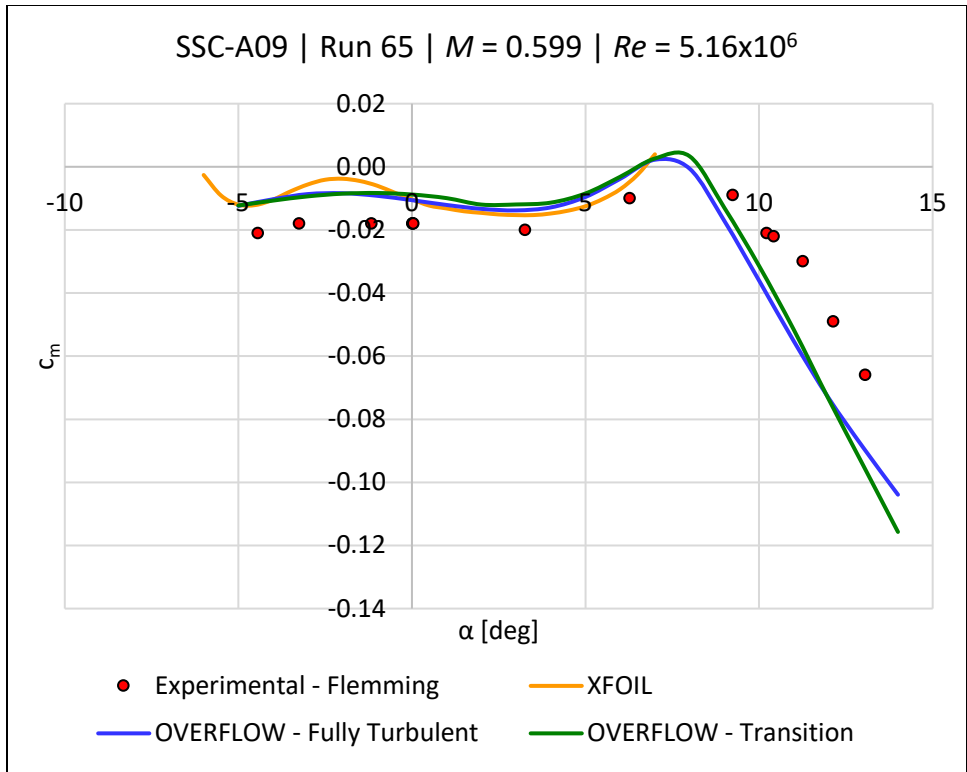


Figure D.25 SSC-A09, Run 65,  $M = 0.599$ ,  $Re = 5.16 \times 10^6$ :  $c_m$  versus  $\alpha$ .

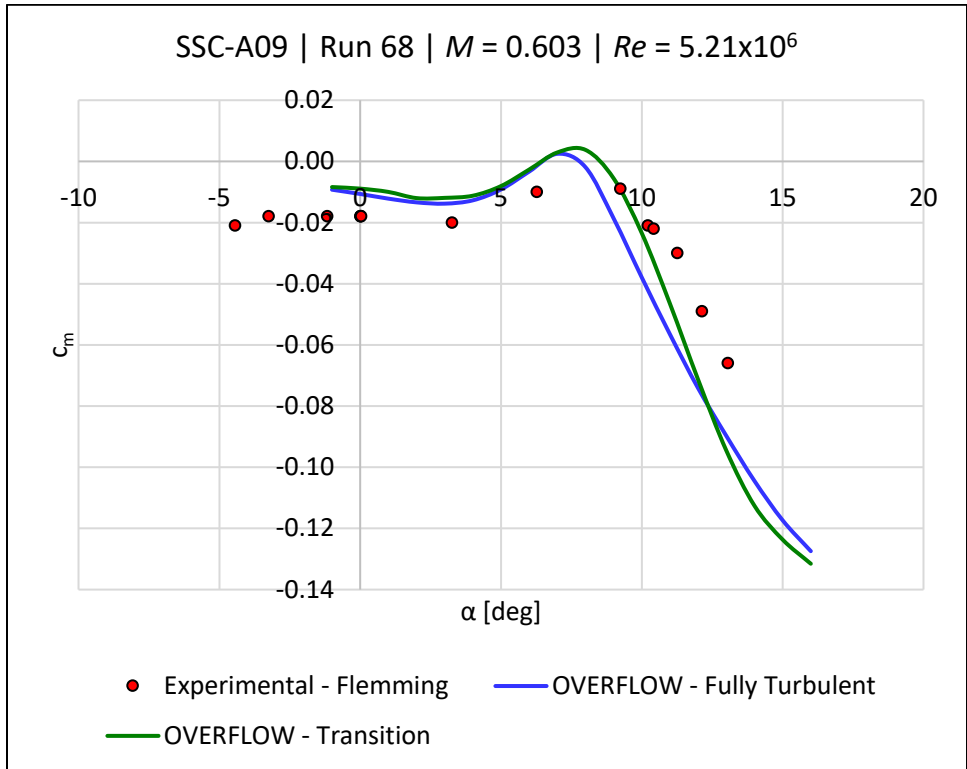


Figure D.26 SSC-A09, Run 68,  $M = 0.603$ ,  $Re = 5.21 \times 10^6$ :  $c_m$  versus  $\alpha$ .

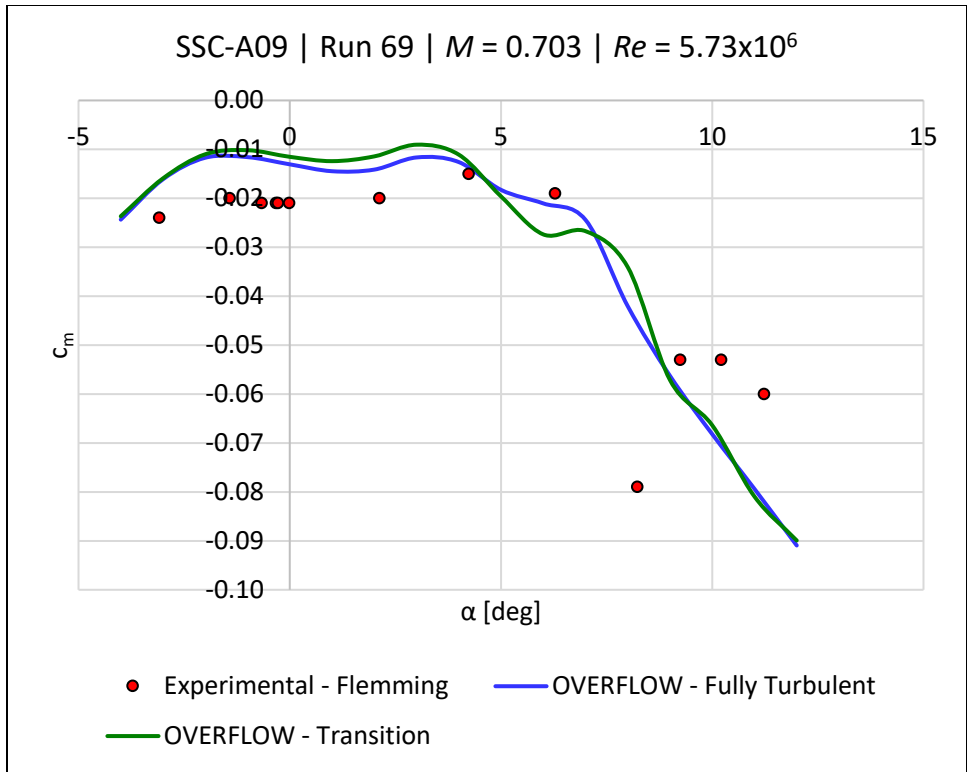


Figure D.27 SSC-A09, Run 69,  $M = 0.703$ ,  $Re = 5.73 \times 10^6$ :  $c_m$  versus  $\alpha$ .

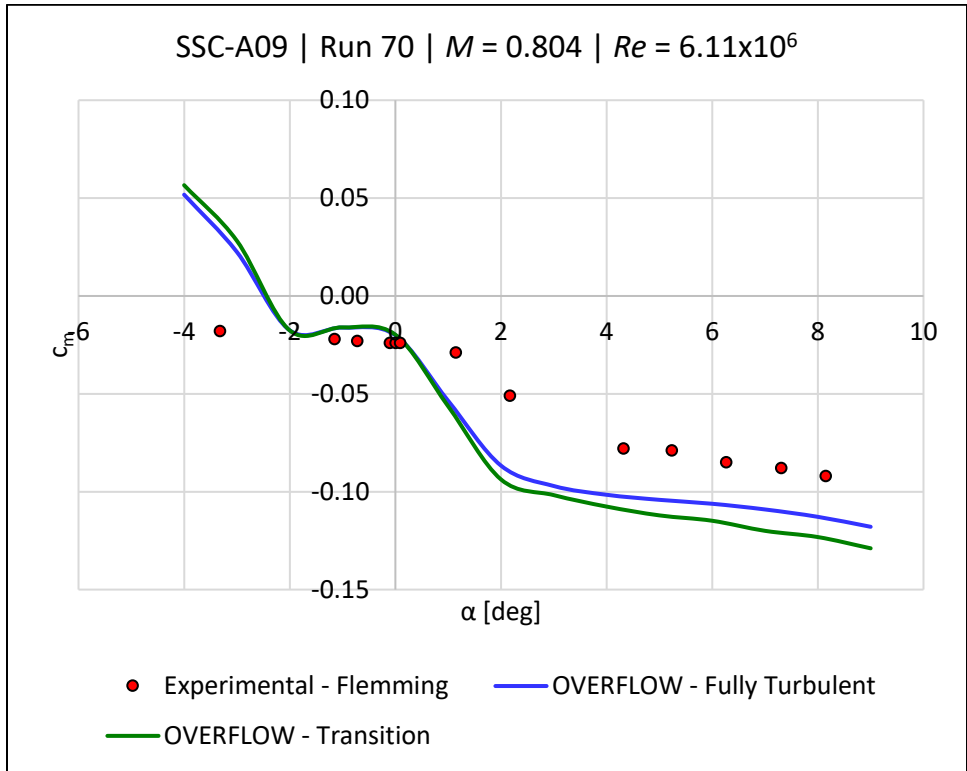


Figure D.28 SSC-A09, Run 70,  $M = 0.804$ ,  $Re = 6.11 \times 10^6$ :  $c_m$  versus  $\alpha$ .